

**Multischaalmodellering van 3D-reactortechnologie
voor verminderde cokesvorming in stoomkraken**

**Multi-Scale Modeling of 3D Reactor Technology
for Reduced Coke Formation in Steam Cracking**

David Van Cauwenberge

**Promotoren: prof. dr. ir. K. Van Geem, prof. dr. ir. G. B. Marin
Proefschrift ingediend tot het behalen van de graad van
Doctor in de ingenieurswetenschappen: chemische technologie**



**UNIVERSITEIT
GENT**

**Vakgroep Materialen, Textiel en Chemische Proceskunde
Voorzitter: prof. dr. P. Kiekens
Faculteit Ingenieurswetenschappen en Architectuur
Academiejaar 2017 - 2018**

ISBN 978-94-6355-065-9
NUR 952
Wettelijk depot: D/2017/10.500/100

EXAMENCOMMISSIE

Leescommissie

Prof. dr. ir. Geraldine J. Heynderickx

Laboratorium voor Chemische Technologie

Vakgroep Materialen, Textiel en Chemische Proceskunde

Faculteit Ingenieurswetenschappen en Architectuur

Universiteit Gent

Prof. dr. ir. Jan Vierendeels

Vakgroep Mechanica van Stroming, Warmte en Verbranding

Faculteit Ingenieurswetenschappen en Architectuur

Universiteit Gent

Prof. dr. ir. Rodney O. Fox

Department of Chemical and Biological Engineering

College of Engineering

Iowa State University

Prof. dr. ir. Georgios D. Stefanidis

Departement Chemische Ingenieurstechnieken

Faculteit Ingenieurswetenschappen

Katholieke Universiteit Leuven

Andere leden

Prof. dr. ir. Kevin M. Van Geem [promotor]

Laboratorium voor Chemische Technologie

Vakgroep Materialen, Textiel en Chemische Proceskunde

Universiteit Gent

Prof. dr. ir. Guy B. Marin [promotor]

Laboratorium voor Chemische Technologie

Vakgroep Materialen, Textiel en Chemische Proceskunde

Universiteit Gent

Ir. Jens Floré [industriële promotor]

Petrochemicals & Derivatives

Chemicals

BASF Antwerpen NV

Prof. dr. ir. Jan Van Campenhout [voorzitter]

Computer Systems Lab

Vakgroep Elektronica en Informatiesystemen

Universiteit Gent

Decaan: Prof. dr. ir. Patrick De Baets

Rector: Prof. dr. ir. Rik Van de Walle

De auteur genoot tijdens de onderzoeksactiviteiten de financiële steun van een Baekeland mandaat van het Agentschap voor Innoveren & Ondernemen Vlaanderen (IWT) in samenwerking met BASF Antwerpen NV.

Acknowledgements

Aan het einde gekomen van mijn doctoraat, had ik graag een dankwoord gericht tot allen die een rechtstreekse of onrechtstreekse, maar in ieder geval onmisbare bijdrage hebben geleverd om dit werk tot stand te brengen.

Vooreerst wens ik uiteraard mijn promotoren prof. Kevin Van Geem en prof. Guy Marin te bedanken voor de kansen en het vertrouwen die ze me geboden hebben gedurende dit doctoraat. Kevin, doorheen de jaren en flinterdunne muren heb ik veel waardering gekregen voor zowel de theoretische als organisatorische vaardigheden die vereist zijn voor een carrière in de wetenschap. Bedankt om mij in beide te helpen groeien, al kostte het hier en daar enkele flessen champagne. Ik wil ook Guy nogmaals bedanken voor de goede verstandhouding en het oog voor detail bij het begeleiden en reviseren van dit werk.

Ik had ook het geluk een derde promotor te hebben in Jens Floré. Je praktische en organisatorische kijk op dit werk maakte een belangrijk deel uit van de ontwikkeling ervan en vormde een grote motivatie om doorheen de voortgangsm meetings vol OpenFOAM-frustraties het doel in zicht te houden. Raf Broers, Guido Demeulemeester, Philippe Van Den Bussche en Dirk Vercauteren wil ik van harte bedanken om zowel bij de meetings als tijdens mijn verblijf in Antwerpen steeds tijd vrij te maken om hun ervaringen te delen. Verder ben ik ook Jos Vankevelaer, Rombout Keldermans, Philippe Alluyn en andere collega's dankbaar om mij steeds welkom te laten voelen in de cracker-familie! Ten slotte wil ik ook Heiner Laib bedanken voor de ondersteuning vanuit Lu en om de vonk te geven tot zowel het bedenken als het tot stand komen van de huidige patentapplicatie.

The opportunity to collaborate with the von Karman Institute was also something I valued greatly. Thanks go out to Marco Virgilio, prof. Tony Arts en prof. Tom Verstraete for the insightful discussions and fruitful collaboration.

Veel dank gaat ook uit naar de thesisstudenten waarvan ik het genoeg heb gehad hen te begeleiden: Pieter V, Laurien, Jens, Moreno en Stef. Waar ik mezelf al zag als eenzame CFD-er, leidde het feit dat jullie telkens bleven plakken intussen tot een mooi team! Hiervoor verdient ook

Carl een pluim, alsook voor zijn belangrijke bijdrage doorheen de eerste jaren van dit doctoraat. In het bijzonder wil ik ook nog Pieter R en Laurien bedanken om steeds “above and beyond” te gaan, het was een plezier om met jullie inzet en genialiteit samen te werken.

Eén van de mooiste aspecten aan het doen van een doctoraat aan het LCT was ongetwijfeld de vele fijne collega’s. Hier mogen naast de studenten zeker ook de “gevestigde waarden” van het LCT niet vergeten worden: Geraldine, Joris, Soise, Petra, Sarah, Stijn, Bert, Michaël, Hans, Erwin, Brecht, Wim, Lambert... Georges wil ik in het bijzonder ook bedanken om ervoor te zorgen dat ons bureau altijd lekker warm bleef door de goed-draaiende workstations.

The warmth of the office was of course never in doubt, given the great colleagues I had the chance to share it with: Yu, Ezgi, Shekhar, and later Ruben DB, Pieter R and Ismaël. You have grown into a group of friends that I hold dearly, along with many others in the TREE group: Natália, Pieter V, Florence, Diana, Ruben VdV, Andres, Carl, Laurien, Jens, Alexander, Moreno, Stijn, Marko, Nenad, Stamatis, Sri Bala, Hans-Heinrich and Arturo. Many thanks also go out to the numerous other colleagues who helped me keep my sanity throughout the difficult times, or who lost it together with me: Kaustav, Kostas, Marita, Roxanne, Daria, Guillermo, Jeroen, Laura, Chanakya, Pieter D, Gilles, Maarten, Stephanie, Lukas, Jonas to name a few.

Graag wil ik ook de vrienden bedanken die me steeds gesteund en van voldoende afleiding voorzien hebben: iedereen van de originele “bende”, de MaChT bende, groep van Dmd en de ploeggenoten van de Flying Spartans. Ten slotte wil ik uiteraard mijn familie en schoonfamilie bedanken die me door dik en dun gesteund hebben. Mijn ouders, die mij steeds alle kansen en vrijheid gaven in mijn studies zonder dat ik me daarvoor om veel zaken moest bekommeren. Mijn broers en zussen, om mij al van jongs af aan te inspireren voor de wetenschap en mij uit te dagen om toch die twee letters meer voor m’n naam te hebben. Bedankt ook Arthur, Hannelore, Kamiel, Jasper, Alexander, Jan, Nora en Annabel om mij zo’n trotse nonkel/peter te maken! Het meest welgemeende woord van dank gaat uiteraard naar mijn vrouw(tje), Roshanak. Bedankt om door je begrip en liefde steeds mijn toevlucht te zijn doorheen deze periode. Het waren misschien niet de gemakkelijkste, maar dankzij jou zeker de mooiste jaren van m’n leven.

David Van Cauwenberge
Gent, 2017

Contents

Notation	VI
Samenvatting	XIV
Summary	XIX
Glossary	XXIV
Chapter 1: Introduction and outline	1
1.1 Introduction	1
1.2 Steam cracking	5
1.3 Enhanced 3D reactor technology	9
1.4 First-principles based simulation	11
1.4.1 Fluid dynamics	12
1.4.2 Chemical kinetics	14
1.5 Outline	15
References	18
Chapter 2: CFD-based design of 3D pyrolysis reactors: RANS vs. LES	23
Abstract	24
2.1 Introduction	24
2.2 Numerical simulation procedure	26
2.2.1 Governing equations	26
2.2.2 Boundary conditions	29
2.2.3 Geometry characteristics	30
2.2.4 Computational grid	31

2.2.5	Solution procedure	33
2.3	Results and discussion.....	34
2.3.1	Pipe flow.....	34
2.3.2	Heat transfer and friction characteristics of enhanced reactor designs	40
2.3.3	Steam cracking reactor simulations.....	50
2.4	Conclusions	53
	References	55
Chapter 3: Numerical and experimental evaluation of heat transfer in helically corrugated tubes		
	Abstract	60
3.1	Introduction	60
3.2	Experimental setup	65
3.2.1	Velocity measurements	65
3.2.2	Heat transfer measurements	66
3.3	Numerical simulation procedure	67
3.3.1	Governing equations.....	67
3.3.2	Turbulence modeling.....	68
3.3.3	Turbulent scalar flux modeling	70
3.3.4	Boundary conditions.....	71
3.3.5	Discretization.....	72
3.4	Results and discussion.....	73
3.4.1	Simulation of the experimental setup.....	73
3.4.2	Fully developed flow characteristics	79
3.5	Conclusions	84
	References	85
Chapter 4: Periodic reactive flow simulation: proof of concept for steam cracking coils		
		89

Abstract	90
4.1 Introduction	90
4.2 Numerical simulation procedure	92
4.2.1 Periodic concept	92
4.2.2 Governing equations.....	101
4.2.3 Chemistry model	103
4.2.4 Computational grid & boundary conditions	103
4.2.5 Solution procedure	105
4.3 Results and discussion.....	107
4.3.1 Bare tubular reactor	109
4.3.2 Finned reactor.....	112
4.3.3 Ribbed reactor	115
4.3.4 Industrial design considerations	118
4.4 Conclusions	121
References	122
Chapter 5: Large-scale computation of industrial naphtha crackers using adaptive detailed chemistry methods.....	125
Abstract	126
5.1 Introduction	127
5.2 SRT-VI furnace simulation	131
5.2.1 Geometry and operating conditions	131
5.2.2 Combustion modeling	135
5.2.3 Radiative heat transfer modeling.....	136
5.2.4 Turbulence modeling and numerical settings.....	139
5.3 Reactor simulation.....	140
5.3.1 Reactor geometry and operating conditions	140

5.3.2	Naphtha representation and kinetic model	142
5.3.3	Dynamic chemistry reduction and tabulation.....	144
5.3.4	Furnace-reactor coupling.....	147
5.4	Results and discussion.....	150
5.4.1	Validation and speedup	150
5.4.2	Furnace simulation results.....	154
5.4.3	Reactor simulation results	163
5.5	Conclusions	170
	References	172
	Chapter 6: Dynamic simulation of fouling in steam cracking reactors using CFD	179
	Abstract	180
6.1	Introduction	180
6.2	CFD model	182
6.2.1	Governing equations.....	182
6.2.2	Chemistry model	183
6.2.3	Numerical model	184
6.2.4	Computational grid and boundary conditions	185
6.2.5	Modeling coke formation	186
6.3	Run length simulation of an industrial propane cracker.....	189
6.3.1	Process conditions and reactor configuration.....	189
6.3.2	Results and discussion.....	191
6.4	Conclusions	204
	References	206
	Chapter 7: Conclusions and perspectives.....	209
7.1	Conclusions	209

7.2	Perspectives	212
7.2.1	Hybrid RANS/LES modeling.....	213
7.2.2	Multi-objective optimization.....	214
7.2.3	Adaptive chemistry methods	214
7.2.4	Coke formation mechanism.....	215
7.2.5	Industrial plant operation.....	215
7.2.6	Combustion modeling	216
	References	219
	Appendix A: EP2017058850 – REACTOR FOR A CRACKING FURNACE.....	221
	Abstract	222
A.1	Field of the invention.....	222
A.2	Background to the invention	222
A.3	Detailed description of invention	224
A.4	Examples	244
A.4.1	Properties and dimensions of dimples.....	244
A.4.2	Exemplary embodiments of dimples.....	246
A.4.3	Results of tested dimple designs.	250
A.4.4	Impact on olefin yields in a steam cracker	253
A.4.5	Self-cleaning effect of the dimpled designs	254
A.5	Summary of the invention	257
A.6	Claims.....	259
	Appendix B: LES grid dependency study	263
	Appendix C: JH-v2 model validation	271
C.1	Pipe flow.....	271
C.2	Square duct flow	272

References	275
------------------	-----

Notation

Roman symbols

A	surface area	[m ²]
A	band absorptance	[m ⁻¹]
A	ISAT mapping gradient matrix	$\frac{\partial R_i(\Psi)}{\partial \Psi_j}$
C _{ε1}	k-ε model constant, C _{ε1} = 1.44	[-]
C _f	skin friction coefficient	$\frac{2\tau_w}{\rho u_b^2}$ [-]
CFL	Courant-Friedrichs-Lewy number	$\sum \frac{u_i \Delta t}{\Delta x_i}$ [-]
c _p	specific heat capacity	[J/kg/K]
D	tube internal diameter	[m]
Da _I	Damköhler number I	$\frac{L_{ref}}{u_{ref}} \frac{ \dot{\omega}_k }{\rho}$ [-]
Da _{III}	Damköhler number III	$\frac{L_{ref}}{u_{ref} T} \frac{ \dot{\omega}_T }{\rho c_p}$ [-]
e	rib/element height	[m]
f _f	Fanning friction factor	$\frac{\Delta p D}{2 \rho u_b^2 L}$ [-]
h	convective heat transfer coefficient	[W/m ² /K]

h	sensible enthalpy	[J/kg]
I	radiation intensity	[W/m ²]
J	mass diffusion flux	[kg/m ² /s]
k	turbulent kinetic energy	[m ² /s ²]
L	mean beam length	[m]
L	periodic module length	[m]
N	discrete number	[-]
Nu	Nusselt number	hD / λ [-]
p	pressure	[Pa]
P	pitch length of a helical structure	[m]
Pr	Prandtl number	$c_p \mu / \lambda$
q	heat flux	[W/m ²]
q_{inc}	incident radiative heat flux	[W/m ²]
Q	thermal power	[W]
r_i	reaction rate of reaction i	[mol/m ³ /s]
R	universal gas constant, $R = 8.314$	[J/mol/K]
R_j	rate of production of species j	[kg/m ³ /s]
Re	Reynolds number	$u_b \rho D / \mu$ [-]
s	stoichiometric ratio	[-]

Sc	Schmidt number	v/D_{ij} [-]
S_h	chemical enthalpy source term	[J/m ³ /s]
T	temperature	[K]
U	global heat transfer coefficient	[W/m ² /K]
u	velocity	[m/s]
u_τ	friction velocity	$(\tau_w / \rho)^{1/2}$ [m/s]
V	volume	[m ³]
x	position	[m]
X	flow separation length	[m]
Y_i	mass fraction of species i	[-]

Greek symbols

α	helix angle	[rad]
β	axial dimensionless pressure gradient	[m ⁻¹]
γ	dimensionless temperature gradient	[m ⁻¹]
Δ	grid spacing	[m]
ε	turbulence dissipation rate	[m ² /s ³]
ε	emissivity	[-]
ε_{tol}	tolerance	[-]

θ	dimensionless temperature	[-]
κ	spectral absorption coefficient	[m ⁻¹]
λ	thermal conductivity	[W/m/K]
λ	wavelength	[μm]
μ	dynamic viscosity	[Pa s]
ν	kinematic viscosity	[m ² /s]
ρ	density	[kg/m ³]
σ	Stefan-Boltzmann constant, $\sigma = 5.67 \times 10^{-8}$	[W/m ² /K ⁴]
σ_s	scattering coefficient	[m ⁻¹]
τ	shear stress	[Pa]
τ	local fluid age / turbulence time scale	[s]
τ	band transmittance	[-]
Φ	scattering phase function	[-]
φ	arbitrary transported variable	
ϕ	local fluid age correction factor	[-]
ψ	compressibility factor	$M_w/(ZRT)$ [-]
ψ	thermochemical state vector	{ Y_1, \dots, Y_N, T, p }
ω	specific turbulence dissipation rate	[s ⁻¹]
Ω	solid angle	[sr]

Abbreviations

ABS	Acrylonitrile Butadiene Styrene
CAD	Computer-Aided Design
CCD	Charge-Coupled Device
CFD	Computational Fluid Dynamics
COP	Coil Outlet Pressure
COT	Coil Outlet Temperature
CPU	Central Processing Unit
CSP	Computational Singular Perturbation
CTO	Coal-To-Olefins
DAC	Dynamic Adaptive Chemistry
(ID)DES	(Improved Delayed) Detached Eddy Simulation
DRG(EP)	Directed Relation Graph (with Error Propagation)
DRSM	Differential Reynolds Stress Model
DOM	Discrete Ordinates Model
EDM	Eddy Dissipation Model
EF	Thermal Enhancement Factor
EFA	Element Flux Analysis

EOA	Ellipsoid Of Accuracy
EWBM	Exponential Wide Band Model
GGD	Generalized Gradient Diffusion
GHG	Greenhouse Gas
ICE-PIC	Invariant Constrained-equilibrium Edge manifold using Pre-Image Curve
ILDM	Intrinsic Low-Dimensional Manifolds
ISAT	In-Situ Adaptive Tabulation
LCT	Liquid Crystal Thermography
LES	Large Eddy Simulation
LM	Log-Mean (Temperature Difference)
MERT	Mixing Element Radiant Tube
ODE	Ordinary Differential Equation
PCA	Principal Component Analysis
PDF	Probability Density Function
PDH	Propane Dehydrogenation
PEA	Partial Equilibrium Assumption
PFA	Path Flux Analysis
PIONA	n-Paraffin – Iso-paraffin – Olefin – Naphthene – Aromatic characterization
PISO	Pressure Implicit with Splitting of Operators algorithm

PIV	Particle Image Velocimetry
PRISM	Piecewise Reusable Implementation of Solution Mapping
PSSA	Pseudo-Steady State Approximation
RANS	Reynolds-averaged Navier-Stokes equations
RCCE	Rate-Controlled Constrained Equilibrium
ROI	Region Of Interest
RTE	Radiative Transfer Equation
SFT	Swirl Flow Tube
SIMPLE	Semi-Implicit Method for Pressure-Linked Equations
SOR	Start-Of-Run
SPBC	Streamwise Periodic Boundary Condition
SRT	Short Residence Time
SST	Shear Stress Transport
TDAC	Tabulated Dynamic Adaptive Chemistry
TLC	Thermochromic Liquid Crystal
TLE	Transfer Line Exchanger
TMT	Tube Metal skin Temperature

Sub- and superscripts

b	bulk quantity
eff	effective, i.e. the sum of laminar and turbulent contributions
f, s	fluid phase, solid phase
fg	flue gas
fu, ox	fuel, oxidizer
i, j, k	running index
int	on the interface between tube metal and flue/process gas
rms	root mean square
SFS	subfilter-scale (cf. subgrid-scale)
t	turbulent contribution
x, r, θ	axial, radial, tangential component
w	wall quantity
τ	based on the friction velocity
+	non-dimensional quantity, scaled by the wall variables
\sim	filtered/time-averaged value
\wedge	periodic component

Samenvatting

De ontdekking van Baekeliet in 1907 door de in Gent geboren Leo Baekeland en de hieruit voortvloeiende introductie van kunststoffen in alle aspecten van ons dagelijkse leven is waarschijnlijk één van de belangrijkste ontwikkelingen van de 20^e eeuw. Ondanks de grote variëteit op vlak van kleuren, vormen, fysische en chemische eigenschappen van deze polymeren, is meer dan 80% van de wereldwijde monomeer productie afkomstig uit één specifiek proces, dat hiermee dus echt aan de grondslag van de chemische industrie ligt. Dit proces waarbij gasvormige of van petroleum afgeleide koolwaterstoffen worden omgezet tot basischemicaliën zoals etheen, propaan, butadieen, benzeen, toluen, xylenen, etc. is beter bekend als stoomkraken. Moderne stoomkrakers zijn werkelijk enorme installaties die tot bijna twee miljoen ton etheen per jaar kunnen produceren.

De endotherme kraakreacties gaan door in buisvormige reactoren gepositioneerd in een oven met aardgasbranders die het procesgas verhitten tot 800-900 °C. Bij deze hoge temperaturen vinden echter ook nevenreacties plaats die resulteren in de afzetting van een laag cokes op de binnenwand van de reactor. Hierdoor wordt de procesvoering aanzienlijk beïnvloed, niet enkel vanwege het risico op verstoppingen in de buis, maar ook door het isolerende effect van de koolstofhoudende laag, waardoor de warmteoverdracht naar het procesgas wordt belemmerd. Commerciële stoomkrakers zijn bijgevolg met regelmatige tussenpozen buiten dienst als het drukverlies over de reactor of de metaaltemperatuur te hoog worden, zodat deze laag cokes afgebrand kan worden door middel van een stoom-luchtmengsel. Deze cyclus van kraken/ontcoken heeft duidelijk een negatief effect op het rendement en de levensduur van de installatie. Onder de verschillende strategieën die onderzocht zijn om cokesvorming te verminderen, richt het huidige werk zich voornamelijk op aanpassingen in de structuur van de reactorbinnenwand in de vorm van zogenaamde 3D-technologie.

De werking van dergelijke gestructureerde buizen steunt op het feit dat cokesvorming een thermisch geactiveerd proces is. Door een verbeterde warmteoverdracht naar het procesgas,

slagen deze alternatieve reactorontwerpen erin de piektemperaturen en de bijhorende hoge vormingssnelheden van cokes te vermijden. De voornaamste controverse rond hun gebruik betreft de hogere drukverliezen die deze structuren veroorzaken ten opzichte van een conventionele gladde buis en de mogelijke negatieve invloed op productopbrengsten die hiermee gepaard gaat. Dergelijke selectiviteitsverliezen zijn moeilijk te kwantificeren op industriële of laboschaal, terwijl klassieke 1D simulaties van nature ongeschikt zijn om verschillen te verklaren die veroorzaakt worden door radiale of tangentiële stromingspatronen. In dit werk wordt bijgevolg gestreefd naar de ontwikkeling van een numeriek simulatiepakket dat er in slaagt de onderliggende 3D stromingen in alternatieve reactorgeometrieën te voorspellen en hun impact op de productopbrengsten en cokesvorming.

Een eerste vraag die zich stelde was het vereiste detail in het modelleren van de turbulente stroming. Hoofdstuk 2 en 3 richten zich om deze reden op een vergelijking tussen een traditionele Reynolds-gemiddelde Navier-Stokes (RANS) simulatie en een simulatie van grote wervelingen (EN: Large Eddy Simulation, LES). Waar de eerste enkel de tijdsgemiddelde stroming beschrijft en dus het globale effect van turbulentie gemodelleerd wordt, worden bij LES de voornaamste turbulente structuren en hun interactie expliciet in rekening gebracht. Deze twee hoofdstukken bevatten tevens de nodige validatiestudies van de gebruikte methodes door vergelijking met geavanceerde numerieke en experimentele datasets voor uiteenlopende configuraties. Hoofdstuk 2 evalueert de volledig ontwikkelde stroming in een longitudinaal gevinde buis en in een commerciële Swirl Flow Tube[®] door het gebruik van periodieke randvoorwaarden in het openbron softwarepakket OpenFOAM. Het potentieel van beide ontwerpen werd bevestigd door een verbetering van de warmteoverdracht met respectievelijk 29% en 37%. Hoewel het $k\omega$ -SST RANS model erin slaagde om deze globale prestaties te voorspellen, legden de lokale stromingspatronen de beperkingen bloot van dergelijke eddy-viscositeit modellen in het beschrijven van stroming met tangentiële snelheden of langs gekromde oppervlakken in het algemeen.

Deze beperkingen waren nog meer uitgesproken voor de helisch geribde buizen in Hoofdstuk 3, aangezien zowel de gegenereerde werveling als de recirculatie van de stroming rond het ribelement een aanzienlijke uitdaging vormen voor klassieke turbulentiemodellen. De gedane

simulaties werden experimenteel gevalideerd door gebruik te maken van de recente PIV (EN: Particle Image Velocimetry) en LCT (EN: Liquid Crystal Thermography) datasets van Mayo et al., vergaard in het von Karman Instituut (VKI). In vergelijking met diverse globale correlaties in de vakliteratuur, zijn dergelijke lokale technieken uitermate waardevol voor het valideren van de lokale fenomenen. Een belangrijke opmerking hierbij is dat het toepassingsdomein van LES met resolutie tot aan de wand nog steeds beperkt is tot Reynoldsgetallen lager dan 10^5 , gezien de rekenkost schaalt met $Re^{13/7}$. Simulatie van industriële stoomkrakers valt hierdoor buiten de huidige mogelijkheden, waardoor de werkelijke waarde van deze fundamentele oplossingsmethoden vooral bestaat uit het verwerven van informatie die een verbetering mogelijk maken van minder rekenintensieve turbulentiemodellen. Dit werd gedemonstreerd door een algebraïsch warmtefluxmodel af te leiden uit de LES gegevens, en dit te combineren met het laag-Reynolds JH-v2 Reynolds-stress-transportmodel (RSTM). Het resulterende model bleek accurater te zijn dan het voorheen gebruikte $k\omega$ -SST model tegen een vergelijkbare rekenkost.

Vanaf Hoofdstuk 4 verschuift de klemtoon naar de combinatie van de stromingsaspecten uit de vorige hoofdstukken met de kinetische modellen die doorheen de jaren werden ontwikkeld aan het Laboratorium voor Chemische Technologie. Door de vrije-radicaalchemie van de pyrolysereacties en de korte kinetische ketenlengtes is het moleculaire spectrum in het procesgas breed, met componenten die reageren over een breed bereik van tijdschalen. Integreren van een dergelijke stelsel van differentiaalvergelijkingen is dus zowel door het aantal vergelijkingen als de numerieke stijfheid ervan een uitdagende opdracht.

In Hoofdstuk 4 wordt hiervoor gecompenseerd door het concept van periodieke randcondities uit te breiden van constante fluïdumeigenschappen naar reactieve stroming. Door middel van een innovatieve transformatie van de ruimte- en tijdsdimensies kan een volledige reactorsimulatie gereduceerd worden tot een klein rekenvolume, wat resulteert in een rekentijd die met één tot zelfs twee grootteordes afneemt. Ondanks de benaderende aard van de methode werd bevestigd dat alle belangrijke productopbrengsten met een relatieve fout van minder dan 1% konden voorspeld worden in vergelijking met de volledige reactorsimulatie. De methode werd vervolgens toegepast in de RANS-simulatie van een industriële propaankraker voor drie verschillende geometrische configuraties, namelijk een gladde buis en twee voorbeelden van 3D-technologie:

een longitudinaal gevinde buis en een buis met een rib loodrecht op de stromingsrichting. Hoewel de rib leidde tot een drukverlies dat een factor vier hoger lag dan voor de gladde buis, was de impact op de totale selectiviteit naar olefinen positief, aangezien een 2,0 rel.% verlies aan etheen werd gecompenseerd door een 3,2 rel.% toename van propeenopbrengsten. Voor de gevinde buis werd een omgekeerd effect voorspeld, waarbij etheen toenam met 0,7 rel.% maar propeen afnam met 1,4 rel.%. Deze verschillende invloed kan verklaard worden door de minder uitgesproken radiale temperatuur- en concentratieprofielen in de geribde buis, terwijl de overmatige temperatuur in de volumes tussen opeenvolgende vinnen in de gevinde buis leidden tot het secundair kraken van propeen. Over het geheel genomen werden deze trends accuraat voorspeld door middel van de periodieke methode, wat diens potentieel illustreert als een efficiënt hulpmiddel voor het screenen van 3D-technologie of zelfs voor het toegankelijk maken van meer fundamentele modellen op vlak van kinetiek of turbulentiemodellering in bestaande simulaties.

Naast een reductie van het rekendomein werd in Hoofdstuk 5 ook gekeken hoe het oplossen van de kinetische modellen efficiënter gemaakt kan worden door gebruik van in-situ optimalisatie. Dit leidde tot een nieuwe chemieroutine in OpenFOAM, waarin in-situ adaptieve tabellering (ISAT) gecombineerd wordt met dynamische netwerkreductie en de pseudostationaire toestandshypothese (PSSA) voor de β -radicalen. Validatie voor een 2D-axisymmetrische simulatie van een propaanstoomkraker toonde de duidelijke synergie tussen de drie in-situ methodes aan, wat resulteerde in een reductie van de rekenkost met een factor 50-200. De ontwikkelde routines werden vervolgens gebruikt voor het evalueren van een helisch geribd reactorontwerp in een industriële SRT-VI naftakraker, waarbij gebruik gemaakt werd van een complex reactienetwerk bestaande uit 152 componenten en 1994 elementaire reacties. Realistische warmtefluxprofielen voor deze simulaties werden verkregen door een 3D-3D koppeling met de stralingssectie van de oven, waarbij straling in rekening gebracht werd door middel van de discrete-ordinaatmethode (DOM) met een exponentieel breedbandmodel voor de stralingseigenschappen van het rookgas. Hieruit werd gezien dat het rookgas geen afschermend effect vertoonde maar zelfs verantwoordelijk is voor 12% van de directe straling naar de reactoren, waarbij het merendeel afkomstig is van de ovenwand. In vergelijking met de gladde reactor vertoonde de geribde reactor 36% lagere cokesvorming aan het begin van de looptijd, ten koste van een 2,9 maal hoger drukverlies. Ondanks dit duidelijk ongewenste effect resulteerde dit

niet in lagere productopbrengsten. Het compenserende effect van verbeterde radiale menging leidde zelfs tot een totale opbrengst olefinen die 0,2 rel.% hoger lag dan bij de gladde reactor.

Doorheen het merendeel van dit werk bleef een belangrijke vraag onbeantwoord, namelijk de manier waarop de prestaties van de alternatieve reactoren evolueren onder invloed van de groeiende laag cokes. Dit werd behandeld in Hoofdstuk 6, waar niet enkel de prestaties aan het begin van de looptijd vergeleken werden. Door het numerieke rekenrooster te vervormen volgens de aangroeiende cokes, werd het mogelijk diens impact op drukverliezen, wandtemperaturen en selectiviteit te kwantificeren. Een vergelijking tussen een glad, gevind en geribd reactorontwerp voor een Millisecond propaankraker illustreerde de inzichten die hieruit volgen, aangezien de verschillende ontwerpen een zeer uiteenlopende evolutie kenden. Hoewel de geribde reactor van bij het begin hoge drukverliezen kent, leiden de lagere wandtemperaturen en de lokale cokesvorming achter het rib-element tot een vrij gelimiteerde toename van de drukverliezen over de 12 dagen looptijd. Voor de gladde en gevindde buizen daarentegen werd reeds na respectievelijk 6 en 8 dagen het einde van de looptijd bereikt, op welk punt hun drukverliezen reeds groter waren dan die van het geribde ontwerp. Het gepresenteerde algoritme is bijgevolg van groot belang bij het beoordelen van het ware industriële potentieel van 3D-technologie voor stoomkraakreactoren.

De inzichten vergaard doorheen dit werk hebben tevens geleid tot een octrooiaanvraag voor een nieuw reactorontwerp. Het ontwerp, zoals beschreven in Appendix A, bestaat uit patronen van concave structuren op het inwendige buisoppervlak. Een parametrische studie over variërende diepte, vorm, patroon en bedekkingsgraad illustreerde potentiële verbeteringen in warmteoverdracht van meer dan 50%. Het ontwerp is aldus vooral veelbelovend voor toepassing in installaties die slechts een beperkte inlaatdruk toelaten en dus geen optimaal gebruik kunnen maken van de bestaande 3D-technologieën. Reactieve simulatie van een industriële propaankraker bevestigde dit potentieel door middel van 45 K lagere wandtemperaturen bij het begin van de looptijd, 39% lagere snelheid van cokesvorming en een opvallende 0,3 rel% verbetering in olefinenopbrengst ten opzichte van een gladde buis. De geprofileerde buis bleek ook aanleiding te geven tot secundaire stromingspatronen die kunnen helpen bij het verwijderen van reeds opgebouwde cokes van de reactorwand, zo bijdragend tot een zelfreinigend effect.

Summary

Arguably one of the biggest inventions of the 20th century, the discovery of Baekelite by Leo Baekeland in 1907 led to plastics being integrated in every aspect of our daily lives since. Despite the broad variety in color, shape, physical and chemical properties of these polymers, over 80% of global monomer feedstock originates from a single process that is hence truly at the foundation of the chemical industry. This process is steam cracking of hydrocarbons from various gaseous or crude oil derived feedstocks, aimed at the production of base chemicals such as ethene, propene, butadiene, benzene, toluene, xylenes, etc. Nowadays, grassroots steam crackers are truly enormous constructions that can produce nearly two million metric tons of ethene per year.

The cracking reactions take place in tubular reactors suspended in a gas-fired furnace that provides the necessary heat for the endothermic reactions, at process gas temperatures of 800-900 °C. At these elevated temperatures, undesired side reactions occur, resulting in the formation of a carbonaceous coke layer on the reactor inner wall. This has a major impact on the process operation as it not only carries the risk of clogging the tube but it also acts as an insulation layer, hampering the heat transfer to the process gas. Commercial steam crackers are taken out of service at regular intervals when the pressure drop or metal temperature become too high, in order to burn off the coke layer with a steam/air mixture. This cyclic operation of cracking/decoking clearly influences the economics and the service life of the installation negatively. Among the different approaches that have been investigated to reduce coke formation, the present work focuses on structural enhancements of the inner wall of the reactor, so-called 3D technologies.

The operational improvements induced by these kind of profiled tubes are based on the fact that coke formation is a thermally activated process. By facilitating heat transfer to the process gas, the designs can reduce the peak temperatures and consequently also reduce the rate of coke formation. The main controversy surrounding the use of enhanced designs is the potentially

negative impact on product yields due to the increased pressure drop compared to a conventional bare tube. These losses in product selectivity are difficult to quantify experimentally or on pilot plant level, while the classical 1D simulation tools inherently fail to account for such enhanced radial and azimuthal flow patterns. The present work hence strives to develop a numerical simulation tool that accounts in detail for the underlying 3D fluid dynamics in order to obtain quantitative predictions of product yields and coke formation in a wide range of enhanced reactor geometries.

The first question to be addressed concerns the necessary level of detail in modeling the prevalent turbulent phenomena. Chapter 2 and 3 focus on comparing traditional Reynolds-averaged Navier-Stokes (RANS) simulation with large eddy simulation (LES). The former only considers averaged flow fields and hence models the effect of turbulence in its entirety while the latter explicitly resolves a large fraction of the turbulent structures and their interaction. These chapters also provide the necessary validation of the applied methods through comparison with direct numerical simulation (DNS) data and various experimental studies for different flow configurations. A streamwise periodic methodology was implemented in the open-source CFD package OpenFOAM and applied in Chapter 2 to assess the cold-flow performance of a longitudinally finned tube and a commercial Swirl Flow Tube[®] (SFT[®]). The potential of both geometries was confirmed with heat transfer improvements of respectively 29% and 37%. While the $k\omega$ -SST RANS model succeeded in predicting this global performance, investigation of the local flow features revealed the limitations of such eddy-viscosity based models in predicting swirling flow and flow along curved surfaces in general.

These limitations were even more pronounced in the helically ribbed tubes studied in Chapter 3, as both the generated swirl and the flow separation in the wake of the rib element provide a significant challenge for any two-equation turbulence model. Experimental validation was provided by a recent particle image velocimetry (PIV) and liquid crystal thermography (LCT) dataset of Mayo et al. obtained at the von Karman Institute for Fluid Dynamics. In contrast to the variety of literature reports on the global flow properties, the experimental techniques used by Mayo et al. provide local information that was especially valuable in providing a strong validation for the simulations. Important to consider is the fact that wall-resolved LES is still

limited to moderate Reynolds numbers of below 10^5 as the computational cost scales with $Re^{13/7}$. As Reynolds numbers inside industrial steam cracking reactors are typically higher, the value of the performed high-fidelity simulations lies also in the acquisition of data that can improve the accuracy of less computationally demanding turbulence modeling approaches. This was demonstrated by using a Reynolds stress transport model in combination with an algebraic heat flux model for which the coefficients were obtained from the LES data. The resulting model was seen to perform significantly better than the two-equation $k\omega$ -SST model over a broad range of Reynolds numbers, at a comparable computational cost.

From Chapter 4, the focus shifts to the efficient integration of the fluid dynamics elements of the previous chapters with the chemistry routines developed over the years at the Laboratory for Chemical Technology. Given the free-radical nature of the pyrolysis reactions and the short kinetic chain lengths, the molecular spectrum in the process gas is broad and has species reacting over a wide range of time scales. Integration of the resulting system of ordinary differential equations is hence challenging both in terms of the size and the stiffness.

In Chapter 4, efficiency gains are achieved by extending the concept of streamwise periodicity from constant-property flows to non-equilibrium reacting flows. Through an innovative transformation of the space and time domains, only a small volume of fluid over time is required for the simulation of a full scale reactor, resulting in decreases in computational cost of one to two orders of magnitude without loss of accuracy. Despite the approximate nature of the method, all major product yields were predicted to be within 1% relative error compared to the full reactor simulation. The approach was applied in the RANS simulation of an industrial propane cracker with three different geometrical configurations, namely a bare tube and two examples of 3D technology: a longitudinally finned tube and a tube with a rib perpendicular to the flow direction. While the rib was seen to increase the pressure drop by close to a factor four relative to the bare tube, the impact on total olefin selectivity was positive, as a 2% relative loss of ethene yield was compensated by a 3.2% relative increase in propene yield. For the finned tube, ethene was seen to increase by 0.7% rel., while propene decreased by 1.4% rel.. The reversed impact can be explained from the more uniform radial temperature and concentration profiles in the ribbed tube, while the finned tube has large regions of elevated temperatures in between subsequent fins,

where considerable secondary cracking of propene takes place. Overall, these differences were well predicted using the periodic approach, indicating its versatility as an efficient 3D reactor screening tool, or even allowing the inclusion of a higher level of theory in existing simulations, such as more complex kinetic mechanisms or even LES turbulence modeling.

While Chapter 4 focused on the potential for speedup through reduction of the computational domain, Chapter 5 investigates how the computational cost can be decreased by implementing the cracking kinetics more efficiently using on-the-fly techniques. This led to a new chemistry library in OpenFOAM, combining in-situ adaptive rate tabulation with dynamic chemistry reduction, while applying the pseudo-steady state approximation to reduce the stiffness of the resulting set of equations. Validation on a 2D axisymmetric simulation of a propane steam cracker demonstrated speedup factors of 50 – 200, as the three on-the-fly methods clearly exhibited strong synergy. The developed library was used to evaluate a helically ribbed reactor geometry for an industrial SRT-VI naphtha cracker using a reaction network consisting of 152 species and 1994 elementary reactions. Realistic heat flux profiles for these simulations were obtained by performing a 3D-3D coupling with the radiant section of the furnace, in which radiation was accounted for in detail by using a discrete ordinates method with an exponential wide band model for the flue gas radiative properties. No shielding effect of the flue gas was observed, as it in fact contributed about 12% of the total direct radiative heat flux towards the tubes, with the majority originating from the refractory walls. Comparison of the helically ribbed reactor with a bare reactor showed a 36% reduction in the rate of coke formation at start-of-run conditions for the former, at the cost of a 2.9 times higher pressure drop. Despite this obviously detrimental effect, no product losses were observed, as the total olefin yield was 0.2 rel.% higher than for the bare reactor due to the compensating effect of improved radial mixing.

A challenge that remained to be addressed is the manner in which the performance of the enhanced reactors is affected over time by the deposition of coke. Chapter 6 achieves this by not only considering start-of-run performance but adapting the computational grid to include the growth of the coke layer and its impact on pressure drop, reactor wall temperatures and product selectivities. Comparison of a bare, finned and ribbed reactor design for a Millisecond propane cracker illustrated the value of this approach, as the different designs were seen to exhibit very

different fouling behavior. While the ribbed reactor has a high base pressure drop, the reduced wall temperatures and the high coke formation in the wake of the element, lead to only a minor increase in pressure drop throughout the roughly 12 days on stream. The bare and finned tubes reach their end-of-run condition already after respectively 6 and 8 days, at which point their pressure drop exceeds that of the ribbed design. The presented methodology is hence crucial in assessing the true potential of enhanced 3D steam cracking reactors in commercial operation.

The insights obtained throughout the core chapters of this thesis, also led to a patent application for a novel tubular reactor design. The design, as described in Appendix A, consists of a plurality of concave dimples on the internal tube surface. A parametric study covering various dimple depths, shapes, patterns and coverages illustrated potential heat transfer improvements of over 50%. The enhancement is especially promising for use in commercial operating units that are pressure limited and hence cannot use current 3D techniques. Reactive simulation of an industrial propane cracker confirmed this potential, as 45 K lower start-of-run metal temperatures, a 39% lower coking rate and a remarkable 0.3 rel% increase of olefin selectivity relative to a bare reactor tube were observed. The dimpled tubes were also seen to induce interesting secondary flow structures that may aid in removing coke that is already built up on the reactor surface, i.e. providing a self-cleaning effect.

Glossary

β radical	A radical that undergoes both mono- and bimolecular reactions, in the present work assumed to include all radicals with less than 6 carbon atoms.
3D reactor technology	The use of reactor designs that enhance heat transfer by means of geometrical modifications to the internal surface of a traditional bare tubular reactor.
Ab initio	Methods derived from first principles, without use of empirical models or parameters. For example computational chemistry, where the energy of a molecule or transition state is determined by solving the Schrödinger equation.
Absorption band	A spectral wavelength range in which a gas emits and absorbs radiation due to a state transition of the atom or molecule.
Choked flow	A compressible flow effect causing the velocity of a fluid to become independent of the pressure downstream of a flow restriction, for example a Venturi nozzle or orifice plate.
COILSIM1D	Fundamental model for the 1D simulation of steam cracking units, developed at the Laboratory for Chemical Technology of Ghent University. Includes the single-event microkinetic CRACKSIM model to describe the gas-phase reactions.

Coke	Solid carbonaceous deposit on the internal surface of the reactor and downstream equipment.
Computational fluid dynamics	A branch of fluid mechanics that uses numerical methods and algorithms to solve and analyze problems that involve fluid flow.
Eddy viscosity	A first-moment turbulence closure, relying on the Boussinesq assumption that transfer of momentum by turbulent eddies can be related to the mean velocity gradients with an eddy viscosity proportionality factor.
Emissivity	The effectiveness of a material in emitting radiative energy compared to a black body at the same temperature.
Feedstock reconstruction	Deriving the detailed composition of a complex feedstock from limited macroscopic information.
Flow separation	Detachment of the laminar or turbulent boundary layer from a solid surface under the influence of an adverse pressure gradient. The separation/reattachment point is defined as the point where the flow reverses direction and the local wall shear stress is zero.
Group additivity	A set of techniques that allows the prediction of thermodynamic, kinetic or transport properties from the molecular structure. For example, within Benson's group additivity method a property can be written as a sum of contributions arising from its constituent groups.

Large Eddy Simulation	A 3D simulation approach in which the large energy-containing eddies are resolved and the effects of subgrid-scale eddies, which are more universal in nature, are parameterized. (LES)
Liquid crystal	A state of matter in which molecules sustain flow while also being aligned in regular patterns. Thermochromic LCs exhibit a periodic spacing that depends on the temperature, causing different wavelengths to be reflected.
Low-Reynolds model	A turbulence model that can be integrated all the way down to a solid surface due to the use of damping functions or variable model coefficients. Also known as near-wall models, these do not require the use of wall-functions.
Lumping	Grouping of species with similar reactivity, generally isomers or homologous species, in order to reduce the total number of species in a kinetic model.
Non-gray gas model	A model for gas radiative properties which expresses the absorption coefficient as a function of the wavelength.
Particle Image Velocimetry	A nonintrusive optical method for velocity measurement in a fluid, based on the displacement of tracer particles between image pairs.
Pseudo-steady state approximation	The approximation that the rates of consumption and production of a species are equal, allowing its concentration to be derived algebraically from the remaining species in the mechanism.

Pyrolysis	The uncatalyzed decomposition of organic components resulting from exposure to high temperature, in the absence of molecular oxygen or steam.
Reynolds-Averaged Navier-Stokes	The equations that result from Reynolds decomposition and time-averaging of the Navier-Stokes equation. (RANS)
Reynolds stress	A “stress” tensor obtained from the Reynolds-averaging of the convective momentum transport by turbulent fluctuations. Solving transport equations for its six components constitutes a second-moment turbulence closure.
Run length	Time of operation of a steam cracking furnace between subsequent decoking operations.
Single-Event MicroKinetic model	A kinetic model that consists of elementary reactions and accounts for all energetically equivalent reaction paths, i.e. single-events, to determine each reaction rate. (SEMK)
Skeletal mechanism	A reduced subset of the species and reactions of a detailed kinetic model that is still able to describe the chemistry with a sufficient level of accuracy over the relevant thermochemical space.
SnappyHexMesh	A parallel grid generation utility that is part of the official OpenFOAM code. It uses octree refinement to divide each computational cell of a Cartesian background grid into $(2^n)^m$ smaller cells, with n the dimensionality of the domain (2 or 3) and m the desired refinement level based on its proximity to a

	solid surface or region of interest.
Spectral window	A spectral wavelength range where the medium does not participate in radiative transfer, also called transparent band.
Steam cracking	A petrochemical process in which saturated hydrocarbons are converted into small unsaturated hydrocarbons by exposure to high temperature in the presence of steam.
Stiffness	Numerical instability in the solution of a system of differential equations. It is characterized by a large disparity in the eigenvalues of the Jacobian.
Swirl flow	A flow with a strong azimuthal velocity component.
Turbulence model	A model to account for the effects of turbulent interactions that are not explicitly resolved in the simulation.
Wall function	Empirical model to circumvent solution of the near-wall region by imposing boundary conditions for the momentum, energy and turbulence transport equations. Standard wall functions are based on the log-law and are hence only accurate for $y^+ > 30$.
Wall shear stress	Component of stress coplanar with a solid wall. For a Newtonian fluid, it is the product of the dynamic viscosity and the derivative normal to the surface of the flow velocity.
y^+	Distance to a solid boundary or “wall”, made dimensionless with the friction velocity u_τ and the kinematic viscosity ν . Velocity

and wall distance scale linearly in the viscous sublayer where $y^+ < 5$. In the outer layer where $y^+ > 30$, velocity is proportional to the logarithm of the wall distance, the so-called law of the wall.

1

Introduction and outline

“I was trying to make something really hard, but then I thought I should make something really soft instead, that could be molded into different shapes.”

Leo Baekeland (Gent BE, 1863 – Beacon NY, 1944)

1.1 Introduction

Arguably one of the biggest inventions of the century, the Belgian Leo Baekeland derived the first synthetic plastic, Bakelite, in 1907. In the years that followed, his work opened the floodgates to a torrent of now familiar plastics, such as polystyrene, polyester, polyvinylchloride, polyethylene and nylon. Initially a thing of glamour, their mass production and introduction in every aspect of life has since made plastics synonymous with “cheap” and “disposable”. A growing public environmental awareness and some very visible issues such as ocean pollution, understandably has people and policy makers wondering whether it is time to cut down on their use. Notwithstanding the need for improved global waste management and recycling strategies however, the negative image of plastics in comparison with other materials is in fact quite unwarranted.

Despite the majority originating from non-renewable resources, plastics account for just 4% of global fossil fuel consumption with over 85% still being combusted for transportation, heating and power generation purposes¹. Paradoxically, producing plastics was found to actually reduce

the overall consumption of fossil fuels and greenhouse gas (GHG) emissions. In the European Denkstatt study of 2010, which is still the broadest available on the matter, 173 different products covering approximately 75% of the plastics market were analyzed with regards to the impact of substituting plastics with alternative competing materials over a full life-cycle². Their conservative estimates show a 3.7 times greater mass for the same functional units, an annual 57% (2.420 GJ/a) increase in energy consumption and 61% (124 Mt/a) increase in GHG emissions if plastics were substituted to a theoretical maximum. These savings are equivalent to 39% of the EU15 Kyoto target regarding the reduction of GHG emissions. In addition to these life-cycle benefits, some plastic products also enable energy savings by economizing their end-product. Examples are insulation materials for household energy savings, wind-power rotor blades or plastic packaging materials that reduce food waste or damage to durable goods.

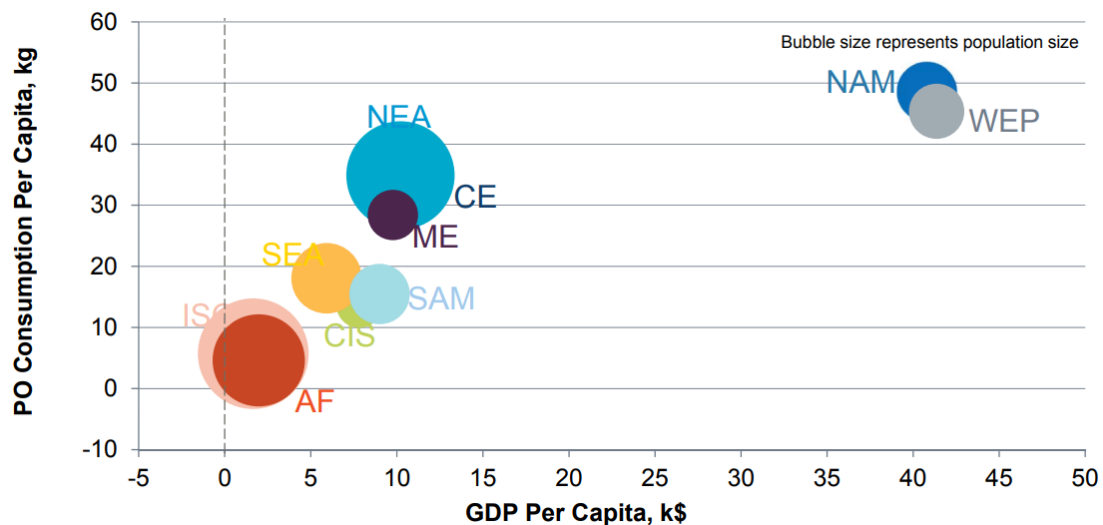


Figure 1-1: Global consumption of polyolefins in relation with GDP per capita³.

In light of these benefits, there is clearly no debate that plastics will continue to be the material of the 21st century. Figure 1-1 shows the per capita consumption of polyolefins in function of the GDP per capita³. Significant market potential can be seen in countries with rapid industrialization and economic growth such as China and especially India. As a result of these global demand drivers, the total commodity plastic market is projected to reach USD 493 billion annually by 2022 with a 5.56% compound annual growth rate between 2016-2022⁴. Looking at the market distribution on Figure 1-2, the largest share by polymer type is occupied by low and high density

polyethylene. The importance of ethylene becomes even more clear when considering that also the vinyl chloride monomer in PVC, ethylene glycol for PET and styrene for PS are derived from this building block molecule. In fact even PP and ABS owe their existence to ethylene, as historically the propylene, butadiene and benzene needed for their production, were merely “by-products” of ethylene production.

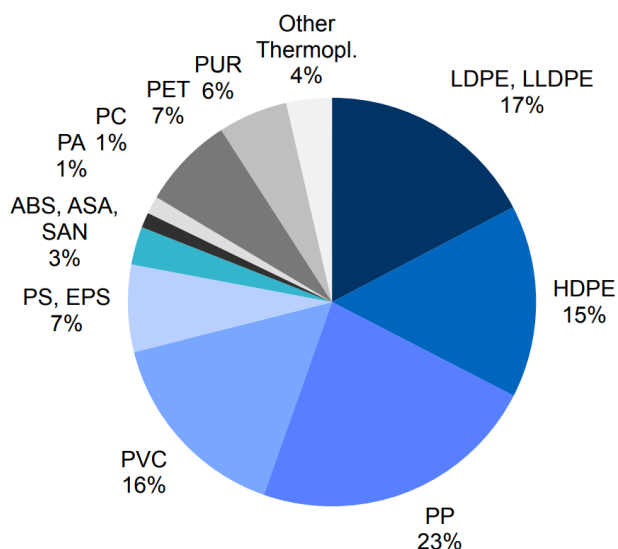


Figure 1-2: Global plastics material demand by polymer type (2015)¹

While monomers make up about two-thirds of the ethylene and propylene market, epoxides and acrylic derivatives also make up a large share, with many important applications as surfactants, coatings or paints. The predominant production processes for all these building block chemicals are shown in Figure 1-3, along with the typical product distribution of each. This picture becomes especially relevant in light of the evolving global energy landscape. In the U.S. the abundance of cheap ethane from shale gas exploitation has revived the local ethylene industry and incited a shift towards lighter feedstocks with lower product propylene-to-ethylene ratios. Combined with the fact that the propylene market grows almost 20% faster than that of ethylene, traditional cracking methods will likely be unable to keep pace with propylene demand.

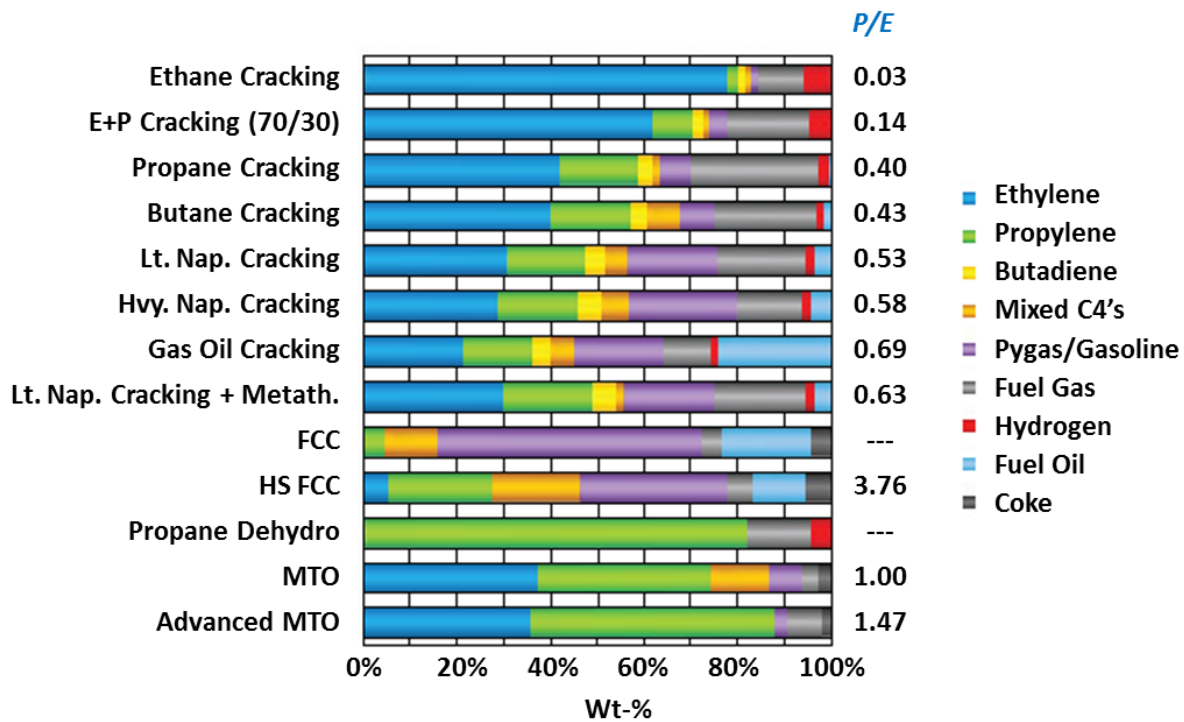


Figure 1-3: Product spectrum of the most common light olefin production processes⁵.

The resulting “propylene gap” has spurred interest in on-purpose production methods, primarily propane dehydrogenation (PDH) and Chinese coal-to-olefins plants (CTO). Around 60 such projects are scheduled to come online in the 2016-2020 timeframe⁶, as shown in Figure 1-4. While these production routes are certain to have an increased share in the future, some investments are being pushed back due to the currently low oil prices⁷. Traditional naphtha cracking in Europe and North-Asia in fact found renewed competitiveness and near-record margins throughout 2015-2016 because of the high propylene yields and low feedstock prices.

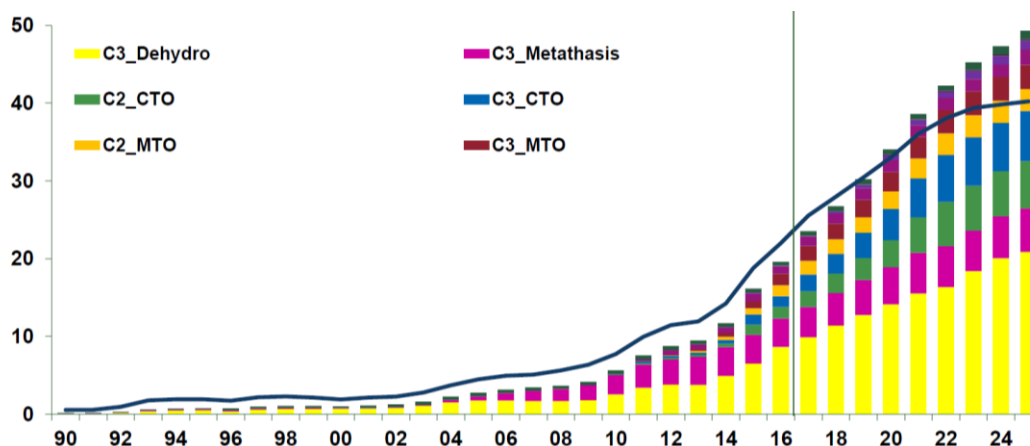


Figure 1-4: Non-conventional light olefin supply by process (million metric tons)⁸.

It is clear that despite the magnitude of the ethylene industry, the fact that it is at the start of the chemicals value chain makes it inextricably linked to the local and global energy market. With the revolution of unconventional energy sources, increased environmental awareness and political uncertainties, the current volatility in olefin margins can be expected to persist in coming years. In this dynamic landscape, the main challenge for the industry will hence lie in the proper balancing between cost-effective feedstock, product distribution and investment. Current cracking processes will continue to be the main source of olefins for the foreseeable future but will need to be designed for flexibility in order to deliver competitive results. This will involve increased backing by model-based optimization solutions, providing a clear incentive for the present work.

1.2 Steam cracking

The process of thermal cracking of hydrocarbon feedstocks with the goal of producing light olefins is known as steam cracking. With these molecules as building blocks for many commercially important chemicals and intermediates, steam cracker installations are at the heart of many petrochemical sites. Benefiting from economies of scale, today's grassroots steam crackers are true mega-plants with ethylene production capacities nearing 2,000 kta.

A steam cracking plant consists of two main sections: a hot section, where the saturated hydrocarbons are broken down into smaller, often unsaturated, hydrocarbons and a cold

separation train, where the desired products are separated from the cracked gas stream. At the core of the hot section are the methane-fired furnaces, consisting of a radiant section, a convection section and a transfer line exchanger (TLE), as illustrated in the schematic drawing of Figure 1-5.

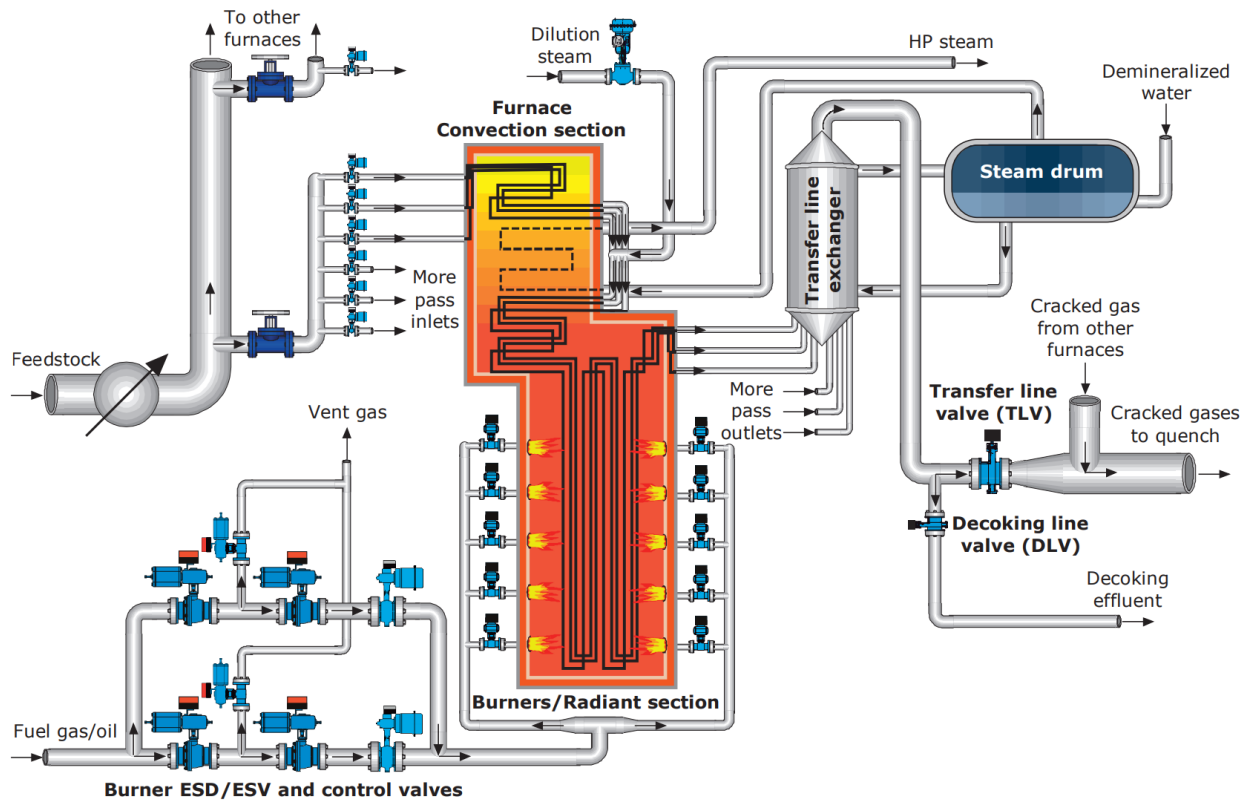


Figure 1-5: Schematic of a possible cracking furnace configuration⁹.

In the convection section, feed and steam are mixed and preheated up to approximately 600 °C by recovering the sensible heat contained in the furnace flue gases. This mixture is then introduced in a set of coils with an internal diameter of 30-150 mm and a length of 10-50 m, suspended in the radiant section. Here the process gas temperature is increased to 750-890 °C, at which point the endothermic cracking reactions commence. In a very simplified form, the complex free-radical kinetics of hydrocarbon pyrolysis can be summarized as a set of primary reactions leading to production of light olefins, hydrogen and methane, while secondary bimolecular reactions between the light olefins form C4-C7 fractions and aromatics. As such, it can easily be understood that ethylene selectivity will be favored by short residence times and

low gas partial pressures^{10, 11}. The latter is achieved by adding dilution steam to the feed, as implied by the name steam cracking. Since this obviously leads to higher energy requirements on the furnace, the steam-to-hydrocarbon mass ratio is usually limited from 0.3 kg/kg for ethane to 0.7 kg/kg for naphtha and heavier fractions^{11, 12}.

As the reactor effluent exits the radiant section, it undergoes a first indirect quench to 350-500 °C in the TLE where energy is recovered to produce high-pressure steam of 100 up to 140 bar. In a second cooling step quench oil is injected, resulting in a separation between the heavy and lighter effluent components. The latter are then compressed to around 30-40 barg and cryogenically split in their respective components in the cold section of the steam cracker installation, at temperatures as low as 120 K. It is clear that both sections are highly energy intensive, making steam cracking one of the most energy-consuming processes in the chemical industry, with approximately 1 ton of CO₂ produced per ton of high-value chemicals¹³.

A major factor for the process energy efficiency is the formation of coke deposits on the inner wall of the tubular cracking reactors. As shown in Figure 1-6, this solid carbonaceous layer blocks part of the cross sectional flow area, leading to an increased pressure drop over the reactor. Because of the fixed back pressure of the downstream installation, the higher hydrocarbon partial pressures in the reactor will cause a loss in olefin selectivity throughout the run length. Furthermore, the highly insulating and often porous coke layer impedes heat transfer towards the reactant stream. In order to maintain the same cracking severity, the heat input from the furnace burners is gradually increased, placing additional demands on the tube metallurgy as tube metal temperatures (TMT) can reach up to 1100 °C. Eventually either the metallurgic constraints of the coils or the excessive pressure drop will force the operators to cease production and to decoke the coils. In order to avoid reactors from completely filling up with cokes as less and less feedstock flows through, most installations maintain a fixed flow distribution to all coils by operating inlet venturis under choked flow. As such, the pressure drop limitation is typically reached when the pressure difference over a venturi reduces to the point that choked flow can no longer be guaranteed. Run lengths for industrial furnaces vary between 30-100 days, depending on cracking conditions and feedstock. Decoking is carried out by passing an air/steam mixture through the coils at high temperature, typically requiring operation to be interrupted for 12-48

hours, having a considerable adverse effect on the economics of the process. With furnace capital costs representing ca. 20% of the total capital cost of an ethylene plant¹¹, the impact of coke formation on the tube service life also becomes an important factor. Carburization of the tubes for example can cause significant embrittlement of the tube material, causing tube failure at the first thermal shock encountered¹⁴. Although the typically applied 35Ni25Cr or 45Ni35Cr steels have a high carburization resistance, carbon diffusion is accelerated by high temperatures and frequent or aggressive decoking practices.

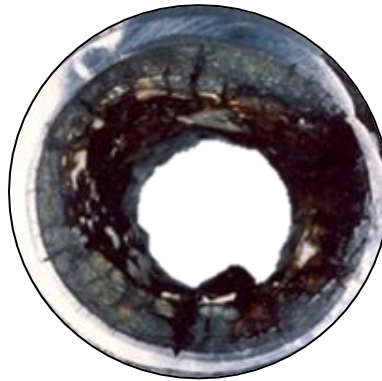


Figure 1-6: Coke deposition in a steam cracker coil.

In light of all these negative effects on the economics and energy efficiency of the steam cracking process, numerous efforts were made towards the development of coke inhibiting technologies. These approaches can be divided in three main categories of technologies: the use of additives, metal surface technologies and mechanical devices. As additives mainly sulfur containing components have been investigated. While a general consensus exists on the beneficial effect for the suppression of CO production, the effect on coke formation is a matter of debate¹⁵⁻¹⁷. Besides sulfur-containing, components containing phosphor, silicon, alkali and alkaline earth metal salts or tin and antimony have also been investigated^{16, 18}. For metal surface technologies, much progress has been made in high temperature alloys, low-coking alloys and (catalytic) coatings¹⁹⁻²³. The focal point of the present thesis is the use of mechanical enhancements to the process in the form of alternative reactor designs. This approach strives to facilitate convective heat transfer to the process gas. In this manner not only the start-of-run metal temperatures are improved, but also the formation of cokes through the thermal mechanism is reduced, yielding dual run length

benefits to the industrial installation. In the following sections the underlying concepts are discussed and background is provided for the evaluation and optimization of such designs.

1.3 Enhanced 3D reactor technology

In the field of heat transfer, the search for lighter, smaller, cheaper or more robust equipment to transfer heat between different fluid streams has always been a driver for innovation. Such heat transfer enhancements exist in various forms, with a primary distinction between active and passive methods. Active methods rely on an external power source, the obvious example of course being mechanical stirring devices, but also jet impingement, disturbance of seeded particles in a magnetic field, vibration generation, etc. have seen applications²⁴. In most industrial heat transfer applications however, it is more practical to use the potential energy of the flow itself to generate so-called “passive” heat transfer enhancements.

These passive enhancements can be categorized according to their main working principle. In the most basic form, heat transfer can be improved by extending the interfacial area between the streams through application of internal or external fin structures. This is easily understood from the basic formula of heat transfer as for a fixed driving force ΔT_{LM} , the transferred energy $Q = AU\Delta T_{LM}$ is impacted by a change in either the surface area A or the overall heat transfer coefficient U . Enhancing the latter is typically achieved by introducing a greater degree of mixing in the flow. This can include both large scale mixing by means of secondary flow patterns that displace hot or cold fluid away from the interface, as well as micro-mixing by increasing the level of turbulent fluctuations in the flow. In turbulent flows the two often coexist, as the large scale secondary motions create shear layers that promote turbulence. Another class of methods that is particularly effective in laminar and transitional flows relies on superimposing swirl on the mean axial flow, causing larger velocity gradients at the surface and hence a thinning of the thermal boundary layer.

Although a wide variety of enhanced internal heat transfer designs are applied in the field of single or multiphase heat exchangers, only a limited number made their way to commercial steam cracking. The main reason for this is the risk of plugging the reactor coils with coke deposits

when obstructions to the flow are introduced²⁵. Additionally, the extreme operating conditions in steam cracking furnaces demand the use of specialized alloys that do not lend themselves so easily to deformations or complex 3D patterns.

One extensively studied enhancement is the addition of longitudinal rounded fins, as shown in Figure 1-7. Studies by various authors²⁶⁻²⁸ have shown that these do not significantly impact the flow, as both the transferred heat and pressure losses scale almost linearly with the increase in internal surface area. Despite this very efficient thermal enhancement, these tubes can be vulnerable to coke plugging for higher fin height-to-diameter ratios, as well as thermal stress generation during decoking. Attempts have been made to avoid these issues by combining surface area increases with a secondary swirl motion, leading to various implementations of rifled fin tubes^{26, 28, 29}.

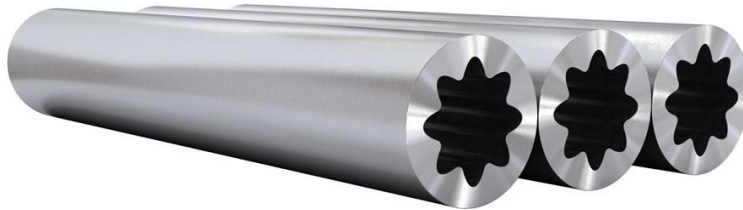


Figure 1-7: Longitudinally finned radiant cracking tubes³⁰.

The most commercially successful design at present is the Mixing Element Radiant Tube (MERT) concept patented by Kubota³¹. In this design a semi-circle rib element is applied helically to the tube internal surface. By this periodic interruption of the laminar boundary layer and turbulence generating structure, large improvements in heat transfer can be obtained. Subsequent optimizations strived to reduce the large pressure penalty that is induced by this geometry^{32, 33}.

While the helically ribbed tubes introduce some degree of swirling motion, more recent developments have tried to harness this effect even more. Noteworthy is the Intensified Heat Transfer (IHT) technology by Lummus/Sinopec and shown in Figure 1-8, which uses a modular application of twisted tape inserts to generate a strong local swirl component that persists further downstream at limited additional pressure losses^{34, 35}. The inserts have been successfully applied in over 50 furnaces in China, though they are reported to be especially sensitive to coke plugging

during decoking due to spalled coke buildup. Another application of swirling flow is found in the Swirl Flow Tube by Technip³⁶⁻³⁸ where the tube itself is bent to follow a small amplitude helical shape. This induces large secondary flows without adding any flow blockage or increasing exposed surface area, again leading to a very efficient enhancement.

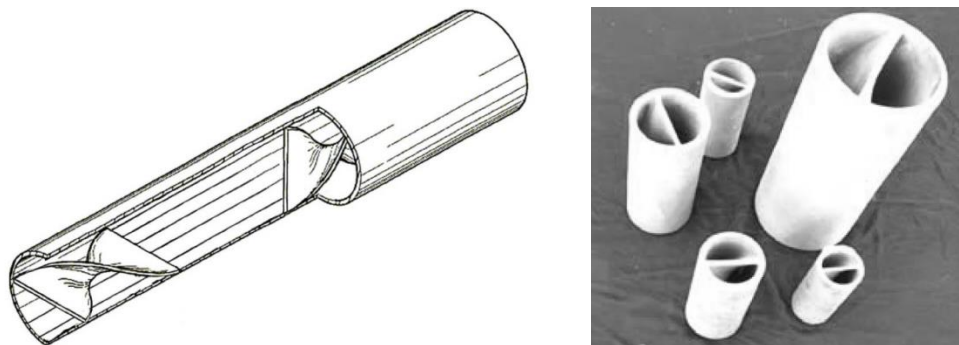


Figure 1-8: IHT-technology as developed by Lummus Technology³⁵

As was mentioned in the previous section, the steam cracking yields benefit from reduced partial pressure of the reactants. This has caused the mentioned enhanced reactor designs to be scrutinized because of the inherently higher pressure losses that they induce, despite the consensus that they positively influence coke formation and run lengths. With this yield impact being too small to measure reliably on an industrial scale but still potentially worth millions a year for a single installation, there is a clear need for improved modeling strategies.

1.4 First-principles based simulation

The fundamental modeling of gas-phase chemical processes such as combustion and pyrolysis, has thrived over the past decades by an improved knowledge on the occurring elementary reaction families, thermodynamic data and reaction rate coefficients. In the field of steam cracking, automatic network generation tools can easily generate kinetic schemes containing several hundreds of intermediates and thousands of elementary reactions³⁹. Because of the inherent chemical complexity, only limited effort has been dedicated in developing the reactor model beyond 1-dimensional plug flow models⁴⁰. Despite the process taking place in a tubular reactor at relatively high Reynolds numbers, the assumption of radial uniformity has been shown

to not always be valid^{41, 42}, in particular when accounting for the formation of cokes near to the reactor surface. Furthermore the assumptions made in these 1D models make it inherently impossible to account for the complex turbulent flow patterns in the mentioned 3D-enhanced reactor geometries. A fundamental modeling of the process hence requires the numerical solution of the Navier-Stokes equations in a computational fluid dynamics (CFD) framework.

1.4.1 Fluid dynamics

Arguably the greatest challenge in simulating single-phase flows is accounting for turbulence. This chaotic process occurs in the presence of shear at high Reynolds numbers when the molecular viscosity is no longer able to damp small fluctuations in the flow and the inertial forces dominate. As these instabilities grow, they develop into spatially coherent, vortical structures called eddies. The kinetic energy contained in these secondary fluid motions enhances mixing in the process in a stochastic manner. Eventually the large-scale motions degenerate into smaller, more uniform eddies that lose their kinetic energy through viscous dissipation. This energy cascade process as proposed by Kolmogorov, is shown in Figure 1-9 and illustrates the turbulent kinetic energy E contained in eddies of a certain wave number k , corresponding to a turbulent length scale $\lambda = 2\pi/k$. In this figure L is the characteristic flow length scale and η is the Kolmogorov length scale at which viscosity dominates. In the field of steam cracking at Reynolds number of around 10^5 , typical values for these length scales are on the order of 0.1 m and $5 \cdot 10^{-6}$ m, respectively. Obviously, resolving the flow to the limit of the smallest turbulent scales, as is done in direct numerical simulation (DNS), can be prohibitively expensive for all but the simplest flow configurations. On the other hand, Reynolds-averaged Navier-Stokes (RANS) approaches result from a classical ensemble averaging of the momentum equations and attempt to describe turbulent interaction over the entire spectrum with a single model. It is clear that due to the disparity in time and length scales in turbulence, developing such models that are universally applicable for various types of flows, is a major challenge. Because of the low computational cost associated with the approach however, RANS methods remain the preferred option for industrial CFD calculations.

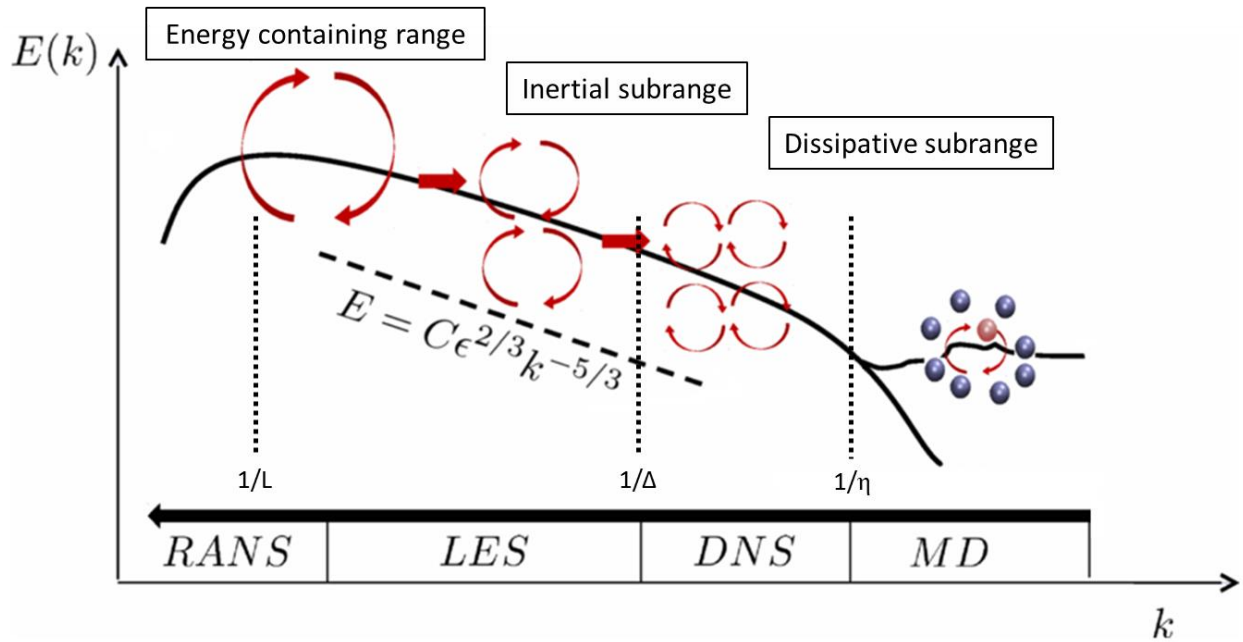


Figure 1-9: Schematic of the turbulent energy cascade in terms of the wave number k [m⁻¹], with validity of modeling.

In the present thesis, the majority of the results were obtained by large eddy simulation (LES), which can be considered an “intermediate” approach both in terms of computational cost and the level of physics that is resolved. Kolmogorov’s theory states that while the energy-containing scales of motion may be inhomogeneous and anisotropic, this information is lost in the cascade so that at much smaller scales the motion is locally homogeneous and isotropic. As such, LES applies a spatial filtering operation with cut-off width Δ , to separate the scales to be modeled from the ones that are resolved. In this manner the large energy containing and anisotropic scales are resolved, while the “sub-filter” scales are more homogeneous and hence more suited for modeling.

The picture becomes slightly more complex when accounting for the effect of solid boundaries on the flow. In such wall-bounded flows, the initial perturbations originate from streak instabilities in the wall shear layer. As the instabilities grow, a reverse $1/k$ cascade from smaller to larger eddies coexists with the classical Kolmogorov cascade, thus sustaining turbulence in the core flow. However, because the small eddies are constricted by the wall, they are also strongly anisotropic and difficult to model. Resolving the energy containing scales in this near-wall region

hence requires significant grid refinement, with the number of grid points for wall-resolved LES scaling with the Reynolds number to the power $13/7$ ⁴³. Similar considerations for wall-modeled LES and DNS lead to grid scaling factors 1 and 37/14, respectively. Accounting for the disparity in time scales adds an additional \sqrt{Re} dependency to the total computational cost, illustrating the Reynolds numbers limitations for each technique. To the author's best knowledge, the highest Reynolds number for a DNS of pipe flow so far is the one by Ahn et al.⁴⁴ at $Re \approx 1.3 \cdot 10^5$. It must be noted that such simulations use spectral or finite-difference methods while application to more complex geometries would likely involve the use of finite-volume codes, that are approximately an order of magnitude slower in achieving this level of detail⁴⁵. With Moore's law coming to an end⁴⁶, current estimates state that we are likely still 30 years removed from simulating commercial aircraft with LES^{47, 48}.

Despite the obvious challenges in using these eddy-resolving methods for industrial scale applications, the increased level of confidence in the obtained results and greater accessibility to high performance computing has already sparked widespread use in both academic and industrial research. With major chemical companies investing in top-tier supercomputer facilities⁴⁹, it is not unlikely that they will see more prominent use in the chemical processing industry as well.

1.4.2 Chemical kinetics

As mentioned above, much progress has already been made on determining the important elementary reaction families in the steam cracking process and systematically calculating the required thermodynamic data and reaction rate coefficients. These have been implemented in various automatic network generation tools, such as NETGEN⁵⁰, RMG^{51, 52}, GENESYS⁵³, REACTION⁵⁴ and RING⁵⁴. Although the generated reaction networks are limited by rate- and/or rule-based criteria, their size and complexity steeply increases with increasing carbon number in order to account for all possible pathways and intermediate species⁵⁵. While the free-radical chemistry for a light gaseous feedstock is hence not particularly demanding, the complexity of both the feedstock and the product spectrum in heavier naphtha feedstocks and various gasoils, poses a much greater challenge in terms of kinetics.

Direct application of such kinetic models in multidimensional CFD simulations for full-scale industrial systems becomes increasingly challenging to the point of being prohibitively expensive. This is not only due to the CPU time required to evaluate the rates of all reactions and to solve the increased number of species conservation equations, but also because of the substantial differences in the species time scales, resulting in a very stiff set of ODE equations. This has led to the use of different reduction techniques such as lumping or applying the pseudo-steady state approximation (PSSA). Tools that implement such strategies are EXGAS^{56, 57}, MAMA/MAMOX^{58, 59} and PRIM⁶⁰⁻⁶². Further network optimization can be achieved in a posteriori application of various reduction techniques, resulting in a so-called skeletal mechanism. Examples of such techniques include sensitivity analysis, graph-based methods, principal component analysis, genetic algorithms and various other optimization-based methods. For a detailed literature review on this topic the reader is referred to the work of Van de Vijver et al.³⁹.

On-the-fly reduction methods offer an additional layer of optimization, as these are not bound by the requirement of being accurate over the broad thermochemical phase space. Instead, a library of reduced mechanisms can be developed by taking into account the local thermochemical conditions, and selecting the most appropriate mechanisms at each point in time and space. These adaptive methods include variations of existing a priori methods, rate tabulation/retrieval methods, but also on-the-fly application of time-scale based methods such as PSSA, PE and ILDM⁶³.

1.5 Outline

This thesis is a compilation of published journal papers and manuscripts that have been submitted or are to be submitted for publication in the near future. Every chapter has a short introduction describing the relevant context.

In Chapter 2 and 3 the focus is on the modeling of the single-phase incompressible flow in order to evaluate heat transfer and pressure drops in different tubular reactor designs. Chapter 2 introduces the implementation of the LES methodology in the open source OpenFOAM

framework and validates the approach with various numerical and experimental datasets. Subsequently, the accuracy of RANS and LES models for predicting the flow in a finned and swirl flow tube is investigated. While general agreement for global flow properties is reasonable, the RANS model clearly fails in capturing the different secondary flows arising in both geometries.

In Chapter 3, the potential of a helically ribbed reactor design known commercially as MERT is investigated. A comprehensive experimental dataset of stereo particle image velocimetry and liquid crystal thermography on the design was obtained at a Reynolds number of 24,000 and compared with simulation results. Excellent agreement was observed, as both datasets predict a heat transfer improvement of over a factor two, at the cost of a roughly six-fold increase in pressure losses. An improved near-wall Reynolds stress transport model was extracted from the LES data, allowing extrapolation of the obtained results to industrial Reynolds numbers.

In Chapter 4 the periodic simulation methodology of the previous chapters is extended to the simulation of non-equilibrium reacting flows in steam cracking reactors. Through an innovative transformation of the space and time domains, only a small volume of fluid over time is required for the simulation of full industrial scale reactors, resulting in speedups of one to two orders of magnitude. Despite the approximative nature of the method, accurate yield predictions were obtained compared to full scale simulations without relying on any tunable parameter. As a result, the method was successfully applied in a screening tool for different reactor designs, demonstrating the potential of each in reducing coke formation.

Chapter 5 presents the results for what are likely the most comprehensive simulations of an industrial steam cracker to date. Through a 3D-3D coupling of the reactor and furnace side, accurate boundary conditions for both are ensured. On the furnace side emphasis was made to account for the detailed burner details, while a discrete ordinates radiation model was combined with an exponential wide band model for gas absorptivity in order to accurately describe radiation. Including naphtha cracking kinetics in the reactor simulations involved development of a new OpenFOAM chemistry library combining dynamic network reduction with in-situ adaptive rate tabulation and on-the-fly application of the pseudo-steady state approximation. This efficient

handling of rate calculations allowed the quantification of the effect on product yields of replacing part of the reactor with an alternative reactor design.

While Chapters 2 to 5 focus on performance at start-of-run conditions, it is clear that the deposition of coke on the reactor structure can significantly impact the resulting operation. Chapter 6 hence accounts for this coke buildup by means of a dynamic meshing procedure. The method generates a new grid at fixed intervals in the run, based on the local rate of coke formation. In this manner, the evolution of tube metal temperatures, pressure losses and product yields can be tracked throughout the run length. As proof-of-concept, the method is applied to an industrial propane cracker using three different reactor designs, with distinctive coking behaviors.

Finally, in Chapter 7, the general conclusions are presented and perspectives for future research are proposed.

As a culmination of the insights obtained throughout the core chapters of the thesis, Appendix A consists of a patent application for a novel profiled tubular design with potential to be used in a steam cracking reactor. Starting from an efficient turbulence generating structure, a geometry is obtained that outperforms existing commercial designs in terms of heat transfer improvement relative to pressure losses. This makes it especially promising for use in commercial operating units that are pressure limited and hence cannot use current 3D techniques. The pattern is also seen to induce interesting secondary flow structures that may aid in removing coke that is already built up on the reactor surface, i.e. providing a self-cleaning effect.

References

1. *Plastics – the Facts 2016*, 2016, PlasticsEurope: Brussels, BE.
2. Pilz, H., B. Brandt, and R. Fehringer, *The impact of plastics on life cycle energy consumption and greenhouse gas emissions in Europe 2010*, Denkstatt: Vienna, AT.
3. *Europe Plastics and Polymers: Market Outlook*, 2016, IHS Markit: London, UK.
4. *Global Commodity Plastic Market Research Report – Forecast, 2016-2022*, M.R. Future, Editor 2017, Market Research Future: Pune, IND.
5. Myers, D., G. Funk, and B. Vora, *Shale Gas Monetization: How to get into the action*, in *Honeywell UOP - Technology Newsletter*, 2013, Honeywell UOP: Morristown, NJ.
6. GlobalData, *60 Planned Projects Set to Push Global Propylene Capacity to New Levels by 2020*, 2016.
7. Chang, J., *Asia's next shift in petrochemicals to be led by China and India*, in *Chemicals Industry News and Analysis - ICIS*, 2017.
8. Eramo, M., *Global Trends in Petrochemical Markets*, in *Ethylene Forum*, IHS, Editor 2017: Rome, IT.
9. Metso, *Steam cracking - cracking furnaces*, 2015. p. 5.
10. Nicolantonio, A.D., *Pyrolysis furnace with an internally finned U-shaped radiant coil*, E. Chemical, Editor 2002: United States.
11. Zimmermann, H. and R. Walzl, *Ethylene*, in *Ullmann's Encyclopedia of Industrial Chemistry*, 2000, Wiley-VCH Verlag GmbH & Co. KGaA.
12. J. Towfighi, R.K., *SHAHAB-A PC-Based Software for Simulation of Steam Cracking Furnaces (Ethane and Naphtha)*. Iranian Journal of Chemical Engineering, 2004. **1**(2): p. 14.
13. Ren, T., M.K. Patel, and K. Blok, *Steam cracking and methane to olefins: Energy use, CO₂ emissions and production costs*. Energy, 2008. **33**(5): p. 817-833.
14. Peter Wolbert, B.G., Dietlinde Jakobi, Rolf Kirchheiner, *Process and finned tube for the thermal cracking of hydrocarbons*, 2005: United States.
15. Wang, J., M.-F. Reyniers, and G.B. Marin, *Influence of Dimethyl Disulfide on Coke Formation during Steam Cracking of Hydrocarbons*. Industrial & Engineering Chemistry Research, 2007. **46**(Inconel 600): p. 15.
16. Jidong Wang, M.-F.R., Kevin M. Van Geem and Guy B. Marin, *Influence of Silicon and Silicon/Sulfur-Containing Additives on Coke Formation during Steam Cracking of Hydrocarbons*. Ind. Eng. Chem. Res., 2008. **47**: p. 15.

17. Olahova, N., M.R. Djokic, R. Van de Vijver, N.D. Ristic, G.B. Marin, M.-F. Reyniers, and K.M. Van Geem, *Thermal Decomposition of Sulfur Compounds and their Role in Coke Formation during Steam Cracking of Heptane*. Chemical Engineering & Technology, 2016. **39**(11): p. 2096-2106.
18. Wang, J., M.-F. Reyniers, and G.B. Marin, *The influence of phosphorus containing compounds on steam cracking of n-hexane*. Journal of Analytical and Applied Pyrolysis, 2006. **77**(2): p. 133-148.
19. Bergeron, M., E. Maharajh, and T. McCall, *A Low Coking Environment for Pyrolysis Furnace – CoatAlloy*, in *11th Annual Ethylene Producers Conference*, 1999: Houston, Texas.
20. Györfy, M., *MERT Technology Update: X-MERT*, in *AIChE: Ethylene Producers Meeting*, 2009: Tampa Bay.
21. Kubota, *Alloy Data Sheet, KHR 45A*, 1999.
22. Zhou, J., Z. Wang, X. Luan, and H. Xu, *Anti-coking property of the SiO₂/S coating during light naphtha steam cracking in a pilot plant setup*. Journal of Analytical and Applied Pyrolysis, 2011. **90**(1): p. 7-12.
23. Schietekat, C.M., P.A. Reyniers, S. Sarris, K.M. Van Geem, G.B. Marin, L.B. Kool, W. Peng, P. Lucas, S. Wang, Y. Gu, and H. Zhou, *Catalytic Coating for Reduced Coke Formation in Ethylene-Producing Steam Crackers: Experimental and Model Validation*, in *2014 Spring National Meeting 2014*: New Orleans.
24. Liu, S. and M. Sakr, *A comprehensive review on passive heat transfer enhancements in pipe exchangers*. Renewable and Sustainable Energy Reviews, 2013. **19**: p. 64-81.
25. Di Nicolantonio, A.R., D.B. Spicer, and V.K. Wei, *Process for the manufacture of olefins by a pyrolysis furnace with an internally finned U shaped radiant coil*, 2004, Google Patents.
26. Albano, J., K. Sundaram, and M. Maddock, *Application of extended surfaces in pyrolysis coils*, 1988, New York, NY; American Institute of Chemical Engineers.
27. Brown, D.J. *Internally finned radiant coils: a valuable tool for improving ethylene plant economics*. in *6th EMEA Petrochemicals Technology Conference, London, UK*. 2004.
28. Schietekat, C.M., D.J. Van Cauwenberge, K.M. Van Geem, and G.B. Marin, *Computational fluid dynamics-based design of finned steam cracking reactors*. AIChE Journal, 2014. **60**(2): p. 794-808.
29. *SCOPE Fusion HTE*, 2017, Schmidt+Clemens GmbH: Lindlar, GE.
30. *Finned and Smooth Ethylene Furnace Tubes*, 2017, Sandvik Materials Technology.
31. Torigoe, T., H. Hamada, M. Inui, and A. Yoshitake, *Mixing element radiant tube (MERT) offers new concept for ethylene steam cracking process*. Am. Chem. Soc, 1998. **43**(2): p. 266-270.
32. Györfy, M., M. Hineno, K. Hashimoto, S.-H. Park, and M.-S. You. *Mert performance and technology update*. in *AIChE Spring Meeting: Ethylene Producers Conference, Tampa Bay, USA*. 2009.

-
33. Higuchi, J. and K. Hamaogi, *Metal tube for pyrolysis reaction*, 2012, Google Patents.
 34. van Goethem, M.W.M. and E. Jelsma, *Numerical and experimental study of enhanced heat transfer and pressure drop for high temperature applications*. Chemical Engineering Research and Design, 2014. **92**(4): p. 663-671.
 35. Carrillo, A., F. Bertola, G. Wang, and L. Zhang. *Intensified heat transfer technology–CFD analysis to explain how and why IHT increases runlength in commercial furnaces*. in *AIChE and EPC 2010 Spring National Meeting, San Antonio, TX*. 2010.
 36. Tallis, W., C. Caro, and C. Dang. *A novel approach to ethylene furnace coil design*. in *AIChE Spring Meeting: Ethylene Producers Conference–Fundamentals of Technology Session*. 2006.
 37. Caro, C.G., P.L. Birch, and W. Tallis, *Olefin production furnace having a furnace coil*, 2012, Google Patents.
 38. Schietekat, C.M., M.W. Van Goethem, K.M. Van Geem, and G.B. Marin, *Swirl flow tube reactor technology: An experimental and computational fluid dynamics study*. Chemical Engineering Journal, 2014. **238**: p. 56-65.
 39. Van de Vijver, R., N.M. Vandewiele, P.L. Bhoorasingh, B.L. Slakman, F. Seyedzadeh Khanshan, H.-H. Carstensen, M.-F. Reyniers, G.B. Marin, R.H. West, and K.M. Van Geem, *Automatic Mechanism and Kinetic Model Generation for Gas- and Solution-Phase Processes: A Perspective on Best Practices, Recent Advances, and Future Challenges*. International Journal of Chemical Kinetics, 2015. **47**(4): p. 199-231.
 40. Dente, M., E. Ranzi, and A.G. Goossens, *Detailed prediction of olefin yields from hydrocarbon pyrolysis through a fundamental simulation model (SPYRO)*. Computers & Chemical Engineering, 1979. **3**(1): p. 61-75.
 41. Van Geem, K.M., G.J. Heynderickx, and G.B. Marin, *Effect of radial temperature profiles on yields in steam cracking*. AIChE Journal, 2004. **50**(1): p. 173-183.
 42. Reyniers, P.A., C.M. Schietekat, D.J. Van Cauwenberge, L.A. Vandewalle, K.M. Van Geem, and G.B. Marin, *Necessity and Feasibility of 3D Simulations of Steam Cracking Reactors*. Industrial & Engineering Chemistry Research, 2015. **54**(49): p. 12270-12282.
 43. Choi, H. and P. Moin, *Grid-point requirements for large eddy simulation: Chapman's estimates revisited*. Physics of Fluids, 2012. **24**(1): p. 011702.
 44. Ahn, J., J.H. Lee, J. Lee, and H.J. Sung, *Large-scale motions for a high-Reynolds-number turbulent pipe flow at $Re\tau = 3008$* , in *67th Annual Meeting of the APS Division of Fluid Dynamics*, 2014: San Francisco (CA).
 45. Piomelli, U., *Large-eddy simulations and Related techniques*, 2014: von Karman Institute Lecture Series.
 46. Simonite, T., *Moore's Law Is Dead. Now What?*, in *MIT Technology Review*, 2016: San Francisco (CA).

-
47. Piomelli, U., *Large eddy simulations in 2030 and beyond*. Philosophical transactions. Series A, Mathematical, physical, and engineering sciences, 2014. **372**(2022): p. 20130320.
 48. Spalart, P.R., *Strategies for turbulence modelling and simulations*. International Journal of Heat and fluid flow, 2000. **21**(3): p. 252-263.
 49. Lau, B., *BASF selects HPE to build supercomputer for global chemical research*, 2017, BASF: Ludwigshafen, DE.
 50. Broadbelt, L.J., S.M. Stark, and M.T. Klein, *Computer Generated Pyrolysis Modeling: On-the-Fly Generation of Species, Reactions, and Rates*. Industrial & Engineering Chemistry Research, 1994. **33**(4): p. 790-799.
 51. William H. Green, J.W.A., Beat A. Buesser, Robert W. Ashcraft, Gregory J. Beran, Caleb A. Class, Connie Gao, C. Franklin Goldsmith, Michael R. Harper, Amrit Jalan, Murat Keceli, Gregory R. Magoon, David M. Matheu, Shamel S. Merchant, Jeffrey D. Mo, Sarah Petway, Sumathy Raman, Sandeep Sharma, Jing Song, Yury Suleymanov, Kevin M. Van Geem, John Wen, Richard H. West, Andrew Wong, Hsi-Wu Wong, Paul E. Yelvington, Nathan Yee, Joanna Yu, *RMG - Reaction Mechanism Generator v4.0.1*, 2013.
 52. Van Geem, K.M., M.-F. Reyniers, G.B. Marin, J. Song, W.H. Green, and D.M. Matheu, *Automatic reaction network generation using RMG for steam cracking of n-hexane*. AIChE Journal, 2006. **52**(2): p. 718-730.
 53. Vandewiele, N.M., K.M. Van Geem, M.-F. Reyniers, and G.B. Marin, *Genesys: Kinetic model construction using chemo-informatics*. Chemical Engineering Journal, 2012. **207**: p. 526-538.
 54. Blurock, E.S., *Reaction: System for Modeling Chemical Reactions*. Journal of Chemical Information and Computer Sciences, 1995. **35**(3): p. 607-616.
 55. Lu, T. and C.K. Law, *Toward accommodating realistic fuel chemistry in large-scale computations*. Progress in Energy and Combustion Science, 2009. **35**(2): p. 192-215.
 56. Bounaceur, R., V. Warth, P.-M. Marquaire, G. Scacchi, F. Dominé, D. Dessort, B. Pradier, and O. Brevart, *Modeling of hydrocarbons pyrolysis at low temperature. Automatic generation of free radicals mechanisms*. Journal of Analytical and Applied Pyrolysis, 2002. **64**(1): p. 103-122.
 57. Glaude, P.A., O. Herbinet, S. Bax, J. Biet, V. Warth, and F. Battin-Leclerc, *Modeling of the oxidation of methyl esters—Validation for methyl hexanoate, methyl heptanoate, and methyl decanoate in a jet-stirred reactor*. Combustion and Flame, 2010. **157**(11): p. 2035-2050.
 58. Pierucci, S., E. Ranzi, M. Dente, and S. Barendregt, *A kinetic generator of hydrocarbon pyrolysis mechanisms*. Computer Aided Chemical Engineering, 2005. **20**: p. 241-246.
 59. Mehl, M., G. Vanhove, W.J. Pitz, and E. Ranzi, *Oxidation and combustion of the n-hexene isomers: A wide range kinetic modeling study*. Combustion and Flame, 2008. **155**(4): p. 756-772.
 60. Clymans, P.J. and G.F. Froment, *Computer-generation of reaction paths and rate equations in the thermal cracking of normal and branched paraffins*. Computers & Chemical Engineering, 1984. **8**(2): p. 137-142.

61. Hillewaert, L.P., J.L. Dierickx, and G.F. Froment, *Computer generation of reaction schemes and rate equations for thermal cracking*. AIChE Journal, 1988. **34**(1): p. 17-24.
62. Van Geem, K.M., M.F. Reyniers, and G.B. Marin, *Challenges of Modeling Steam Cracking of Heavy Feedstocks*. Oil Gas Sci. Technol., 2008. **63**(1): p. 79-94.
63. Battin-Leclerc, F., J.M. Simmie, and E. Blurock, *Cleaner Combustion: Developing Detailed Chemical Kinetic Models*. 2013, London: Springer London. 658.

2

CFD-based design of 3D pyrolysis reactors: RANS vs. LES

*"If I had six hours to chop down a tree,
I'd spend the first four hours sharpening the axe."*

Abraham Lincoln (1809 – 1865)

This chapter has been published as :

Van Cauwenberge, D.J., Schietekat, C.M., Floré, J., Van Geem, K.M., Marin, G.B. CFD-based design of 3D pyrolysis reactors: RANS vs. LES. Chem. Eng. J. 2015;282:66-76.

Abstract

The design of novel steam cracking reactor geometries has received considerable attention recently. To correctly predict the improved heat transfer and reduced fouling in these 3D geometries it is essential to accurately account for turbulence. Instead of assuming that a universal model exists for all flow scales such as in a classically applied Reynolds-Averaged Navier-Stokes (RANS) approach, in this work the use of eddy-resolving techniques has been investigated. A large eddy simulation (LES) methodology was implemented in OpenFOAM and validated experimentally and with direct numerical simulations (DNS). The dynamic Smagorinsky model formulated by Germano et al. was used to model the subfilter scales. Simulations were performed for internally finned and swirl flow steam cracking reactors at Reynolds numbers ranging from 11,000 to 38,000. The potential of both geometries is confirmed as heat transfer is augmented by 29 to 37 % at the cost of a pressure drop that is only 31 to 39 % higher compared to a bare straight tube. Although general agreement is reasonable, the applied RANS model clearly fails to capture some secondary flow phenomena arising from the anisotropy of the Reynolds stresses and their influence on global heat transfer and friction. The additional level of accuracy provided by eddy-resolving techniques clearly offers substantial advantages for use as a design and optimization tool, and can even provide validation and closure to existing RANS models in cases where experimental data is unavailable.

2.1 Introduction

Steam cracking of hydrocarbons is the main industrial processes for the production of light olefins such as ethene and propene. The endothermic cracking reactions occur at temperatures over 1050K and proceed mainly through a gas-phase free radical reaction mechanism¹. During this thermal cracking a carbonaceous layer is deposited on the inner walls of the tubular reactors²,³ and transfer line heat exchangers⁴, leading to an additional heat transfer resistance and a narrowing of the cross-sectional flow area. In order to retain the same cracking severity, additional heat input from the burners is required as the thermal efficiency of the furnace decreases⁵. Eventually either the metallurgical constraints of the reactor alloy or an excessive

pressure drop forces the operators to stop production and burn off the accumulated coke with a steam/air mixture.

In light of these economical and operational drawbacks, significant efforts have been spent in the past 30 years in finding appropriate methods to suppress coke formation⁶⁻⁸. One field that has recently attracted renewed interest is the application of enhanced reactor designs that promote heat transfer^{9, 10}. The latter do not only allow to operate at a reduced metal temperature at start-of-run conditions but also make it possible to reduce coke formation, leading to increased run lengths. Designs can be divided into two classes based on the physical reason behind the increased heat transfer. In the category of extended surfaces, both longitudinal and helicoidal fins have been successfully applied in steam cracking reactors since the 80s^{11, 12}. A second category is the use of so-called turbulators which augment heat transfer by promoting turbulence and introducing secondary radial or swirling flow patterns. A more extensive review of some of the commercially available technologies can be found in the work of Schietekat et al.¹⁰.

At present all the reported numerical studies on these enhanced reactor designs make use of the Reynolds-averaged Navier-Stokes (RANS) equations where the nonlinear Reynolds stress terms are closed by solving additional partial differential equations (PDEs). Although this approach remains the industry standard and significant progress was made in the development of more advanced algebraic¹³ and stress transport models¹⁴, a large number of additional model parameters are always introduced. While accurate agreement with experimental data has been reported, it is seen repeatedly that strongly varying results are obtained with different RANS-based turbulence models and that not all of the physical effects of the flow are captured¹⁵. Hence, in order to obtain confidence in these models for the problem at hand, significant investments are required to provide the necessary ad-hoc experimental validation.

With the increase in computational power, the use of turbulence-resolving techniques has gained importance both in academia and industry. Eggels¹⁶ and Redjem-Saad¹⁷ were among the first to perform Direct Numerical Simulation (DNS) of turbulent pipe flow at a relatively low Reynolds number of 5500 ($Re_\tau = 186$). While more recent papers have dealt with Reynolds numbers of up to 37,700 ($Re_\tau = 1,000$)¹⁸, these simulations remain limited to simple geometries due to the need for highly accurate, non-dissipative spectral or finite difference methods.

In Large Eddy Simulations (LES), the contribution of the large, energy-carrying structures to momentum and energy transfer is computed exactly, while only the effect of the smallest scales is modeled. As the smallest scales are more homogeneous and universal in nature, the modeling assumptions are significantly reduced, leading to potentially more accurate results. Although the computational cost of LES in wall-bounded flows remains considerable, most commercial finite-volume CFD packages now include LES capabilities which have been applied successfully to chemical engineering problems¹⁹⁻²². Application of LES for the detailed evaluation of heat transfer enhancement has remained focused on the fields of heat exchanger design²³ and turbine blade internal cooling^{24, 25}. To the authors' knowledge, in the present work for the first time industrially applied steam cracking reactor designs are investigated by means of eddy-resolving techniques.

In this study OpenFOAM[®] (Open Field Operation and Manipulation)^{26, 27} was used. This open-source software package offers a wide range of CFD tools and full user customizability. Due to the rapid gain in interest from both academia and industry, a successful application of the LES capabilities of OpenFOAM[®] towards optimization of an industrial process is of great interest to many. The current contribution will discuss the use of wall-resolved large eddy simulation (WRLES) in a streamwise periodic pipe section. The methodology was validated by comparison with DNS results for turbulent heat transfer in pipes¹⁷. Comparison with traditional RANS turbulence modeling is carried out focusing on the abilities of WRLES and RANS to capture the observed flow features. Also global friction factors and Nusselt numbers have been determined and the values have been compared with recently measured experimental values for a range of Reynolds numbers. Finally the presented methodology is used to assess the potential of the studied geometries as steam cracking reactors focusing on the reduction of coke formation.

2.2 Numerical simulation procedure

2.2.1 Governing equations

The flow is modeled incompressible and temperature is treated as a passive scalar by neglecting viscous dissipation and buoyancy effects. The filtered incompressible Navier-Stokes and energy

equations, normalized with radius R , friction velocity u_τ , kinematic viscosity ν and friction temperature $T_\tau = q_w / \rho C_p u_\tau$, can be written in Einstein notation as:

$$\frac{\partial \tilde{u}_i}{\partial x_i} = 0, \quad (2.1)$$

$$\frac{\partial \tilde{u}_i}{\partial t} + \frac{\partial \tilde{u}_i \tilde{u}_j}{\partial x_j} = -\frac{1}{\rho} \frac{\partial \tilde{p}}{\partial x_i} + \frac{1}{Re_\tau} \frac{\partial^2 \tilde{u}_i}{\partial x_j^2} - \frac{\partial \tau_{ij}^R}{\partial x_j}, \quad (2.2)$$

$$\frac{\partial \tilde{\theta}}{\partial t} + \frac{\partial \tilde{\theta} \tilde{u}_j}{\partial x_j} = \frac{1}{Re_\tau Pr} \frac{\partial^2 \tilde{\theta}}{\partial x_j^2} + \frac{\partial q_j}{\partial x_j} \quad (2.3)$$

Where $\tau_{ij}^R = \tilde{u}_i \tilde{u}_j - \tilde{u}_i \tilde{u}_j$ is the residual stress tensor and $q_j = \tilde{\theta} \tilde{u}_j - \tilde{\theta} \tilde{u}_j$ is the residual energy flux which both require modeling in order to close Eq. (2.2) and (2.3). Note that although the underlying approach is fundamentally different, the governing equations in LES and RANS are analogous. The tilde accent indicating the spatial filtering operator can hence also be interpreted as the Reynolds averaging operator in RANS. The key difference lies in the physical meaning of the residual stress tensor, which in the case of RANS includes the entire turbulent contribution, whereas in LES only the influence of the smallest subfilter-scales (SFS) requires modeling.

In the present work, the Boussinesq eddy-viscosity assumption²⁸ is used to calculate the anisotropic residual stress tensor.

$$\tau_{ij}^R = -2\nu_T \tilde{S}_{ij} + \frac{1}{3} \tau_{kk} \delta_{ij} \quad (2.4)$$

where ν_T is the eddy viscosity of the modeled motions and \tilde{S}_{ij} is the resolved rate-of-strain

$$\tilde{S}_{ij} = \frac{1}{2} \left(\frac{\partial \tilde{u}_i}{\partial x_j} + \frac{\partial \tilde{u}_j}{\partial x_i} \right) \quad (2.5)$$

A filter length scale based on the cell size of the computational grid was chosen by taking the cube root of the cell volume. The subfilter eddy viscosity model applied in this study is the dynamic Smagorinsky model formulated by Germano²⁹ including the modifications made by Lilly³⁰. In this model an additional LES test filter is introduced, denoted $\hat{\cdot}$, larger than the grid

LES filter τ by a factor α . The residual stress tensors obtained by the grid filtering and by the combined filtering operations, respectively, are given by:

$$\tau_{ij} = \widetilde{u_i u_j} - \widetilde{u_i} \widetilde{u_j} \quad (2.6)$$

$$T_{ij} = \widehat{\widetilde{u_i u_j}} - \widehat{\widetilde{u_i}} \widehat{\widetilde{u_j}} \quad (2.7)$$

while the resolved turbulent stress (or Leonard stress) tensor is defined as

$$\mathcal{L}_{ij} = \widehat{\widetilde{u_i} \widetilde{u_j}} - \widehat{\widetilde{u_i}} \widehat{\widetilde{u_j}} \quad (2.8)$$

These quantities are algebraically related, leading to the Germano identity:

$$\mathcal{L}_{ij} = T_{ij} - \widehat{\tau_{ij}} \quad (2.9)$$

By applying the Smagorinsky model to both the test and grid subfilter-scale stresses and explicitly calculating the resolved turbulent stresses, the following equality can be written:

$$c_s^2 M_{ij} = \mathcal{L}_{ij}, \text{ where } M_{ij} = -2\Delta^2 \left(\alpha \widehat{|\widehat{S}| \widehat{S}_{ij}} - \widehat{|\widehat{S}| \widehat{S}_{ij}} \right) \quad (2.10)$$

Since this equality should hold at every point, time and for each tensor element, it is an over-determined system which a single parameter c_s is unlikely to satisfy exactly. Lilly³⁰ hence proposed the calculation of the dynamic coefficient using a least-squares procedure:

$$c_s^2 = \frac{\langle \mathcal{L}_{ij} M_{ij} \rangle}{\langle M_{ij} M_{ij} \rangle} \quad (2.11)$$

In this way, the Smagorinsky coefficient³¹ is dynamically determined by using the information contained in the resolved flow scales that are just above the filter length. The only adjustable parameter in the model is the ratio of the test and grid filter length, where $\alpha = 2$ was chosen in accordance with Germano et al.²⁹. Local face-averaging of the coefficient was performed in order to smooth out the instabilities inherent to the model. Furthermore, the sum of the subfilter eddy and molecular viscosity was limited to a minimum of zero in order to allow the desirable backscatter of energy while avoiding unphysical behavior.

In the context of RANS modeling, the shear-stress transport (SST) $k-\omega$ model³² was used to calculate the eddy viscosity. This two-equation model uses a pure $k-\omega$ formulation in the inner parts of the boundary layer which makes the model directly usable all the way down to the wall, while in the free-stream it switches to a $k-\epsilon$ behavior, making it reliable in a wide class of flows. Boundary conditions and near-wall damping functions were applied according to the recommendations of Wilcox¹⁴.

The energy flux q_j is similarly modeled using an eddy diffusivity approach:

$$q_j = \frac{\nu_T}{Pr_x} \frac{\partial \tilde{\theta}}{\partial x_j} \quad (2.12)$$

where the turbulent Prandtl number Pr_x relates the modeled turbulent transport of momentum and energy. In the context of RANS modeling this parameter corresponds to the turbulent Prandtl number Pr_t , whereas the LES equivalent is typically referred to as the subfilter-scale Prandtl number Pr_{SFS} . Values of 0.85 and 0.5 were chosen for these respective parameters, in accordance to the typical recommendations for gaseous flows³³⁻³⁵.

2.2.2 Boundary conditions

Experimental data for tubular geometries is typically obtained in a set-up where a blower or compressor is connected to a test tube in which temperature and pressure is measured at several intervals along the tube axial coordinate. In order to avoid any entrance effects, an inlet section is applied to assure fully developed flow in the test tube. Most computational studies have followed this approach, causing a significant amount of computational effort to be wasted on a region that is of no practical interest. In the present work, periodic boundary conditions are applied on the streamwise boundaries:

$$\tilde{\phi}(x + nL, y, z, t) = \tilde{\phi}(x, y, z, t) \quad (2.13)$$

Although the streamwise velocity gradients are non-zero, the velocity field repeats itself in a succession of cross sections that are separated by the periodic module length L . Hence, for the periodic boundaries, the velocity and pressure at any position can be written as

$$\mathbf{u}(x, y, z) = \mathbf{u}(x + nL, y, z) \quad (2.14)$$

$$p(x, y, z) - p(x + nL, y, z) = n \cdot [p(x, y, z) - p(x + L, y, z)] \quad (2.15)$$

When applying a uniform heat flux on the domain boundaries, both temperature and pressure are made periodic by isolating the fluctuating components from the mean streamwise gradient, as demonstrated by Patankar et al.³⁶:

$$p(x, y, z) = -\beta x + \hat{p}(x, y, z) \quad (2.16)$$

$$T(x, y, z) = -\gamma x + \hat{T}(x, y, z) \quad (2.17)$$

In these equations $\gamma = 4 q_w / \rho C_p u_b$ is the axial temperature gradient corresponding to the imposed heat flux and β is the linear component of non-dimensional pressure which is adjusted dynamically to keep the mass flow rate to a predefined value. Substitution of Eq. (2.16) and (2.17) in the dimensionless Navier-Stokes and scalar transport equations, Eq. (2.2) and (2.3), lead to an additional term on the right-hand side of these: $\delta_{i1}\beta(t)$ and $4 \tilde{u}_x / u_b$, respectively.

No-slip and isoflux heating boundary conditions were imposed on all solid walls.

2.2.3 Geometry characteristics

Two distinct tubular geometries were evaluated in the present work. Firstly, a tube enhanced with longitudinal fins was studied. The fins are rounded with a concave-convex structure that can be described by two touching circles as shown in Schietekat et al.¹⁰. Previous experimental and computational studies on this geometry can be found in the work of Albano et al.¹¹, De Saegher et al.³⁷ and Schietekat et al.¹⁰, where the latter also included a parametric study on optimization of the fin shape. Based on these results, a geometry consisting of 8 fins with a relative element height e/D of 0.134 was chosen, leading to 28.2% increase in internal surface area. The tube dimensions were scaled in order to preserve the same cross-sectional area.

Secondly, the Swirl Flow Tube (SFT) technology was evaluated. This geometry is also known as Small Amplitude Helical Tube (SMAHT), which refers to the shape of the tube centerline following a helical pathline with an amplitude smaller than the diameter, whereas the cross

section remains circular. Previous studies include the work of Caro et al.³⁸ and Schietekat et al.³⁹. Based on the SFT-M geometry experimentally studied in the latter paper, an identical relative amplitude of 0.218 and relative pitch P/D of 10.22 were chosen for the present simulations. The resulting computational domains for both geometries are shown in Figure 2-1.

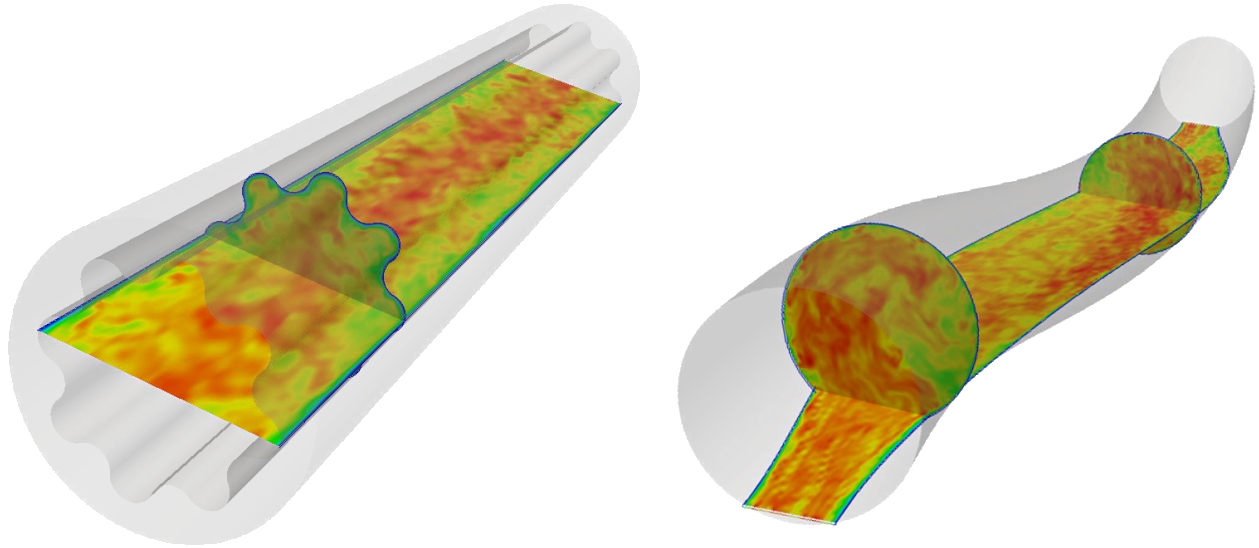


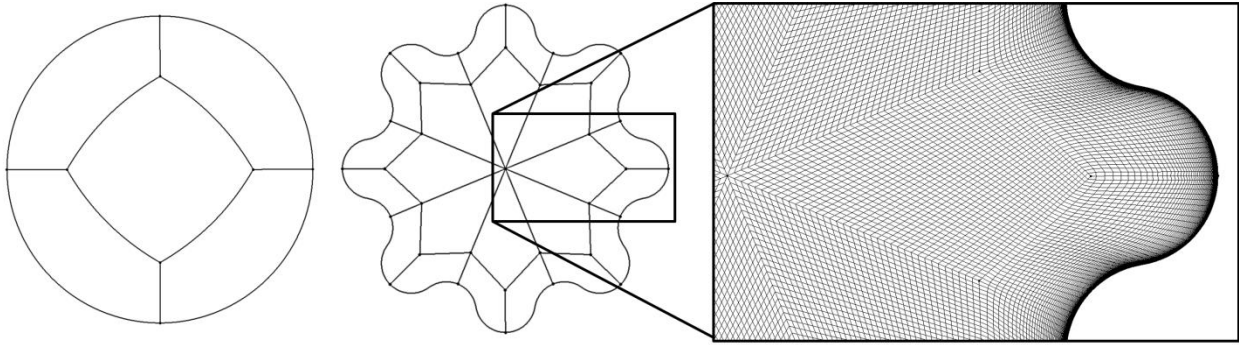
Figure 2-1: Representation of the computational domain of the finned tube (left), and the Swirl Flow Tube (right). Slices of instantaneous velocity magnitude at $Re = 38,000$ are included for illustrative purposes.

2.2.4 Computational grid

Discretization was done on a body-fitted structured grid generated using the commercial meshing software Pointwise^{®40}. The multi-block ‘butterfly’ topology allows the use of high quality hexahedral grids with good control over the mesh spacing as shown in Figure 2-2. The grid resolution was initially chosen according to the recommendations of Kravchenko⁴¹ and Chapman⁴² for wall-resolved LES: $\Delta x^+ \approx 50 \sim 130$, $r\Delta\theta^+ \approx 15 \sim 30$ and $n_r (y^+ < 100) \approx 10 \sim 30$. A grid independency study was performed and is discussed extensively in Appendix B. It was seen that the values suggested in literature did not offer sufficient solution accuracy and hence further refinement was introduced. The details of the resulting computational grids that were used throughout the present work are summarized in Table 2-1. Although the grid requirements are less stringent for RANS simulations, at each Reynolds number the same computational grid was used for both modeling approaches in order to avoid any additional sources of discrepancies.

Table 2-1: Grid resolution adopted in the present work

Re	Re_τ	$L_r \times L_\theta \times L_x$	Grid spacing				$N_r \times N_\theta \times N_x$
			Δr^+	$(r\Delta\theta)^+_{\max}$	Δx^+	$n_r (y^+ < 100)$	
11,000	342	$R \times 2\pi \times 15R$	0.3 - 5	9	28	≥ 30	$3.7 \cdot 10^6$
24,000	674	$R \times 2\pi \times 15R$	0.4 - 6	12	55	≥ 30	$9.9 \cdot 10^6$
38,000	1012	$R \times 2\pi \times 15R$	0.5 - 6	13	68	≥ 30	$1.7 \cdot 10^7$

Figure 2-2: Structured multi-block meshing concept and cross-section of the resulting computational grid for the finned tube at $Re = 24000$.

When applying streamwise periodicity, care must be taken that the domain length is sufficient to accommodate the largest scale structures. Chin et al.⁴³ reported different requirements for this parameter, based on the order of the desired statistics. For lower order statistics such as mean velocity profiles and turbulent intensity, convergence was achieved for a domain length of $2-4\pi R$. Although this indicates that the value of $15R$ applied in the present work should be sufficient, further confirmation was obtained by calculation of streamwise two-point correlations. These can be used in the identification of coherent structures in the flow and thus give an indication of the suitable computational length. The correlation between any two fluctuating quantities I and J is defined as

$$R_{IJ} = \frac{\overline{I(r, r\theta, x)J(r, r\theta, x + \Delta x)}}{\sigma_I \sigma_J} \quad (2.18)$$

where σ refers to the standard deviation and Δx is the spatial distance in the streamwise direction. The overbar denotes the spatial average.

2.2.5 Solution procedure

OpenFOAM[®] is based on the finite-volume method using collocated grids and Gaussian integration. The Pressure Implicit with Splitting of Operators (PISO) algorithm was employed with 2 corrector steps and an additional non-orthogonal correction when required. A 2nd order central differencing spatial discretization scheme was used, with minor high-frequency filtering. The cell face values of the Gauss surface integral were obtained through linear interpolation. Time integration was performed using a second order backward differencing scheme (BDF2):

$$\left(\frac{\partial \phi}{\partial t}\right)^n = \frac{\frac{3}{2}\phi^n - 2\phi^{n-1} + \frac{1}{2}\phi^{n-2}}{\Delta t} \quad (2.19)$$

The maximal Courant number was kept below 0.8 according to the CFL condition, leading to time steps of approximately $1 \cdot 10^{-5}$ s. Turbulent statistics were gathered over 20 flow-through times, following an initial period of 6 flow-through times to ensure fully developed flow. The simulations were parallelized on 64 to 128 CPUs (Intel Xeon E5-2670) depending on the grid size. Total simulation time amounted to approximately 200,000 CPU hours. As a rule of thumb for the present work, the computational cost for each outer iteration in RANS was similar to the cost per time step in the transient LES. Because of the long sampling time, the total computational cost of LES was a factor 4 higher than for RANS simulations. It should however be emphasized that identical grids were used in both sets of simulations, while in fact the grid requirements for each method are quite different³⁵. This will cause the true cost ratio to be considerably higher, especially for the higher Reynolds numbers.

2.3 Results and discussion

2.3.1 Pipe flow

As one of the canonical examples of wall-bounded flows, turbulent pipe flow has been covered by a wide array of numerical and experimental studies. In the present work simulation results obtained for a bulk Reynolds number of 11,000 ($Re_\tau = 342$, $Pr = 0.71$) were compared with the DNS data of El Khoury et al.¹⁸ ($Re_\tau = 361$), Redjem-Saad et al.¹⁷ ($Re_\tau = 186$, $Pr = 0.71$) and Piller⁴⁴ ($Re_\tau = 180$, $Pr = 0.71$).

The mean streamwise velocity profile normalized by friction velocity is depicted in Figure 2-3(a). The viscous sublayer ($y^+ < 5$) and the buffer region ($5 < y^+ < 30$) are well resolved. The skin friction coefficient ($C_f = 7.21 \cdot 10^{-3}$) is slightly underestimated in comparison with the DNS predictions ($C_f = 7.61 \cdot 10^{-3}$), leading to a deviation in the logarithmic region ($y^+ > 30$). The obtained profiles however confirms the well-known deviation from the law of the wall in pipe flow⁴⁵. A good match is also obtained using the RANS model, as typically the model constants are calibrated based on DNS results for these kind of canonical turbulent flows. Root-mean-square velocity fluctuations as shown on Figure 2-3(b) also tend to agree well with the DNS results, albeit with a slight underprediction of the radial and tangential components. This was expected as the contribution of the smallest scale motions is not included in LES. The normal stress profiles shown for the RANS simulations originate from the modeled turbulent kinetic energy k , but here the assumption of isotropic turbulence ($u'_{r,\theta,x} = \sqrt{2k/3}$) is obviously lacking.

Profiles of the Reynolds shear stress τ_{turb} , viscous shear stress τ_{vis} and the modeled subfilter-scale stresses τ_{sfs} are shown in Figure 2-4. Good agreement with DNS results is obtained for both modeling approaches, though a minor overprediction of the resolved stresses is observed. The importance of the subfilter-scale model is seen to be relatively small for the present grid refinement as the maximal contribution to the shear stresses is less than 1.5% of the total shear stress.

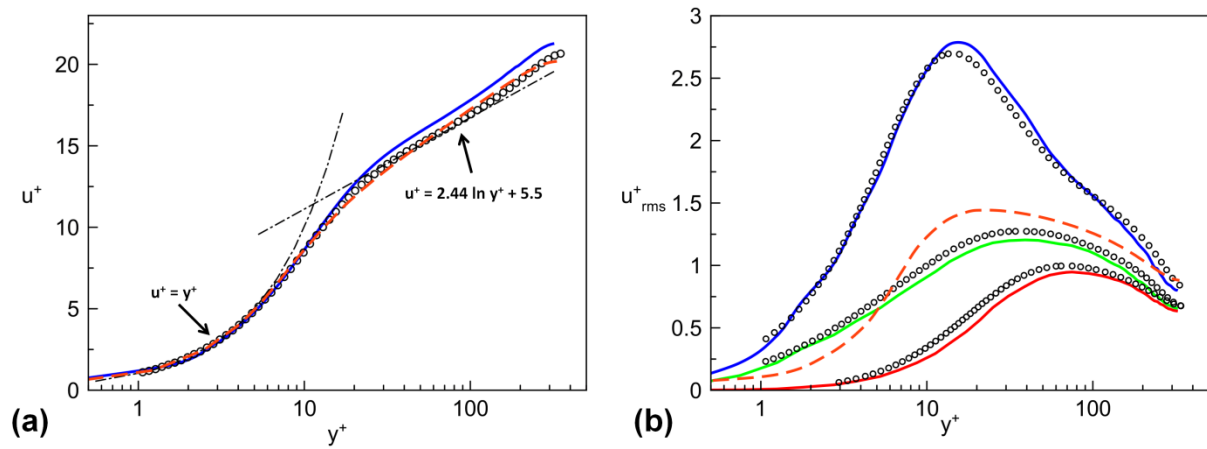


Figure 2-3: (a) Mean streamwise velocity profile in wall coordinates. (b) Normalized root-mean-square velocity fluctuations. — LES $u_{x,rms}$; — LES $u_{0,rms}$; — LES $u_{r,rms}$; - - RANS; ○ - DNS El Khoury et al.¹⁸

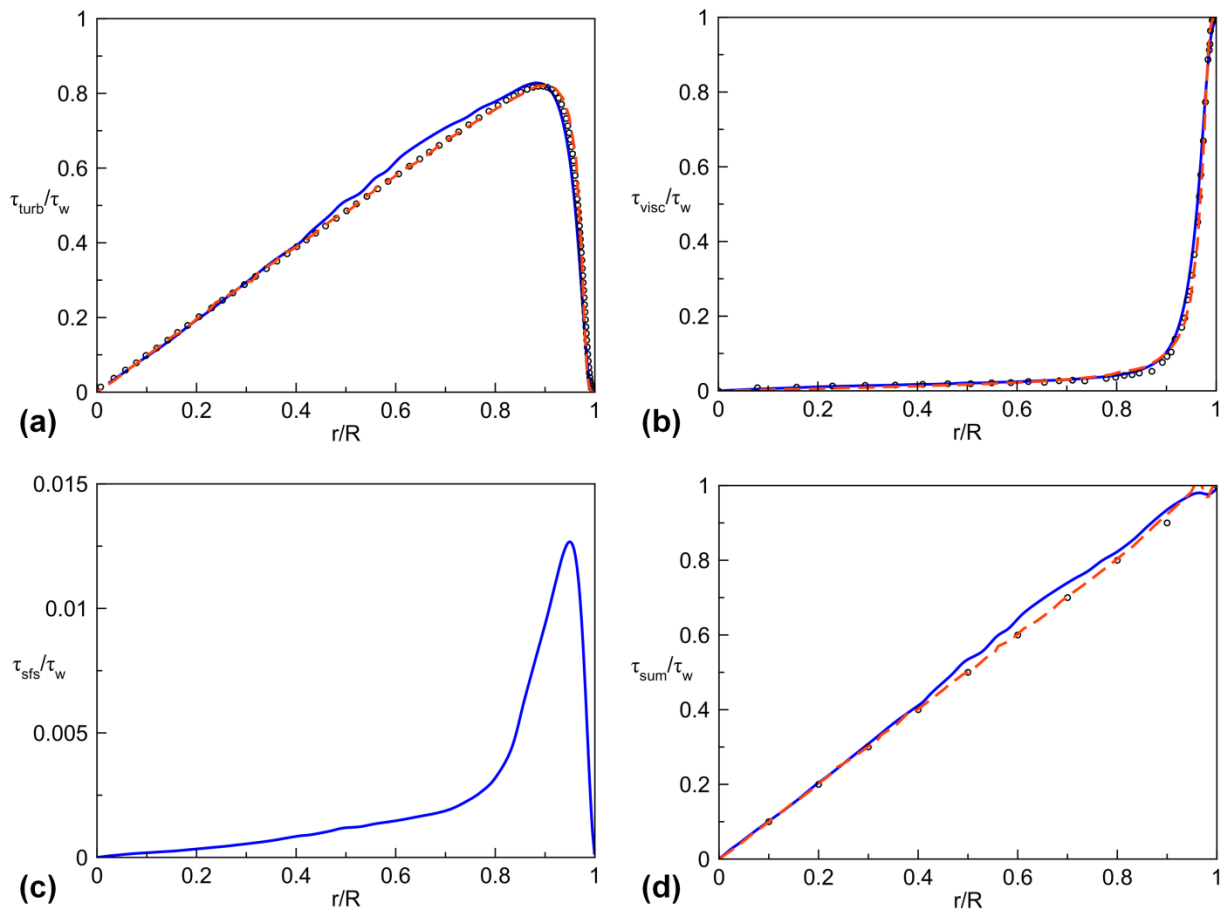


Figure 2-4: Shear stress distributions scaled by wall shear stress. — LES; - - RANS; ○ - DNS El Khoury et al.¹⁸;

The mean dimensionless temperatures and temperature fluctuations are plotted in wall units on Figure 2-5(a) and (b). In the conductive sublayer the linear $\theta^+ = \text{Pr } y^+$ profile is discerned, followed by a logarithmic region, as previously observed for the velocity profile. Although no heat transfer DNS data in pipe flow was available at the present Reynolds number, the simulated overall trends correspond to those observed for the lower Reynolds number DNS data. The empirical correlation of Kader⁴⁶ is also showing reasonable agreement with the present data. The near-wall behavior of temperature fluctuations is seen to depend on the type of boundary condition that is applied. For the ideal iso-flux case, as performed by Piller⁴⁴, a finite value is obtained near the wall. The fixed wall temperature conditions applied by Redjem-Saad et al.¹⁷ however dampens all fluctuations.

Around $y^+ = 20$, a peculiar underprediction of the thermal resistance can be seen in the RANS mean temperature profile. As the momentum transfer did closely match the DNS data, the reason for the discrepancy lies in the assumption of a constant turbulent Prandtl number Pr_t . This ratio of eddy diffusivities for heat and momentum can be calculated directly from the LES results as:

$$\text{Pr}_t = \frac{\varepsilon_M}{\varepsilon_H} = \frac{\overline{u'v'}}{\overline{v'\theta'}} \cdot \frac{\partial\theta/\partial y}{\partial u/\partial y} \quad (2.20)$$

and is shown on Figure 2-6. The turbulent Prandtl number remains close to unity for $y^+ < 50$, after which it gradually decreases towards a value of 0.6 at the centerline. Though the applied value of $\text{Pr}_t = 0.85$ for the RANS case is acceptable, it is clear that assuming this parameter to be a constant will always induce a certain amount of error in the modeling of turbulent heat transfer. This confirms the value of LES and especially DNS as a tool to provide model constants or correlations that can be applied in existing RANS models.

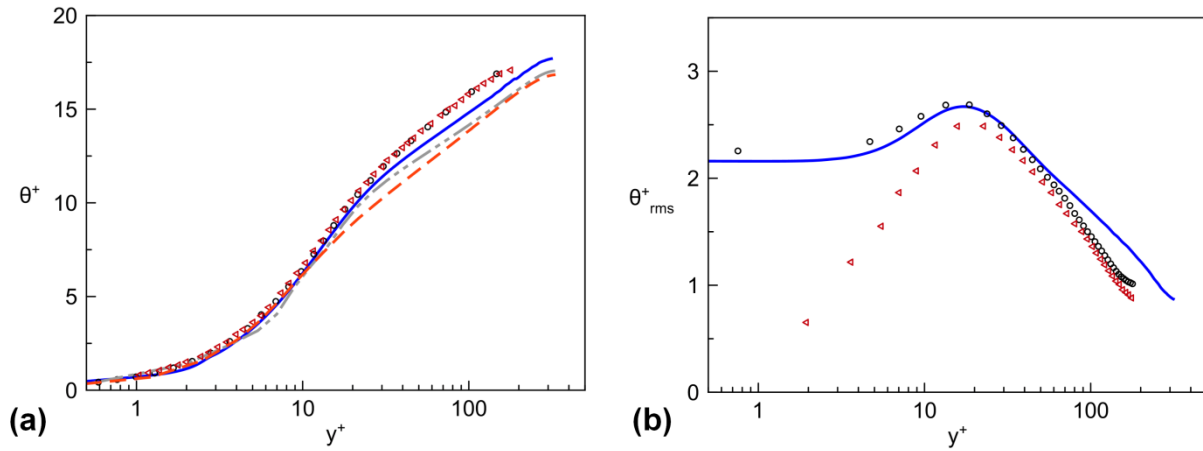


Figure 2-5: Mean (a) and root-mean-square (b) temperature profile. — - LES; - - - RANS; ○ - DNS Piller⁴⁴; ◀ - DNS Redjem-Saad et al.¹⁷; - - - Kader correlation⁴⁶;

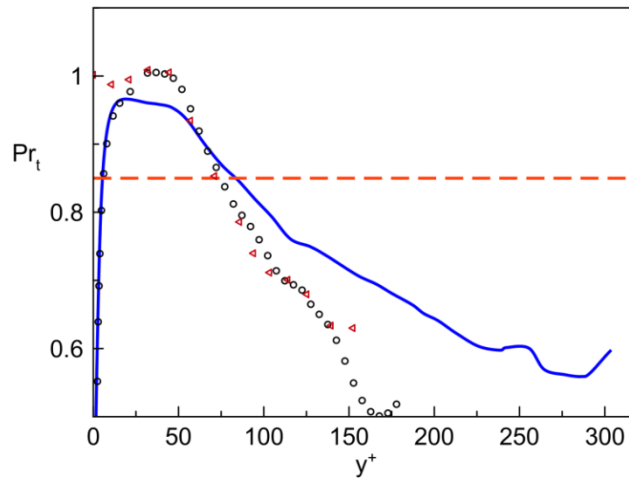


Figure 2-6: Radial profiles of the turbulent Prandtl number. — - LES; - - - RANS; ○ - DNS Piller⁴⁴; ◀ - DNS Redjem-Saad et al.¹⁷;

In addition to the profiles of velocity and temperature, the average friction coefficients and Nusselt numbers were compared to DNS results and various empirical correlations. The Fanning friction factor is obtained from the time-average of the dynamically adjusted momentum source term β :

$$f_f = \frac{\Delta p D}{2\rho u_b^2 \Delta x} = \frac{\beta}{4} \quad (2.21)$$

The simulated global Nusselt number is calculated according to Eq. (2.22):

$$\text{Nu} = \frac{D_{eq} \left(\frac{\partial \tilde{\theta}}{\partial r} \right)_{y=0}}{(\tilde{\theta}_{wall} - \tilde{\theta}_{bulk})} \quad (2.22)$$

A full overview of the applied correlations and simulation results is shown in Table 2-2 and Table 2-3. Results are seen to compare well with the empirical correlations, demonstrating the capability of the applied finite volume formulation towards performing accurate large eddy simulations. The suitability of the applied SST $k-\omega$ model in predicting general pipe flow characteristics is also confirmed by the good agreement with the literature data.

Table 2-2: Comparison of the predicted Fanning friction factors with DNS data and various empirical correlations

Source	Equation	$f_f \times 10^3$	% diff
Present LES	-	7.209	-5.3
Present RANS	-	7.659	+0.6
DNS El Khoury et al. ¹⁸	-	7.614	-
Blasius ⁴⁷	$0.079 Re^{-0.25}$	7.714	+1.4
Churchill ⁴⁸	$2((8/Re)^{12} + (A + 37530/Re)^{-24})^{1/12}$ $A = -2.2113 \ln(7/Re)$	7.551	-0.8
Petukhov ⁴⁹	$(3.64 \log_{10}(Re) - 3.28)^{-2}$	7.653	+0.6
Kays and Crawford ⁵⁰	$0.046 Re^{-0.2}$	7.153	-6.1

Table 2-3: Comparison of the predicted Nusselt number with various empirical correlations

Source	Equation	Nu	% diff
Present LES	-	32.04	-2.1
Present RANS	-	34.64	+5.8

Kader profile ⁴⁶	-	32.74	-
McAdams ⁵¹	$0.021 Re^{0.8} Pr^{0.4}$	31.32	-4.4
Gnielinski ⁵²	$\frac{(C_f/2)(Re - 1000)Pr}{1 + 12.7(C_f/2)^{1/2}(Pr^{2/3} - 1)}$	32.36	-1.2
Kays and Crawford ⁵⁰	$0.022 Re^{0.8} Pr^{0.5}$	31.71	-3.2

Two-point correlations calculated according to Eq. (2.18) for cells with a y^+ of 5 and 150 are shown in Figure 2-7(a) and (b), respectively. All correlation curves quickly fall off below $R_{\phi\phi} = 0$, indicating a sufficient axial extent of the domain. Additionally, the turbulent kinetic energy spectrum was calculated as shown in Figure 2-8. A clear $-5/3$ slope is discerned, signifying a well-resolved inertial subrange³⁵.

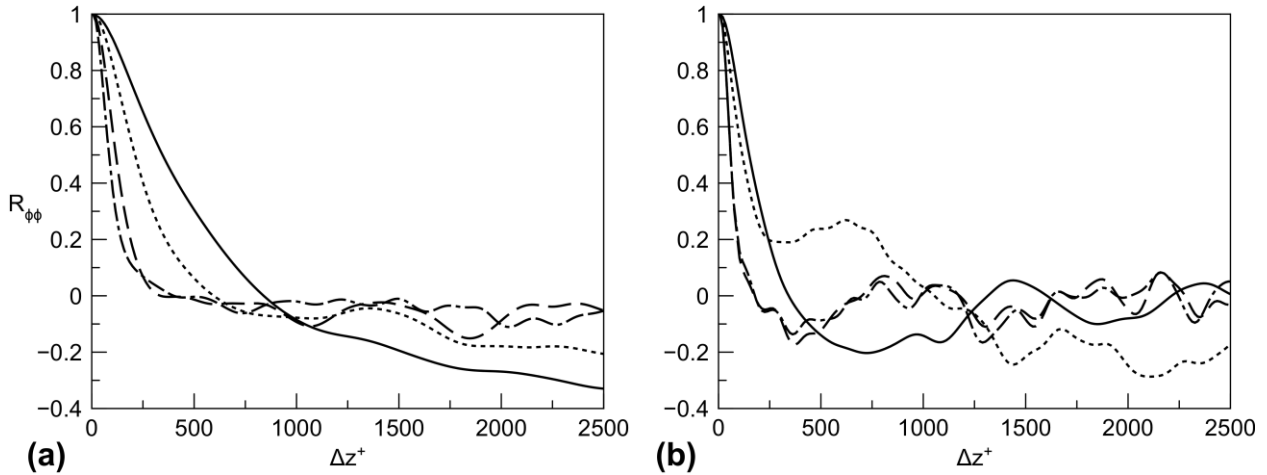


Figure 2-7: Streamwise two-point correlations at wall-normal locations (a) $y^+ = 5$ and (b) $y^+ = 150$. — u ; - - - v ; ···· w .

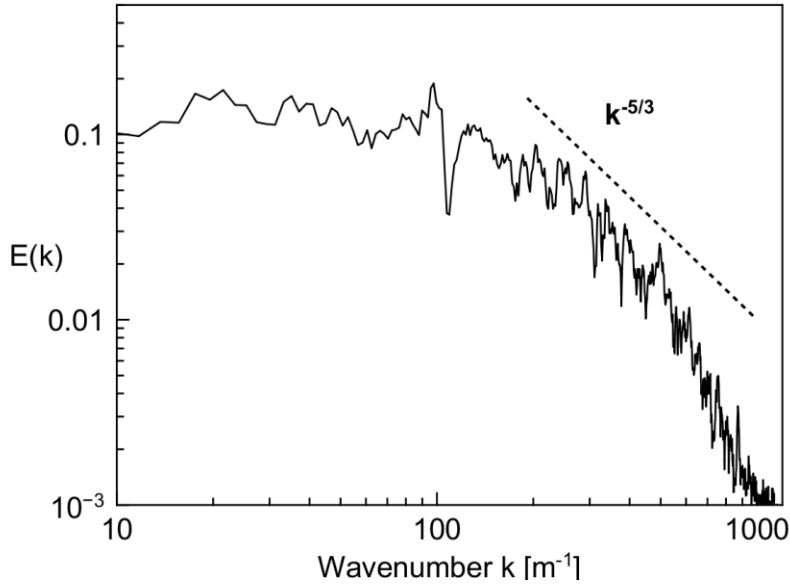


Figure 2-8: Energy spectrum of the streamwise velocity component u_z^+ in the center of the tube.

2.3.2 Heat transfer and friction characteristics of enhanced reactor designs

In this section the time-averaged LES results are compared with simulations using the SST $k-\omega$ turbulence model and recently acquired experimental data. The influence of secondary flows on local wall shear stress is analyzed, by calculating the local skin friction coefficient $C_f = 2\tau_w/\rho u_b^2$. Additionally, the temperature probability density function in these geometries is evaluated in order to determine the level of over- and under-cracking that may occur under actual reactor conditions.

2.3.2.1 Finned tube

For a longitudinally finned tube no significant curvature or pressure gradient effects are expected because of the relatively simple geometry with constant cross section. Figure 2-9 compares the distribution of the skin friction coefficient along the internal surface for both the LES and RANS modeling approach. This property is directly related to the momentum and thermal boundary layer thickness, and hence, can be seen as a quantitative evaluation of the local heat transfer characteristics. A clear overprediction by RANS of the shear stress is seen on the top of the fins, while in-between the fins the RANS model leads to a significant underprediction of the skin

friction compared to LES. This can be better understood by considering the in-plane velocities for the LES, as shown in Figure 2-10. Although lower in magnitude than the streamwise velocity profile, a clear secondary flow pattern consisting of two counter-rotating vortices appears in each of the inter-fin regions. The structures are very similar to those first measured indirectly by Nikuradse⁵³ for a square duct and are typically referred to as secondary flows of Prandtl's second kind⁵⁴. Unlike the first kind which is caused by a deflection of existing vorticity by a skewing of the mean flow, the second kind involves the generation of vorticity due to a Reynolds stress imbalance. Though still a matter of discussion, this purely turbulent phenomenon is typically attributed to the statistically preferred locations of near-wall coherent structures^{54, 55}. The applied RANS model does not resolve any of the turbulent structures in the flow and hence fails to capture both the existence of the secondary currents and their effect on the mean velocity profile. As the flows are always directed towards the corners, momentum, vorticity and energy of the mean motion is convected into the inter-fin region, leading to the higher shear stresses seen in Figure 2-9. The dimensionless tangential and radial velocity profiles at different angular locations are shown on Figure 2-11. The profiles are seen to be largely independent of the Reynolds number, aside from a minor shift in the location of peak velocity towards the wall for the higher Reynolds numbers. Particle image velocimetry (PIV) or laser Doppler anemometry (LDA) experiments could provide the necessary validation for the existence of these patterns, and will be considered in future work.

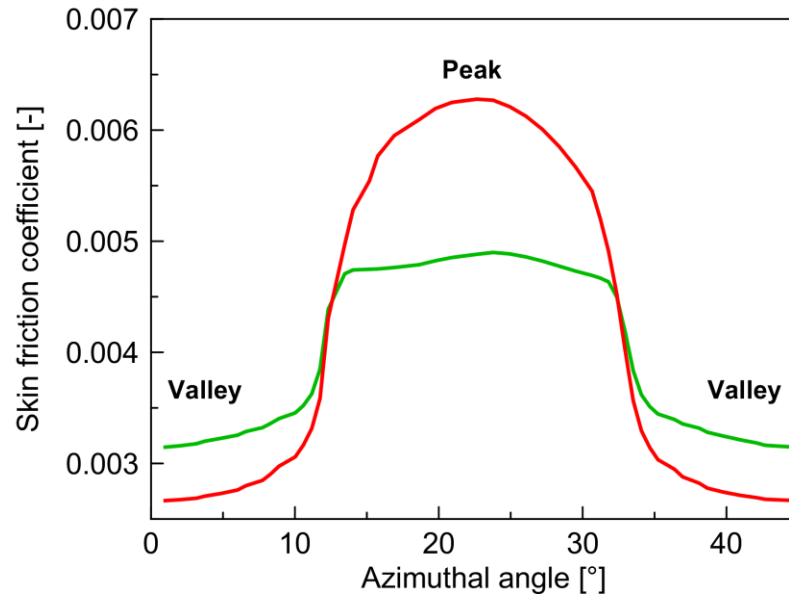


Figure 2-9: Skin friction coefficients in a cross section of a finned tube, $Re = 11,000$. — LES; — RANS: SST $k-\omega$

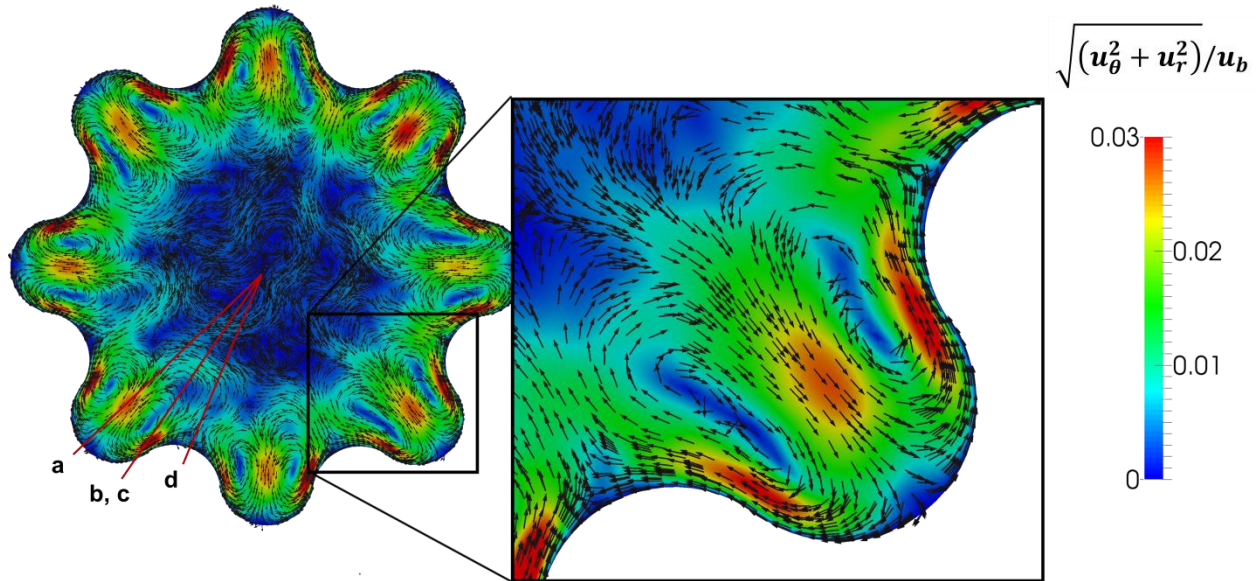


Figure 2-10: Time-averaged in-plane velocity vectors and contours of in-plane velocity magnitude in a finned tube, $Re = 11,000$.

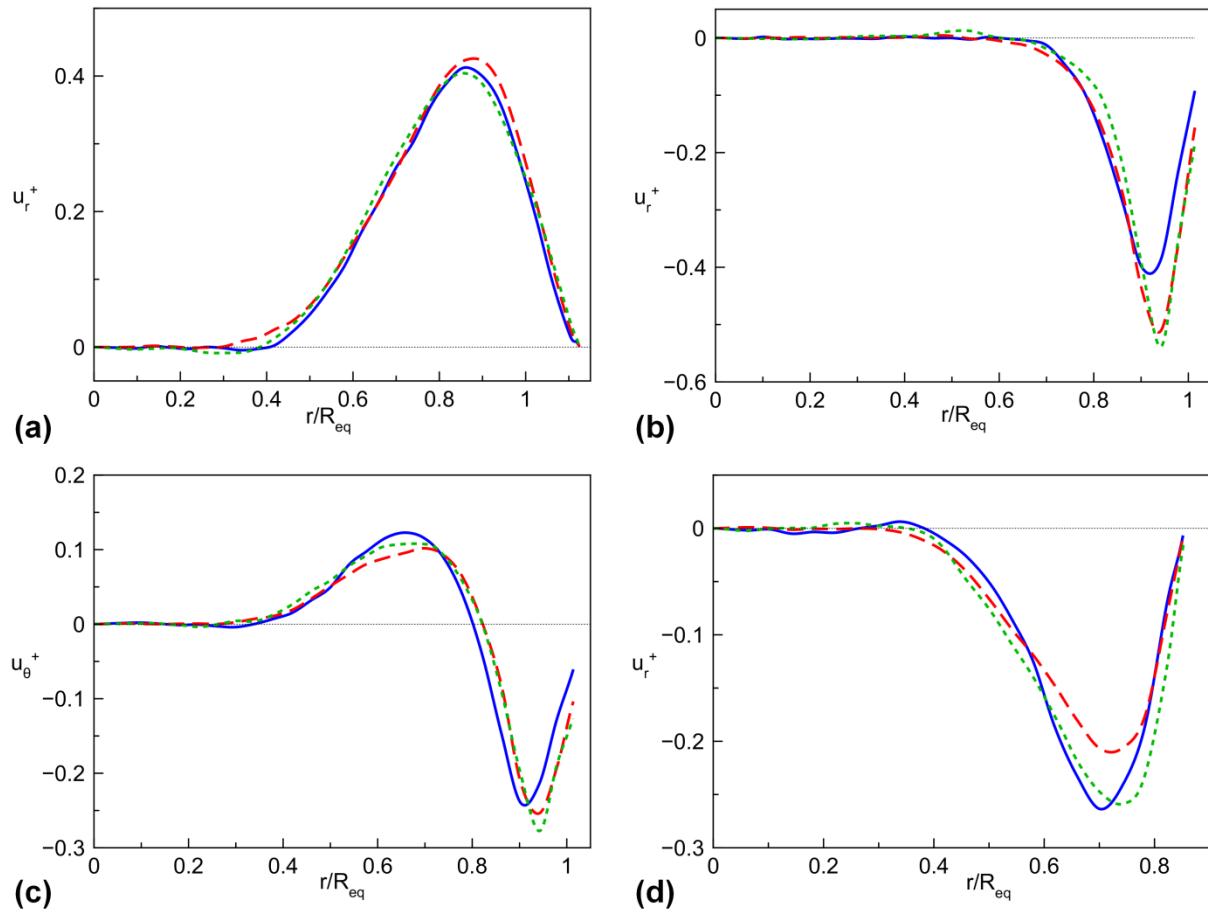


Figure 2-11: Mean radial and azimuthal velocity profiles in wall units. Angular locations corresponding to the valley of the fin (a), the top of the fin (d) and at the bisecting angle (b, c), as indicated on Figure 2-10. — $\text{Re} = 11,000$; - - $\text{Re} = 24,000$; . . . $\text{Re} = 38,000$

Figure 2-12 and Figure 2-13 show the simulated global Fanning friction factors and Nusselt numbers for both modeling approaches. The local over- and underprediction of the shear stresses appear to compensate as a relatively good agreement between the RANS and LES results is seen. Both dimensionless quantities also exhibit a similar Reynolds number dependency as the bare tube, with a multiplication factor that is roughly equal to the ratio of the internal surface area of the finned tube to that of a bare tube.

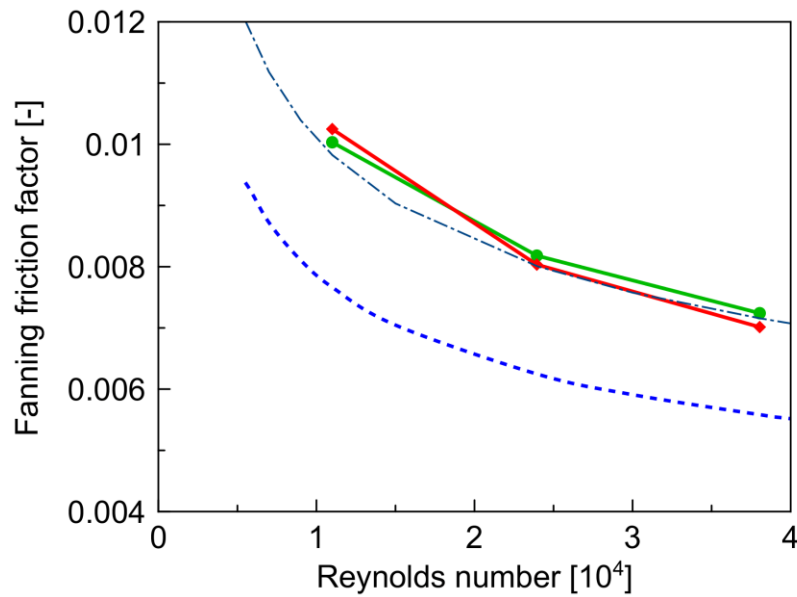


Figure 2-12: Fanning friction factor as a function of Reynolds number: —●— - LES; —◆— - RANS; - - - - Petukhov correlation (cf. Table 2-2) for a bare tube ; - · - · - Petukhov correlation (cf. Table 2-2) multiplied by the internal surface area ratio, $f_f \cdot A/A_0$.

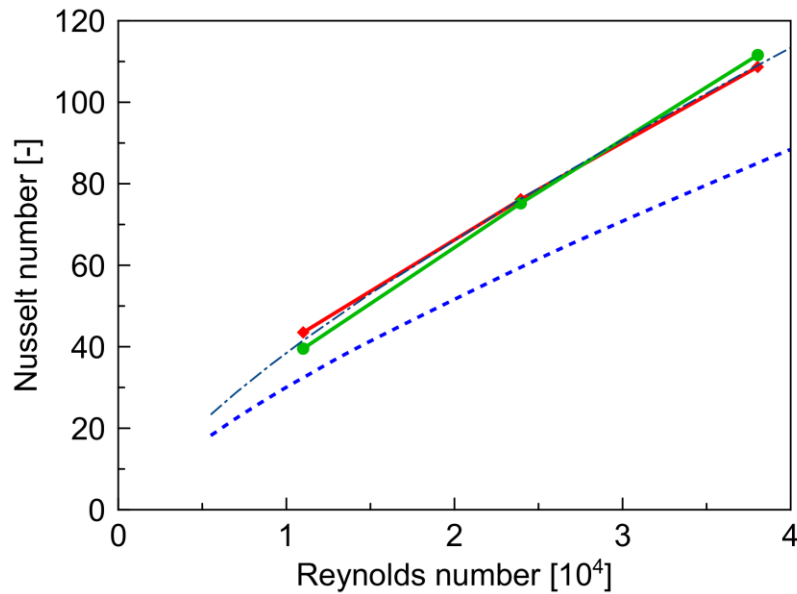


Figure 2-13: Nusselt number as a function of Reynolds number. —●— - LES; —◆— - RANS; - - - - Gnielinski correlation (cf. Table 2-3) for a bare tube; - · - · - Gnielinski correlation (cf. Table 2-3) multiplied by the internal surface area ratio, $Nu \cdot A/A_0$.

2.3.2.2 Swirl flow tube

Figure 2-14(a) shows the time-averaged in-plane velocity magnitude and vectors in a cross section of the swirl flow tube. A high tangential velocity is introduced in the C-shaped region furthest away from the tube axis, because of the centrifugal forces acting on the fluid. In the region where the two vortices touch, the flow leaves the tube inner wall and a low tangential velocity is prevalent. Figure 2-14(b) shows the secondary flow pattern that appears by isolating the mean swirling motion from the total velocity field, according to:

$$\vec{u} - \omega(\vec{r} \times \vec{1}_n) \quad (2.23)$$

where $\omega = u_b 2\pi/P$ is the angular velocity induced by the helicoidal path of the centerline and $\vec{1}_n$ is the unity vector normal to the visualization plane. This type of twin-vortex pattern is a typical example of a secondary current of Prandtl's first kind⁵⁴. As these structures are not turbulence induced but simply arise from the skew of the mean flow, both the RANS and LES approach were seen to offer accurate predictions of the phenomenon. The resulting local wall shear stresses are plotted in Figure 2-15. Results obtained with LES show a rather uniform stress distribution over the majority of the surface, followed by a clear stagnation zone near the tube axis. From the RANS simulations a less uniform profile with an even sharper drop in shear stress is observed. Additionally, the local minimum is predicted at a location further downstream than that predicted with LES. Figure 2-16 shows the instantaneous internal skin temperature of the tube, where a high-temperature zone on the inside of the helical bends exists due to the low local shear stress. The low- and high-speed streaks are also clearly discerned by the elongated thermal structures on the surface.

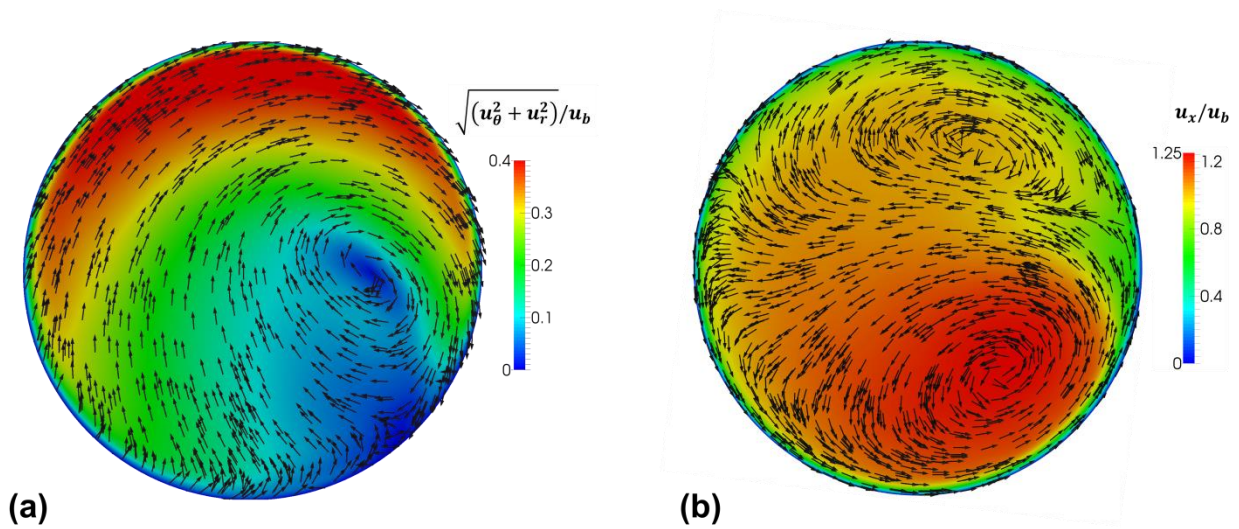


Figure 2-14: (a) In-plane velocity vectors and contours of in-plane velocity magnitude. (b) Vector visualization of the secondary motions and contours of axial velocity, $Re = 11,000$.

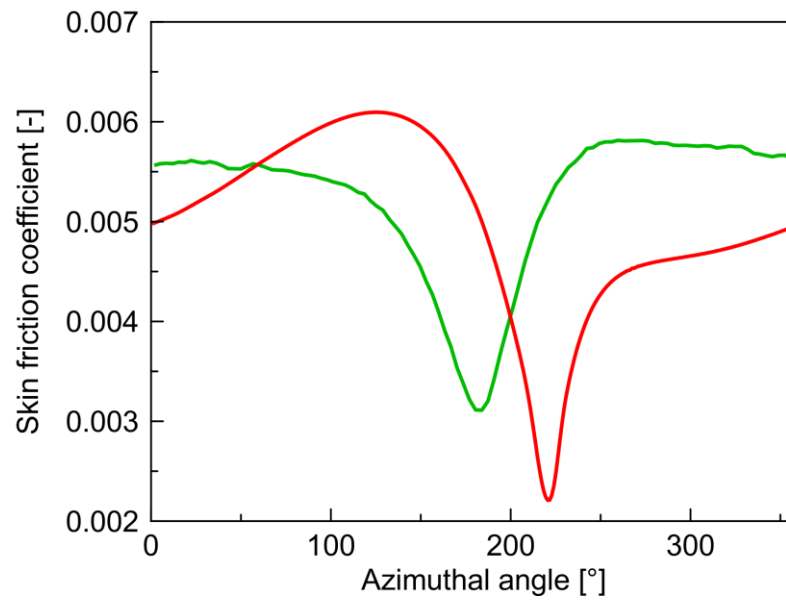


Figure 2-15: Skin friction coefficients in a cross section of a swirl flow tube, $Re = 11,000$. — - LES; — - RANS: SST $k-\omega$

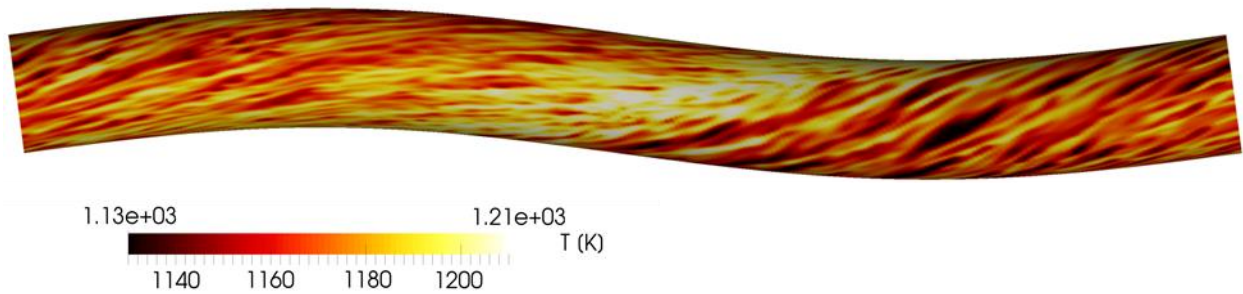


Figure 2-16: Temperature on the internal surface of a swirl flow tube, $Re = 38,000$, $T_b = 1100K$, $\gamma = 20 K/m$.

Despite the significant local differences, predictions of global friction factors and Nusselt numbers shown in Figure 2-17 and Figure 2-18 are seen to be quite similar for both modeling approaches. Comparison with the experimental data of Schietekat et al.³⁹ indicates an underprediction of the friction factors along with an overprediction of the Nusselt numbers. Similar deviations are spotted however when comparing the empirical correlations with the experimental data obtained on the same setup for a straight tube. A more reliable basis of comparison of the experimental and numerical predictions is hence obtained through calculation of the friction and heat transfer characteristics relative to those of a straight tube. This led to simulated enhancement factors of 1.37 and 1.39 for heat transfer and friction, while the experiments conducted at those Reynolds numbers indicated enhancement factors of 1.31 and 1.37, respectively.

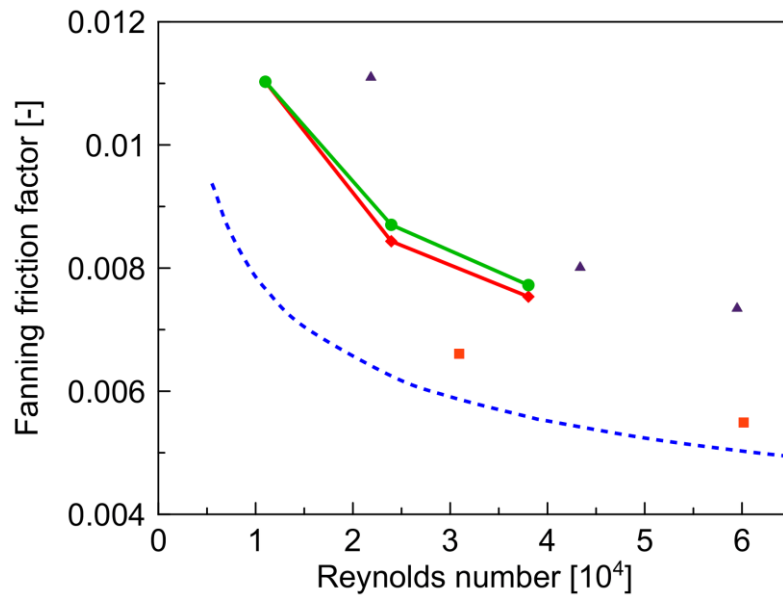


Figure 2-17: Fanning friction factor of a swirl flow tube as function of Reynolds number. —●— LES; —◆— RANS; - - - Petukhov correlation (cf. Table 2-2) for a bare tube; ▲ - SFT Schietekat et al.³⁹; ■ - Straight tube Schietekat et al.³⁹

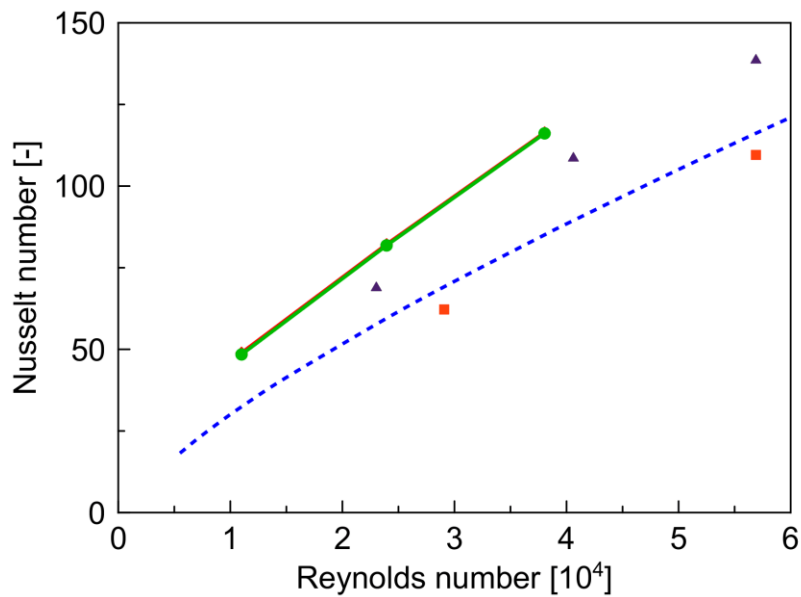


Figure 2-18: Nusselt number as function of Reynolds number. —●— - LES; —◆— - RANS; - - - - Gnielinski correlation (cf. Table 2-3) for a bare tube; ▲ - SFT Schietekat et al.³⁹; ■ - Straight tube Schietekat et al.³⁹

2.3.3 Steam cracking reactor simulations

The obtained simulation results allow assessing the potential of the studied finned and swirl flow tubes as industrial steam cracking reactors. The focus is here specifically on assessing the coking tendency of these different designs.

In order to qualitatively evaluate the effect of the reactor geometry on their coking tendency, the heat transfer and friction augmentation factors calculated in the previous section for $Re = 38,000$ are applied in COILSIM1D^{1, 56}. Simulations are performed for a typical industrial ethane cracker in which a Pyrocrack 4-2 reactor configuration⁵⁷ is applied. The coil outlet temperature (COT), the coil outlet pressure (COP), steam dilution and ethane mass flow rate are assumed fixed for the three considered geometries. Detailed reactor geometry and process conditions are provided in Supplementary Information. Table 2-4 lists the most significant differences between the three simulations and shows that slightly higher conversions are obtained for the coils with a higher pressure drop because of their longer residence time. Nevertheless, ethene yields are seen to be lower due to the increased importance of secondary reactions leading to heavier fractions. Note that in these 1D simulations potential positive effects of improved mixing on the yields are not accounted for because the focus is on run length improvements. Table 2-4 shows that the tube metal temperatures are substantially improved for straight fin and swirl flow designs, and hence, the reactors could be operated at either an increased load or for increased run lengths. This will be further amplified by the significant reduction in coking rates of respectively 33.9% and 40.2%.

Table 2-4: Comparison between simulated reactor properties, product yields and coking characteristics for different reactor designs based on the cold flow LES results.

	Bare straight	Straight fins	Swirl Flow
$\Delta P/\Delta P_{\text{Bare}} (Re = 38,000)$	1.00	1.30	1.39
$U/U_{\text{Bare}} (Re = 38,000)$	1.00	1.31	1.37
Pressure drop [bar]	1.067	1.295	1.360
Residence time [s]	0.495	0.526	0.535
Conversion [%]	65.88	65.97	66.00

Y C ₂ H ₄ [%]	51.73	51.53	51.47
Y C ₃ H ₆ [%]	1.00	1.03	1.04
Max T _{metal} [K]	1252.7	1213.8	1209.6
Max coking rate [nm/s]	3.86	2.55	2.31

As these simulations are performed at start-of-run conditions, the reduced thickness of the coke layer will cause the pressure drop and metal temperature to rise slower than in the bare tube. Over the length of a run it is very plausible that for the enhanced coil geometries even a reduced pressure drop is achieved compared to the bare starting from a specific point in time, reversing the olefin yield penalty. An important consideration to make however is that these coking rates are average values and both geometries exhibited considerable local non-uniformity. For the finned tube, this might cause the higher temperature zone in-between the fins to coke faster than the fins themselves leading to a reduced effect of the structure over time. Similarly, the stagnation zone in the center of the SFT can cause a local high coking rate which can influence the fluid dynamics over time. Reactive CFD simulations could provide further insight into this behavior but this was considered outside the scope of this work.

Note that although steam cracking reactors are typically modeled as a 1D plug flow reactor^{1, 58}, the existence of radial temperature gradients can also influence the product distribution. For the case of ethane cracking, it has been shown that a reduction of the high temperatures near the wall reduces the number of secondary reactions that lead to higher molecular weight species such as propylene and butadiene⁵⁹. On the other hand, cold zones where the gas mixture has not yet reached cracking temperatures are of course equally undesirable. In this way, a higher ethylene yield can be achieved by improving the heat transfer characteristics of the reactor.

In order to determine the radial temperature distribution in the three geometries, the temperature field is dimensioned by choosing a bulk temperature of 1100 K and axial temperature gradient of 10 K/m which are typical values in steam cracking. Figure 2-19 shows the volumetrically weighted temperature probability density function obtained in this way. It can be seen that although the fins offer an improved Nusselt number, the fact that a significant fraction of the gas is overheated in the zones between the fins leads to a decreased uniformity. The volumetric

fractions of the process gas within 10 K of the “optimal” cracking temperature are respectively 92.8 %, 94.8 % and 97.9 %.

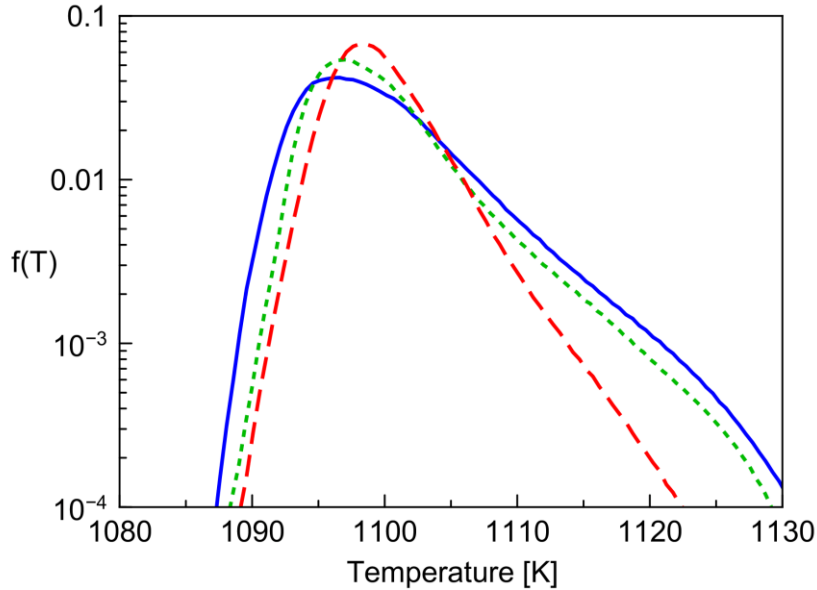


Figure 2-19: Probability density function of temperature at $Re = 11,000$; — - Bare straight; - - - - Finned tube; - - - - Swirl Flow Tube

2.4 Conclusions

The open-source CFD package OpenFOAM[®] has been used for wall-resolved LES. Streamwise periodic boundary conditions were applied in order to limit the computational domain and allow to study higher Reynolds numbers of up to 38,000. Good agreement was seen for the mean and 2nd order velocity and temperature statistics compared to pipe flow DNS data. Comparison with RANS for a tube enhanced with longitudinal fins revealed that the RANS model did not capture the secondary flows induced by the anisotropic turbulence. This led to inaccurate predictions of the local shear stress distribution while global quantities were seen to be in excellent agreement with the LES results. For the swirl flow tube the RANS simulations overpredict the turbulence induced by the rotating flow, leading to a shift in the location of peak wall temperatures. Nevertheless, comparison of global characteristics with the recently acquired experimental data of Schietekat et al.³⁹, showed good agreement for both modeling approaches with errors within 5% for the relative heat transfer and friction enhancement factors.

The finned and swirl flow tube were seen to offer an average improvement in heat transfer over the bare tube of respectively 29 % and 37 %. This came at the cost of a higher pressure drop of respectively 31 % and 39 %. Radial temperature uniformity was seen to be larger for the swirl flow tube, as a fraction of the gas in the finned tube remains isolated in-between the fins where local overheating occurs. A qualitative evaluation of coking behavior was performed by applying the obtained characteristics to a 1D reactor simulation, showing significant potential in terms of run length improvements for both enhanced geometries. Both designs were seen to cause large circumferential non-uniformities in the internal wall temperature, which may lead to uneven growth of the coke layer or thermal stresses in the material that can significantly affect the reactor life-cycle. In order to quantify this and evaluate the influence of the additional pressure drop on product yields, reactive simulations will be performed in the future. Finally, although the use of LES at these high Reynolds number ($> 10^5$) reactive simulations is today out of reach, the methods applied in the present work can be used to provide validation for RANS models in cases where reliable experimental data is limited or when local phenomena are of importance.

References

1. Van Geem, K.M., M.F. Reyniers, and G.B. Marin, *Challenges of Modeling Steam Cracking of Heavy Feedstocks*. Oil Gas Sci. Technol., 2008. **63**(1): p. 79-94.
2. Wauters, S. and G.B. Marin, *Kinetic Modeling of Coke Formation during Steam Cracking*. Industrial and Engineering Chemistry Research, 2002. **41**(10): p. 2379-2391.
3. Van Geem, K.M., R. Žajdlík, M.-F. Reyniers, and G.B. Marin, *Dimensional analysis for scaling up and down steam cracking coils*. Chemical Engineering Journal, 2007. **134**(1-3): p. 3-10.
4. Van Geem, K.M., I. Dhuyvetter, S. Prokopiev, M.F. Reyniers, D. Viennet, and G.B. Marin, *Coke Formation in the Transfer Line Exchanger during Steam Cracking of Hydrocarbons*. Industrial and Engineering Chemistry Research, 2009. **48**(23): p. 10343-10358.
5. Zhang, Y., F. Qian, C.M. Schietekat, K.M. Van Geem, and G.B. Marin, *Impact of flue gas radiative properties and burner geometry in furnace simulations*. AIChE Journal, 2015. **61**(3): p. 936-954.
6. Zhou, J., Z. Wang, X. Luan, and H. Xu, *Anti-coking property of the SiO₂/S coating during light naphtha steam cracking in a pilot plant setup*. Journal of Analytical and Applied Pyrolysis, 2011. **90**(1): p. 7-12.
7. Muñoz Gandarillas, A.E., K.M. Van Geem, M.-F. Reyniers, and G.B. Marin, *Influence of the Reactor Material Composition on Coke Formation during Ethane Steam Cracking*. Industrial and Engineering Chemistry Research, 2014. **53**(15): p. 6358-6371.
8. Wang, J.D., M.F. Reyniers, K.M. Van Geem, and G.B. Marin, *Influence of silicon and silicon/sulfur-containing additives on coke formation during steam cracking of hydrocarbons*. Industrial and Engineering Chemistry Research, 2008. **47**(5): p. 1468-1482.
9. van Goethem, M.W.M. and E. Jelsma, *Numerical and experimental study of enhanced heat transfer and pressure drop for high temperature applications*. Chemical Engineering Research and Design, 2014. **92**(4): p. 663-671.
10. Schietekat, C.M., D.J. Van Cauwenberge, K.M. Van Geem, and G.B. Marin, *Computational fluid dynamics-based design of finned steam cracking reactors*. AIChE Journal, 2013. **60**(2): p. 794-808.
11. Albano, J.V., K.M. Sundaram, and M.J. Maddock, *Applications of extended surfaces in pyrolysis coils*. Energy Progress, 1988. **8**(3): p. 9.
12. Wölpert, P., B. Ganser, D. Jakobi, and R. Kirchheiner, *Process and finned tube for the thermal cracking of hydrocarbons*, 2005, Schmidt + Clemens GmbH + Co., KG: United States.
13. Wallin, S. and A.V. Johansson, *An explicit algebraic Reynolds stress model for incompressible and compressible turbulent flows*. Journal of Fluid Mechanics, 2000. **403**: p. 89-132.
14. Wilcox, D.C., *Turbulence Modeling for CFD*. 2006: D C W Industries.

15. Thakre, S.S. and J.B. Joshi, *CFD modeling of heat transfer in turbulent pipe flows*. AIChE Journal, 2000. **46**(9): p. 1798-1812.
16. Eggels, J.G.M., F. Unger, M.H. Weiss, J. Westerweel, R.J. Adrian, R. Friedrich, and F.T.M. Nieuwstadt, *Fully developed turbulent pipe flow: a comparison between direct numerical simulation and experiment*. Journal of Fluid Mechanics, 1994. **268**: p. 175-210.
17. Redjem-Saad, L., M. Ould-Rouiss, and G. Lauriat, *Direct numerical simulation of turbulent heat transfer in pipe flows: Effect of Prandtl number*. International Journal of Heat and Fluid Flow, 2007. **28**(5): p. 847-861.
18. El Khoury, G.K., P. Schlatter, A. Noorani, P.F. Fischer, G. Brethouwer, and A.V. Johansson, *Direct Numerical Simulation of Turbulent Pipe Flow at Moderately High Reynolds Numbers*. Flow Turbul. Combust., 2013. **91**(3): p. 475-495.
19. Dhotre, M.T., B. Niceno, and B.L. Smith, *Large eddy simulation of a bubble column using dynamic sub-grid scale model*. Chemical Engineering Journal, 2008. **136**(2-3): p. 337-348.
20. Hu, L.W. and M.S. Kazimi, *LES benchmark study of high cycle temperature fluctuations caused by thermal striping in a mixing tee*. International Journal of Heat and Fluid Flow, 2006. **27**(1): p. 54-64.
21. Jafari, A., P. Zamankhan, S.M. Mousavi, and K. Pietarinen, *Modeling and CFD simulation of flow behavior and dispersivity through randomly packed bed reactors*. Chemical Engineering Journal, 2008. **144**(3): p. 476-482.
22. Nilsen, K.M., B. Kong, R.O. Fox, J.C. Hill, and M.G. Olsen, *Effect of inlet conditions on the accuracy of large eddy simulations of a turbulent rectangular wake*. Chemical Engineering Journal, 2014. **250**(0): p. 175-189.
23. Hernadi, Z. and G. Kristof, *Prediction of pressure drop and heat transfer coefficient in helically grooved heat exchanger tubes using large eddy simulation*. P. I. Mech. Eng. A - J. Pow., 2014. **228**(3): p. 317-327.
24. Sewall, E.A., D.K. Tafti, A.B. Graham, and K.A. Thole, *Experimental validation of large eddy simulations of flow and heat transfer in a stationary ribbed duct*. International Journal of Heat and Fluid Flow, 2006. **27**(2): p. 243-258.
25. Elyyan, M.A. and D.K. Tafti, *Large Eddy Simulation Investigation of Flow and Heat Transfer in a Channel With Dimples and Protrusions*. J. Turbomach., 2008. **130**(4): p. 9.
26. *OpenFOAM - The Open Source CFD Toolbox - User's Guide*, 2013, OpenCFD Ltd: United Kingdom.
27. *OpenFOAM - The Open Source CFD Toolbox - Programmer's Guide*, 2013, OpenCFD Ltd: United Kingdom.
28. Boussinesq, J., *Essai sur la théorie des eaux courantes*. Mémoires présentés par divers savants à l'Académie des Sciences, 1877. **23**: p. 680.

-
29. Germano, M., U. Piomelli, P. Moin, and W.H. Cabot, *A dynamic subgrid-scale eddy viscosity model*. Physics of Fluids A, 1991. **3**(7): p. 1760-1765.
 30. Lilly, D.K., *A proposed modification of the Germano subgrid-scale closure method*. Physics of Fluids A, 1992. **4**: p. 3.
 31. Smagorinsky, J., *General circulation experiments with the primitive equations*. Mon. Weather Rev., 1963. **91**(3): p. 99-164.
 32. Menter, F.R., *Two-equation eddy-viscosity turbulence models for engineering applications*. AIAA Journal, 1994. **32**(8): p. 1598-1605.
 33. Moin, P., K. Squires, W. Cabot, and S. Lee, *A dynamic subgrid-scale model for compressible turbulence and scalar transport*. Physics of Fluids A, 1991. **3**(11): p. 2746-2757.
 34. William Kays, M.C., Bernhard Weigand, *Convective Heat and Mass Transfer*. 4th ed. 2004: McGraw-Hill (Tx).
 35. Pope, S.B., *Turbulent Flows*. 2000: Cambridge University Press.
 36. Patankar, S.V., C.H. Liu, and E.M. Sparrow, *Fully Developed Flow and Heat Transfer in Ducts Having Streamwise-Periodic Variations of Cross-Sectional Area*. Journal of Heat Transfer, 1977. **99**(2): p. 180-186.
 37. De Saegher, J.J., T. Detemmerman, and G. Froment, *Three dimensional simulation of high severity internally finned cracking coils for olefins production*. Oil Gas Sci. Technol., 1996. **51**(2): p. 245-260.
 38. Caro, C.G., N.J. Cheshire, and N. Watkins, *Preliminary comparative study of small amplitude helical and conventional ePTFE arteriovenous shunts in pigs*. J. R. Soc. Interface, 2005. **2**: p. 6.
 39. Schietekat, C.M., M.W.M. van Goethem, K.M. Van Geem, and G.B. Marin, *Swirl flow tube reactor technology: An experimental and computational fluid dynamics study*. Chemical Engineering Journal, 2014. **238**(0): p. 56-65.
 40. Pointwise, I., *Pointwise Mesh & Grid Generation Software*, 2014, Pointwise: Fort Worth, TX.
 41. Kravchenko, A.G. and P. Moin, *On the Effect of Numerical Errors in Large Eddy Simulations of Turbulent Flows*. J. Comput. Phys., 1997. **131**(2): p. 310-322.
 42. Chapman, D.K., *Computational Aerodynamics Development and Outlook*. AIAA Journal, 1979. **17**(12): p. 1293-1313.
 43. Chin, C., A.S.H. Ooi, I. Marusic, and H.M. Blackburn, *The influence of pipe length on turbulence statistics computed from direct numerical simulation data*. Physics of Fluids, 2010. **22**(11).
 44. Piller, M., *Direct numerical simulation of turbulent forced convection in a pipe*. International Journal for Numerical Methods in Fluids, 2005. **49**(6): p. 583-602.
 45. Lawn, C.J., *The determination of the rate of dissipation in turbulent pipe flow*. Journal of Fluid Mechanics, 1971. **48**(03): p. 477-505.

46. Kader, B.A., *Temperature and concentration profiles in fully turbulent boundary layers*. International Journal of Heat and Mass Transfer, 1981. **24**(9): p. 1541-1544.
47. Blasius, H., *Das Aehnlichkeitsgesetz bei Reibungsvorgängen in Flüssigkeiten*, in *Mitteilungen über Forschungsarbeiten auf dem Gebiete des Ingenieurwesens*, 1913, Springer Berlin Heidelberg. p. 1-41.
48. Churchill, S.W., *Friction Factor Equations Spans all Fluid Flow Regimes*. Chemical Engineering, 1977. **84**: p. 91-102.
49. Petukhov, B.S., *Heat Transfer and Friction in Turbulent Pipe Flow with Variable Physical Properties*, in *Advances in Heat Transfer*, T.F.I. J. P. Hartnett, Editor 1970, Academic Press: New York.
50. Kays, W.M., M.E. Crawford, and B. Weigand, *Convective heat and mass transfer*. 2012: Tata McGraw-Hill Education.
51. McAdams, W.H., *Heat transmission*. Vol. 3. 1954, New York: McGraw-Hill.
52. Gnielinski, V., *New equations for heat and mass-transfer in turbulent pipe and channel flow*. International Chemical Engineering, 1976. **16**(2): p. 359-368.
53. Nikuradse, J., *Untersuchungen über die Geschwindigkeitsverteilung in turbulenten Strömungen*, 1926, Göttingen: VDI Forsch. 281.
54. Prandtl, L., *Essentials of fluid dynamics*. 1952: Hafner Publishing Company, New York, U.S.
55. Uhlmann, M., A. Pinelli, G. Kawahara, and A. Sekimoto, *Marginally turbulent flow in a square duct*. Journal of Fluid Mechanics, 2007. **588**: p. 153-162.
56. Pyl, S.P., T. Dijkmans, J.M. Antonykuty, M.-F. Reyniers, A. Harlin, K.M. Van Geem, and G.B. Marin, *Wood-derived olefins by steam cracking of hydrodeoxygenated tall oils*. Bioresource Technology, 2012. **126**(0): p. 48-55.
57. Lemme, V., *Petrochemical Furnaces*, 2011, SELAS-LINDE GmbH.
58. van Goethem, M.W.M., F.I. Kleinendorst, C. van Leeuwen, and N. van Velzen, *Equation-based SPYRO® model and solver for the simulation of the steam cracking process*. Computers and Chemical Engineering, 2001. **25**(4-6): p. 905-911.
59. Van Geem, K.M., G.J. Heynderickx, and G.B. Marin, *Effect of radial temperature profiles on yields in steam cracking*. AIChE Journal, 2004. **50**(1): p. 173-183.

3

Numerical and experimental evaluation of heat transfer in helically corrugated tubes

“What most experimenters take for granted before they begin their experiments is infinitely more interesting than any results to which their experiments lead.”

Norbert Wiener (1894 – 1964)

This chapter has been submitted as :

Van Cauwenberge, D.J., Dedeyne, J.N., Floré, J., Van Geem, K.M., Marin, G.B. Numerical and experimental evaluation of heat transfer in helically corrugated tubes. AIChE J. 2017.

Abstract

The enhancement of convective heat transfer in single-phase heat transfer through the use of helicoidally corrugated tubes has been studied numerically. By comparing the large eddy simulation (LES) results with detailed Stereo-PIV and Liquid Crystal Thermography measurements obtained at the von Karman Institute for Fluid Dynamics (VKI), a validated numerical framework was obtained. Heat transfer enhancements of 83-119% were seen, at the cost of pressure losses that were approximately 5.6 to 6.7 times higher than for a bare tube. In order to extrapolate the results to industrial Reynolds numbers at which experimental data is scarce, the simulation data was used to develop an improved near-wall Reynolds stress transport model (RSTM) that more accurately describes the heat flux vector. Comparison of both global and local flow characteristics at different Reynolds numbers confirms that the approach allows more accurate predictions over a wider range of design and operating parameters than using two-equation turbulence models, while the computational cost is still significantly lower than LES.

3.1 Introduction

Heat transfer in pipe flow is a key component in a wide array of industries, ranging from refrigeration, air conditioning, to automotive, turbomachinery and petrochemical industries. Attempts to increase the “normal” single phase heat transfer coefficients and reduce equipment cost and size have been reported in technical literature for well over a century. While the first generation passive enhancements consisted of plain fins, the majority of current devices act to increase secondary flows and turbulence levels to enhance mixing and advection of heat away from or towards the tube surface. Examples include rib turbulators, dimpled surfaces, twisted tapes, wire coils, micro-fins, coiled tubes, etc. Recent and comprehensive literature reviews on these techniques can be found in Bergles¹, Liu², Ligrani³ and Ji et al.⁴.

A recurring theme in these review papers is that despite the numerous investigations and the “routine” involved in the application of enhanced heat transfer, the field remains full of experimental, numerical and analytical difficulties. Even for devices that have been investigated

Numerical and experimental evaluation of heat transfer in helically corrugated tubes

for over half a century, completely satisfactory and unified correlations in terms of geometrical parameters are not available yet. Modeling of the important phenomena has proven equally challenging, despite the exponential rise in computational power and use of advanced numerical methods. While the number of publications in the heat transfer enhancement field has all but tapered off, Ligrani notes that “improvements in our ability to provide better overall, spatially averaged thermal protection have been minimal since 2003”³.

Although the added value is clear, industry has also been slow in adapting to new devices, despite the progress in manufacturing of all sorts of complex geometries. As the most energy consuming process in the chemical industry, globally amounting to 8% of the sector’s total primary energy use⁵, the production of light olefins by steam cracking could benefit significantly from improved energy efficiency. In order to heat the process gas to temperatures of around 1100 K within less than a second, the reactor coils are suspended in a gas-fired furnace and exposed to radiative heat fluxes on the order of 10^5 W/m². This puts an enormous stress on the coil metallurgy and reactor lifetimes are typically limited to a few years due to the combined effect of creep and carburization^{6, 7}. Additionally, the high metal temperatures cause the formation of coke deposits on the internal surface of the reactors, leading to additional maintenance considerations that significantly impact the economics of the process. While these issues could be alleviated by facilitating the convective heat transfer to the process gas, many commercial installations still use bare reactor tubes or “old technology” such as extended surfaces in the form of internal fins.

One of the few devices that managed to achieve success on a commercial scale is the so-called Mixing Element Radiant Tube (MERT)^{8, 9}, where a semi-circular rib element is applied in a continuous or interrupted helical manner on the internal surface. The enhancement hence falls under the category of surface roughness and is closely related to the well-studied corrugated tube type. These kinds of geometries aim to interrupt the development of the thermal boundary layer and increase turbulence levels in order to enhance radial mixing.

Deciding on an optimal design for a certain set of reactor conditions is however not straightforward. Firstly, the mentioned disagreement between the numerous experimental studies in literature does not allow the use of a single unified correlation that is valid over a wide range

Numerical and experimental evaluation of heat transfer in helically corrugated tubes

of geometrical parameters and Reynolds numbers¹. Figure 3-1 lists a number of experimental studies on such rib-roughened tubes and illustrates the parameter ranges explored in each of them. Note that the geometry is fully determined by two parameters, namely the rib height e and the pitch length p between two subsequent ribs. For single-start ribs, the helix angle α enclosed by the tube axis and the rib element directly follows from this as $\tan \alpha = \pi D/p$. In the present work, the values of 0.036 and 0.42 have been investigated for the e/D and p/D ratio, respectively. While these values are rather low with regards to the full parameter range, a number of experimental studies are seen to have been performed in their proximity. It is hence reasonable to assume at least some degree of accuracy in the correlations proposed in these works.

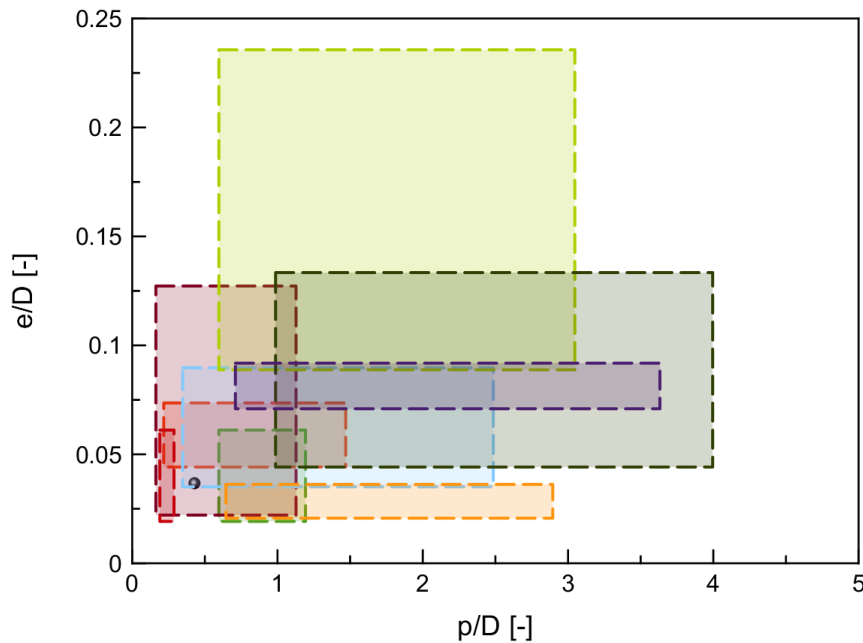


Figure 3-1: Geometrical parameter range of some experimental studies on helicoidally corrugated tubes.

— Sethumadhavan¹⁰; — Zhang¹¹; — Ravigururajan¹²; — Webb¹³; — Vicente¹⁴; — Saha¹⁵; — Pethkool¹⁶; — Slaiman¹⁷; — Ali¹⁸; ● Present work

Looking at the Nusselt number and friction factor predictions in Figure 3-2 however, this assumption appears to be debatable, as the respective correlations predict heat transfer enhancements ranging from 60% to 174%, while pressure losses are increased by between 95%

Numerical and experimental evaluation of heat transfer in helically corrugated tubes

and 560%. With such data disparity, it is evident that existing correlations, even based on recent data obtained for well-studied devices, are of limited use for optimization.

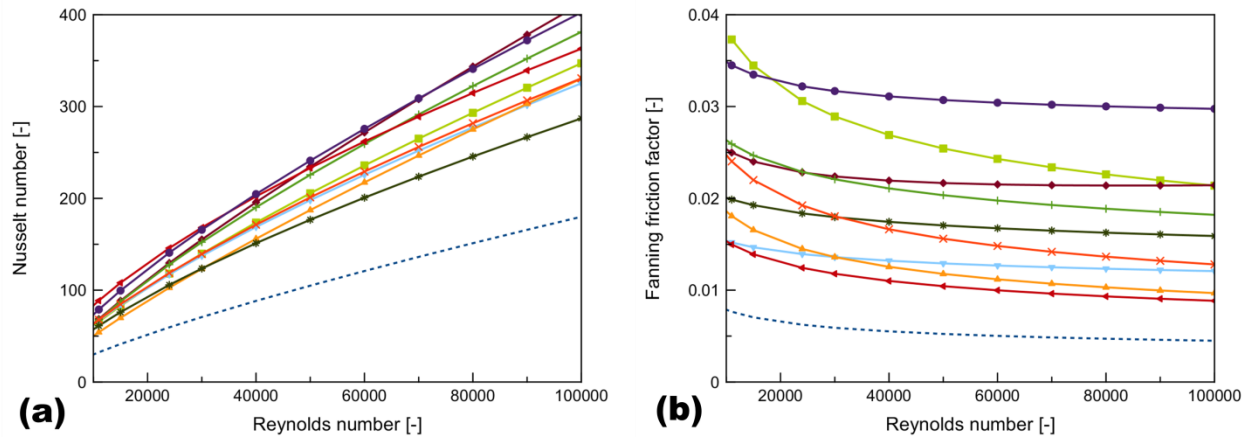


Figure 3-2: (a) Nusselt number and (b) friction factor for a helicoidally corrugated tube according to literature correlations. ■■■■ Bare tube – Nu from Eqn. (3.2)¹⁹, C_f from Eqn. (3.3)²⁰; — Sethumadhavan¹⁰; — Zhang¹¹; — Ravigururajan¹²; — Webb¹³; — Vicente¹⁴; — Saha¹⁵; — Pethkool¹⁶; — Slaiman¹⁷; — Ali¹⁸

A second argument against the applicability of existing correlations is the limited range of Reynolds numbers covered in these studies. Although they are all obtained in the fully turbulent regime, no data could be found for Reynolds numbers above 10^5 . Because of trends towards greater volumes coupled with shorter residence times, this is the range in which most state of the art steam crackers operate, and in which accurate predictions are most critical.

While numerical simulation is the logical alternative, its predictive power has also been shown to depend strongly on the applied turbulence model^{21, 22}. Including a greater level of theory in the form of eddy-resolving techniques is known to offer a more geometry-independent approach but is only slowly gaining popularity in industrial settings due to their associated computational cost. While resolving the near-wall region is critical in heat transfer calculations, the important turbulent length scales in this region are also significantly smaller than in the bulk of the flow and follow an inverse relation with the Reynolds number. This causes the required grid density for

Numerical and experimental evaluation of heat transfer in helically corrugated tubes

such simulations to exhibit a $N_x N_y N_z \sim \text{Re}^{9/5}$ dependency, effectively preventing the use of eddy-resolving techniques beyond Reynolds numbers of 10^5 .

It is the aim of the present paper to demonstrate how these detailed numerical simulations can yet be of use in realizing heat transfer enhancements outside of the well-known or easily accessible parameter range when used in combination with state-of-the-art experimental techniques. Such techniques can include the use of tomographic or stereoscopic particle image velocimetry (PIV) for accurate information on the physical phenomena and flow patterns, while liquid crystal thermography (LCT) on the tube surface allows evaluation of the local heat transfer characteristics^{23, 24}. The spatial resolution of these techniques is particularly powerful compared to traditional globally measured data such as pressure drops and total transferred heat, as they allow the validation of high-fidelity computations. Such validated computational setups can then be extended and applied to similar devices, but over a wider parameter range and at a reduced cost compared to the original experiments.

To demonstrate this concept, use is made of the recently acquired experimental dataset obtained at the von Karman Institute for Fluid Dynamics (VKI) by Mayo et al.²⁵. This kind of reliable datasets are invaluable sources of experimental validation for numerical approaches. Additionally, the study focuses on the performance of a helically corrugated tube, which is of particular interest in the field of steam cracking because of the mentioned similarity with the commercial MERT design.

A short overview of the experimental setup is given in the following section, but for a more detailed description, reference can be made to the original publication. The adopted numerical procedure to simulate the experiments using OpenFOAM is described, along with the necessary steps in order to incorporate the experimental dataset into the improved simulation framework. Additional validation for the proposed models is provided by comparison with a numerical dataset. Finally, an industrially relevant helically corrugated tube is simulated, demonstrating the feasibility of using anisotropy-resolving Reynolds-averaged Navier-Stokes models for these complex configurations.

3.2 Experimental setup

In order to accurately investigate the complex physical phenomena in helically corrugated tubes, two distinct experimental setups were employed to capture the detailed flow field and heat transfer. For the aerodynamic investigation, Stereoscopic Particle Image Velocimetry (S-PIV) was applied. This allows capturing of mean flow quantities, turbulence statistics and vortical structures produced due to the presence of the tube enhancements. Next to this, steady-state Liquid Crystal Thermography (LCT) was combined with Infrared Thermography (IRT) in order to measure the temperatures on the tube surface. Data from both setups was obtained at a Reynolds number of 24,000.

3.2.1 Velocity measurements

The dedicated testing facility for the S-PIV measurements, designed in order to minimize the experimental error, consists of five sections. For a detailed description of the settling chamber, development duct, outlet channel and discharge chamber, the reader is referred to Mayo et al.²⁵.

The actual test section of the setup, which has an internal diameter of 150 mm and a length of 980 mm, is made of transparent acrylic glass to provide optical access to the flow field. The helically corrugated rib, made of ABS (acrylonitrile butadiene styrene) is mounted inside the section and extends over 10 pitches. Measurements are performed in the channel symmetry plane downstream of the 7th rib as it is believed that no entrance effects can be seen after six rib pitches. The working fluid, which is water for the velocity measurements, is seeded with 20 g/m³ of Cospheric fluorescent polyethylene spheres of 10-45 μm diameter. These seeding particles are illuminated with a double pulsed Nd:YAG laser. Two double-shutter CCD cameras equipped with Nikon Nikkor lenses acquire 1500 realizations at a frequency of 1 Hz. These realizations are processed with the commercial software DaVis 8.2 resulting in a resolution of about 1.3 x 1.3 mm². The in-situ calibration of this setup was performed following the method proposed by Soloff et al.²⁶.

3.2.2 Heat transfer measurements

Similarly to the experimental facility for velocity measurements, the heat transfer measurement setup can be split up into multiple sections of which only the relevant test section will be discussed in more detail. This test section has the same dimensions and building materials as the S-PIV setup. An important difference is the use of air as a working fluid, rather than water as was the case for the PIV experiments. Two K-type thermocouples are used to measure the fluid temperature in the center of the inlet and outlet cross sections. On the test section's inner wall, a layer of TLCs is deposited followed by a matt black paint layer to increase contrast. An Inconel foil of 0.02 mm thickness is then applied to this paint by means of a thin acrylic adhesive layer. The ABS ribs are mounted on top of the foil. A DC voltage is applied to the Inconel layer, which heats up due to the Joule effect and allows heat transfer to the air flow inside the setup. Due to the low resistivity of the Inconel, a uniform heating per unit area is achieved and hence a small region of interest (ROI) can be chosen for the measurement. For each point in this ROI, a heat balance is solved to evaluate the thermal efficiency of the ribs. To solve this heat balance, LCT is used to determine the internal temperature and an infrared camera is used to measure the external cylinder temperature. After accounting for conduction losses in the axial and tangential directions, the heat transfer coefficient h , is calculated as:

$$h(x, \theta) = \frac{q_{conv}(x, \theta)}{T_w(x, \theta) - T_b(x)} \quad (3.1)$$

where x is the axial coordinate, θ the angle with the horizontal plane and $T_b(x)$ is calculated by linear interpolation between inlet and outlet temperatures as measured by the two thermocouples. To assess the heat transfer enhancement, the resulting Nusselt number is compared to Nu_0 , which is the Nusselt number of a fully developed flow in a smooth circular pipe, estimated from the Gnielinski correlation¹⁹, using the Petukhov²⁰ correlation for the Fanning friction factor:

$$Nu_0 = \frac{(f_{f,0}/2)(Re - 1000)Pr}{1 + 12.7\sqrt{f_{f,0}/2}(Pr^{2/3} - 1)} \quad (3.2)$$

$$f_{f,0} = (1.58 \ln Re - 3.28)^{-2} \quad (3.3)$$

In order to assess the accuracy of this method, benchmark measurements were carried out in the smooth test section that gave excellent overall agreement with the applied correlations.

3.3 Numerical simulation procedure

3.3.1 Governing equations

While the experimental procedure made use of two separate test sections with different working fluids, the dynamic similitude because of identical geometries and equal Reynolds numbers allows a reproduction of both datasets from a single simulation. The flow is modeled as incompressible and temperature is treated as a passive scalar by neglecting viscous dissipation and buoyancy effects. The filtered Navier-Stokes and temperature equations, normalized with the radius R , the friction velocity u_τ , the kinematic viscosity ν and the friction temperature $\theta_\tau = q_w / \rho c_p u_\tau$, can be written in Einstein notation as:

$$\frac{\partial \tilde{u}_i}{\partial x_i} = 0 \quad (3.4)$$

$$\frac{\partial \tilde{u}_i}{\partial t} + \frac{\partial \tilde{u}_i \tilde{u}_j}{\partial x_j} = -\frac{1}{\rho} \frac{\partial \tilde{p}}{\partial x_i} + \frac{1}{Re_\tau} \frac{\partial^2 \tilde{u}_i}{\partial x_j^2} - \frac{\partial \tau_{ij}^R}{\partial x_j} \quad (3.5)$$

$$\frac{\partial \tilde{\theta}}{\partial t} + \frac{\partial \tilde{\theta} \tilde{u}_j}{\partial x_j} = \frac{1}{Re_\tau Pr} \frac{\partial^2 \tilde{\theta}}{\partial x_j^2} + \frac{\partial q_j}{\partial x_j} \quad (3.6)$$

Where $\tau_{ij}^R = \widetilde{u_i u_j} - \tilde{u}_i \tilde{u}_j$ is the residual stress tensor and $q_j = \widetilde{\theta u_j} - \tilde{\theta} \tilde{u}_j$ is the residual heat flux which both require modeling in order to close Eqn. (3.5) and (3.6). When tilde represents a time-averaging operator, the classical Reynolds-averaged Navier-Stokes (RANS) equations are retrieved. In an eddy-resolving framework, tilde implies a spatial filtering operation and the model terms include only sub-filter contributions to the stress tensor and the heat flux.

3.3.2 Turbulence modeling

In the present work, simulations are performed using three different approaches in terms of turbulence modeling.

At the highest level of theory, a large eddy simulation (LES) approach is chosen in order to provide comparison with the experimental dataset. The sub-filter scales are modeled using the model of Kim and Menon²⁷, wherein non-local and history effects are included by solving a transport equation for the sub-filter kinetic energy. The model is also dynamic in that the model coefficients are optimized locally depending on the resolved flow scales just above the filter width.

A less computationally demanding set of simulations was performed using Menter's SST $k-\omega$ RANS model²⁸. In this well-known model, an eddy viscosity approach is used to relate the turbulent stresses to the mean flow while solving two additional transport equations for the turbulent kinetic energy and turbulence dissipation rate. By switching between an ε and an ω formulation in the free stream and the near-wall region, respectively, the model has shown to be reliable for a wide range of flows. A comparison was made between this model and an LES approach for a number of benchmark flows²². As expected, the large eddy simulations proved to be more reliable as soon as the flow became more complex and deviated further from the canonical flow configurations for which the RANS model was tuned. The well-known drawback however is the marked dependency of the computational cost on the Reynolds number, which warrants it from being applied to industrial configurations.

The search for modeling approaches that are able to capture a similar amount of physics as LES, while having a cost that is closer to a traditional RANS model, has been a key research topic in fluid dynamics for the past few decades.

One development direction consists in the use of so-called hybrid RANS/LES methods which aim at suitably combining some RANS model in attached boundary layers with some turbulence resolving method in separated regions where RANS models are known to fail. A very successful member of this class is Detached Eddy Simulation (DES), first proposed by Spalart in 1997²⁹.

Numerical and experimental evaluation of heat transfer in helically corrugated tubes

Along with its later adaptations in the form of (Improved) Delayed DES (DDES/IDDES)^{30, 31}, these techniques have shown considerable improvements in simulation accuracy for flows with massive separation at industrially relevant Reynolds numbers. Nevertheless they remain expensive because of their need to resolve the unsteady turbulent motion reasonably well down to some small scale. Additionally, they struggle in flows where the boundary layer thickness is of the order of the grid spacing or when dealing with shallow separation bubbles³², as it is the case in the present application.

Another common approach is the use of a second moment closure by employing the exact equations for the transport of the differential Reynolds stresses:

$$\frac{D\tau_{ij}^R}{Dt} = D_{ij} + P_{ij} + \Pi_{ij} + \Omega_{ij} - \epsilon_{ij} \quad (3.7)$$

where D_{ij} and Ω_{ij} denote the transport by respectively diffusion and rotation, P_{ij} the production, Π_{ij} the redistribution term due to pressure-strain interaction and ϵ_{ij}^h the stress dissipation. The main advantage of these differential Reynolds stress models (DRSMs) is that the stress production tensor P_{ij} can be calculated exactly, and hence a larger amount of physics is included. The relatively limited additional computational cost, steered much effort towards their development throughout the 70s and 80s. With the increase in computational capacity however, focus gradually shifted more towards eddy-resolving methods rather than Reynolds stress models. Experts such as Speziale cited the difficulties in stabilizing the models for complex wall-bounded flows and the poor performance in non-equilibrium flows or when integrating the models directly to a solid boundary³³. Nevertheless, a recent resurgence of interest in the topic was seen, in part because of the mentioned success of hybrid RANS/LES methods. Evolving from the original implementation using the Spalart-Allmaras model in the RANS region, recent studies have achieved successes in performing DES in combination with differential stress models that can be integrated towards the wall^{34, 35}.

Noteworthy in this aspect are the elliptic relaxation and elliptic blending models of Durbin³⁶ and Manceau and Hanjalic³⁷, respectively, in which an elliptic function is used to blend between the

Numerical and experimental evaluation of heat transfer in helically corrugated tubes

near-wall form of the stress redistribution tensor and the free-stream form. The Jakirlić/Hanjalić JH-v2 model applied in the present work achieves something similar by calibrating the model coefficients to be expressed in terms of turbulence anisotropy invariants, such that the wall limits for the dissipation components are exactly satisfied³⁸. The model was implemented into the open-source CFD code OpenFOAM according to its original description but using the specific homogeneous dissipation rate ω^h instead of the homogeneous dissipation rate ϵ^h , as described by Jakirlić and Maduta³⁹. The full JH-v2 model equations and the necessary implementation steps to improve robustness, are listed in more detail in Morsbach et al.⁴⁰. Validation of the model was performed by simulation of flow through a pipe and through a square duct, and comparing the results with high-fidelity DNS data. The details of these simulations can be found in Appendix C.

3.3.3 Turbulent scalar flux modeling

While many successful alternatives to classical eddy-viscosity turbulence models have been developed, remarkably little attention is being given to the correct modeling of the turbulent heat fluxes. Several computations using sophisticated DRSMs still rely on a simple gradient-diffusion model for the heat fluxes, even though its deficiencies in more complex or buoyant flows are well-known^{41, 42}. Industry-leading CFD packages such as ANSYS Fluent do not even include anything other than a simple gradient-diffusion model with the turbulent Prandtl number being the sole parameter.

It is one of the goals of the present study to demonstrate how the additional level of physics incorporated in the flow by using a Reynolds stress model, can be used in deriving a more appropriate model for the turbulent scalar fluxes. Table 3-1 lists some of the scalar flux models that were evaluated for this purpose. As part of the omega formulation used in the present work, the turbulent time-scale τ_d was taken as $(C_\mu \omega)^{-1}$, with $C_\mu = 0.09$.

Table 3-1: Turbulent scalar flux models evaluated in the present work.

Simple gradient-		$-\widetilde{u_i \theta} = C_1 k \tau_d \frac{\partial \tilde{\theta}}{\partial x_i} \quad (3.8)$
---------------------	--	---

diffusion		
Generalized gradient- diffusion	Daly & Harlow (1970) ⁴³	$-\widetilde{u}_i \theta = C_2 \tau_d \widetilde{u}_i \widetilde{u}_j \frac{\partial \tilde{\theta}}{\partial x_j} \quad (3.9)$
Quadratic generalized gradient	Abe et al. (2001) ⁴⁴	$-\widetilde{u}_i \theta = C_3 \tau_d \frac{\widetilde{u}_i \widetilde{u}_k \widetilde{u}_k \widetilde{u}_j}{k} \frac{\partial \tilde{\theta}}{\partial x_j} \quad (3.10)$
Stress- production- related	Younis et al. (2005) ⁴²	$-\widetilde{u}_i \theta = C_4 \tau_d^2 \left(\widetilde{u}_i \widetilde{u}_k \frac{\partial \tilde{u}_j}{\partial x_k} + \widetilde{u}_j \widetilde{u}_k \frac{\partial \tilde{u}_i}{\partial x_k} \right) \frac{\partial \tilde{\theta}}{\partial x_j} = -C_4 \tau_d^2 P_{ij} \frac{\partial \tilde{\theta}}{\partial x_j} \quad (3.11)$

3.3.4 Boundary conditions

No-slip boundary conditions were applied on the tube surface. For the temperature equation, a fixed wall-normal temperature gradient was set, corresponding to the isoflux conditions that are achieved experimentally using the Inconel heating. In terms of turbulence modeling, low-Re models for the near-wall values were used, i.e. fixed zero fluctuations at the tube surface and turbulence dissipation rate according to the recommendations of Wilcox⁴⁵.

In the simulations of the experimental setup, transient velocity inflow conditions were imposed, taken from a separate simulation of fully developed pipe flow. A fixed mean pressure condition was imposed on the outlet, which was positioned at a sufficient distance from the test section to avoid any upstream disturbances.

The fully developed flow simulations were performed using periodic boundary conditions in the streamwise direction. By applying an isoflux condition on the tube surface, both temperature and pressure can be made periodic by isolating the linear streamwise gradient, as demonstrated by Patankar et al.⁴⁶:

$$p(x, y, z) = -\beta x + \hat{p}(x, y, z) \quad (3.12)$$

$$\theta(x, y, z) = -\gamma x + \hat{\theta}(x, y, z) \quad (3.13)$$

In these equations, $\gamma = 4 \theta_t u_\tau / u_b$ is the streamwise temperature gradient corresponding to the imposed heat flux and β is the linear component of non-dimensional pressure which is adjusted dynamically to keep the mass flow rate to a predefined value.

3.3.5 Discretization

OpenFOAM[®] is based on the finite-volume method using collocated grids and Gaussian integration. A fully structured O-H butterfly grid topology was used, allowing excellent control of the near-wall grid spacing. Grid refinement was well within the recommendations by Kravchenko and Moin⁴⁷, as non-dimensional grid spacings of 8.4, 7.5, 0.2-8 were used in the tangential, axial and radial direction, respectively. Identical grids were used for all simulation approaches in order to eliminate additional sources of discrepancies.

All convective terms were discretized using a 2nd order central differencing spatial scheme, with minor high-frequency filtering for the LES. Time integration was performed using a second order backward differencing scheme (BDF2), while the CFL condition was kept below 0.5. Transient simulation data was sampled and time-averaged over a minimum of 10 flow-through times.

3.4 Results and discussion

As discussed in the previous section, two sets of simulations were performed. In the first phase, the full experimental setup was simulated in order to demonstrate the accuracy of the applied numerical setup. The simulation domain is shown in Figure 3-3 along with the key geometry parameters.

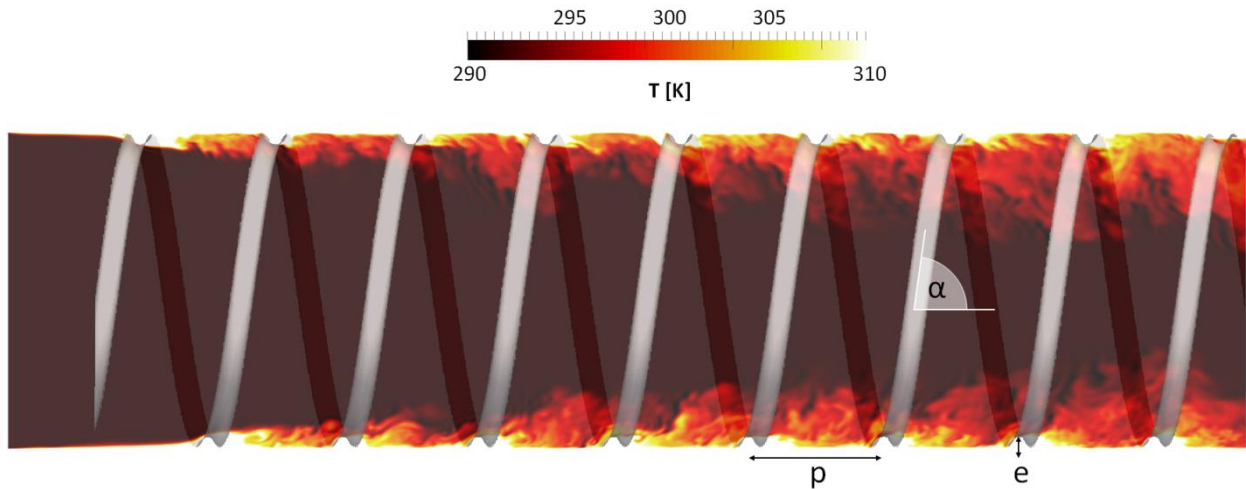


Figure 3-3: Illustration of the setup test section and the geometry parameters, along with a simulated contour plot of instantaneous temperature. $\{p/D, e/D, \alpha\} = \{0.42, 0.036, 82^\circ\}$

In industrial applications, these rib-roughened tubes typically operate under fully developed flow conditions. For this reason a second set of simulations was performed on an “infinite domain” through the use of periodic boundary conditions. Due to the reduced computational cost, the development of improved RANS modeling strategies was also performed using this approach.

3.4.1 Simulation of the experimental setup

When performing any kind of large eddy simulations, setting appropriate inlet conditions is crucial for obtaining accurate predictions. In the current set of simulations, inlet profiles are taken from a separate simulation of fully developed pipe flow at $Re = 24,000$, in order to avoid simulation of the entire experimental inlet section. Time-averaged profiles of streamwise velocity and velocity fluctuations are shown in Figure 3-4. General agreement is seen to be quite satisfactory, though turbulence levels in the core of the flow are higher than the experimental values reported by Mayo et al.²⁵. The flat velocity profile measured at the tube center indicates that this may have to do with an insufficiently long entrance section. Nevertheless, agreement in the near-wall region is excellent and interaction with the ribbed surface should be accurately captured using these inlet conditions.

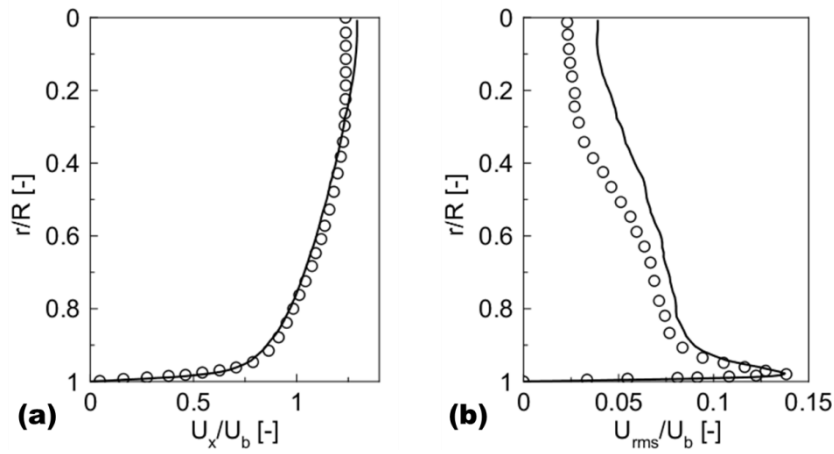


Figure 3-4: Profiles of mean (a) streamwise velocity and (b) velocity fluctuations at the inlet of the test section.

○ PIV – Mayo et al.²⁵; — LES

3.4.1.1 Velocity profiles

Figure 3-5 shows the simulated streamlines in the 7th rib section, revealing all the typical flow features that are expected for flow over ribbed surfaces. A major recirculation bubble is seen downstream of the rib, extending to approximately 4.49 times the rib height e , at which point the flow reattaches to the tube surface and the boundary layer is reestablished. Upstream of the subsequent rib, a second recirculation bubble of length $0.86e$ is discerned. These separation lengths correspond well with the reported experimental ones of 4.3 and 0.9 times the rib height²⁵. Additionally, the simulations show a third region of separated flow, just upstream of the larger recirculation bubble. Because of its small size and proximity to the non-transparent rib however, it was not discernible in the experiments.

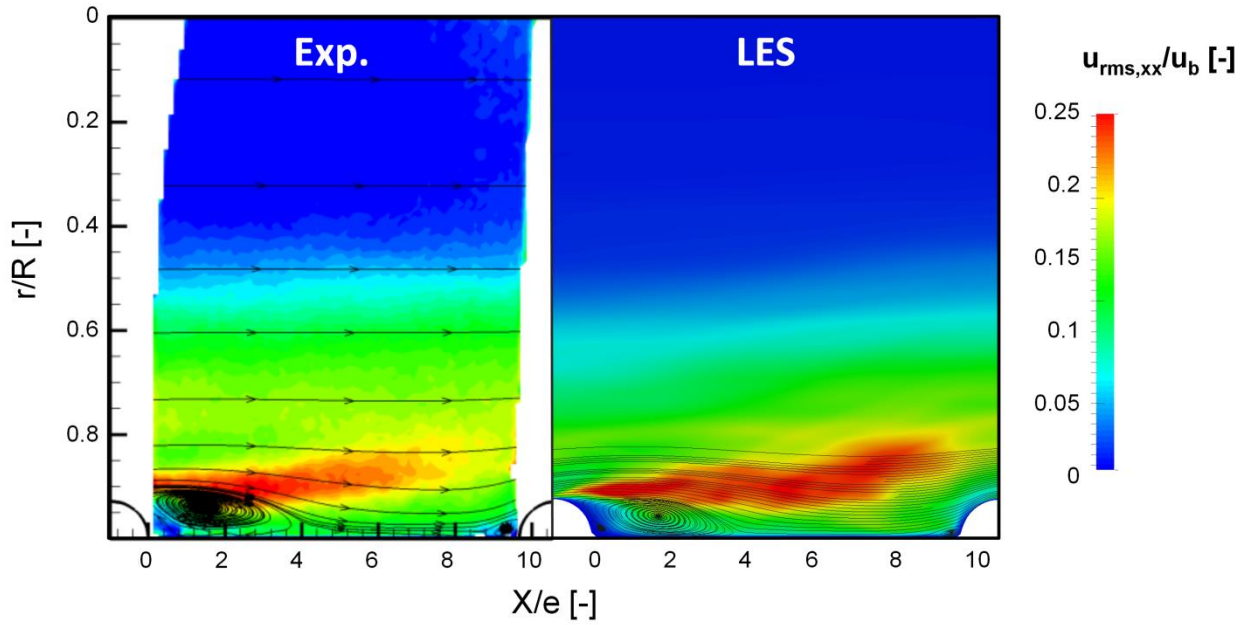


Figure 3-5: Streamlines over the ribbed tube surface, along with contour plot of streamwise velocity fluctuations²⁵.

From the contours of streamwise turbulent velocity, it is clear that turbulence is generated by interaction with the rib and in the shear layers surrounding the separation bubble. Most of the turbulence is constrained to this region near the wall, as the intensity gradually decreases between $0.4 < r/R < 0.8$ while the core of the flow remains virtually unaffected.

Similar as described by Mayo et al.²⁵, the ridge of peak turbulent intensity is seen to not be parallel with respect to the tube axis, but rather makes an angle of approximately $5-6^\circ$. This appears to be an entrance effect rather than a true feature of the geometry however, as the same angle is retrieved from the spreading of the turbulent structures in Figure 3-3.

Simulated streamwise velocity profiles at various positions between the ribs are shown in Figure 3-6(a), along with the corresponding PIV measurements. The x-axis represents the streamwise velocities, shifted in position according to the distance in rib heights from the trailing edge of the obstacle. The region of separated flow in the wake of the rib is seen to be well predicted, as well as the subsequent reattachment of the boundary layer.

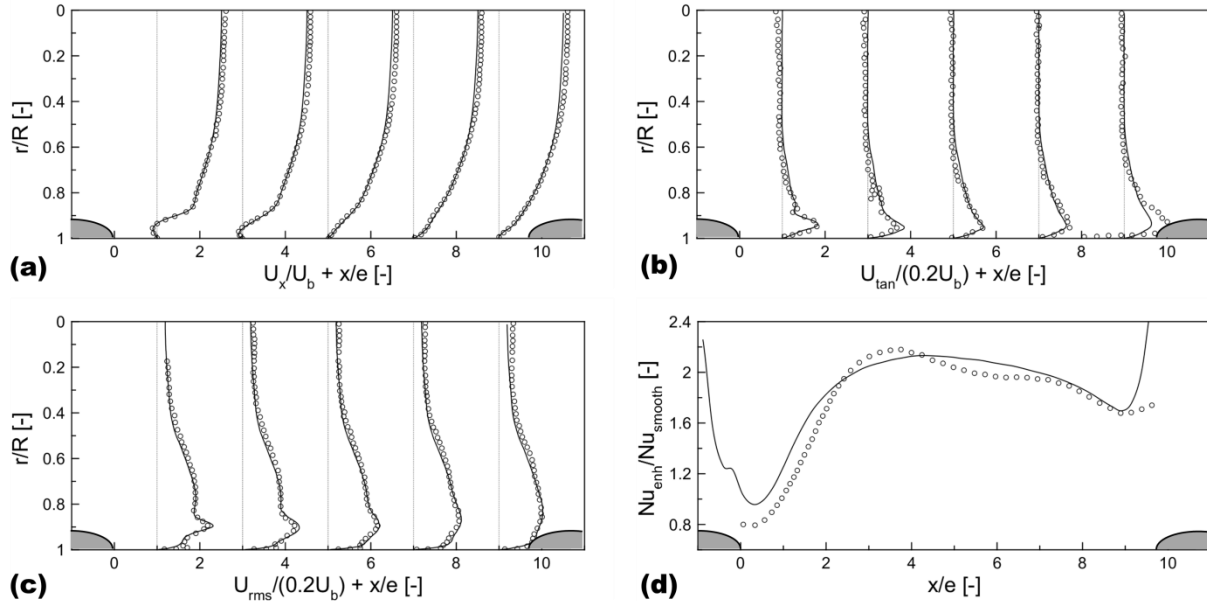


Figure 3-6: Profiles of mean (a) streamwise velocity, (b) tangential velocity, (c) streamwise velocity fluctuations, (d) and thermal enhancement factor on the tube surface, obtained between the 7th and 8th rib of the test section. ○ PIV – Mayo et al.²⁵; — LES

Figure 3-6(b) shows high tangential velocities being generated by the helicoidal rib, that extend up to approximately $r/R \sim 0.7$. In general the swirling flow motion remains mostly limited to the inter-rib region, while the core flow remains aligned with the tube axis. A small secondary tangential velocity peak carried over from the previous rib section can be seen at $x/e = 1$. A deviation from the experimental results appears at $x/e = 9$, in front of the rib leading edge. In this region the flow is locally accelerated due to the blockage imposed by the obstacle, resulting in high tangential and radial velocities. Directly in front of the rib, the experiments even show counter-clockwise tangential velocities, opposite to the direction induced by the helicoidal rib. Though the simulation captures the separation bubble accurately, these reversed tangential velocities are not apparent from the simulations. It must be noted however that the S-PIV values in this region are at the very edge of the optical interrogation window where measurement errors are greater, especially for the out-of-plane velocity component.

Excellent predictions of the turbulent velocities can be seen from Figure 3-6(c). Peak turbulent intensities occur at the inflection point of the streamwise velocity profile, around $r/R = 0.9$. As

Numerical and experimental evaluation of heat transfer in helically corrugated tubes

the flow reattaches to the wall, the peak broadens and the turbulent kinetic energy is gradually lost.

A quantitative comparison between the experimental and simulated datasets was performed by integrating the overall difference between the two over the radius, calculated for a variable ϕ as:

$$\Delta\phi = \frac{\sqrt{\int_0^1 (\phi_{LES} - \phi_{exp})^2 d\left(\frac{r}{R}\right)}}{\int_0^1 \phi_{exp} d\left(\frac{r}{R}\right)} \quad (3.14)$$

Table 3-2 shows the resulting values at the different positions downstream of the rib. General agreement is again seen to be good, with most errors below 8%. The largest deviations are consistently seen at position $x/e = 9$, where uncertainty on both the experimental measurements and the sampling of the numerical data is greatest, due to it being just a few millimeters upstream of the next obstacle. The primary source of tangential velocity differences is at the core of the flow, where the experimental measurement does not exactly tend to zero at the tube axis. This systematic deviation and the fact that the reported differences are relative, explain this seemingly worse agreement.

Table 3-2: Overall differences between the experimental and large eddy simulation velocity profiles.

x/e	U_x/U_b	U_{tan}/U_b	U_{rms}/U_b
1	5.6%	9.2%	5.4%
3	6.4%	12.1%	5.4%
5	7.4%	7.8%	4.9%
7	6.5%	7.2%	5.8%
9	7.5%	13.4%	7.4%

Numerical and experimental evaluation of heat transfer in helically corrugated tubes

3.4.1.2 Heat transfer characteristics

The heat transfer performance was investigated in terms of a thermal enhancement factor EF, which represents the relative local Nusselt number of the enhanced tube, with that of a smooth tube. While the latter Nusselt number is taken from the Gnielinski equation¹⁹, Eqn. (3.2), the simulated one is calculated based on the local wall temperatures, leading to the following overall equation:

$$EF = \frac{Nu_{enh}}{Nu_{smooth}} = \frac{Re_t Pr}{\theta_w - \theta_b} \frac{1}{Nu_{smooth}} \quad (3.15)$$

Figure 3-6(d) shows both the experimental values and numerical predictions between the 7th and 8th rib of the test section. Peak heat transfer performance is seen at a distance of approximately 3.7 times the rib height behind the obstacle, which is slightly upstream of the reattachment point. This can easily be understood from the flow field as the separated flow bubble causes cold fluid from the core of the flow to recirculate along the hot tube surface, increasing the local driving force for heat transfer. The area of improved performance also extends further downstream of the obstacle because of the high level of turbulent mixing that is induced. As the turbulent kinetic energy dissipates and the stable boundary layer develops again, a decrease of the thermal performance is seen. Nevertheless, virtually the entire tube surface exhibits an enhancement factor greater than unity, with the only exception of the section just downstream of the rib trailing edge. Though small, this local hot spot could have implications for industrial scale reactors⁴⁸, as deposition of cokes and fouling in general will be greater in this region of low shear and long residence times.

Excellent agreement exists between the experimentally measured values and the simulated trends, as both the drastic improvement near the reattachment point and the slow descent towards the next obstacle are well captured. The peak enhancement factor relative to a bare tube is well predicted at 2.13, compared to the experimentally measured 2.18, though the position of the peak is slightly further downstream in the simulations, corresponding to the difference in reattachment point previously seen for the flow field. Integration of the profile deviations over the pitch length

(cf. Eqn. (3.14)) yields an overall difference of 6.8%. The primary source of this error is the region just downstream of the obstacle, for which Mayo et al.²⁵ note that this is where the lateral to radial conduction ratio leads to maximal uncertainty.

3.4.2 Fully developed flow characteristics

Having successfully validated the numerical approach, it becomes interesting to look at fully developed flow characteristics of these enhanced tubular geometries. Indeed, while accounting for entrance effects in experimental datasets is crucial, most industrial applications of these devices are situated in the field of heat exchangers and tubular reactors where aspect ratios are generally much higher and the assumption of fully developed flow is valid. Additionally, as the velocity profiles stay periodic, the numerical evaluation of the flow becomes less computationally demanding since periodic boundary conditions can be used in the streamwise direction. This not only allows a reduction of the computational domain, but also alleviates the often challenging task of providing appropriate turbulent inlet and outlet boundary conditions.

3.4.2.1 Velocity profiles

The profiles of streamwise and tangential velocity and streamwise velocity fluctuations for this set of simulations are shown in Figure 3-7(a)-(c). As was the case for the non-periodic profiles, the data is plotted on the x-axis and shifted according to its position. From these results similar global flow patterns can be discerned as for the non-periodic case. The turbulence and swirl generated by the ribs in the fully developed flow case extends further away from the wall in comparison to what was previously seen in the experimental setup. This clearly indicates that while the flow enters the test section in a fully developed turbulent state, the measurements obtained after 6 pitch lengths were not sufficiently far downstream in order to see the full rib-induced flow patterns.

With regards to the streamwise velocity, both RANS models succeed reasonably well at predicting the near-wall flow, though the logarithmic law-of-the-wall is more clearly discerned in the LES results. Important differences between the simulation approaches can be seen in the profiles for tangential velocity, with both RANS models considerably underpredicting the peak

Numerical and experimental evaluation of heat transfer in helically corrugated tubes

swirl component. Interestingly, the SST $k-\omega$ formulation exhibits a linear decay of the swirl towards the center of the tube, whereas the JH-v2 model correctly captures the quadratic decay rate that is seen for the eddy-resolving simulation. As was reported in the validation stage of the JH-v2 model, under Supplementary Information, near-wall turbulence levels are slightly underpredicted compared to the LES data. While the JH-v2 model manages to capture the strong fluctuations in the shear layer of the separation bubble much better than the SST $k-\omega$ model, the prediction of the subsequent spreading and dissipation is clearly lacking.

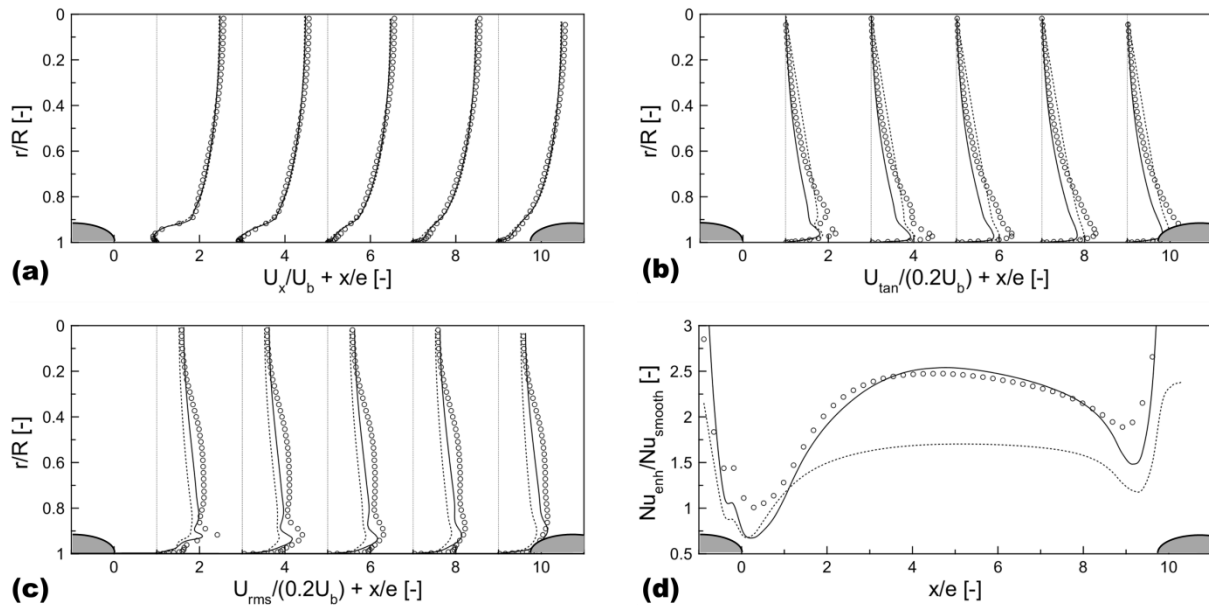


Figure 3-7: Fully-developed profiles of mean (a) streamwise velocity, (b) tangential velocity, (c) streamwise velocity fluctuations, (d) and thermal enhancement factor on the tube surface. \circ LES; — JH-v2; - - - SST $k-\omega$

3.4.2.2 Heat transfer characteristics

As discussed in Section 3.3, one of the advantages of applying a second moment closure to the Navier-Stokes equation is that these differential Reynolds stresses can also be used to close terms in other transport equations. While most RANS simulations make use of a simple gradient-diffusion model for the Reynolds heat fluxes, it is entirely possible to solve transport equations for these terms or model them algebraically. In the present work, the suitability of Eqns. (3.8)-

Numerical and experimental evaluation of heat transfer in helically corrugated tubes

(3.11) was investigated by a-posteriori calculation of the appropriate coefficients from the differential scalar fluxes obtained in the LES. This was performed for pipe flow in the absence of mean streamline curvature, i.e. a bare tube, and for the corrugated pipe under investigation.

Model discrimination was performed based on both the magnitude and direction of the heat flux vector. In Figure 3-8 the angle between this direction and the flow axis is plotted for the different tested models. While the GGD hypothesis is seen to offer a better prediction than a simple gradient-directed flux, it still underestimates the streamwise component, as was seen by both Younis et al. and Abe et al.^{42, 44}. In both geometries, only the more advanced models of the aforementioned authors align well with the actual flux direction. Further model discrimination was done based on the correlation between the simulated and modeled radial components of the heat flux. This proved rather inconclusive, as correlation coefficients for all the models listed in Table 3-1 were between 0.7 and 0.75. Finally, the quadratic generalized gradient model of Abe et al.⁴⁴, Eqn. (3.10), was selected over that of Eqn. (3.11), because of stability considerations. The model coefficient in this equation was determined by minimizing the sum-of-squares between the datasets. This yielded a value of 0.495, in relatively good agreement with the value of 0.6 reported in the original paper.

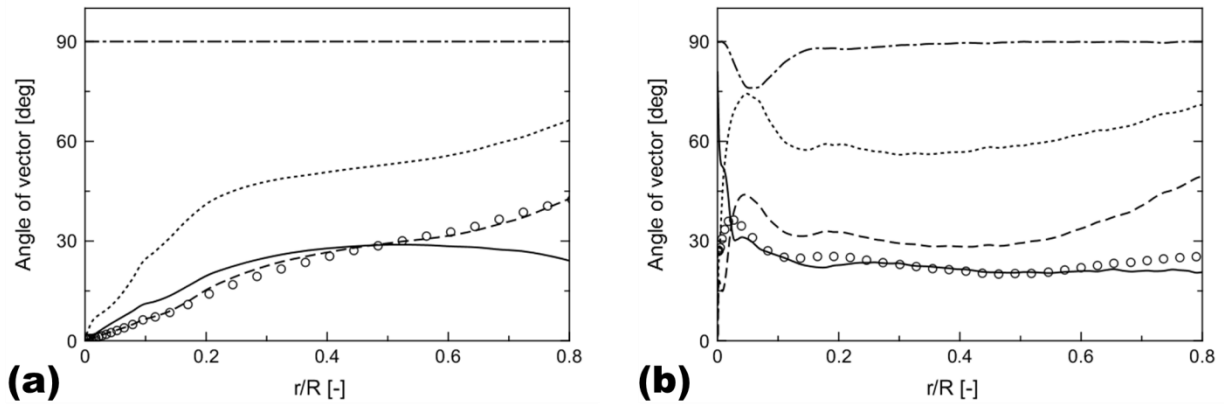


Figure 3-8: Angle between the scalar flux vector and the tube axis (a) in a bare tube and (b) in the studied corrugated tube, at $x/e = 5$. \circ LES, $---$ Simple gradient-diffusion – Eqn. (3.8), \cdots GGD – Eqn. (3.9), $- \cdot -$ Quadratic form – Eqn. (3.10), $—$ Stress-production form – Eqn. (3.11)

Numerical and experimental evaluation of heat transfer in helically corrugated tubes

Figure 3-7(d) shows the thermal enhancement factor obtained for this algebraic Reynolds flux model in combination with the JH-v2 model for the Reynolds stresses. A marked improvement over the predictions obtained using the two-equation model can be seen. Despite the excellent performance of the SST $k-\omega$ formulation in standard pipe flow, the heat transfer improvement of the ribbed tube is dramatically underpredicted by over a factor two. Good overall agreement of the RSM and LES data is seen, with slight deviations in the immediate vicinity of the ribs.

3.4.2.3 Reynolds number dependency

A summary of all performed simulations is given in Table 3-3 and Table 3-4. A good indication of the model performance can be found in the predictions of the two main recirculation bubbles. The pressure drag induced by these regions of separated flow is the dominant contribution to total pressure losses in corrugated tubes, and their length is hence a key parameter when comparing turbulence modeling approaches. They are strongly related with heat transfer as well, as the separated boundary layer acts as an additional resistance to heat transfer and will hence decrease thermal performance. On the other hand, the conversion of potential energy in the form of pressure, into turbulent kinetic energy, will contribute to the turbulent mixing. The overall net positive impact on heat transfer can be seen as a trade-off between these effects.

The second order closure JH-v2 clearly outperforms the standard SST $k-\omega$ model in terms of both flow and heat transfer predictions. While this improved accuracy comes at the cost of five additional transport equations and distinctly affected stability, the more universally applicable approach is valuable when exploring wider parameter and condition ranges. In order to demonstrate this, an additional set of simulations was performed at a Reynolds number of 40,000, compared to the original value of 24,000 at which also the experimental dataset was gathered. It is seen that the overall JH-v2 predictions are in line with the LES results. The predictions of the regions of separated flow are still satisfactory, although the trend of faster flow reattachment does not appear to be captured completely. While the SST $k-\omega$ results in terms of flow properties do not significantly deviate from those obtained at the lower Reynolds number, a much more significant heat transfer enhancement is predicted. Estimating a Reynolds number dependency based on the two datasets available yields a $Nu \sim Re^{1.08}$ dependency. Such an exponent clearly

Numerical and experimental evaluation of heat transfer in helically corrugated tubes

does not correspond with the values of 0.75 and 0.72 obtained in the respective LES and JH-v2 simulations, or with any available literature on the subject of heat transfer. It is clear that applying a higher-order closure to the momentum and energy equations, can significantly extend the confidence interval in the design space.

Table 3-3: Global characteristics for all simulations and experiments performed at $Re = 24,000$.

24k	Fully developed	X_1/e [-]	X_2/e [-]	$\Delta p/\Delta p_0$ [-]	Nu/Nu_0 [-]
LES	Yes	4.45	0.86	5.57	2.18
SST k- ω	Yes	6.95	1.36	4.18	1.53
JH-v2	Yes	4.52	0.79	4.99	2.19
Exp. – Mayo et al. ²⁵	No	4.30	0.90	6.25	1.83
LES	No	4.49	0.86	6.68	1.90

Table 3-4: Global characteristics for all simulations performed at $Re = 40,000$.

40k	Fully developed	X_1/e [-]	X_2/e [-]	$\Delta p/\Delta p_0$ [-]	Nu/Nu_0 [-]
LES	Yes	4.30	0.77	6.22	2.16
SST k- ω	Yes	6.71	1.16	4.64	1.79
JH-v2	Yes	4.53	0.87	5.64	2.13

3.5 Conclusions

A helicoidally corrugated tube design was investigated numerically in order to determine its potential as a reactor design for highly endo- or exothermic single-phase processes. Comparison was made with the recent experimental PIV and LCT data of Mayo et al.²⁵. Good agreement with this high-quality dataset is obtained when the largest turbulent flow scales are explicitly resolved, with overall differences on the local velocity profiles under 8%. Heat transfer was seen to improve by 83% compared to a standard bare tube, at the cost of a 6.25 times higher pressure drop. A strong relation between these performance parameters and the flow reattachment point in the wake of the rib was seen. Predictions for these global parameters also matched well with the experimental measurements, as relative errors for friction factors and Nusselt numbers were limited to within 7% and 4%, respectively.

Extrapolating the results to industrially relevant Reynolds numbers however, required a multi-scale approach in which the obtained insights from the eddy-resolving simulations are applied in a more affordable RANS turbulence model. This was achieved by combining a validated near-wall Reynolds stress transport model with a custom algebraic heat flux model. Despite the well-known difficulties in predicting recirculation zones using RANS models, the approach was able to reproduce the pressure losses and heat transfer enhancements from the LES data to within 10% and 2% error, respectively. Results at different Reynolds numbers indicate greatly improved reliability compared to classical two-equation models over a wider range of design and operating parameters.

References

1. Bergles, A.E., *Recent developments in enhanced heat transfer*. Heat and Mass Transfer, 2011. **47**(8): p. 1001-1008.
2. Liu, S. and M. Sakr, *A comprehensive review on passive heat transfer enhancements in pipe exchangers*. Renewable and Sustainable Energy Reviews, 2013. **19**: p. 64-81.
3. Ligrani, P., *Heat Transfer Augmentation Technologies for Internal Cooling of Turbine Components of Gas Turbine Engines*. International Journal of Rotating Machinery, 2013. **2013**: p. 32.
4. Ji, W.-T., A.M. Jacobi, Y.-L. He, and W.-Q. Tao, *Summary and evaluation on single-phase heat transfer enhancement techniques of liquid laminar and turbulent pipe flow*. International Journal of Heat and Mass Transfer, 2015. **88**: p. 735-754.
5. Ren, T., M. Patel, and K. Blok, *Olefins from conventional and heavy feedstocks: Energy use in steam cracking and alternative processes*. Energy, 2006. **31**(4): p. 425-451.
6. Muñoz Gandarillas, A.E., K.M. Van Geem, M.-F. Reyniers, and G.B. Marin, *Influence of the Reactor Material Composition on Coke Formation during Ethane Steam Cracking*. Industrial & Engineering Chemistry Research, 2014. **53**(15): p. 6358-6371.
7. Sarris, S.A., N. Olahova, K. Verbeken, M.-F. Reyniers, G.B. Marin, and K.M. Van Geem, *Optimization of the in Situ Pretreatment of High Temperature Ni–Cr Alloys for Ethane Steam Cracking*. Industrial & Engineering Chemistry Research, 2017. **56**(6): p. 1424-1438.
8. Torigoe, T., K. Hamada, M. Furuta, M. Sakashita, K. Otsubo, and M. Tomita, *Mixing Element Radiant Tube (MERT) Improves Cracking Furnace Performance*, in *11th Ethylene Producers' Conference*, 1999: Houston, TX.
9. Györfy, M., *MERT Technology Update: X-MERT*, in *AICHE: Ethylene Producers Meeting*, 2009: Tampa Bay.
10. Sethumadhavan, R. and M. Raja Rao, *Turbulent flow heat transfer and fluid friction in helical-wire-coil-inserted tubes*. International Journal of Heat and Mass Transfer, 1983. **26**(12): p. 1833-1845.
11. Zhang, Y.F., F.Y. Li, and Z.M. Liang, *Heat transfer in spiral-coil-inserted tubes and its applications*, in *Advances in heat transfer augmentation and mixed convection*, 1991, ASME HTD. p. 31-36.
12. Ravigururajan, T.S. and A.E. Bergles, *Development and verification of general correlations for pressure drop and heat transfer in single-phase turbulent flow in enhanced tubes*. Experimental Thermal and Fluid Science, 1996. **13**(1): p. 55-70.

Numerical and experimental evaluation of heat transfer in helically corrugated tubes

13. Webb, R.L., R. Narayanamurthy, and P. Thors, *Heat Transfer and Friction Characteristics of Internal Helical-Rib Roughness*. Journal of Heat Transfer, 1999. **122**(1): p. 134-142.
14. Vicente, P.G., A. García, and A. Viedma, *Experimental investigation on heat transfer and frictional characteristics of spirally corrugated tubes in turbulent flow at different Prandtl numbers*. International Journal of Heat and Mass Transfer, 2004. **47**(4): p. 671-681.
15. Saha, S.K., *Thermal and friction characteristics of turbulent flow through rectangular and square ducts with transverse ribs and wire-coil inserts*. Experimental Thermal and Fluid Science, 2010. **34**(5): p. 575-589.
16. Pethkool, S., S. Eiamsa-ard, S. Kwankaomeng, and P. Promvonge, *Turbulent heat transfer enhancement in a heat exchanger using helically corrugated tube*. International Communications in Heat and Mass Transfer, 2011. **38**(3): p. 340-347.
17. Slaiman, Q.J. and A.N. Znad, *Enhancement of Heat Transfer in The Tube-Side of A Double Pipe Heat Exchanger by Wire Coils*. Nahrain University College of Engineering Journal, 2013. **16**(1): p. 51-57.
18. Ali, R.K., M.A. Sharafeldein, N.S. Berbish, and M.A. Moawed, *Convective heat transfer enhancement inside tubes using inserted helical coils*. Thermal Engineering, 2016. **63**(1): p. 42-50.
19. Gnielinski, V., *New equations for heat and mass transfer in turbulent pipe and channel flow*. Int. Chem. Eng., 1976. **16**(2): p. 359-368.
20. Petukhov, B.S., *Heat Transfer and Friction in Turbulent Pipe Flow with Variable Physical Properties*, in *Advances in Heat Transfer*, T.F.I. J. P. Hartnett, Editor 1970, Academic Press: New York.
21. Menter, F.R., M. Kuntz, and R. Langtry, *Ten Years of Industrial Experience with the SST Turbulence Model*, in *Turbulence, Heat and Mass Transfer 4*, K. Hanjalic, Y.Nagano, and M.Tummers, Editors. 2003, Begell House, Inc. p. 625-632.
22. Van Cauwenberge, D.J., C.M. Schietekat, J. Floré, K.M. Van Geem, and G.B. Marin, *CFD-based design of 3D pyrolysis reactors: RANS vs. LES*. Chemical Engineering Journal, 2015. **282**: p. 66-76.
23. Çakan, M., *Aero-Thermal Investigation of Fixed Rib-Roughened Cooling Passages*, 2000, Université Catholique de Louvain: von Karman Institute for Fluid Dynamics.
24. Casarsa, L. and T. Arts, *Experimental Investigation of the Aerothermal Performance of a High Blockage Rib-Roughened Cooling Channel*. Journal of Turbomachinery, 2005. **127**(3): p. 580-588.
25. Mayo, I., B.C. Cernat, M. Virgilio, A. Pappa, and T. Arts, *Aerothermal Investigation on the Flow and Heat Transfer in a Helically Corrugated Cooling Channel*, in *ASME Turbo Expo 2016*, 2016: Seoul, South Korea. p. 1-11.

Numerical and experimental evaluation of heat transfer in helically corrugated tubes

26. Soloff, S., *Distortion compensation for generalized stereoscopic particle image velocimetry*. Measurement Science and Technology, 1997. **8**: p. 1441-1454.
27. Kim, W.-W. and S. Menon, *A new dynamic one-equation subgrid-scale model for large eddy simulations*, in *33rd Aerospace Sciences Meeting and Exhibit*, 1995, AIAA: Reno, NV. p. 1-9.
28. Menter, F.R., *Two-equation eddy-viscosity turbulence models for engineering applications*. AIAA Journal, 1994. **32**(8): p. 1598-1605.
29. Spalart, P., W. Jou, M. Strelets, and S. Allmaras. *Comments of feasibility of LES for wings, and on a hybrid {RANS/LES} approach*. in *International Conference on {DNS/LES}*, Aug. 4-8, 1997, Ruston, Louisiana. 1997.
30. Spalart, P.R., S. Deck, M.L. Shur, K.D. Squires, M.K. Strelets, and A. Travin, *A New Version of Detached-eddy Simulation, Resistant to Ambiguous Grid Densities*. Theoretical and Computational Fluid Dynamics, 2006. **20**(3): p. 181.
31. Shur, M.L., P.R. Spalart, M.K. Strelets, and A.K. Travin, *A hybrid RANS-LES approach with delayed-DES and wall-modelled LES capabilities*. International Journal of Heat and fluid flow, 2008. **29**(6): p. 1638-1649.
32. Spalart, P.R., *Detached-Eddy Simulation*. Annual Review of Fluid Mechanics, 2009. **41**(1): p. 181-202.
33. Speziale, C.G., *A review of Reynolds stress models for turbulent shear flows*, 1995, NASA: Hampton, VA.
34. Probst, A., R. Radespiel, and T. Knopp, *Detached-Eddy Simulation of Aerodynamic Flows Using a Reynolds-Stress Background Model and Algebraic RANS/LES Sensors*, in *20th AIAA Computational Fluid Dynamics Conference*, 2011, American Institute of Aeronautics and Astronautics.
35. Zhuchkov, R.N. and A.A. Utkina, *Combining the SSG/LRR- ω differential reynolds stress model with the detached eddy and laminar-turbulent transition models*. Fluid Dynamics, 2016. **51**(6): p. 733-744.
36. Durbin, P.A., *A Reynolds stress model for near-wall turbulence*. Journal of Fluid Mechanics Digital Archive, 1993. **249**(-1): p. 465-498.
37. Manceau, R. and K. Hanjalić, *Elliptic blending model: A new near-wall Reynolds-stress turbulence closure*. Physics of Fluids, 2002. **14**(2): p. 744-754.
38. Jakirlić, S. and K. Hanjalic, *A new approach to modelling near-wall turbulence energy and stress dissipation*. Journal of Fluid Mechanics Digital Archive, 2002. **4**: p. 139-166.
39. Jakirlić, S. and R. Maduta, *Extending the bounds of 'steady' RANS closures: Toward an instability-sensitive Reynolds stress model*. International Journal of Heat and fluid flow, 2015. **51**: p. 175-194.

Numerical and experimental evaluation of heat transfer in helically corrugated tubes

40. Morsbach, C., M. Franke, and F. di Mare, *Application of a Low Reynolds Differential Reynolds Stress Model to a Compressor Cascade Tip-Leakage Flow*, in *Differential Reynolds Stress Modeling for Separating Flows in Industrial Aerodynamics*, B. Eisfeld, Editor 2015, Springer International Publishing: Cham. p. 1-17.
41. Kenjereš, S., S.B. Gunarjio, and K. Hanjalić, *Contribution to elliptic relaxation modelling of turbulent natural and mixed convection*. International Journal of Heat and fluid flow, 2005. **26**(4): p. 569-586.
42. Younis, B.A., C.G. Speziale, and T.T. Clark, *A rational model for the turbulent scalar fluxes*. Proceedings of the Royal Society A: Mathematical, Physical and Engineering Science, 2005. **461**(2054): p. 575.
43. Daly, B.J. and F.H. Harlow, *Transport Equations in Turbulence*. The Physics of Fluids, 1970. **13**(11): p. 2634-2649.
44. Abe, K. and K. Suga, *Towards the development of a Reynolds-averaged algebraic turbulent scalar-flux model*. International Journal of Heat and fluid flow, 2001. **22**(1): p. 19-29.
45. Wilcox, D.C., *Turbulence Modeling for CFD*. 3rd ed, ed. I. DCW Industries, La Canada CA. 2006.
46. Patankar, S.V., C.H. Liu, and E.M. Sparrow, *Fully Developed Flow and Heat Transfer in Ducts Having Streamwise-Periodic Variations of Cross-Sectional Area*. Journal of Heat Transfer, 1977. **99**(2): p. 180-186.
47. Kravchenko, A.G. and P. Moin, *On the Effect of Numerical Errors in Large Eddy Simulations of Turbulent Flows*. J. Comput. Phys., 1997. **131**(2): p. 310-322.
48. Vandewalle, L.A., D.J. Van Cauwenberge, J.N. Dedeyne, K.M. Van Geem, and G.B. Marin, *Dynamic simulation of fouling in steam cracking reactors using CFD*. Chemical Engineering Journal, 2017.

4

Periodic reactive flow simulation: proof of concept for steam cracking coils

“Complexity is the prodigy of the world. Simplicity is the sensation of the universe. Behind complexity, there is always simplicity to be revealed. Inside simplicity, there is always complexity to be discovered”

Gang Yu

This chapter has been published as :

Van Cauwenberge, D.J., Vandewalle, L.A., Reyniers, P.A., Floré, J., Van Geem, K.M., Marin, G.B. Periodic reactive flow simulation: Proof of concept for steam cracking coils. *AIChE J.* 2017; 63(5):1715-1726.

Abstract

Streamwise periodic boundary conditions (SPBCs) have been successful in reducing the computational cost of simulating high aspect ratio processes. Extending beyond the classic assumptions of constant property flows, a novel approach incorporating non-equilibrium kinetics was developed and implemented for the simulation of an industrial propane steam cracker. Comparison with non-periodic benchmarks provided validation as relative errors on the main product yields were consistently below 1% for different reactor configurations. A further order-of-magnitude reduction of the radial errors on product concentrations was obtained via an intuitive correction method based on the concept of local fluid age. The computational speedup achieved through application of SPBCs was a factor 16 to 250 compared to the non-periodic simulations. The presented methodology thus serves as a quick screening tool for the development of novel reactor designs and unlocks the potential for using more elaborate kinetic models or a more fundamental approach towards turbulence modeling.

4.1 Introduction

In many processes involving wall-bounded flows, the velocity distribution becomes virtually independent of the streamwise coordinate at a certain distance from the inlet. This region of fully developed flow is of particular interest in many engineering applications, as it allows the use of proven empirical correlations for global quantities such as Nusselt numbers, friction factors, etc¹⁻³. In recent years, there has been a surge of computational studies determining these characteristics for a wide range of flow regimes, geometrical configurations and levels of theory⁴⁻⁶. Directly embracing the concept of fully developed velocity profiles through application of streamwise periodic boundary conditions (SPBCs) allows a considerable simplification of the problem by avoiding the relatively difficult or costly task of solving the entrance region. Additionally, it permits the use of spectral methods which are particularly attractive for eddy-resolving techniques due to the lack of artificial dissipation. Direct Numerical Simulations (DNS) and Large Eddy Simulation (LES) methods relying on this approach have already granted

Periodic reactive flow simulation: proof of concept for steam cracking coils

unprecedented insights in the underlying mechanisms of turbulence generation and mixing processes in both canonical and more complex configurations⁷⁻⁹.

Many problems of physical interest however do not admit fully developed solutions. A variety of techniques have been developed that allow the application of SPBCs to problems in which the variables of interest are essentially non-periodic in nature such as transitional and turbulent boundary layer growth, heat transfer and chemical reaction. Patankar et al.¹⁰ studied a generalized fully developed regime by reformulating the state variables to obtain a set of cyclic equations, leading to volumetric source terms in the momentum and passive scalar transport equations. Spalart¹¹ introduced the fringe region technique, dividing the computational volume in a region of interest and a fringe region. In this absorbing layer, a volume forcing function is applied to modify the flow before it is recycled back as inflow. The method has shown to be very efficient and accurate in describing instability growths in developing boundary layers and even in other fields of computational physics¹². A more simple method was suggested by Lund et al.¹³ for flows with a self-similar evolution, where each flow field component is decomposed into a mean and a fluctuating part, and the appropriate scaling law is applied to each part separately. An alternative approach was followed by Beale¹⁴ through the application of staggered grids and slip terms on the periodic boundaries to invert the processes inside the domain of interest. The difficulty with both techniques lies in the correct choice of the respective scaling laws and slip terms to preserve a physical solution. Extension of the technique by Lund et al. to variable density flows is even more difficult since rescaling laws for thermodynamic variables must be provided as well. Examples of this approach were presented by Urbin and Knight¹⁵ and Stolz and Adams¹⁶.

Literature on the use of SPBCs in reacting wall-bounded flows is almost non-existing. Noteworthy is the work of Cabrit and Nicoud¹⁷ and Martin and Candler¹⁸, where the influence of equilibrium chemistry on turbulent boundary layers is investigated in low- and high Mach number flows, respectively. However, to the authors' knowledge, except for the recent work by Zhu¹⁹, no literature is available on the use of SPBCs in the simulation of non-equilibrium chemical processes. The work of Zhu¹⁹ and coworkers shows some similarities with the present

Periodic reactive flow simulation: proof of concept for steam cracking coils

work, as periodic boundary conditions are applied in the comparison of a ribbed and non-ribbed reactor geometry. However, the work is not validated using experimental or simulation data and does not address the physical implications of assuming periodicity in the concentration field. Among others it is one of the aims of the present work to resolve these issues with the goal of developing and demonstrating a novel methodology for the general case of wall-bounded reacting flows, different from the methodology proposed by Zhu. Paramount in this novel approach is the assumption of fully developed velocity and temperature fields throughout the length of the physical domain. Although the technique relies on some degree of one-dimensionality in the flow, it is demonstrated that the method allows detailed investigations of the true flow characteristics for a variety of configurations. In this work first the accuracy of the proposed methodology is assessed by benchmarking the simulations for reference cases. The computational cost savings that can be obtained through reduction of the computational domain by means of SPBCs are determined. Finally the applicability of the method as screening tool for reactor design optimization or to account for a higher level of theory in terms of kinetics or turbulence modeling is demonstrated for the industrially relevant case of steam cracking.

4.2 Numerical simulation procedure

4.2.1 Periodic concept

Fully developed flow occurs in all wall-bounded flows when at a certain distance from the inlet the velocity distribution becomes independent of the streamwise coordinate. In the case of a constant cross section, this corresponds to a constant radial velocity profile, while for a geometry with a periodically repeating section, the velocity distribution within subsequent modules will be constant after a certain hydraulic entrance length. Bhatti and Shah²⁰ reported the entrance length for laminar pipe flow to be a strong function of the Reynolds number as $L_{h, \text{lam}} = 0.056 \text{ Re} D_h$, while for turbulent flow a weaker dependency was seen: $L_{h, \text{turb}} = 1.359 \text{ Re}^{1/4} D_h$. With x being the streamwise direction, this periodic velocity distribution can then be written as:

$$\mathbf{u}(x, y, z) = \mathbf{u}(x + nL, y, z) \quad (4.1)$$

Periodic reactive flow simulation: proof of concept for steam cracking coils

This expression is typically not valid for the temperature and pressure fields, as heat fluxes through the domain boundaries cause an increase or decrease of the fluid temperature, and friction leads to a loss of pressure in the streamwise direction x . After a certain thermal entrance length however, temperature becomes fully developed as well, as the shape of the temperature distribution remains constant, with a steadily increasing or decreasing mean. Following the generalized periodic approach of Patankar et al.¹⁰ and assuming constant fluid properties and heat flux, one can write:

$$p(x + nL, y, z) - p(x, y, z) = n \cdot [p(x + L, y, z) - p(x, y, z)] = n\beta L \quad (4.2)$$

$$T(x + nL, y, z) - T(x, y, z) = n \cdot [T(x + L, y, z) - T(x, y, z)] = n\gamma L \quad (4.3)$$

$$\beta = \frac{\int_{\partial V} \tau_w dA}{\frac{1}{4}\pi D^2 L} + \frac{\tau_{form}}{L} = 4 \frac{\tau_w}{D} + \frac{\tau_{form}}{L} \quad (4.4)$$

$$\gamma = \frac{\int_{\partial V} q_w dA}{\int_V \rho c_p u_x dV} \quad (4.5)$$

in which β is the negative mean pressure gradient due to both skin friction and form drag losses and γ corresponds to the streamwise temperature gradient due to the imposed heat flux q_w . Under these assumptions, the following linear substitution can be made:

$$p(x, y, z) = \hat{p}(x, y, z) + \beta x \quad (4.6)$$

$$T(x, y, z) = \hat{T}(x, y, z) + \gamma x \quad (4.7)$$

In other words, the pressure and temperature field are decomposed into a periodic component and a linear streamwise gradient. Substitution of these identities in the corresponding momentum and temperature conservation equation leads to volumetric source terms that act as driving forces to maintain a constant mass flow rate and radial heat transfer, see for example Van Cauwenberge et al.⁷. As the solution to these conservation equations is now periodic, the considered heat transfer problem can be fully described on a single periodic module. Equations (4.1) - (4.7) outline the standard procedure for heat transfer simulations in a streamwise periodic geometry, which is

Periodic reactive flow simulation: proof of concept for steam cracking coils

exact under the assumptions of temperature being a passive scalar and of uniform fluid properties.

The aim of the present work is to extend this concept to non-equilibrium reacting flows and to demonstrate both the benefits and limitations by quantifying the associated errors. It is important to note that although the methodology is inspired by the standard procedure, the objective is substantially different. In the existing generalized periodic approach, a linearization is performed in order to eliminate the streamwise gradient of e.g. pressure and temperature, and achieve a single steady state. In a flow reactor however, the fluid properties and reaction rates vary over the space domain, and there can only be a local steady state at a certain axial position. This steady state relies on upstream information and thus in theory only solving over the full length of the reactor is meaningful.

The information contained within a single periodic volume can hence capture nothing more than a snapshot of the fluid properties and composition at a certain position inside the reactor. The goal of the presented method is to continuously calculate these snapshots in order to reconstruct the flow in the entire reactor. The snapshots, each representing a certain position in the reactor, need to be obtained by advancing the periodic simulation in time because of the translation of the problem from the space to time domain. An additional challenge is that instead of maintaining constant boundary conditions, which is done in the standard procedure, at each time step the boundary conditions are updated to match the conditions at the corresponding position in the flow reactor, hence obtaining a truly unsteady simulation from the point of view of the periodic volume. The resulting simulation results then are available as function of time, even if the considered full reactor is steady-state in nature. The main advantages are that while the computational volume remains limited to a stationary periodic module, the concepts of locally fully developed velocity and temperature can be applied to describe the flow profiles as the volume traverses the length of the physical reactor, resulting in a substantially reduced computational cost .

In other words, the tracking of this volume through time essentially corresponds to the simulation of the reactor in a Lagrangian frame of reference. Through this transformation, the original

Periodic reactive flow simulation: proof of concept for steam cracking coils

profiles $\varphi(x,y,z)$ as function of the Eulerian axial coordinate x , are now expressed as $\varphi(x(x_{\text{local}},t),y,z)$, as function of the simulation time t and the local coordinate within the periodic volume x_{local} . The motion of this periodic volume through the flow reactor follows the axial direction, while the magnitude of its velocity is the bulk velocity, i.e. the axial velocity of its center of mass. The applied mapping function, as demonstrated in Figure 4-1, becomes:

$$x(x_{\text{local}}, t) = x_{\text{local}} + \int_{t_0}^t u_b dt = x_{\text{local}} + \int_{t_0}^t \frac{\int_V u_x \rho dV}{\int_V \rho dV} dt \quad (4.8)$$

The periodic simulation is then run for a duration corresponding to the mean residence time for the full reactor. The main advantage of describing the reactor in the Lagrangian frame of reference is that the convective term in the flow direction vanishes as it becomes part of the material derivative along the streamline of the periodic volume. Additionally, the high Peclet number in long tubular reactors allows axial diffusion to be neglected. Under these conditions, periodicity of the flow variables over the reduced volume can be imposed, with errors proportional to the length of the periodic volume.

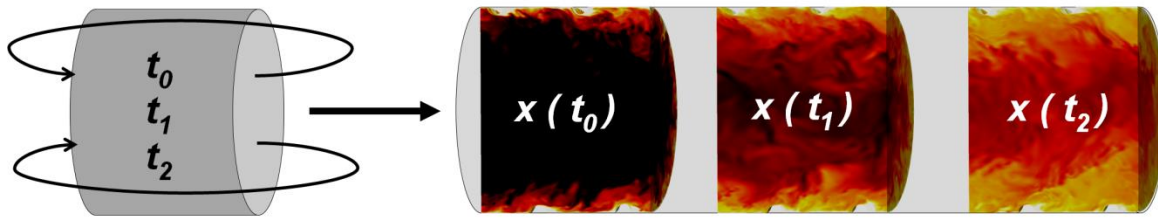


Figure 4-1: Visual interpretation of the link between the periodic simulations and the equivalent position in the physical reactor.

With aspect ratios L/D of tubular reactors ranging from 25 to up to 10,000²¹, the potential savings in terms of computational cost are significant, especially when more advanced turbulence models are used. When a time-averaged Reynolds-Averaged Navier-Stokes (RANS) approach is used, the reactor itself is steady and the gains obtained by reducing the computational domain are partly negated by the added time dependency. Nevertheless, a significant speedup remains as the

Periodic reactive flow simulation: proof of concept for steam cracking coils

velocity field inside the periodic module no longer relies on up- or downstream transfer of information. As will be demonstrated in the present work, this translates in large gains in computational cost, since the pressure correction is typically the most costly step in solving the Navier-Stokes equations. Though not part of the present work, it can be reasoned that the proposed methodology will be even more efficient when applying an eddy-resolving turbulence model, such as Large Eddy Simulation (LES). In this case, the statistically steady flow in the reactor will already exhibit time dependency in the turbulent profiles. Applying periodicity to such simulations can hence be expected to result in several orders of magnitude gains in performance. It is important to note, that performing such a simulation corresponds to the tracking of a single ensemble of eddies through the length of the reactor and hence will only result in a single transient realization of the flow reactor. While this does not allow the calculation of local mean flow statistics, these can potentially still be obtained if a homogeneous averaging direction exists within the periodic module, which is the case for most industrially applied flow reactors.

Although the described transformation is intuitive, the inclusion of chemical species leaves two additional issues to be addressed:

4.2.1.1 Fluid property profiles

First of all, the occurrence of temperature changes and compositional changes due to chemical reaction inside the fluid causes the fluid properties to be both non-uniform and non-constant. A critical issue arises from the flow experiencing both molecular and thermal expansion or contraction, leading to changes in density over the length of the reactor. This implies that the amount of mass contained in a single periodic section is not constant either. In a simulation framework with a traditional inlet and outlet boundary, this would be compensated by temporary flux imbalances between the two, which disappear as the final steady-state solution is approached. In the present transient methodology however, mass conservation at each time step is crucial, and hence, control is needed about mass potentially leaving or entering the system in order to reproduce the true physical situation at every streamwise location. Without addressing this issue, the pressure is artificially decreased or increased throughout the simulation to

Periodic reactive flow simulation: proof of concept for steam cracking coils

compensate for the difference between the density calculated with the equation of state and the one following from the continuity equation. In order to eliminate this non-physical effect, a mass source term S_ρ is introduced in the continuity equation to mimic the real situation. All other transport equations are modified accordingly to satisfy the respective conservation laws.

$$\frac{\partial \rho}{\partial t} + \frac{\partial \rho u_i}{\partial x_i} = S_\rho \quad (4.9)$$

$$\frac{\partial \rho \varphi}{\partial t} + \frac{\partial \rho \varphi u_i}{\partial x_i} = \frac{\partial \Gamma \varphi}{\partial x_i \partial x_i} + \varphi S_\rho \quad (4.10)$$

Through combination of Eq. (4.6) and Eq. (4.8), the term S_ρ can further be written as:

$$\begin{aligned} S_\rho &= \frac{d\rho}{dt} = \frac{d}{dt}(p\psi) \\ &= \psi \frac{dp}{dx} \frac{dx}{dt} + p \frac{d\psi}{dt} = \psi \beta u_b + \psi \frac{d\hat{p}}{dt} + p \frac{d\psi}{dt} \end{aligned} \quad (4.11)$$

In this manner the pressure losses due to friction over the length of the reactor are explicitly accounted for by including the instantaneous pressure gradient β .

4.2.1.2 Local fluid age distribution

The second critical issue that needs to be addressed is that the transformation of Eq. (4.8) is uniform throughout the periodic module. This essentially corresponds to a plug flow assumption, as it implies that all fluid elements within a cross-sectional slice of the physical reactor correspond to a single time instance in the periodic simulation. The true situation however is closer to what is shown in Figure 4-2 for an imaginary tracer pulse originating from a certain point in the reactor. Initially, convective transport causes the tracer front to undergo severe deformation due to the non-uniform axial velocity caused by the no-slip conditions imposed at the wall. Throughout the length of the reactor, the tracer also undergoes radial mixing, broadening the tracer distribution by Taylor dispersion effects, until finally a typical non-ideal plug flow distribution is seen at the reactor outlet. Although the global deviation from plug flow

Periodic reactive flow simulation: proof of concept for steam cracking coils

becomes smaller with increasing length of the reactor and increasing radial mixing, it is clear that the suggested uniform transformation yields flawed solutions when evaluating radial mixing processes at intermediate locations.

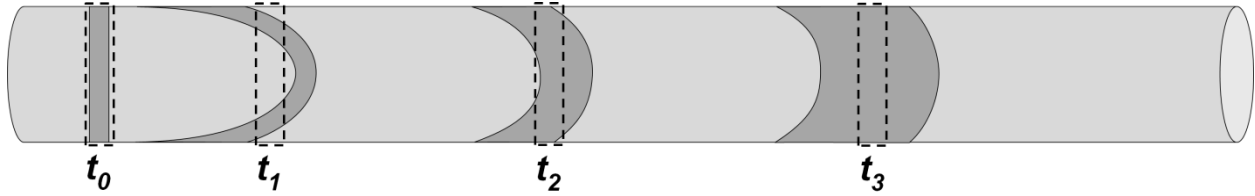


Figure 4-2: Illustration of the transport of a passive tracer (shaded) in a tubular reactor and deviation from the plug flow assumption (dotted)

In what follows, the physical reason behind this phenomenon is further examined and a method for eliminating the errors associated with the uniform transformation is investigated. Imagine for this purpose the situation within a single plug with axial dimensions L_{ref} . The time required to traverse this distance L_{ref} will be less for a fluid element in the core of the flow than for an element moving at the average bulk velocity. Likewise, a fluid element moving slowly along the tube surface, will statistically require a longer time to reach the exit of the plug and will have had more time to undergo reaction. Because of the uniform link between physical space and simulation time introduced by Eq. (4.8) however, all elements are assumed to have spent an equal time L_{ref}/u_b traversing this distance. This causes a non-uniform dilation of the convective time scales:

$$\phi = \frac{\tau_{conv}}{\tau_{conv,sim}} = \frac{\frac{L_{ref}}{u_{ref}}}{\frac{L_{ref}}{u_b}} = \frac{u_b}{u_{ref}} \approx \frac{u_b}{u_x} \quad (4.12)$$

with the last approximation in Eq. (4.12) valid only in the absence of diffusion and turbulent mixing. The time scales for reaction on the other hand remain unchanged as these are purely determined by the chemical kinetics. This leads to a discrepancy of the local first and third Damköhler numbers between the physical solution and the periodic simulation:

$$Da_I = \frac{\tau_{conv}}{\tau_{chem}} = \frac{L_{ref}}{u_{ref}} \frac{|R_k|}{\rho} = \phi \frac{\tau_{conv,sim}}{\tau_{chem}} = \phi Da_{I,sim} \quad (4.13)$$

$$Da_{III} = \frac{\tau_{conv\ heat}}{\tau_{heat\ gen}} = \frac{L_{ref}}{u_{ref} T} \frac{|S_h|}{\rho c_p} = \phi \frac{\tau_{conv,sim}}{\tau_{heat\ gen}} = \phi Da_{III,sim} \quad (4.14)$$

The Damköhler numbers in the simulation hence differ by a factor ϕ from the physical ones, with ϕ being a local variable relating the true convective time scales to those in the simulation.

In the present work, a correction for this “time skewness” is proposed by dividing the chemical time scales by ϕ , in order to preserve the real Damköhler numbers. As shown in Eq. (4.12), determining this variable involves explicit calculation of a local reference velocity, which can be obtained by relating the position in the reactor with the average time it took for the fluid element to travel to this position. This quantity is known as the local fluid age and is not straightforward to acquire, as it is determined by the historical accumulation of all flow and mixing effects experienced by the fluid element, including turbulent and laminar diffusion, separated flow patterns, density changes, etc. It is clear from Eq. (4.12) that neglecting these effects and only accounting for axial convection leads to infinite or even negative local fluid ages for elements located in regions with zero or negative local axial velocities. In reality however, even elements “trapped” in a region of separated flow will slowly diffuse out of it, ensuring finite positive values for the local fluid age at each point in a reactor.

Experimental measurement of fluid age distributions is traditionally performed by means of tracer experiments in which the transient response to an inlet tracer pulse or step input is monitored. In a simulation framework, this passive tracer can be treated as a generic chemical species that is transported along with the known flow field, and its time response can be rewritten as a transport equation for a generic “quantity of age” τ . This concept was first introduced by Sandberg²² and later extended by Ghirelli and Leckner²³ to transient variable-density flows. For a unity Schmidt number, a typical convection-diffusion equation is obtained, written in Einstein notation as:

Periodic reactive flow simulation: proof of concept for steam cracking coils

$$\frac{\partial \rho \tau}{\partial t} + \frac{\partial \rho \tau u_i}{\partial x_i} = \frac{\partial \mu_{eff} \tau}{\partial x_i \partial x_i} + \rho \quad (4.15)$$

with no-flux boundary conditions set on all solid domain boundaries. The dilation factor ϕ of the convective time scale is then retrieved by dividing this local fluid age with the theoretical age if all elements were moving at the bulk velocity without interaction with their surroundings. To avoid problems near the periodic inlet where a division by zero would occur, a streamwise periodic boundary condition with a 50% slip term is imposed on the inlet. In this manner a one-period history effect is introduced in the calculation of the local fluid age. Finally this yields the following expression for the factor ϕ :

$$\phi = \tau \frac{u_b}{x_{local} + L} \quad (4.16)$$

Figure 4-3 shows the fluid age distribution and the corresponding correction factor ϕ for a typical wall-bounded flow. Values are seen to be finite, positive and distributed around the volume-weighted average of unity, with higher values typically corresponding to regions with low velocity and lower values in the core of the flow. The attractiveness of the method lies in its intuitive approach, by using the true flow field and mixing characteristics readily available in the simulation. As such, it can invariably be applied to both laminar and eddy-resolved or modeled turbulent flows without requiring any modeling or fitting parameters.

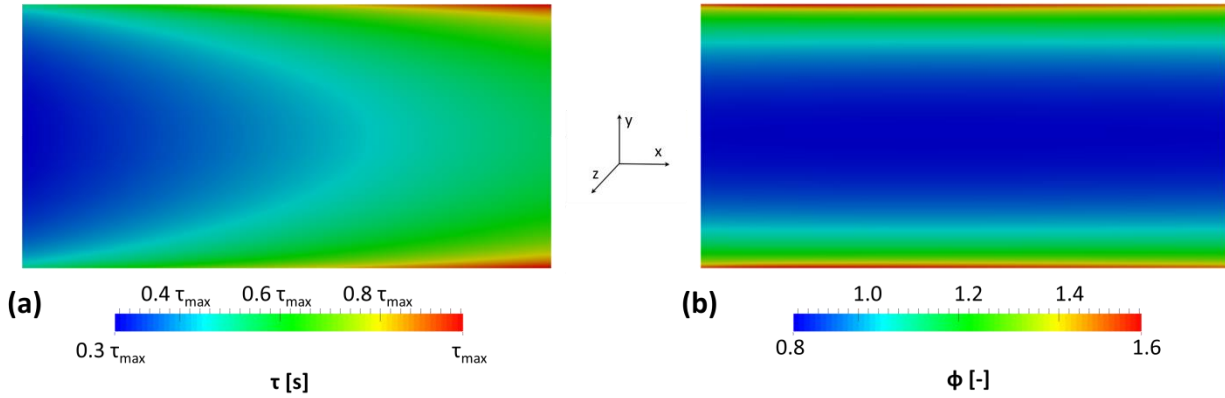


Figure 4-3: (a) Local fluid age distribution in a turbulent wall-bounded flow and (b) resulting correction factor ϕ .

4.2.2 Governing equations

The conservation equations for three-dimensional, compressible, turbulent reacting flows are well-known²⁴. Under low Mach number assumptions, the continuity, momentum transport, sensible enthalpy transport and species transport equations combined with the previously discussed correction terms can be written in Einstein notation as follows:

$$\frac{\partial \rho}{\partial t} + \frac{\partial \rho u_i}{\partial x_i} - S_\rho = 0 \quad (4.17)$$

$$\frac{\partial \rho u_i}{\partial t} + \frac{\partial \rho u_i u_j}{\partial x_j} - u_i S_\rho = -\frac{\partial \hat{p}}{\partial x_i} + \frac{\partial \tau_{ij}}{\partial x_j} - \beta \delta_{i1} \quad (4.18)$$

$$\frac{\partial \rho \hat{h}}{\partial t} + \frac{\partial \rho \hat{h} u_i}{\partial x_i} - \hat{h} S_\rho = \frac{\partial q_i}{\partial x_i} + (u_b - u_x) \overline{\rho c_p \gamma} + \phi S_h \quad (4.19)$$

$$\frac{\partial \rho \hat{Y}_k}{\partial t} + \frac{\partial \rho \hat{Y}_k u_i}{\partial x_i} - \hat{Y}_k S_\rho = -\frac{\partial J_{k,i}}{\partial x_i} + \phi R_k \quad (4.20)$$

with R_k and S_h the chemical species and enthalpy source terms due to reaction. τ_{ij} is the viscous shear stress tensor modeled using the Boussinesq approximation. q and J_k are the sensible enthalpy flux and the diffusion flux of species k , respectively, and are both modeled using an eddy diffusivity approach as:

Periodic reactive flow simulation: proof of concept for steam cracking coils

$$\tau_{ij} = (\mu + \mu_t) \left(\frac{\partial u_i}{\partial x_j} + \frac{\partial u_j}{\partial x_i} \right) - \frac{2}{3} k \delta_{ij} \quad (4.21)$$

$$q_i = c_p (\mu / Pr + \mu_t / Pr_t) \frac{\partial \hat{T}}{\partial x_i} \quad (4.22)$$

$$J_{k,i} = (\mu / Sc + \mu_t / Sc_t) \frac{\partial \hat{Y}_k}{\partial x_i} \quad (4.23)$$

where the turbulent Prandtl number Pr_t and turbulent Schmidt number Sc_t relate the modeled turbulent transport of momentum with that of energy and mass, respectively. A value of 0.85 was selected for these numbers, in accordance with the typical recommendations for gaseous flows²⁵⁻²⁷.

The derivation of the system of Eqs. (4.17) - (4.23) is performed under the assumption of negligible Soret diffusion, radiation heat transfer and buoyancy forces. It has previously been shown that these assumptions are valid in the present application domain of steam cracking²⁸.

The additional $(u_b - u_x) \overline{\rho c_p \gamma}$ term in the sensible enthalpy equation, Eq. (4.19), follows from a similar consideration as was previously made in Eq. (4.7) for the passive scalar T. The heat flux through the domain boundaries will now yield an axial gradient $\overline{\rho c_p \gamma}$, allowing the following linearization to arrive at the periodic variable \hat{h} :

$$h(x, y, z) = \hat{h}(x, y, z) + \overline{\rho c_p \gamma} x_{local} \quad (4.24)$$

Equation (4.19) is then obtained through substitution of Eqs. (4.8) and (4.24) in the sensible enthalpy conservation equation, leading to an additional term in both the accumulation and convection contributions:

$$\frac{\partial \rho h}{\partial t} = \frac{\partial \rho \hat{h}}{\partial t} + \overline{\rho c_p \gamma} \frac{\partial x_{local}}{\partial t} = \frac{\partial \rho \hat{h}}{\partial t} - \overline{\rho c_p \gamma} u_b \quad (4.25)$$

$$\frac{\partial \rho h u_i}{\partial x_i} = \frac{\partial \rho \hat{h} u_i}{\partial x_i} + \overline{\rho c_p \gamma} \frac{\partial x_{local} u_x}{\partial x} = \frac{\partial \rho \hat{h} u_i}{\partial x_i} + \overline{\rho c_p \gamma} u_x \quad (4.26)$$

It is important to note that a similar linearization of the species concentrations would not be possible, as the non-equilibrium assumption implies that no fully developed state for these concentrations is reached. Instead, the correction factor ϕ was introduced with the same goal of correcting for the transformation imposed by Eq. (4.8).

The turbulent eddy viscosity appearing in Eqs. (4.21) - (4.23) is calculated using the SST k- ω model of Menter²⁹, in combination with the near-wall damping functions of Wilcox³⁰. This two-equation model uses a pure k- ω formulation in the inner parts of the boundary layer which makes the model directly applicable all the way down to the wall, while in the free-stream it switches to a k- ϵ behavior, making it reliable for a wide class of flows.

4.2.3 Chemistry model

Steam cracking of hydrocarbons mainly proceeds through a free radical mechanism, which is characterized by a vast number of species and reactions^{31, 32}. In the present work, the computational cost was limited by reducing the full single-event microkinetic CRACKSIM model^{33, 34} to its relevant core for propane cracking. The final network consists of 203 reactions between 26 species, of which 13 radical species. The stiffness was diminished through on-the-fly application of the pseudo-steady state assumption to the short-lived radical reaction intermediates, transforming the ODEs for these species into algebraic equations. The adopted procedure is described in more detail in Reyniers et al.³⁵, where the validity of the approach was also confirmed.

Molecular viscosity and Prandtl numbers were quantified with the Chapman-Enskog formula, for which the L-J model parameters were estimated using RMG's TransportDataEstimator³⁶. Properties of the multicomponent mixture were calculated by ideal gas mixing laws. Given the dominance of turbulent over laminar diffusion in steam cracking, a unity Lewis number (Sc/Pr) was assumed in order to simplify the diffusion terms.

4.2.4 Computational grid & boundary conditions

The methodology is validated for a bare reactor tube and subsequently applied to two enhanced tubular geometries, namely a longitudinally finned reactor and a reactor with a rounded rib orthogonal to the flow. Because the bare and 90°-ribbed reactor tubes both exhibit axisymmetry, the cases were discretized on 2D wedge grids generated using the commercial meshing software Pointwise^{®37}. The 3D computational grid required for the longitudinally finned case was generated using the OpenFOAM octree-refinement cut-cell based snappyHexMesh utility. Near-wall grid resolution was fixed to 10^{-5} m for all cases, satisfying the $y^+ < 1$ condition and ensuring the first cell center is located within the viscous sublayer.

As described in the previous sections, the presented simulation approach makes use of streamwise periodic boundary conditions for all variables:

$$\varphi(x + nL, y, z, t) = \varphi(x, y, z, t) \quad (4.27)$$

Fully developed non-reactive velocity and temperature profiles are used as inlet conditions in the non-periodic simulation, corresponding to the initial conditions for the periodic simulations.

The reactor surface is treated as a no-slip, no species flux solid wall. Thermal energy for the endothermic reactions inside the reactor is supplied by means of a heat flux profile imposed on this solid wall. This heat flux profile is identical to that used by Reyniers et al.³⁵ and was taken from a furnace simulation where the boundary condition applied to the reactor tubes was the industrially measured outer wall temperature profile. In order to avoid potential differences originating from the coupling procedure, the heat flux profile was fixed for all simulations considered in the present work and no direct coupling with the furnace was performed. This profile was scaled inversely to the internal surface area of each geometry, in order to ensure the same total amount of heat to be transferred to the process gas. For the full non-periodic simulations, the heat flux profile was applied as a fixed flux boundary function, dependent on the axial position in the reactor. In the periodic approach, the corresponding physical position in the reactor was calculated with Eq.(4.8), from which the instantaneous value of the time-varying flux

Periodic reactive flow simulation: proof of concept for steam cracking coils

boundary condition was determined. An overview of all applied boundary conditions is given in Table 4-1.

Table 4-1: Overview of the applied boundary conditions.

	Periodic Inlet/Outlet	Wall
Pressure – p	cyclic	no-flux
Velocity – U	cyclic	no-slip
Sensible enthalpy – h	cyclic	time-varying iso-flux
Species mass fraction – Y	cyclic	no-flux
Fluid age – τ	cyclic slip (0.5)	no-flux
Turbulent kinetic energy – k	cyclic	fixed – 0
Specific dissipation rate – ω	cyclic	fixed – Menter ²⁹

4.2.5 Solution procedure

The open-source CFD package OpenFOAM^{®38} is based on the finite-volume method using collocated grids and Gaussian integration. The Pressure Implicit with Splitting of Operators (PISO) algorithm was employed with two corrector steps and one additional non-orthogonal correction step where necessary. The uniform momentum source β is updated at the start of each iteration in order to maintain a fixed mass flux through the periodic boundaries. Monitoring of these fluxes during the simulation shows that despite fluctuating values of β , the response is sufficiently fast and relative deviations on the specified mass flow rate are maintained below 10^{-7} . The overall structure of the top-level solver implemented in OpenFOAM[®] is shown in Figure 4-4.

Periodic reactive flow simulation: proof of concept for steam cracking coils

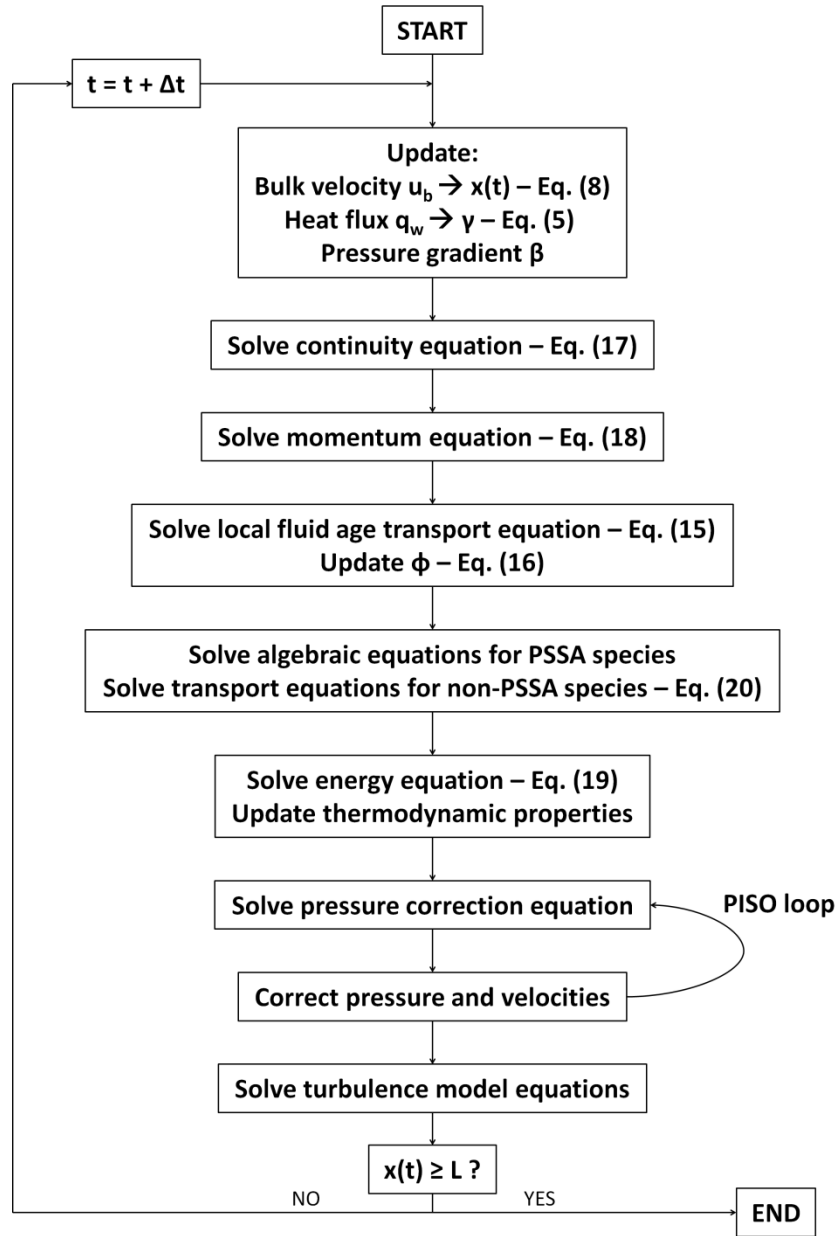


Figure 4-4: Structure of the proposed top-level solver implemented in OpenFOAM®.

A second order central differencing spatial discretization scheme was used, with minor high-frequency filtering. The cell face values of the Gaussian surface integral were obtained through linear interpolation. Time integration was performed using a second order backward differencing scheme (BDF2):

$$\left(\frac{\partial \varphi}{\partial t}\right)^n = \frac{\frac{3}{2}\varphi^n - 2\varphi^{n-1} + \frac{1}{2}\varphi^{n-2}}{\Delta t} \quad (4.28)$$

The maximal Courant number was kept below 0.5 according to the CFL condition, leading to time steps of approximately $3 \cdot 10^{-6}$ s to $1 \cdot 10^{-5}$ s.

4.3 Results and discussion

First the accuracy of the proposed methodology was evaluated by comparing simulation results using the periodic approach with results obtained using a classical non-periodic discretization over the entire domain. This initial validation is carried out for a simple cylindrical tube. Extension to more complex flow patterns is performed through simulation of a 3D longitudinally finned reactor and a reactor with a periodic obstruction in the tube cross section. An overview of the studied geometries and corresponding local fluid age correction factors is shown in Figure 4-5.

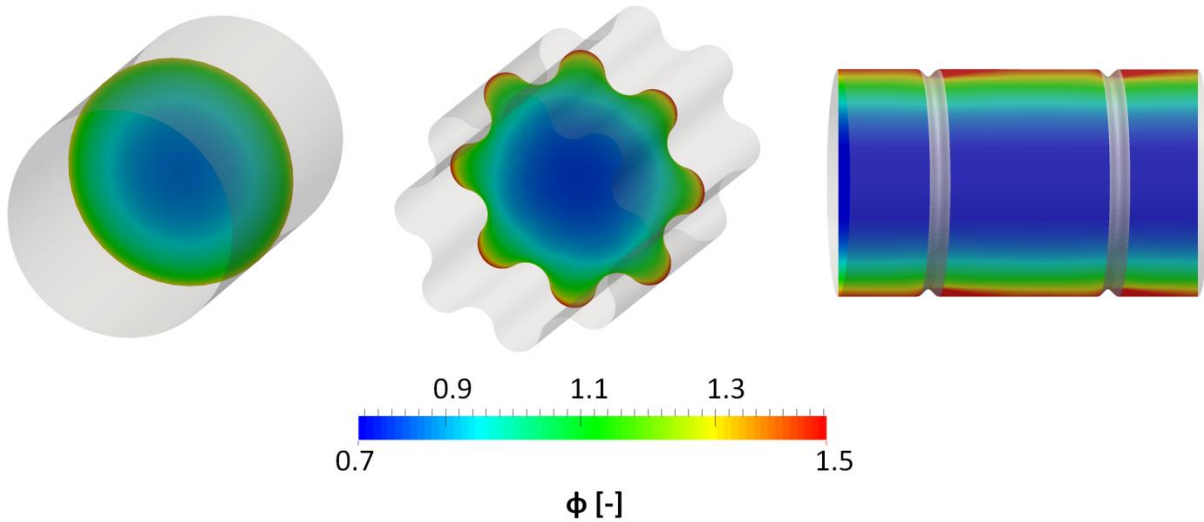


Figure 4-5: Three-dimensional representation of the studied reactor designs with contour plots of the corresponding local fluid age correction factors, from left to right: a bare tubular reactor, a longitudinally finned reactor and a transversally ribbed reactor.

Periodic reactive flow simulation: proof of concept for steam cracking coils

The use of these enhanced tubular reactors has recently received increased attention in the field of steam cracking as a way of limiting the unwanted side reactions that lead to coke deposition on the reactor surface. Application of alternative, 3D reactor designs allowing operation at reduced inner wall temperatures is believed to result in increased run lengths and hence significant economic gains^{7, 28, 39, 40}.

The simulated reactor was previously described by Schietekat et al.²⁸ and is in principle a simple straight tube, i.e. the feedstock enters at the bottom of the furnace, close to the gas-fired floor burners, and exits at the top of the radiant section without turns or bends. This industrially applied reactor type is known to achieve a high selectivity towards light olefins due to the short residence times in the order of milliseconds. On the downside, the narrow diameter of 0.0302 m and the intense heating applied to these reactors over a length of just 10.56 m, causes severe coke formation. The hydrocarbon and steam flow rate were fixed at 0.03292 and 0.01075 kg/s, respectively, corresponding to a steam dilution of 0.326 kg_{H2O}/kg_{HC}. The reactor inlet temperature was equal to 903 K, whereas the reactor outlet pressure, that is, upstream of the transfer line exchanger, was set to the industrially applied value of 203 kPa.

Unless stated otherwise, all listed yields and temperatures are mixing cup averages at the outlet of the reactor, defined as:

$$\overline{\varphi_{mixcup}} = \frac{\int_{\partial V} \rho u_x \varphi dA}{\int_{\partial V} \rho u_x dA} \quad (4.29)$$

For each case, comparison is also made with 1D simulations performed using the same reaction kinetics in CHEMKIN^{®41}. The pressure and azimuthally averaged internal tube metal temperature profiles in these simulations are fixed and taken from the respective full reactor simulations. In this manner, their influence on yield and coking rate predictions is minimized, and a clearer evaluation of the importance of the flow profiles is obtained.

4.3.1 Bare tubular reactor

The bare reactor simulations were performed on a 2D wedge grid, assuming azimuthal homogeneity. For the non-periodic simulation this grid was extruded over the entire length of 10.56 m, while the periodic domain remained limited to a length of 0.05 m, with equal resolution in the axial direction. The total computational cost amounted to approximately 10 CPU hours for the full case, compared to 0.04 hours for the periodic case.

Table 4-2 shows the results for the bare reactor comparing the traditional approach with the novel periodic approach and 1D simulations performed using CHEMKIN^{®41}. The importance of resolving the 2D radial temperature and species profiles is demonstrated in all cases, in line with previous work^{35, 42}. Despite the higher coil outlet temperature, the 1D simulation underpredicts the propane conversion compared to the 2D simulations. As a direct consequence of this, relative differences for the ethene and propene yields amount to -2.3% and +2.4%, respectively. Despite the significant simplification of the flow domain through application of streamwise periodicity, the results from both the periodic reference and the periodic corrected case are seen to agree well with the full non-periodic simulation. Figure 4-6 plots the mixing cup average pressure, temperature and concentration profiles along the length of the reactor, showing no discernible differences for the periodic approach compared to the non-periodic case. Upon closer inspection of the outlet concentrations however, the influence of the fluid age correction in Periodic_{cor} is clearly seen to be vital to the accuracy of the periodic simulation approach. Neglecting this effect leads to errors on the COT, conversion and olefin yields that are of the same order of magnitude as those made by treating the system as a 1D plug flow reactor, clearly not justifying the additional cost of performing a 2D simulation. By including the fluid age correction term, improved results are obtained, as relative errors for the primary products drop below 0.3%, compared to the full non-periodic simulation.

Periodic reactive flow simulation: proof of concept for steam cracking coils

Table 4-2: Comparison of the simulation results for a bare reactor; 1D plug flow simulation, 2D non-periodic simulation and 2D periodic without and with local fluid age correction.

Bare	1D	Full	Periodic_{ref}	rel. err. %	Periodic_{cor}	rel. err. %
COT [K]	1155.6	1152.6	1153.6	+0.1	1152.6	0.0
T _{wall, max} [K]		1232.3	1231.0	-0.1	1230.6	-0.1
Δp [Pa]	27766	27766	27832	+0.2	27682	-0.3
Conversion [%]	74.4	74.9	75.4	+0.7	75.0	+0.1
<i>Yields [wt%]</i>						
H ₂	1.84	1.85	1.86	+0.7	1.86	+0.6
CH ₄	13.81	13.98	14.09	+0.8	13.96	-0.1
C ₂ H ₂	1.52	1.61	1.63	+1.6	1.64	+1.9
C ₂ H ₄	26.92	27.53	27.72	+0.7	27.60	+0.3
C ₂ H ₆	1.14	1.24	1.24	+0.2	1.23	-0.1
C ₃ H ₆	23.50	22.94	23.05	+0.5	22.91	-0.1
1,3-C ₄ H ₆	2.77	2.89	2.92	+1.1	2.91	+0.7
1-C ₄ H ₈	1.94	1.91	1.92	+0.5	1.92	+0.6
2-C ₄ H ₈	0.23	0.22	0.22	+1.0	0.22	0.0

Periodic reactive flow simulation: proof of concept for steam cracking coils

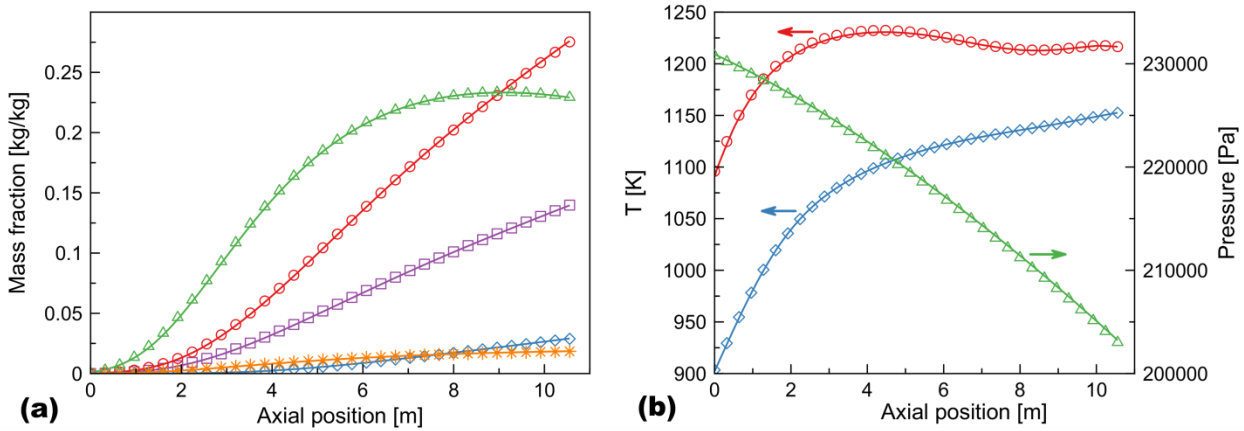


Figure 4-6: Mixing cup averaged profiles along the length of the reactor: symbols represent the full non-periodic simulation, lines Periodic_{cor}; (a) (○) ethene, (△) propene, (□) methane, (★) ethane and (◇) 1,3-butadiene; (b) process gas (△) pressure and (◇) temperature, (○) reactor inner wall temperature.

Figure 4-7 illustrates the influence of the fluid age correction term through comparison of the bulk flow variables and the values on the internal reactor surface. The Periodic_{ref} simulations, in which the local Damköhler number is not preserved, are seen to underpredict the extent of reactions occurring close to the hot gas-metal interface. This implies a reduced local heat consumption from the endothermic reactions, allowing more heat to be dissipated radially into the core of the flow. As such, reaction rates in the core of the tube are promoted and the influence on the global reaction rates remains minimal as was seen in Table 4-2. It can be expected however that the importance of reactions with a high activation energy, such as those leading to the formation of coke precursors, is underestimated when the fluid age correction is not implemented.

Periodic reactive flow simulation: proof of concept for steam cracking coils

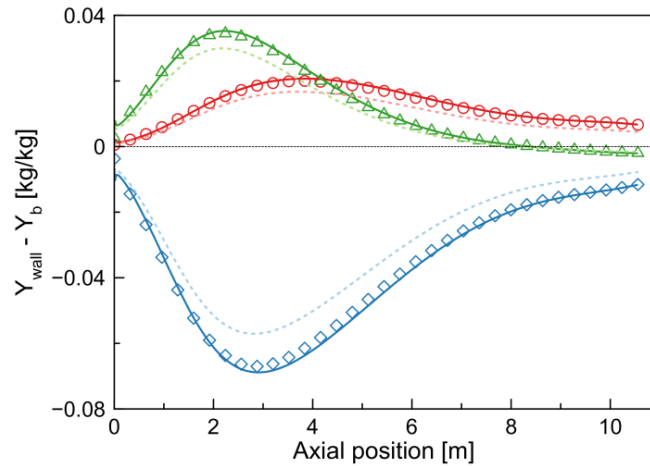


Figure 4-7: Difference between the mixing cup averaged and the inner reactor wall mass fractions for a bare reactor: symbols represent the full non-periodic simulation, light dotted lines $\text{Periodic}_{\text{ref}}$ and dark full lines $\text{Periodic}_{\text{cor}}$; (○) ethene, (△) propene, (◇) propane.

4.3.2 Finned reactor

The addition of fins on the internal tube surface is a well-known method for improving the performance of heat exchangers at a relatively low additional pressure loss. In the field of steam cracking, rounded concave-convex fins are frequently applied in order to increase the area available for heat transfer while avoiding the potential operational difficulties associated with sharp edges. Previous experimental and computational studies on this design can be found in the work of Albano et al.⁴³, Schietekat et al.²⁸ and Van Cauwenberge et al.⁷. The finned reactor geometry consists of 8 rounded fins with a fin height of 0.00358 m. This corresponds to a fin height-to-diameter ratio of 0.128 and a surface area enhancement factor of 1.28, while the cross-sectional flow area was held fixed to that of the bare tube. The 3D computational domain was limited to a quarter of the full cross-section and extruded over a length of 10.56 m and 0.05 m for the full case and the periodic case, respectively, with an identical axial resolution. Total CPU time amounted to approximately 3000 hours for the full simulation, compared to about 20 hours for the periodic case.

Table 4-3 shows the results for the four simulation approaches, giving similar differences as those reported in Table 4-2 for the bare tube. Results obtained using the periodic approach again

Periodic reactive flow simulation: proof of concept for steam cracking coils

show good agreement with the full 10.56 m reactor simulation at a 150 times smaller computational cost. Including the fluid age correction is seen to further improve the results with relative errors on conversion and the main product yields below 0.5%.

Table 4-3: Comparison of the simulation results for a finned reactor; 1D plug flow simulation, 3D non-periodic simulation and 3D periodic without and with local fluid age correction.

Finned	1D	Full	Periodic_{ref}	rel. err. %	Periodic_{cor}	rel. err. %
COT [K]	1155.6	1151.5	1153.0	+0.1	1151.6	+0.0
T _{wall, max} [K]		1224.7	1222.9	-0.1	1222.7	-0.2
Δp [Pa]	29195	29195	29364	+0.6	29061	-0.7
Conversion [%]	74.4	74.9	75.6	+1.0	75.0	+0.1
<i>Yields [wt%]</i>						
H ₂	1.84	1.84	1.86	+1.1	1.85	+0.7
CH ₄	13.83	14.06	14.21	+1.0	14.04	-0.2
C ₂ H ₂	1.52	1.64	1.67	+2.0	1.69	+2.8
C ₂ H ₄	26.93	27.77	28.01	+0.9	27.87	+0.4
C ₂ H ₆	1.15	1.27	1.27	-0.2	1.27	-0.1
C ₃ H ₆	23.50	22.61	22.80	+0.9	22.50	-0.5
1,3-C ₄ H ₆	2.77	2.94	2.98	+1.3	2.97	+1.0
1-C ₄ H ₈	1.94	1.88	1.90	+0.9	1.89	+0.5
2-C ₄ H ₈	0.23	0.22	0.22	+1.4	0.22	-0.4

Periodic reactive flow simulation: proof of concept for steam cracking coils

In Figure 4-8 the difference between the mixing cup and the near-wall yields are plotted, which are seen to be even more significant than those in the bare reactor. This can be attributed to the lower process gas velocities in the valley between two subsequent fins. As a consequence, local heat transfer deteriorates and local fluid ages are higher, causing larger radial concentration gradients even though overall heat transfer is promoted. This effect is also clearly illustrated in Figure 4-9, where local high propane conversions are seen for the full simulation, but these are clearly underestimated in the periodic approach without the fluid age correction. Comparing results of the finned reactor with those previously obtained for the original bare reactor design, the influence on the pressure drops remains limited to around 5%. From past literature^{7, 43} however, a value closer to the surface area enhancement factor would be expected. Two reasons can be responsible for these differences. First, although the applied SST $k-\omega$ model was previously validated for incompressible flow in finned tubes⁷, it appears that its performance is worsened in the compressible formulation of the model. Second, the 2D axisymmetric approach used for the bare tube could overestimate the base pressure drop. While hence somewhat qualitative, it is interesting to note the influence of the flow profile on the yields, as the observed differences now originate almost solely from the in-plane temperature and species profiles.

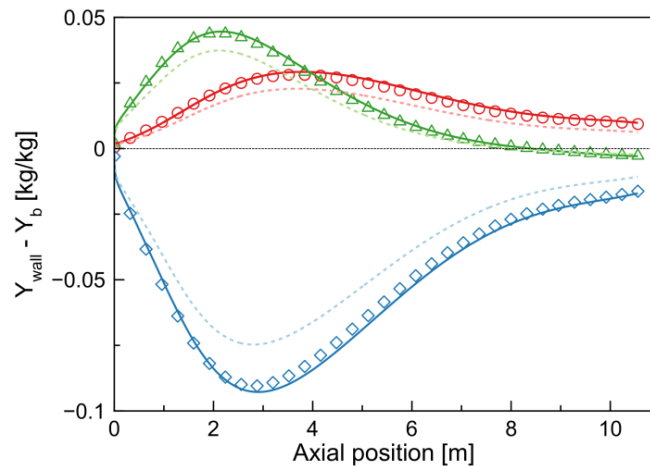


Figure 4-8: Difference between the mixing cup averaged and the inner reactor wall mass fractions for a finned reactor: symbols represent the full non-periodic simulation, light dotted lines $\text{Periodic}_{\text{ref}}$ and dark full lines $\text{Periodic}_{\text{cor}}$; (○) ethene, (△) propene, (◇) propane.

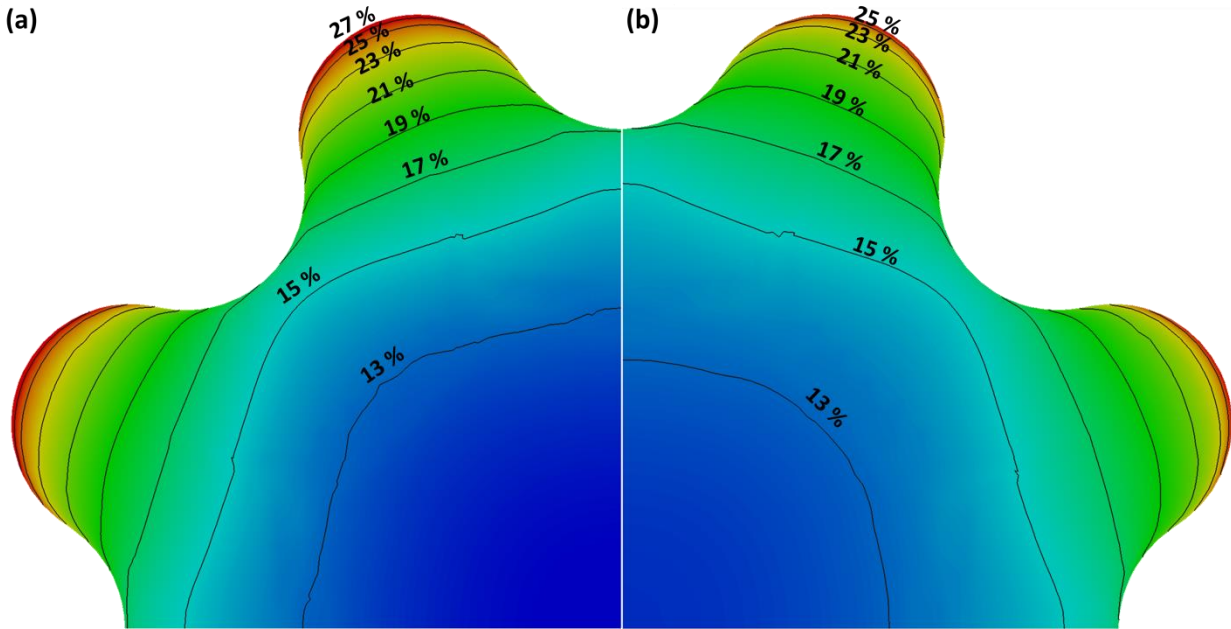


Figure 4-9: Contour plot of propane conversion at a distance of 2.8 m from the reactor inlet (a) in the full simulation and (b) for the periodic simulation without fluid age correction factor $\text{Periodic}_{\text{ref}}$.

4.3.3 Ribbed reactor

In the previous sections, both the bare and finned reactor design had a constant cross-section and hence the velocity profiles along the axial length essentially had a constant shape, instead of exhibiting true periodic behavior. In this section, a transverse rib perpendicular to the flow direction is introduced onto the internal reactor wall as shown in Figure 4-5. This kind of ribbed reactor is extensively used in industry with varying rib shapes and angular configurations^{44, 45}. By acting as a turbulator that breaks up the laminar boundary layer, significantly improved heat transfer can be obtained, with the drawback of an increased pressure drop. The rib geometry is of a sinusoidal shape with a height of 0.001 m and width of 0.003 m, repeating itself every 0.024 m. These parameters implies a blockage ratio of 0.128, which is expected to cause flow separation and reattachment in the wake of the rib. As this phenomenon is usually accompanied by an increased resistance towards heat transfer and high local fluid ages, it is a challenging test case to

Periodic reactive flow simulation: proof of concept for steam cracking coils

validate the performance of the proposed periodic methods. A grid for this geometry was generated by normal extrusion of the 0.024 m ribbed surface into a 2D wedge shape, which was repeated many times to form the grid for the full simulation.

The computational cost of the periodic approach was significantly affected by the acceleration of the flow over the refined ribbed surface, with the corresponding very large local Courant numbers. In order to maintain stability and accuracy, the simulation time step size was reduced by roughly a factor 9 compared to the previous cases. It is expected that introducing some degree of upwind into the central differencing discretization scheme would alleviate part of this problem but for the sake of consistency over the different simulations, this was not implemented. In the end, CPU times for this case amounted to around 50 hours for the periodic approach, compared to 800 hours for the full simulation. Though the obtained speedup is reduced to a factor 16, it still provides an opportunity for the application of a higher level of theory with regard to turbulence modeling, e.g. performing large eddy simulations (LES) to better account for the separated flow region.

The results for the different simulation approaches are shown in Table 4-4. Discrepancies between the simulations are seen to be significantly reduced compared to the previous cases, with even the 1D method offering relatively accurate yield predictions. This can be easily understood from the turbulence generating effect of the rib on the internal surface, strongly reducing the radial temperature and species gradients throughout the entire reactor. As this implies that the flow pattern is closer to plug flow, the errors on the 1D assumption are reduced. The primary effect influencing the product distribution is hence the high pressure drag on the rib structure, leading to higher pressures throughout the reactor. This will translate in an increased importance of bimolecular reactions towards byproducts. If the pressure profile is hence known beforehand or a good estimate for the relative friction factor is available, 1D simulations can succeed quite well in predicting the yields of the major species.

Periodic reactive flow simulation: proof of concept for steam cracking coils
Table 4-4: Comparison of the simulation results for a ribbed reactor; 1D plug flow simulation, 2D non-periodic simulation and 2D periodic without and with local fluid age correction.

Ribbed	1D	Full	Periodic_{ref}	rel. err. %	Periodic_{cor}	rel. err. %
COT [K]	1155.5	1155.5	1155.8	+0.0	1155.2	+0.0
T _{wall, max} [K]		1176.7	1177.3	+0.1	1177.2	+0.0
Δp [Pa]	110518	110518	110011	-0.5	110001	-0.5
Conversion [%]	75.6	76.2	76.4	+0.3	76.2	+0.0
<i>Yields [wt%]</i>						
H ₂	1.81	1.82	1.83	+0.3	1.83	+0.3
CH ₄	14.36	14.57	14.63	+0.4	14.54	-0.2
C ₂ H ₂	1.48	1.54	1.55	+0.7	1.55	+0.6
C ₂ H ₄	27.33	27.74	27.84	+0.3	27.74	+0.0
C ₂ H ₆	1.29	1.32	1.33	+0.2	1.32	-0.7
C ₃ H ₆	23.69	23.51	23.55	+0.2	23.52	+0.0
1,3-C ₄ H ₆	2.79	2.87	2.89	+0.6	2.88	+0.2
1-C ₄ H ₈	1.90	1.89	1.89	+0.1	1.89	+0.4
2-C ₄ H ₈	0.23	0.23	0.23	+0.4	0.23	+0.0

With the reduction of the radial temperature differences, concentration differences between the inner wall and the core of the flow are also expected to be significantly smaller because of the Arrhenius law rates. This is confirmed by Figure 4-10 with the absolute differences in mass fraction remaining limited to +/- 1%, compared to over 5% in the previous cases. While the

Periodic reactive flow simulation: proof of concept for steam cracking coils

contribution of the reaction rates decreases, the importance of the local fluid age however appears to be more pronounced as the relative difference between the set of periodic simulations is larger than what was previously seen. Especially near the exit of the reactor, radial differences are underestimated by a factor 3-4 as the increased fluid age in the region of separated flow is not fully accounted for without the correction factor.

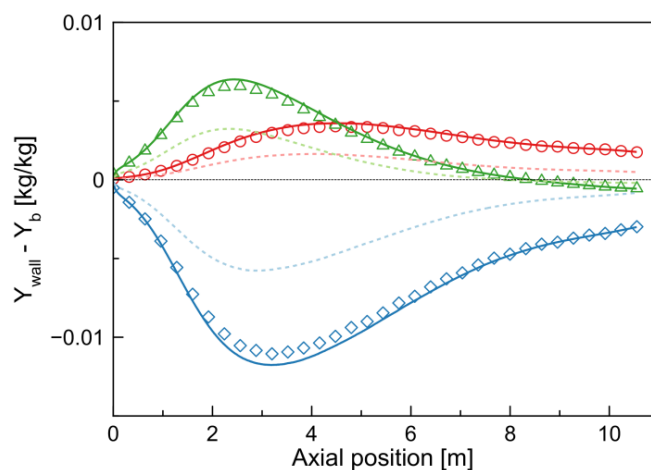


Figure 4-10: Difference between the mixing cup averaged and the inner reactor wall mass fractions for a ribbed reactor: symbols represent the full non-periodic simulation, light dotted lines $\text{Periodic}_{\text{ref}}$ and dark full lines $\text{Periodic}_{\text{cor}}$; (○) ethene, (△) propene, (◇) propane.

4.3.4 Industrial design considerations

What is essential for determining the industrial relevance of the developed methodology is that the differences between alternative 3D reactor designs are correctly predicted, in particular in reference to the state of the art. As the choice for a commercial design often boils down to balancing a tradeoff between reduced coke formation and a potentially undesired impact on product yields, a correct prediction of these deltas is critical. Therefore in Table 4-5 a summary is given of the relative differences at start-of-run conditions between the different reactor designs studied in this work.

Periodic reactive flow simulation: proof of concept for steam cracking coils

The potential effect of an enhanced reactor design on the industrial run length can be estimated based on the maximal rate of coke formation, as this will determine how quickly the reactor coils fill up with cokes and experience reduced thermal efficiency and olefin selectivity losses. A commonly applied coking model for light feedstocks such as propane is the semi-empirical model of Plehiers et al.⁴⁶, in which the coking rate is a function of temperature and the concentration of the main coke precursors ethene and propene. Both the finned and ribbed reactor are seen to benefit from their improved heat transfer characteristics by exhibiting a reduced tube metal temperature and corresponding coking rates.

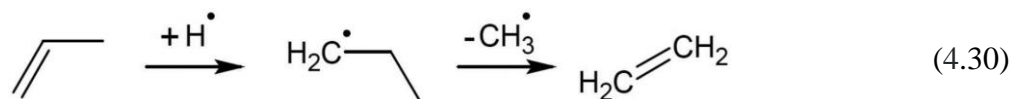
Table 4-5: Summary of the difference in operating variables and yields between a bare, finned and ribbed reactor design.

	Finned vs Bare			Ribbed vs Bare		
	1D	Full	Periodic _{cor}	1D	Full	Periodic _{cor}
ΔP [%]	+5.1	+5.1	+5.0	+298	+298	+297
$T_{\text{wall, max}}$ [K]	-7.6	-7.6	-7.9	-55.6	-55.6	-53.4
$r_{\text{cokes, max}}$ [%]	-7.3	-5.4	-5.9	-52.5	-50.9	-50.3
Conversion [%]	+0.03	+0.08	+0.04	+1.60	+1.78	+1.63
C_2H_4 yield [%]	+0.04	+0.87	+0.97	+1.52	+0.76	+0.51
C_3H_6 yield [%]	+0.00	-1.44	-1.79	+0.81	+2.48	+2.66
CPU time	-	128 days	0.8 days	-	33 days	2.1 days

Looking at the yield differences, the high temperature zones in the concave regions of the finned tubes are clearly seen to cause an increase in ethene selectivity, while conversion remains mostly constant. In the ribbed tubes on the other hand, conversion is increased because of the high pressure drop and corresponding higher reactant concentrations. Though high conversion is typically associated with a decrease in propene selectivity, the opposite is seen to be the case as

Periodic reactive flow simulation: proof of concept for steam cracking coils

the ribbed reactor exhibits the highest propene yield. A rate of production analysis reveals that an important fraction of propene is consumed through an addition reaction of the hydrogen radical, resulting in a 1-propyl radical that decomposes further to ethene and a methyl radical:



Hydrogen radicals exhibit a very strong temperature sensitivity and their concentration may vary an order of magnitude between the core of the flow and the near-wall values. The reduced radial temperature gradient of the ribbed reactor will hence cause near-wall concentrations of hydrogen radicals to also be lower, explaining the increased propene yields.

It is clear that, in line with previous studies^{35, 42}, the 1D simulations fail to account for such effects of enhanced reactor geometries. Though it is possible to impose a modified pressure and wall temperature profile based on Nusselt number and friction factor correlations, such modifications are seen to only improve the conversion and coking rate predictions³⁵. The influence on the specific product yields however remains dominated by the radial species, temperature and residence time profiles, which require a multidimensional reactive simulation approach.

Despite the challenge in calculating the small deltas between the different sets of simulations, the results using the novel periodic methodology show good agreement with the full-scale simulations. Though the method retains an inherently approximate nature, the proposed fluid age correction succeeds in reducing relative errors to the 0.x % levels. It is reasonable to expect that the speedup of 1 to 2 orders of magnitude will more than make up for this by unlocking a previously unobtainable level of theory in terms of kinetics and turbulence modeling. The latter was already demonstrated in the recent work by Zhu¹⁹ where a large eddy simulation approach was combined with free-radical kinetics in the simulation of a steam cracker coil. Performing such simulations at the industrially relevant Reynolds numbers would normally not be possible, even with the current High Performance Computing resources.

4.4 Conclusions

A novel approach employing streamwise periodic boundary conditions was developed and successfully validated for the simulation of tubular reactors with high aspect ratios. It can be summarized as modeling a flow reactor by transforming the space into the time domain and following the changes of a small volume of fluid over time. In this manner it becomes possible to simulate the full reactor at substantially reduced computational cost and almost equal accuracy. This was demonstrated for three different reactor designs, as speedup factors of up to 250 were seen, while relative errors for all major product yields were below 1%, without relying on any tunable parameters. Proving this concept is key for applying the method as an efficient screening tool for different reactor designs, or as a means of including a higher level of theory in existing simulations. In particular, the method is expected to aid in enabling the implementation of more complex kinetic mechanisms or even application of eddy-resolving techniques such as LES for industrial scale simulations.

References

1. Moody, L.F., *Friction factors for pipe flow*. Transactions of the ASME, 1944. **66**(8): p. 671-684.
2. DeWitt, D.P., *Fundamentals of Heat and Mass Transfer*. 6th ed. 2007, Hoboken: Wiley.
3. Van Geem, K.M., M.F. Reyniers, and G.B. Marin, *Challenges of Modeling Steam Cracking of Heavy Feedstocks*. Oil Gas Sci. Technol., 2008. **63**(1): p. 79-94.
4. Kalteh, M., A. Abbassi, M. Saffar-Avval, and J. Harting, *Eulerian–Eulerian two-phase numerical simulation of nanofluid laminar forced convection in a microchannel*. International Journal of Heat and fluid flow, 2011. **32**(1): p. 107-116.
5. Ahlers, G., S. Grossmann, and D. Lohse, *Heat transfer and large scale dynamics in turbulent Rayleigh–Bénard convection*. Reviews of Modern Physics, 2009. **81**(2): p. 503-537.
6. Tominaga, Y. and T. Stathopoulos, *Turbulent Schmidt numbers for CFD analysis with various types of flowfield*. Atmospheric Environment, 2007. **41**(37): p. 8091-8099.
7. Van Cauwenberge, D.J., C.M. Schietekat, J. Floré, K.M. Van Geem, and G.B. Marin, *CFD-based design of 3D pyrolysis reactors: RANS vs. LES*. Chemical Engineering Journal, 2015. **282**: p. 66-76.
8. El Khoury, G.K., P. Schlatter, A. Noorani, P.F. Fischer, G. Brethouwer, and A.V. Johansson, *Direct Numerical Simulation of Turbulent Pipe Flow at Moderately High Reynolds Numbers*. Flow Turbul. Combust., 2013. **91**(3): p. 475-495.
9. Schlatter, P. and R. Örlü, *Assessment of direct numerical simulation data of turbulent boundary layers*. Journal of Fluid Mechanics, 2010. **659**: p. 116-126.
10. Patankar, S.V., C.H. Liu, and E.M. Sparrow, *Fully Developed Flow and Heat Transfer in Ducts Having Streamwise-Periodic Variations of Cross-Sectional Area*. Journal of Heat Transfer, 1977. **99**(2): p. 180-186.
11. Spalart, P.R., *Direct simulation of a turbulent boundary layer up to $Re_\theta = 1410$* . Journal of Fluid Mechanics, 1988. **187**: p. 61-98.
12. Nordström, J., N. Nordin, and D. Henningson, *The Fringe Region Technique and the Fourier Method Used in the Direct Numerical Simulation of Spatially Evolving Viscous Flows*. SIAM Journal on Scientific Computing, 1999. **20**(4): p. 1365-1393.
13. Lund, T., S., X. Wu, and K. Squires, D., *Generation of Turbulent Inflow Data for Spatially-Developing Boundary Layer Simulations*. J. Comput. Phys., 1998. **140**(2): p. 233-258.
14. Beale, S.B., *Use of Streamwise Periodic Boundary Conditions for Problems in Heat and Mass Transfer*. Journal of Heat Transfer, 2006. **129**(4): p. 601-605.

Periodic reactive flow simulation: proof of concept for steam cracking coils

15. Urbin, G. and D. Knight, *Large-Eddy Simulation of a Supersonic Boundary Layer Using an Unstructured Grid*. AIAA Journal, 2001. **39**(7): p. 1288-1295.
16. Stolz, S. and N.A. Adams, *Large-eddy simulation of high-Reynolds-number supersonic boundary layers using the approximate deconvolution model and a rescaling and recycling technique*. Physics of Fluids, 2003. **15**(8): p. 2398-2412.
17. Cabrit, O. and F. Nicoud, *Direct simulations for wall modeling of multicomponent reacting compressible turbulent flows*. Physics of Fluids, 2009. **21**(5): p. 055108.
18. Martin, M.P. and G.V. Candler, *Temperature fluctuation scaling in reacting boundary layers*, in *15th AIAA Computational Fluid Dynamics Conference*, 2001: Anaheim, CA.
19. Zhu, M., *Large Eddy Simulation of thermal cracking in petroleum industry*, in *Institut National Polytechnique de Toulouse*, 2015, Université de Toulouse: Toulouse.
20. Bhatti, M.S. and R.K. Shah, *Turbulent and transition flow convective heat transfer in ducts*, in *Handbook of Single Phase Heat Transfer*, S. Kacmak, R.K. Shah, and W. Aung, Editors. 1987, John Wiley: New York.
21. Levenspiel, O., *Chemical Reaction Engineering*. 3rd ed. 1999, New York, NY: Wiley.
22. Sandberg, M., *What is Ventilation Efficiency?* Building and Environment, 1981. **16**: p. 123-135.
23. Ghirelli, F. and B. Leckner, *Transport equation for the local residence time of a fluid*. Chemical Engineering Science, 2004. **59**(3): p. 513-523.
24. Fox, R.O., *Computational Models for Turbulent Reacting Flows*. 2003: Cambridge University Press.
25. Moin, P., K. Squires, W. Cabot, and S. Lee, *A dynamic subgrid-scale model for compressible turbulence and scalar transport*. Physics of Fluids A, 1991. **3**(11): p. 2746-2757.
26. William Kays, M.C., Bernhard Weigand, *Convective Heat and Mass Transfer*. 4th ed. 2004: Mcgraw-Hill (Tx).
27. Pope, S.B., *Turbulent Flows*. 2000: Cambridge University Press.
28. Schietekat, C.M., D.J. Van Cauwenberge, K.M. Van Geem, and G.B. Marin, *Computational fluid dynamics-based design of finned steam cracking reactors*. AIChE Journal, 2013. **60**(2): p. 794-808.
29. Menter, F.R., *Two-equation eddy-viscosity turbulence models for engineering applications*. AIAA Journal, 1994. **32**(8): p. 1598-1605.
30. Wilcox, D.C., *Turbulence Modeling for CFD*. 3rd ed, ed. I. DCW Industries, La Canada CA. 2006.

Periodic reactive flow simulation: proof of concept for steam cracking coils

31. Van Geem, K.M., D. Hudebine, M.F. Reyniers, F. Wahl, J.J. Verstraete, and G.B. Marin, *Molecular reconstruction of naphtha steam cracking feedstocks based on commercial indices*. Computers & Chemical Engineering, 2007. **31**(9): p. 1020-1034.
32. Ranzi, E., A. Frassoldati, S. Granata, and T. Faravelli, *Wide-Range Kinetic Modeling Study of the Pyrolysis, Partial Oxidation, and Combustion of Heavy n-Alkanes*. Industrial & Engineering Chemistry Research, 2005. **44**(14): p. 5170-5183.
33. Clymans, P.J. and G.F. Froment, *Computer-generation of reaction paths and rate equations in the thermal cracking of normal and branched paraffins*. Computers & Chemical Engineering, 1984. **8**(2): p. 137-142.
34. Hillewaert, L.P., J.L. Dierickx, and G.F. Froment, *Computer generation of reaction schemes and rate equations for thermal cracking*. AIChE Journal, 1988. **34**(1): p. 17-24.
35. Reyniers, P.A., C.M. Schietekat, D.J. Van Cauwenberge, L.A. Vandewalle, K.M. Van Geem, and G.B. Marin, *Necessity and Feasibility of 3D Simulations of Steam Cracking Reactors*. Industrial & Engineering Chemistry Research, 2015. **54**(49): p. 12270-12282.
36. William H. Green, J.W.A., Beat A. Buesser, Robert W. Ashcraft, Gregory J. Beran, Caleb A. Class, Connie Gao, C. Franklin Goldsmith, Michael R. Harper, Amrit Jalan, Murat Keceli, Gregory R. Magoon, David M. Matheu, Shamel S. Merchant, Jeffrey D. Mo, Sarah Petway, Sumathy Raman, Sandeep Sharma, Jing Song, Yury Suleymanov, Kevin M. Van Geem, John Wen, Richard H. West, Andrew Wong, Hsi-Wu Wong, Paul E. Yelvington, Nathan Yee, Joanna Yu, *RMG - Reaction Mechanism Generator v4.0.1*, 2013.
37. Pointwise, I., *Pointwise Mesh & Grid Generation Software*, 2014, Pointwise: Fort Worth, TX.
38. *OpenFOAM - The Open Source CFD Toolbox - User's Guide*, 2013, OpenCFD Ltd: United Kingdom.
39. Carrillo, A., *Intensified Heat Transfer Technology – CFD Analysis to Explain How and Why IHT Increases Runlength in Commercial Furnaces*, in *AIChE and EPC 2010 Spring National Meeting*, 2010: San Antonio, TX.
40. van Goethem, M.W.M. and E. Jelsma, *Numerical and experimental study of enhanced heat transfer and pressure drop for high temperature applications*. Chemical Engineering Research and Design, 2014. **92**(4): p. 663-671.
41. *CHEMKIN 10101*, 2013, Reaction Design: San Diego.
42. Van Geem, K.M., G.J. Heynderickx, and G.B. Marin, *Effect of radial temperature profiles on yields in steam cracking*. AIChE Journal, 2004. **50**(1): p. 173-183.
43. Albano, J.V., K.M. Sundaram, and M.J. Maddock, *Applications of extended surfaces in pyrolysis coils*. Energy Progress, 1988. **8**(3): p. 9.

Periodic reactive flow simulation: proof of concept for steam cracking coils

44. Torigoe, T., K. Hamada, M. Furuta, M. Sakashita, K. Otsubo, and M. Tomita, *Mixing Element Radiant Tube (MERT) Improves Cracking Furnace Performance*, in *11th Ethylene Producers' Conference*, 1999: Houston, TX.
45. Györfy, M., *MERT Technology Update: X-MERT*, in *AICHE: Ethylene Producers Meeting*, 2009: Tampa Bay.
46. Plehiers, P.M., G.C. Reyniers, and G.F. Froment, *Simulation of the run length of an ethane cracking furnace*. *Industrial & Engineering Chemistry Research*, 1990. **29**(4): p. 636-641.

5

Large-scale computation of industrial naphtha crackers using adaptive detailed chemistry methods

*"I do not know what I may appear to the world, but to myself I seem to have been
only like a boy playing on the sea-shore, and diverting myself in now and then
finding a smoother pebble or a prettier shell than ordinary,
whilst the great ocean of truth lay all undiscovered before me."*

Isaac Newton (1643 – 1727)

Abstract

The potential of a new chemistry library implemented in the OpenFOAM framework, combining dynamic chemistry reduction with in-situ adaptive rate tabulation (ISAT) and on-the-fly application of the pseudo-steady state approximation (PSSA) was investigated. In the context of hydrocarbon pyrolysis, validation on a 2D propane steam cracking case resulted in speedup factors of over 200, as significant synergy between the three methods was seen. This allowed to apply the new chemistry library in the simulation of a full industrial naphtha cracking furnace, where both the furnace and reactor side were described using computational fluid dynamics (CFD). The 3D-3D thermal coupling between the different computational domains was achieved in an efficient manner based on incident radiative flux coupling. The naphtha cracking kinetics inside the reactor coils were described using a detailed reaction network consisting of 152 species, 856 reversible elementary reactions and 1138 lumped reactions. With this previously unattainable level of detail in a coupled 3D-3D furnace simulation, the impact of an alternative reactor design on product yields could be investigated. In contrast with previous studies implementing less detailed chemical schemes, no olefin yield losses were observed by application of the alternative reactor geometry when operating at a fixed cracking severity. The improved radial mixing of the alternative design however was seen to decrease the rate of coke deposition on the tube inner surface by 36%, indicating the significant potential of enhanced 3D reactors for improving run lengths and coil service life.

5.1 Introduction

Accurate simulation of reactive fluid flow requires an equal level of confidence in both the fluid dynamics and the chemical kinetics. In the field of combustion, oxidation and pyrolysis, the fundamental modeling of gas-phase chemistry has thrived over the last two decades driven by an improved knowledge on the occurring elementary reaction families, the availability of thermodynamic data and reaction rate coefficients¹, and the automation of kinetic model generation through dedicated computer codes²⁻¹¹. This increase in modeling accuracy is

accompanied by a steep increase in the model size, with state-of-the-art combustion and pyrolysis kinetic models easily containing several hundreds of species and thousands of elementary reactions¹²⁻¹⁵ to account for all possible reaction pathways and intermediate species. Figure 5-1 displays the size of selected kinetic models for thermal decomposition, oxidation and combustion processes over the last two decades. It is clear that the number of species and reactions in these kinetic models has increased drastically in recent years.

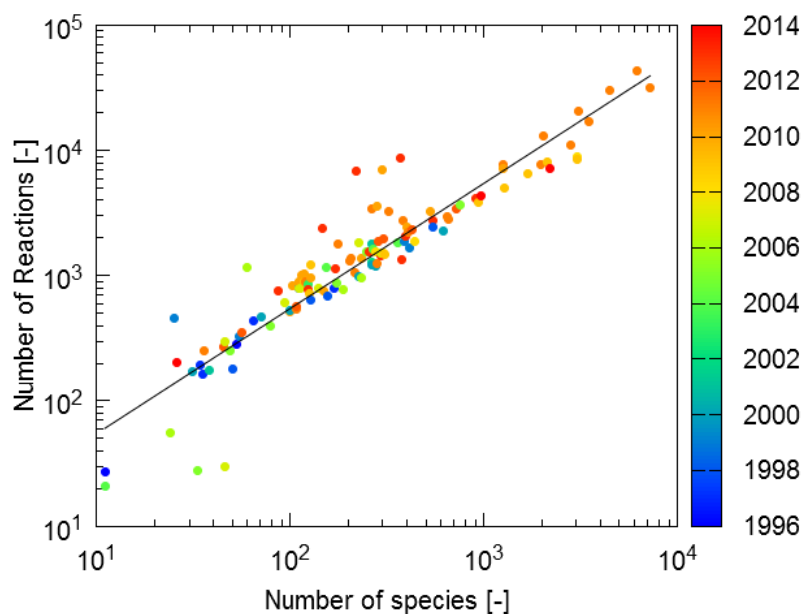


Figure 5-1: Number of reactions as a function of number of species for selected reaction models describing oxidation, pyrolysis and combustion; evolution over the last two decades (after Lu and Law¹⁶).

Direct application of such kinetic models in computational fluid dynamics (CFD) simulations for full-scale industrial systems becomes increasingly challenging to the point of being prohibitively expensive. This is not only due to the CPU time required to evaluate the rates of all reactions and to solve the increased number of species conservation equations, but also because of the substantial differences in the species lifetime leading to a very stiff set of ordinary differential equations (ODEs).

Numerous *a priori* dimension reduction techniques have been developed to alleviate these challenges. An essential first step consists of deriving a skeletal mechanism, i.e. a selected subset

of the species and reactions of the detailed mechanism that is still able to describe the chemistry with a sufficient level of accuracy but at a significantly reduced computational cost. This can be achieved using classical sensitivity analysis, graph-based methods such as directed relation graph (DRG)¹⁷, principal component analysis (PCA)¹⁸, genetic algorithm and various other optimization-based methods¹⁹⁻²¹. Another major category of methods is lumping, of e.g. isomers with similar reaction pathways or thermal and transport properties, in order to reduce the number of variables to be tracked^{22, 23}. Reduction methods based on time-scale analysis form a third category and include classical methods like the Pseudo-Steady State Approximation (PSSA) and Partial Equilibrium Assum (PEA) but also more systematic approaches such as Intrinsic Low Dimensional Manifolds (ILDM)²⁴ and Computational Singular Perturbation (CSP)²⁵. While a combination of the mentioned reduction techniques forms an indispensable first step in reducing the full reaction network, they are limited in their application by the inherent requirement that the performed operations cover the entire or at least a broad range of conditions.

In order to create a further speedup, various adaptive techniques have been developed during the past few decades. These can be roughly divided into storage-retrieval methods and adaptive chemistry methods. In-situ adaptive tabulation (ISAT)²⁶ and piecewise reusable implementation of solution mapping (PRISM)²⁷ are two examples of on-the-fly tabulation methods, with the former using Taylor series and the latter using polynomial regression to obtain rates of formation from previously tabulated points. The advantage of using adaptive tabulation, such as ISAT, rather than pre-generated look-up tables is that not the entire thermochemical phase space needs to be covered, but only the accessed region.

Adaptive chemistry or on-the-fly reduction methods exhibit clear analogies to some of the methods used for skeletal network reduction. Unlike the global approaches however, they develop a library of reduced mechanisms by taking into account the local thermochemical conditions, and continuously select the most appropriate mechanism at that point in time and/or space. Some examples include the dynamic adaptive chemistry (DAC) method of Liang et al.²⁸ and the transport-flux-based method of Tosatto et al.²⁹, where network reduction is based on rate of production analysis using the DRG method¹⁷. On-the-fly methods based on path flux analysis

(PFA) and dynamic element flux analysis (EFA) have also been proposed and applied successfully^{30, 31}.

While the use of adaptive chemistry can significantly reduce the cost of reaction rate evaluations, a drawback compared to *a priori* removal of those species is that conservation equations still need to be solved for all the species in the original mechanism. For networks with a large spread on species lifetimes, applying the pseudo-steady state approximation on-the-fly can resolve this problem. Based on the PSSA, their concentration can be determined via a set of algebraic equations, hence reducing the size and the stiffness of the system of ODEs. Selecting these PSS species can be a key issue, requiring significant user expertise or methods such as CSP²⁵ that can be complex to implement in an automated manner.

As each of the discussed techniques operates at a different stage of the rate evaluation procedure, it is possible to combine them and apply them in an appropriate sequence so as to maximize the extent and efficiency of the overall reduction effort. Some recent examples include the combination of ISAT with RCCE³², DAC³³ and ICE-PIC³⁴. In the present work, the tabulated dynamic adaptive chemistry (TDAC) implementation in OpenFOAM 2.3.x by Contino et al.³³ was extended with an on-the-fly PSSA method. Given the interest in pyrolysis kinetics, the method was validated for a propane steam cracking reactor.

Next, the focus is shifted towards the simulation of a full industrial naphtha cracking furnace, in which both the furnace and the reactor were simulated in 3D using OpenFOAM. In the radiant section, effort is made to include the detailed burner geometry, while accounting for flue gas radiation with an exponential wide band absorption model. On the reactor side, a detailed free-radical kinetic network was implemented to describe the naphtha cracking kinetics.

Performing CFD on the reactor side was mainly motivated by the aim to investigate the potential of a reactor design enhanced with an internal helical rib. Such so-called 3D reactor technologies are often applied commercially because of their beneficial effect on convective heat transfer to the process gas. Through the resulting reduction of the tube metal temperatures, they are expected to prolong the coil service life and also reduce the rate of deposition of coke on the internal

surface of the reactor. Hence, the run length between subsequent decoking operations can be increased, providing maximal on-stream time. However, the negative side effect of an additional pressure drop, has placed them under scrutiny for potentially impacting olefin yields.

Though this enhanced pressure profile can be imposed in a 1D simulation, such an approach cannot include the radial profiles for temperatures and species concentrations and their impact on the final product distribution. As demonstrated by Van Geem et al.³⁵ and confirmed in recent work of the author, this impact is at least comparable to that caused by the pressure profile along the reactor coordinate³⁶. Hence in order to properly evaluate the enhanced reactor geometries, full 3D simulations accounting for radial and azimuthal gradients should be carried out. In previous work by the current author and coworkers, this allowed the quantification of product yields in various embodiments of an industrial propane cracker^{36, 37}. Rather than a clear loss of olefin selectivity, these studies showed a shift from ethene to propene, while total olefin yields remained unaffected or even increased. It is the aim of the present work to determine if and to what extent such effects occur in industrial-scale naphtha cracking units.

5.2 SRT-VI furnace simulation

5.2.1 Geometry and operating conditions

An overview of the Lummus SRT-VI furnace geometry is given in Figure 5-2. The in- and outlets of the reactors are both situated at the top of the radiant section, as the reactor coils make two passes. The process gas enters through the five smaller diameter inlet tubes, allowing a fast heating of the process gas because of the large surface-to-volume ratio, before it is mixed in the manifold at the bottom of the radiant section. These manifolds are situated in a groove in the center of the furnace bottom in order to shield them from direct radiation. This radiation shielding provides a good protection against coke formation in these mixing zones where local hot spots are likely due to the existence of separated flow regions. The outlet leg has a larger diameter, preserving the total cross sectional flow area but offering a reduced pressure drop and less chance of blockage due to local accumulation of formed coke.

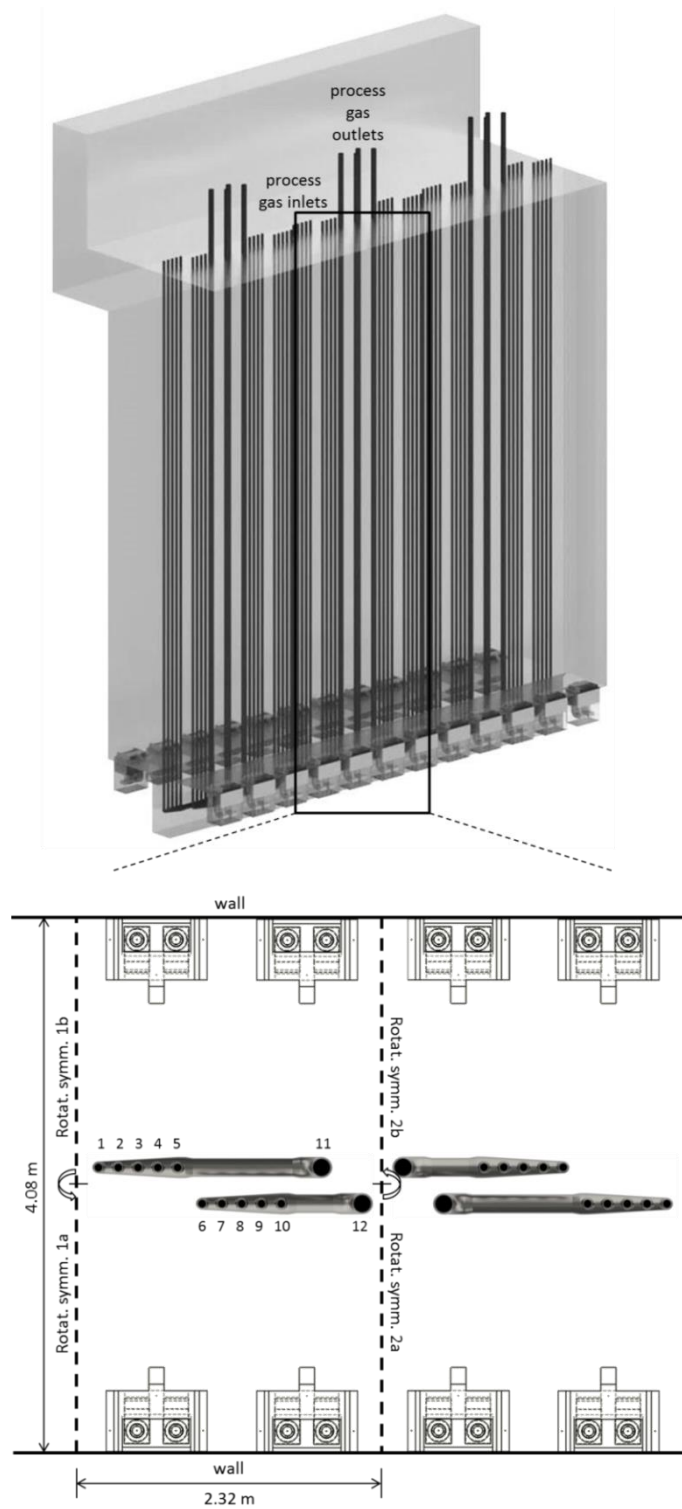


Figure 5-2: Drawing of the SRT-VI furnace, with a top view of the simulated unit cell and the applied boundary conditions.

The furnace comprises of 24 floor burners and 12 reactors, the latter being arranged in groups of four. To reduce the computational cost, only the unit cell indicated in Figure 5-2 is simulated, comprising of two reactors and four burners. Because of the staggered positioning of the reactors, a 180° rotational symmetry boundary condition is applied to the sides of the domain rather than a simple symmetry condition. The effect of the side walls is disregarded, making the simulation most representative of the middle furnace section.

All geometrical details of the PLSFFR-60M John Zink burners, as shown in Figure 5-3, are included in the simulation in order to accurately capture the flame profile. The main air inlet is situated at the bottom and introduces ambient air. Two flue gas channels are directed towards the center of the furnace to allow for the recirculation of hot flue gas. Because of the flow acceleration and low pressure induced by the venturis, flue gas is drawn through these channels. Eventually it preheats and dilutes the fuel entering through the primary fuel tips. Three staged burner tips with secondary drillings are situated at the sides and the top of the burner. This sort of fuel staging lowers the peak flame temperature and hence is crucial in reducing NO_x emissions.

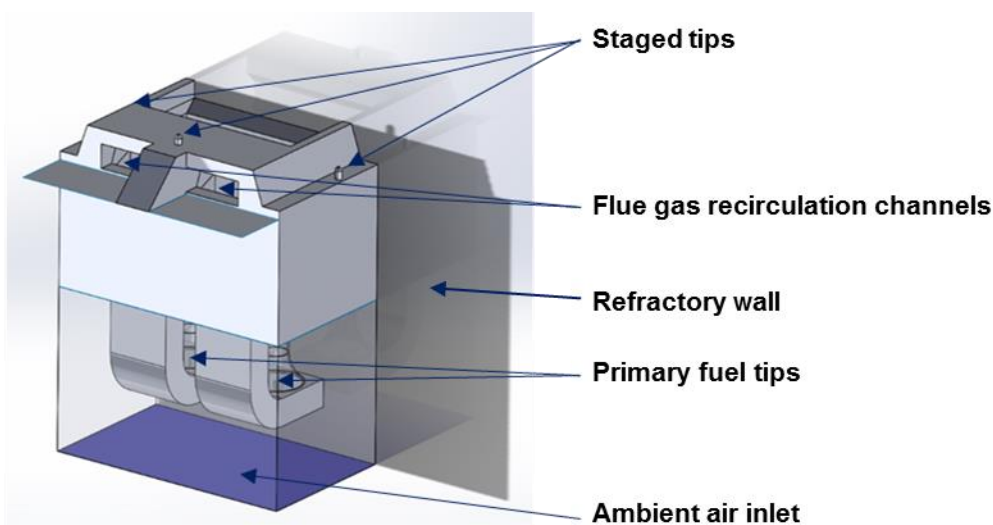


Figure 5-3: CAD drawing of the John Zink floor burners in the SRT-VI furnace.

As the SRT-VI furnace geometry comprises a wide range of spatial dimensions, strong local grid refinement is required to resolve the small burner tips, while a coarser grid should be used for the upper parts of the furnace to limit the number of cells. This was achieved through use of stepwise octree refinement based on the distance from important features. The geometry was made to conform to the curved sections of the CAD drawing by using the OpenFOAM cell snapping tool `snappyHexMesh`. Cells were also refined in certain regions of the domain without cutting away internal cells. In this manner, additional refinement could be added to the regions around the fuel jets. A cone with an opening angle of 12° originating from the burner tips with secondary drillings is chosen to be refined further to account for the necessary detail needed in the combustion region, i.e. the region where oxidizer and fuel are mixed and react. An overview of the mesh in the vicinity of the burners is given in Figure 5-4. The resulting computational grid for the considered furnace segment amounted to 15.3 million cells.

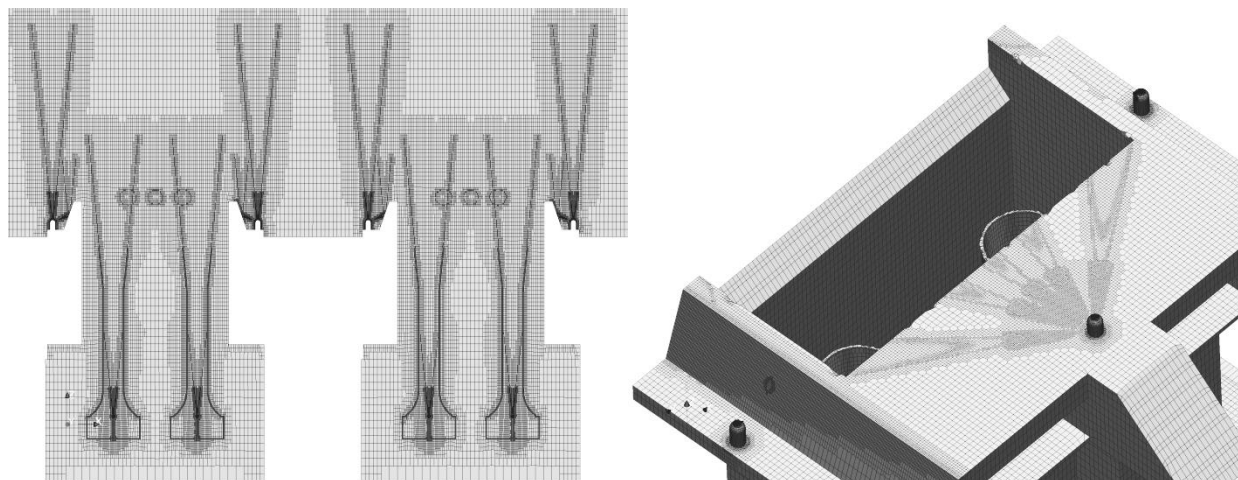


Figure 5-4: Mesh refinement near the primary fuel tips and staged fuel tips with secondary drillings.

Furnace operating conditions, along with fuel and material properties are listed in Table 5-1. Although the industrial fuel gas consists of 95 wt% methane, 2.7 wt% hydrogen and small amounts of ethene and C4-C6, a pure methane fuel was assumed in order to simplify the combustion kinetics.

Table 5-1: Configuration and operating conditions of the simulated section of the SRT-VI furnace.

Simulated furnace dimensions	
Length [m]	2.32
Width [m]	4.08
Height [m]	13.71
Number of burners	4
Firing conditions	
Fuel flow rate per burner [kg/s]	0.0504
Air flow rate per burner [kg/s]	1.024
Air equivalence ratio	1.184
Fuel/air inlet temperature [K]	293
Furnace outlet pressure [Pa]	101325
Fuel composition [wt%]	
CH ₄	100
Material properties	
Furnace refractory emissivity	0.75
Reactor tube skin emissivity	0.90

5.2.2 Combustion modeling

A simplified two-step global reaction network is used to describe the combustion of the fuel gas. The first step consists of a partial oxidation of methane towards carbon monoxide. This carbon monoxide is then further oxidized towards carbon dioxide in the second step.



The kinetic parameters of the steps are taken from Westbrook and Dryer³⁸, resulting in the following reaction rates, with units in m-s-J-K:

$$r_{CH_4} = 1.5 \cdot 10^7 e^{\frac{-125580}{RT}} C_{CH_4}^{-0.3} C_{O_2}^{1.3} \quad (5.3)$$

$$r_{CO} = 1.259 \cdot 10^{10} e^{\frac{-167430}{RT}} C_{CO} C_{O_2}^{0.25} C_{H_2O}^{0.5} \quad (5.4)$$

The eddy dissipation model (EDM) with finite rate approximation is used to account for the influence of turbulent mixing on combustion. This model proposed by Spalding³⁹ and later modified by Magnussen and Hjertager⁴⁰ uses a fast chemistry approach in which the reaction rate is determined by the rate of mixing of reactants. In diffusion flames, fuel and oxidizer are present in separate flow structures called eddies. They appear as fluctuating intermittent quantities and hence there is a relation between the mean reaction rate and the rate of mixing of these small structures. The turbulent dissipation rate ε can hence be expressed to be inversely proportional to the eddy mixing time scale, leading to the following equation for the combustion rate R_{fu} :

$$R_{fu} = A \frac{\varepsilon}{k} \rho \min \left(Y_{fu}, \frac{Y_{ox}}{s_{fu}} \right) \quad (5.5)$$

where A is an empirical constant equal to 4, Y_{ox} and Y_{fu} the mass fraction of oxidizer and fuel respectively, s_{fu} the stoichiometric oxygen requirement, ε the turbulent dissipation rate and k the turbulent kinetic energy. By using the minimum the equation is valid in the whole domain, both where fuel containing eddies and where oxidizer containing eddies are rate-determining. EDM is adopted here in an extended form, introducing the Arrhenius reaction rate as a “switch” for the kinetically governed flame region^{41, 42}. This so-called finite-rate/EDM takes the minimum of the Arrhenius reaction rate and the eddy-dissipation reaction rate as the net reaction rate.

5.2.3 Radiative heat transfer modeling

The discrete ordinates model (DOM), first suggested by Chandrasekhar⁴³ for one-dimensional astrophysical problems and further developed by Carlson and Lathrop⁴⁴, is adopted to solve the radiative transfer equation (RTE):

$$\hat{\mathbf{s}} \cdot \nabla I_{\lambda}(\mathbf{r}, \hat{\mathbf{s}}) + (\kappa_{\lambda} + \sigma_s) I_{\lambda}(\mathbf{r}, \hat{\mathbf{s}}) = \kappa_{\lambda} I_{b\lambda} + \frac{\sigma_s}{4\pi} \int_{4\pi} I_{\lambda}(\mathbf{r}, \hat{\mathbf{s}}') \Phi(\hat{\mathbf{s}} \cdot \hat{\mathbf{s}}') d\Omega \quad (5.6)$$

$I_{\lambda}(\mathbf{r}, \hat{\mathbf{s}})$ represents the spectral intensity of wavelength λ at location \mathbf{r} in direction $\hat{\mathbf{s}}$, κ_{λ} is the spectral absorption coefficient, σ_s denotes the scattering coefficient, $I_{b\lambda}$ is the spectral black body intensity at wavelength λ , Φ represents the scattering phase function and Ω is the solid angle. In the DOM, the solid angle range of 4π is discretized into n discrete vector directions. The polar angle θ is divided in N_{θ} discretizations over a range of π , ranging from the positive z -axis to the negative z -axis. The azimuthal angle ϕ is divided in N_{ϕ} discretizations over a range of $\frac{\pi}{2}$, ranging from the y -axis to the x -axis. This configuration is copied for each quadrant in the x - y space, resulting in the complete solid angle space to be discretized into $4 \times N_{\theta} \times N_{\phi}$ solid angles. In the present work a 4×2 discretization was applied, resulting in 32 radiative transfer equations for each considered wavelength.

On top of the directional aspect of radiation, the absorption-emission spectrum of the flue gas has a strong wavelength dependency. This wavelength dependency can be accounted for by several models. One of the simpler models is the sum of gray gases model, which considers the gas to be a mixture of gray gases. However, to accurately account for the radiative properties of the flue gas in a furnace, a wavelength dependent model is crucial.

One of the possible wavelength dependent models is the Edwards exponential wide band model (EWBM), developed by Edwards and Menard⁴⁵. The model is applied to the absorption-emission contributions of CO_2 and H_2O explicitly by using approximate absorption “bands” in the wavelength spectrum. The other species in the flue gas were considered to have a negligible

effect on the total amount of gas radiation, as previously shown by Stefanidis et al.⁴⁶. An overview of the considered absorbing bands is given in Table 5-2.

Table 5-2: Band information of the nine-band model based on the EWBM⁴⁷

Band Nr.	Lower wavelength limit [μm]	Upper wavelength limit [μm]	Absorption coefficient [m ⁻¹]	Absorbing species
1	0	2.50	0	-
2	2.50	2.84	EWBM	H ₂ O and CO ₂
3	2.84	4.15	0	-
4	4.15	4.69	EWBM	H ₂ O
5	4.69	5.48	0	-
6	5.48	7.27	EWBM	CO ₂
7	7.27	12.42	0	-
8	12.42	18.92	EWBM	CO ₂
9	18.92	150.00	0	-

The EWBM is based on the assumption that the line intensity decreases exponentially at the band boundaries far away from the band center. The absorption coefficient is calculated for each absorption band using Beer's law⁴⁶:

$$\kappa = \frac{1}{L} \ln \left(\frac{1}{\tau} \right) \quad (5.7)$$

in which L is the mean path length calculated as $L = 3.6 V/A$, where V is the volume of all cells in the mesh combined and A is the sum of the surface areas of all cells. τ is the band transmittance calculated by:

$$\tau = \frac{\tau_0}{A^*} \frac{dA^*}{d\tau_0} \quad (5.8)$$

The dimensionless band absorptance $A^* = A/\omega$ is calculated according to Edwards four region expression⁴⁸ under the assumption that the line intensity decreases exponentially in the band

wings far away from the center. This is described in more detail in the work of Zhang et al.⁴⁷, where the proposed nine-band model method is validated for CO₂ and H₂O by comparison with Leckner's correlation based on spectrally integrated emissivities⁴⁹.

The furnace refractory wall and reactor tubes were treated as gray diffusive walls, with a wavelength independent emissivity, as listed in Table 5-1, and a black-body spectrum according to Planck's law. Heat losses through the refractory walls were accounted for by assuming a uniform heat transfer coefficient to the environment of 5 W/m²K. This value was calculated based on typical insulation properties and thicknesses, and the heat transfer by free convection on the exterior of the firebox. The resulting total losses amounted to 1.5% of the total heat of combustion, which corresponds to what is typically assumed for industrial furnaces^{47, 50}.

5.2.4 Turbulence modeling and numerical settings

According to standard practice for industrial furnace simulations, a Reynolds Averaged Navier-Stokes (RANS) framework was applied, using the Boussinesq eddy-viscosity hypothesis to close the Reynolds stresses. A two-equation k- ϵ model was combined with standard wall functions for the turbulent quantities and velocity. The temperature law-of-the-wall was set according to the formula of Jayatilke⁵¹.

The closure coefficients were adjusted according to the well-known round-jet anomaly where two-equation models succeed very well in predicting planar jets, but overestimate the spreading rate for axisymmetric round jets by 40%. Because of the direct impact of jet spreading on the fuel reaction rate, adjusting the model parameters was critical to obtain a proper flame shape. As seen by multiple authors, including Pope⁵², adjusting the $C_{\epsilon 1}$ constant from a value of 1.44 to 1.6 in the turbulent dissipation rate equation produces the desired effect, and as such this was the value used in the present work.

The governing equations were discretized using the finite volume CFD framework OpenFOAM 2.3.x. The Semi-Implicit Method for Pressure-Linked Equations (SIMPLE) was used for pressure-velocity coupling. Because of the detail in the burner design and the large gradients in the vicinity of the jets, achieving convergence proved to be difficult. To maintain stability, the

convection operator for the turbulent quantities was set to a first-order upwind scheme, while those of temperature, velocity and species use a second-order central differencing scheme with 20-50% Sweby flux limiting⁵³.

5.3 Reactor simulation

5.3.1 Reactor geometry and operating conditions

As described in the section 5.2.1, the reactor is of the Lummus SRT-VI type where the feedstock enters from the top of the furnace and flows downward through the five smaller diameter inlet legs before being mixed in the manifold at the bottom and exiting again at the top after passing through a wider diameter outlet leg. The length of the vertical sections of the reactors is 14.65 m, while the manifold is approximately 1.35 m in length. After exiting the radiant section, the process gas passes through a 4 m long adiabatic section before being quenched in the transfer line exchanger (TLE), effectively stopping the reactions by decreasing the temperature of the gas. As the temperature in the adiabatic section is still close to the coil outlet temperature, a significant amount of reaction still takes place. Therefore, the adiabatic section is included in the simulations as an additional tubular section connected to the outlet leg. Further dimensions and operating conditions are listed in Table 5-3.

In order to optimize calculation time, the simulation was split into two separate parts: the inlet section on one hand and the manifold and outlet sections on the other hand are handled in different but coupled simulations. Only a single inlet leg was simulated explicitly, assumed to be the one positioned in the center of the inlet strand. The values at the outlet of this section were patched to the five entrances of the manifold included in the second simulation. This reduction of the computational domain was considered to be justified as from the simulation of manifold and outlet leg, the pressure difference between the five entrances of the manifold was seen to be minor, i.e. no more than 5000 Pa. Additionally, since the inlet Venturi nozzles located just upstream of the reactor inlet legs operate in the choked flow regime, the difference in absolute

pressure downstream of these nozzles has no impact on the mass flow rate through each inlet leg⁵⁴, i.e. the feed flow rate is equally distributed over all five inlet legs.

Table 5-3: Configuration and operating conditions for the simulated SRT-VI reactor.

Operating conditions	
Naphtha flow rate [kg/s/reactor]	0.875
Steam dilution [kg _{H2O} /kg _{HC}]	0.41
Crossover temperature [K]	908.15
Coil outlet pressure [Pa]	210000
Severity index: C3=/C2= [kg/kg]	0.705
Reactor dimensions	
Number of passes	2
Inlet leg internal diameter [m]	0.057
Outlet leg internal diameter [m]	0.127
Coil wall thickness [m]	0.00675
Total reactor + adiabatic section length [m]	34.65

One of the main motivations for performing full 3D CFD simulations on this industrial scale reactor is to determine the true potential for enhanced reactor geometries. In 1D simulations, the effects of the enhanced geometries can only be approximated by applying correction factors to the correlations used for the Nusselt number and friction factor. In this way the calculated pressure drop and the tube wall temperatures can be matched with those observed in the industrial furnace and consequently the impact on yields and coking rates of the enhanced reactor design is assessed to some degree. However, since radial gradients for temperature and species concentrations are by definition not considered in the corrected 1D framework, their impact on the product distribution is neglected. As demonstrated by Van Geem et al.³⁵ and confirmed in recent work of the author, this impact is at least comparable to that caused by the pressure profile

along the reactor coordinate³⁶. Hence in order to properly evaluate the enhanced reactor geometries, full 3D simulations accounting for radial and azimuthal gradients should be carried out.

Two simulations were performed: one with a bare reactor tube and one in which the outlet leg is a helically ribbed tube, corresponding to the commercially applied Mixing Element Radiant Tube (MERT) type⁵⁵. In the current work, a semi-circle-shaped rib with a height e of 5.7 mm and a pitch distance p of 0.145 m was selected, corresponding to a helix angle α of 70° .

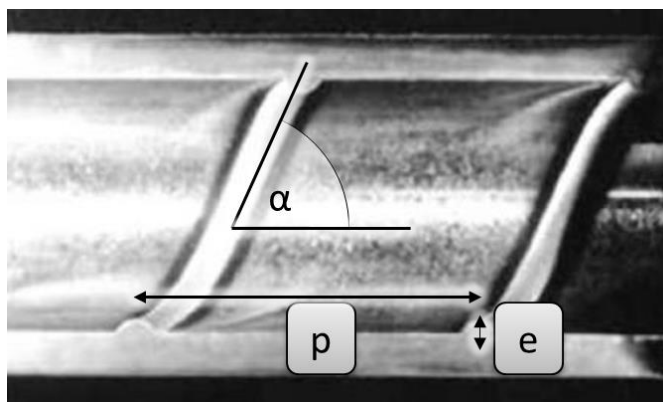


Figure 5-5: Commercial MERT design⁵⁵

The mesh for both geometries was constructed using the stepwise octree refinement method of the OpenFOAM tool snappyHexMesh that was previously used for the fireside. Near-wall refinement was carried out by extruding layers normal to the surface. The mesh resolution in the streamwise, tangential and radial direction was respectively 4 mm x 3 mm x 0.02-3 mm for the bare tube, corresponding to $540 \times 400 \times 3\text{-}400$ in wall units. For the helically ribbed geometry, an additional level of grid refinement in the vicinity of the rib was carried out, leading to local streamwise and tangential spacings that were a factor three smaller compared to the bare tube. The final computational grid consisted of $4.1 \cdot 10^6$, $9.4 \cdot 10^6$ and $22.8 \cdot 10^6$ cells in the fluid domain of the single inlet, the bare outlet, and the ribbed outlet respectively. Radial and tangential conduction within the reactor walls was accounted for by explicitly including the metal domain in the reactor simulations. This was achieved by radially extruding the fluid-metal interface grid

over the metal thickness, amounting to an additional, $1.6 \cdot 10^6$, $3.5 \cdot 10^6$ and $8.9 \cdot 10^6$ cells for these respective parts.

5.3.2 Naphtha representation and kinetic model

As discussed extensively in section 5.1, modeling pyrolysis reactors requires the use of detailed kinetic models considering a significant amount of species and reactors to cover the wide range of possible process conditions and feedstocks⁵⁶. While progress in computational power, network reduction and tabulation techniques, has brought the implementation of accurate first-principle based kinetic models within reach for many industrial applications, one important aspect remains the specification of the feedstock composition in sufficient detail to be able to use the accurate kinetic models. In the present work, the detailed composition of the commercial naphtha was reconstructed based on a detailed PIONA analysis via a Shannon entropy maximization method developed by Pyl et al.⁵⁷. The reconstructed naphtha consists of 71 species in the range of C₄-C₁₀ and agrees well with the commercial naphtha with respect to the available commercial indices.

Table 5-4: Lumped PIONA analysis for the commercial naphtha feedstock.

Feedstock PIONA [wt %]				
n-Paraffins	i-Paraffins	Olefins	Napthenes	Aromatics
33	36.1	0.0	25.2	5.7

The adopted single-event microkinetic model was automatically generated using the same methodology as previously described by Van Geem et al.⁵⁸. In order to limit the number of species in the final model, three main strategies are applied: (i) application of a pseudo-component representation of the feedstock by *a posteriori* lumping, (ii) lumping of primary product molecules, and (iii) application of the pseudo-steady state approximation to the so-called μ radicals, as proposed by Ranzi et al.²². The resulting network contains 152 species, of which 45 radicals, 856 reversible elementary reactions and 1138 lumped reactions.

The thermodynamic data of the C4- molecules and β radicals was derived from first-principles CBS-QB3 calculations of Sabbe et al.⁵⁹. Heavier species were estimated using RMG's ThermoDataEstimator¹¹ which is based on Benson's group additivity⁶⁰. An extension to this concept⁶¹ was also applied for the calculation of the Arrhenius parameters that determine the reaction rate coefficients, as previously discussed in detail by Dijkmans et al.⁶².

The network was validated by comparing it with the full microkinetic model for steam cracking and pyrolysis (CRACKSIM⁵⁸), implemented in the in-house developed commercial software package COILSIM1D. In order to match the results of the skeletal network to those obtained with the reference network, the pre-exponential factors for the reaction rate coefficient of four specific reactions were adjusted, namely the recombination of methyl radicals to form ethane, the methyl addition to benzene to form the benzyl radical and the β scission of ethyl and isobutyl to form ethene and isobutene respectively. The logarithms of the corresponding pre-exponential factors were adjusted within a -1 / +1 range, corresponding to the generally accepted estimated uncertainty on rate coefficients obtained from *ab initio* calculations⁶¹.

5.3.3 Dynamic chemistry reduction and tabulation

As mentioned in section 5.1, one of the areas of interest of the present work is the combination of the TDAC implementation in OpenFOAM by Contino et al.³³ with an on-the-fly PSSA method.

Figure 5-6 clearly illustrates how the three selected methods, i.e. tabulation, dynamic mechanism reduction and time-scale reduction, work on separate levels. At the top stage, the tabulation routine receives a query Ψ^q from the CFD solver containing the concentration vector along with temperature and pressure in a given computational cell. If the query falls within the (hyper-) ellipsoid of accuracy (EOA) around a previously tabulated point, the retrieval operation succeeds and the desired reaction mapping $R(\Psi^q)$ is returned. The EOA is defined as the phase space over which the error on the retrieval of queries is below a predefined tolerance ε_{tol} :

$$\delta\Psi^T \mathbf{A}^T \mathbf{B}^T \mathbf{B} \mathbf{A} \delta\Psi \leq \varepsilon_{tol}^2 \quad (5.9)$$

where \mathbf{A} is the mapping gradient matrix computed according to the Jacobian of the chemical source term, \mathbf{B} is an optional scaling matrix and $\delta\Psi = \Psi^q - \Psi^0$.

When a reaction mapping cannot be interpolated with sufficient accuracy, i.e. when it falls outside of the EOA of all previously tabulated points, a direct evaluation of the reaction rates is required. The TDAC library is different from the traditional ISAT approach in the sense that it will first go through a dynamic mechanism reduction step based on the local thermochemical conditions included in the query Ψ^q . In the present work, the dynamic adaptive chemistry (DAC) method was used as the dynamic mechanism reduction layer, although the TDAC library also includes other techniques such as DRG, DRGEP, PFA and EFA, the performance of which was evaluated by Contino⁶³.

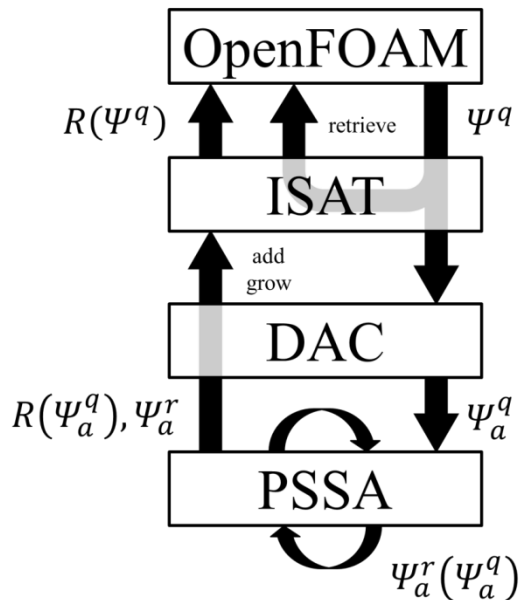


Figure 5-6: Algorithm for evaluating the reaction mapping, showing the different layers of cost reduction methods in evaluating the reaction rates

The reaction rate calculation is then performed using the reduced set of active species Ψ_a^q . Due to the large spread in species lifetimes for processes governed by free-radical chemistry, the system of species conservation equations inherently exhibits a high stiffness that can severely limit the integration time step size. In the field of steam cracking in particular, it was previously demonstrated that on-the-fly PSSA can resolve this issue as all the β -radicals have lifetimes that

are much smaller than those of the molecules, and applying PSSA incurs minimal errors⁶⁴. Due to the occurrence of radical-radical recombination reactions, the reaction rates are nonlinear in the species concentrations, preventing an *a priori* elimination of the radical concentrations, as was done for the μ radicals. Instead, the reduced radical concentration vector Ψ_a^r is calculated on-the-fly by computing the respective rates of consumption and production in an iterative way until the rate of change of the concentration for each PSS species equals zero.

Once the reaction mapping is calculated using all species in the reduced set of active species Ψ_a^q , it can be compared with that of the nearest tabulation point in the ISAT table. If the error is less than ε_{tol} , the original EOA is apparently overly conservative, i.e. the reaction mapping could have been used instead of the direct evaluation, and a growth operation can be performed to include Ψ_q in the larger EOA of the already tabulated point. Otherwise, the newly calculated reaction map is stored in the ISAT lookup table along with the matrix A and the radical concentrations Ψ_a^r . Even though the radical concentrations vector Ψ_a^r is not explicitly used in the upper levels, it is nonetheless included in the tabulated reaction mapping. This aids in maintaining a good initial estimate for the iterative solution of the system of algebraic equations in the PSSA routine upon the next direct evaluation of the reaction rate mapping.

Aside from integrating the PSSA routine into the TDAC framework, two additional adaptations to the original library were made. First, the methods were optimized for use in steady Reynolds-averaged Navier-Stokes (RANS) simulations. In contrast with transient flows, these cases exhibit variation in thermochemical composition primarily in the spatial domain, rather than in the time dimension. As the solution converges to steady state, repeatedly applying the network reduction algorithm hence becomes less valuable. An option was therefore implemented to allow the storage of previously reduced networks and reusing them over a certain number of iterations, the value of which was set to 100 in the present work. Another adaptation was the storage of species indices, stoichiometry and exponents for all reactions in pre-generated matrices, thus avoiding the continuous lookup of these values from the accompanying CHEMKIN reactions file and improving parallel performance.

5.3.4 Furnace-reactor coupling

Because of the cost associated with multiscale simulations for both the reactor side and the furnace side, an efficient coupling between the two is indispensable. Traditionally, this is achieved by fixing a reactor wall temperature profile in the simulation of the furnace side, and imposing the obtained heat flux profiles to the simulation of the reactors⁶⁵. This iterative loop is then continued until differences in tube metal temperature (TMT) obtained from the reactor simulation between two subsequent iterations reach a certain user-defined threshold.

In the present work, fields of incident radiative heat flux rather than total heat flux are applied as boundary condition to the reactor simulation. Zhang et al.⁶⁶ recently demonstrated that this approach reduces the required number of iterations between the furnace side and reactor side in order to reach convergence. Although it was developed for simulating the run length of an industrial steam cracker, the method has been extended to be used in start-of-run simulations of 3D-3D coupled furnace-reactor simulations. Additionally, the reactor wall boundary condition in the furnace simulation was altered to consider the heat balance with the process gas explicitly. This was achieved by stating that the net heat flux going through the reactor wall is governed by a certain global heat transfer coefficient U_{int} and the process gas temperature T_{gas} . In this way, the radiative heat balance on the tube surface is included explicitly in both the reactor and furnace simulation, by using the respective (a) and (b) parts of the following equality:

$$\lambda \frac{\partial T}{\partial n} = q_{conv} + \varepsilon q_{inc} - \sigma \varepsilon T^4 \quad (5.10a)$$

$$q_{conv} + \varepsilon q_{inc} - \sigma \varepsilon T^4 = U_{int}(T - T_{gas}) \quad (5.10b)$$

where λ is the tube metal thermal conductivity, q_{conv} is the convective contribution from the flue gas, ε the absorbed fraction of the incident radiative flux towards the reactor q_{inc} and T the temperature on the interface between the furnace and reactor simulation domains, being the tube outer surface.

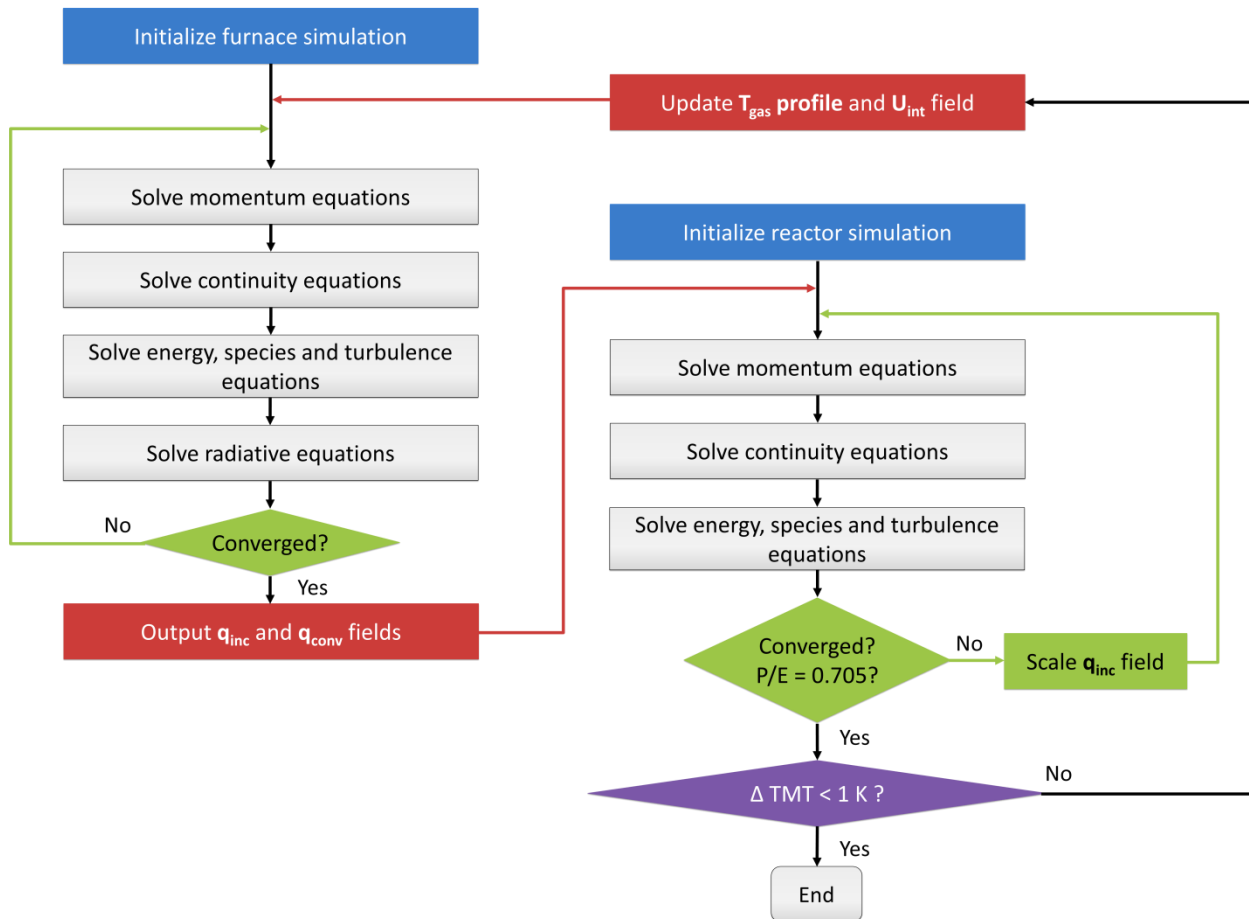


Figure 5-7: Procedure for the 3D-3D coupling between the furnace and reactor simulations, in which one axial profile and three solution fields are exchanged and interpolated for improved convergence of the outer loop.

Introducing these new variables requires more information to be exchanged between the furnace side and the reactor side than just the tube wall temperature and the total heat flux. In the proposed approach, the furnace simulation provides fields of incident radiative heat flux and convective heat flux to the reactor simulation, whereas the reactor simulation returns the axial profile of process gas temperature and the field of the global heat transfer coefficient between the reactor outer surface and the process gas. The main advantage of this approach is that these four fields vary significantly less throughout the outer iteration loop, hence allowing faster convergence of this computationally expensive part of the simulation. Whereas the simple coupling procedure requires approximately five iterations back and forth between the furnace and

reactor simulations and vice versa, the present method only requires approximately two iterations⁴⁷.

The rate of convergence for the furnace and reactor simulations itself was not significantly affected by the change in boundary conditions, as a Neumann condition is still imposed in the reactor simulation, while the boundary condition in the furnace simulation is still of the Dirichlet type. On the reactor side the Neumann conditions are easily implemented as Eqn. (5.10a), while on the furnace side, imposing the Dirichlet conditions implies the solution of a quartic equation of the form $a \cdot T^4 + b \cdot T + c = 0$, through transformation of Eqn. (5.10b). The convective heat flux from the flue gas towards the reactor q_{conv} can be written as $\lambda_{eff,fg}(T_{fg} - T)/\Delta$, with $\lambda_{eff,fg}$ the sum of the laminar and turbulent thermal conductivity, T_{fg} the flue gas temperature at the neighboring cell center and Δ the distance to this cell center. This leads to the following coefficients in the quartic equation:

$$a = \sigma \varepsilon; \quad b = \frac{\lambda_{eff,fg}}{\Delta} + U_{int}; \quad c = -\varepsilon q_{inc} - \frac{\lambda_{eff,fg}}{\Delta} T_{fg} - U_{int} T_{gas} \quad (5.11)$$

For typical furnace conditions, only one physically meaningful root of this equation exists, which can be determined in the following manner:

$$\begin{aligned} p_1 &= 27ab^2; \quad p_2 = p_1 + \sqrt{-4(12ac)^3 + p_1^2}; \\ p_3 &= \frac{4c}{\sqrt[3]{0.5p_2}} + \frac{\sqrt[3]{0.5p_2}}{3a}; \quad p_4 = \frac{2b}{a\sqrt{p_3}} \end{aligned} \quad (5.12)$$

$$T = \frac{1}{2}(\sqrt{p_4 - p_3} - \sqrt{p_3}) \quad (5.13)$$

5.4 Results and discussion

5.4.1 Validation and speedup

Validation of the implemented OpenFOAM chemistry library was performed using a tubular reactor of length 10 m and diameter 0.032 m. A 2D axisymmetric wall-resolved grid was used consisting of approximately 280,000 cells. A pure propane mass flow rate of 0.01 kg/s was imposed, entering the reactor at a temperature of 873 K and with a steam dilution of 0.333 kg_{H₂O}/kg_{C₃H₈}. A reaction network consisting of 100 reactions amongst 24 species, of which 11 radicals, was implemented. This validation case is similar to the one previously used by Reyniers et al.⁶⁴ to validate the implementation of PSSA in ANSYS Fluent. A minor difference originates from the tube wall temperature, as in the present work a linear profile was imposed with a gradient of +35 K/m and a value at the inlet of 973 K. To mimic industrial operation, one would typically start from a fixed heat flux profile. However, the choice for a fixed wall temperature profile should aid in eliminating negative feedback effects that may occur due to the endothermic nature of the process.

Figure 5-8 shows the averaged time per iteration spent at every stage of the species rate of production calculation for each of the investigated methods. For the base case, the only contribution is the calculation of the reaction rates for the full network via direct evaluation. For the PSSA method, no speedup is expected as the iterative calculation of the radical concentrations is costly, especially at the start of the simulation. In practice however, the number of iterations required to calculate the radical concentrations often levels out at around 1-2 as the final steady-state solution is approached. Because of the gradual speedup associated with fewer and fewer required iterations and the more efficient storage of the rate coefficients and exponents compared to the original OpenFOAM libraries mentioned in section 5.3.3, it is observed that the average calculation time per iteration in the PSSA procedure is essentially no different from that using the base chemistry library for this rather small reaction network. Noticeable performance gains of up to a factor two are seen when using DAC network reduction. The additional cost of reducing the network is clearly offset by the reduced cost of calculating the reaction rates. When using ISAT

standalone, 94% of the rate queries could be solved via retrieval and hence almost no time was spent on direct evaluation of the rates. However, adding of entries to the table and even retrieving entries appears to be very costly. This may be a consequence of the chosen tabulation settings, as Contino et al.³³ report speedups of around a factor ten. Possibly the tabulation settings need to be adapted to the size and the nature of the implemented network.

Remarkable synergies between the different methods is observed when two or more methods are combined. Though fundamentally different in concept, the dimensionality reduction by both the DAC and PSSA routines significantly speeds up the tabulation process as well since the lookup of tabulation values in an n -dimensional space is more efficient when n is smaller. An even bigger gain in efficiency is seen in the addition of new tabulated points to the ISAT, as the calculation of the gradient matrix \mathbf{A} requires an evaluation of the Jacobian and inversion of this $n \times n$ matrix, operations that scale with $O(n^2)$ and $O(n^3)$ respectively. Additionally, the total number of rate evaluations decreased since the ISAT EOA in the n -dimensional space is calculated based on the Euclidean distance. As this distance decreases with decreasing dimensionality, the fraction of retrieval operations increased to over 99.9%. It could hence be argued that the tabulation tolerance ε_{tol} should not be fixed and rather be adaptive to the network size as well. This was however not investigated in the present work, nor in the original implementation of Contino et al.³³. In total, the speedup per iteration achieved by combining PSSA and ISAT was approximately a factor 8 compared to applying only PSSA or using the base chemistry libraries, for this rather small reaction network.

Other than the calculation time per iteration, the stiffness of the resulting system of ordinary differential equations is another important factor determining the total calculation cost. As steam cracking chemistry is dominated by free-radical reactions, the short lifetimes of the reactive intermediates require very small time steps in the ODE integration, leading to a high computational cost. In a steady-state CFD simulation, the problem is similar as the finite rates can only be applied with strong under-relaxation of the radical mass fractions, often on the order of 10^{-5} , in order to preserve stability. To assess the influence of stiffness reduction, a sensitivity study was performed to detect the largest possible under-relaxation factor that still allowed

smooth convergence. This resulted in values of $2 \cdot 10^{-5}$ and 0.8 for the under-relaxation factors of respectively the radical and non-radical species. Figure 5-9 shows the convergence profile for the ethene mass fraction at the reactor outlet in all performed simulations.

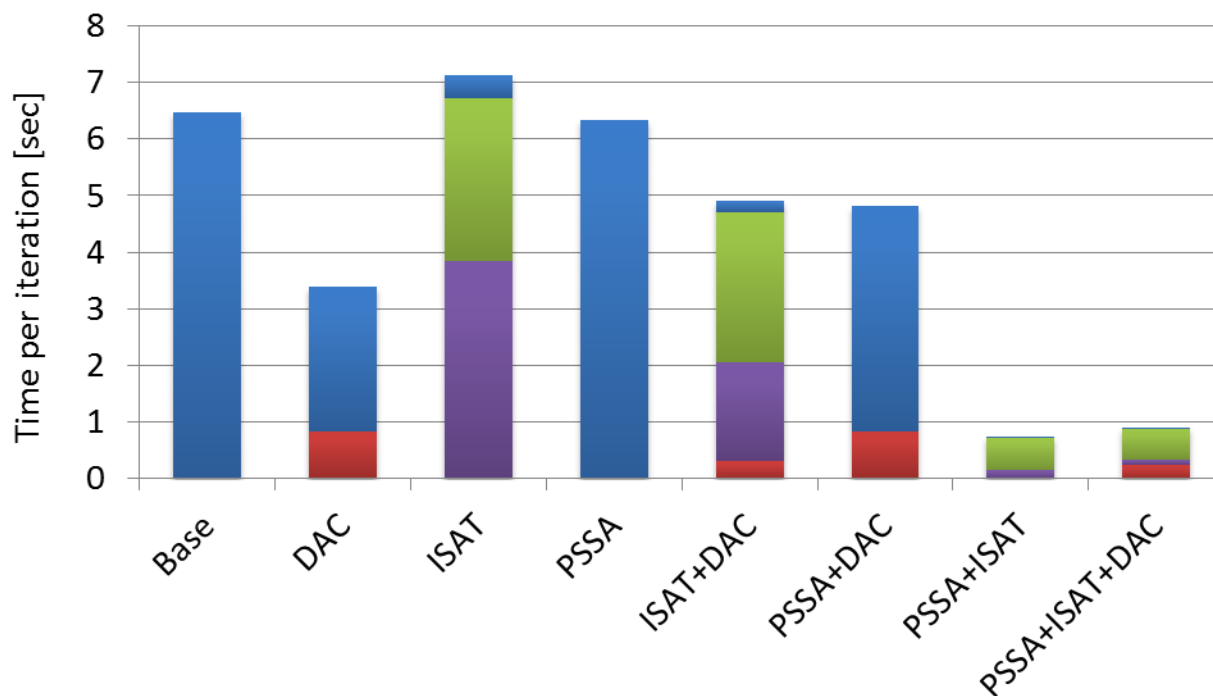


Figure 5-8: CPU time per iteration for the respective steps of the chemistry routines. ■ - direct integration, ■ - tabulated solution retrieval, ■ - addition of a tabulated point to the ISAT library, ■ - DAC network reduction step.

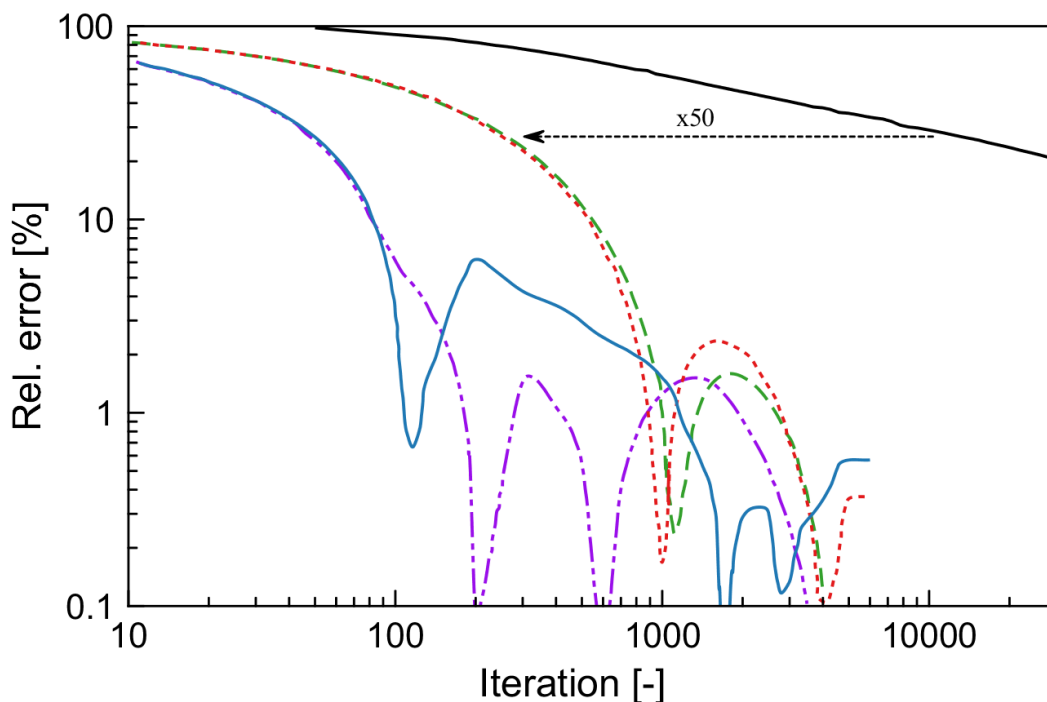


Figure 5-9: Convergence history for the outlet mass fraction of C_2H_4 . — - Base / DAC / ISAT; - - - PSSA; - - - PSSA+DAC; - - - PSSA+ISAT; — - PSSA+ISAT+DAC.

It is clear that the system of ODEs including the radicals conservation equations is unstable and due to the required solution under-relaxation, PSSA provides a marked speedup. An improvement in the number of required iterations with approximately a factor 50 can be seen, which agrees with the value Reyniers et al.⁶⁴ reported when the same test case was run using ANSYS Fluent. More interestingly, when combining PSSA with DAC, a further improvement in the rate of convergence was observed. Although intuitively one would think that dynamic chemistry reduction does not affect the rate of convergence, the observed efficiency gain is caused by the initial insignificance of consumption reactions for species that are low in concentration. As those reactions are added to the dynamic network at a later stage than the formation reactions, any produced specie first accumulates to some extent and is transported along the reactor coordinate by convection. Only when the concentrations reach a certain value, and consequently their consumption reactions become significant, will the kinetics be extended to include those consumption reactions, leading to a stabilization of the species mass fraction at an

intermediate value. The downside is that the species mass fractions tends to exhibit an overshoot before stabilizing to the intermediate value as the consumption reactions are only added to the kinetic network once a certain threshold is reached. The effect was not limited to ethene but was seen for the entire product spectrum. Note that the above reasoning only applies to the case of steady-state simulations where the initial solution fields deviate strongly from the final solution. In transient simulations, the results need to be time-accurate and hence tighter tolerances will be required in the network reduction stage.

5.4.2 Furnace simulation results

Figure 5-10 shows the simulated fields of flue gas temperature, fuel mass fraction and total gas absorption coefficient in the radiant section of the furnace. The combustion reactions are seen to start almost immediately, as all methane is consumed within the first few meters above the burners. This is a direct consequence of the burner recirculation channels that bring hot flue gas in contact with the fuel injected via the primary fuel jets, causing the fuel to preheat and ignite as soon as it encounters the air flow. Burners employing this kind of fuel staging allow operation at lower peak temperatures and greatly reduced NO_x emissions.

The hot flue gasses are drawn in from the center of the furnace, as visible in the velocity profiles along the furnace height in Figure 5-11. This recirculation pattern extends all the way from the bottom of the furnace up to a height of 9 m, with peak downward velocities up to 8.3 m/s at a height of 6 m. Towards the top of the furnace, higher velocities are seen at the right side of the furnace, as flue gas is drawn sideways into the stack.

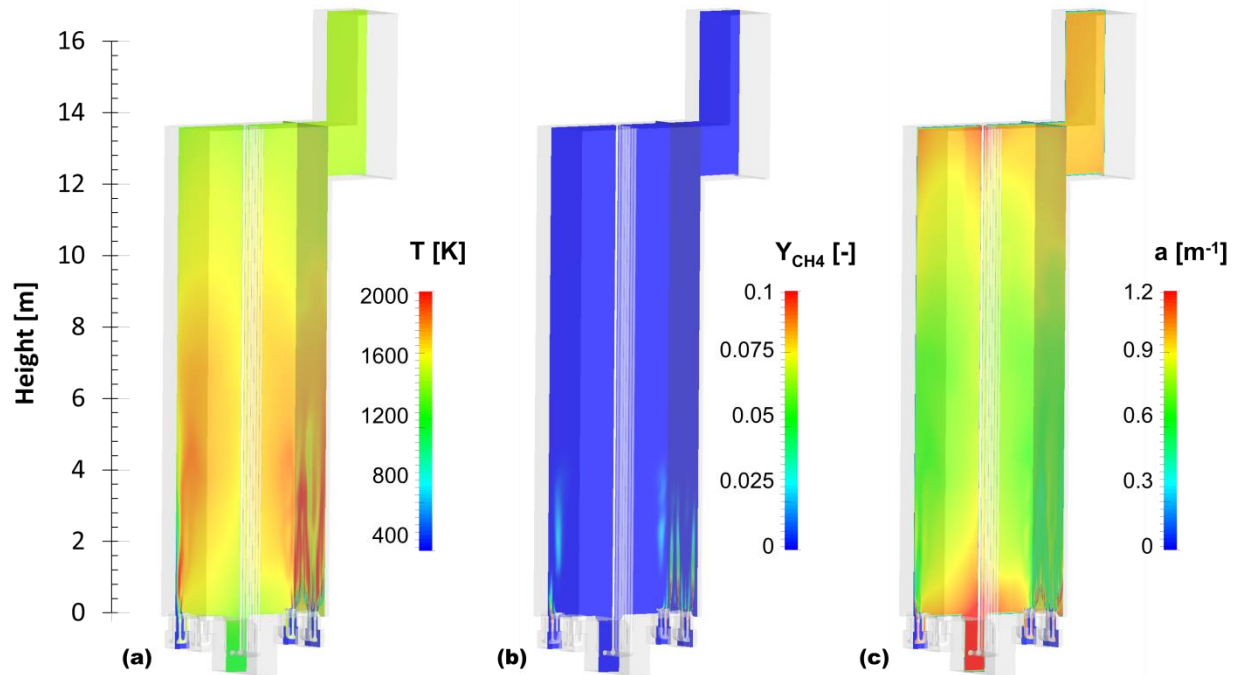


Figure 5-10: Fields of flue gas temperature, methane mass fraction and total gas absorption coefficient in the SRT-VI furnace.

Figure 5-12 shows the temperatures of the flue gas and the refractory wall along the furnace height. The flue gas temperature reaches a maximum at a height of approximately 4 m, and gradually decreases towards the stack as heat is transferred to the reactors. The refractory wall temperature profile is more uniform and varies only in a window of 89 K around its mean value of 1353 K, as the high surface emissivity leads to significant smoothing of the temperature field through predominantly radiative heat exchange with the flame and surrounding walls. A peak wall temperature within the firebox can be seen at a height of approximately 6.7 m. This corresponds to the position of flame attachment to the walls around this height, which is discerned in Figure 5-10(a). As the refractory wall is no longer surrounded by cooler air flow but in immediate contact with the hot flue gas, a significant increase in the convective heat transfer towards the refractory walls causes the occurrence of a local peak temperature on the refractory wall. Even higher refractory wall temperatures are observed at heights above 13.7 m, where the draft accelerates the flue gasses towards the convection section of the furnace. This acceleration

and increased turbulence enhances convective heat exchange with the wall, causing the bridge wall temperatures at these heights to be close to the flue gas temperatures.

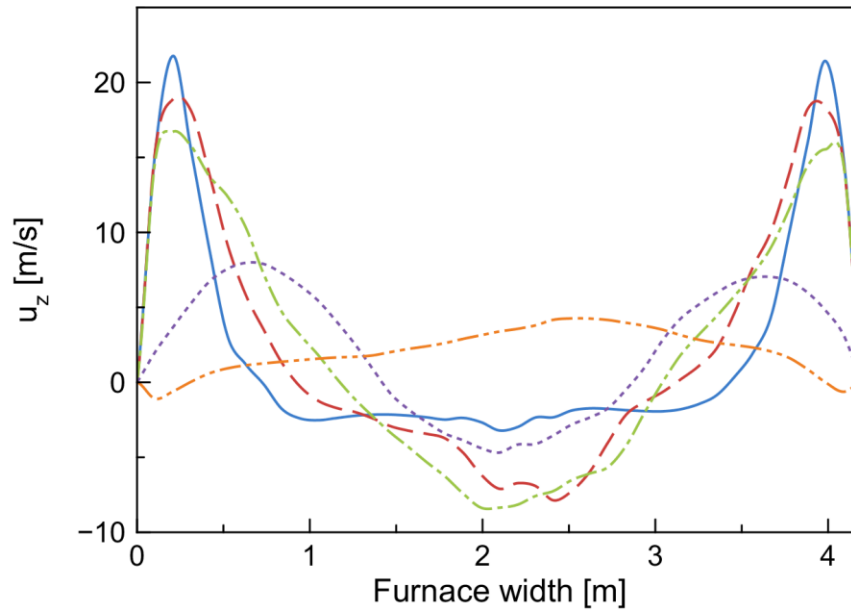


Figure 5-11: Area-averaged vertical velocity of the flue gas at furnace heights: — - 2 m; - - - 4 m; - . - 6 m; . . . 8 m; - - - - 10 m.

The absorption coefficient of the flue gas is depicted in Figure 5-10(c). This is calculated by summing the emissivities of the individual absorption bands to obtain the total absorption coefficient of the flue gas mixture based on Beer's law in Eqn. (5.7). The absorption coefficient is seen to be clearly negatively correlated with the flue gas temperature, as a higher absorption coefficient is seen towards the top of the furnace and in the center groove of the furnace where flue gas temperatures are lower. Low absorption coefficients are also seen near the fuel and air inlets, simply due to the absorbing species CO_2 and H_2O not yet being formed there.

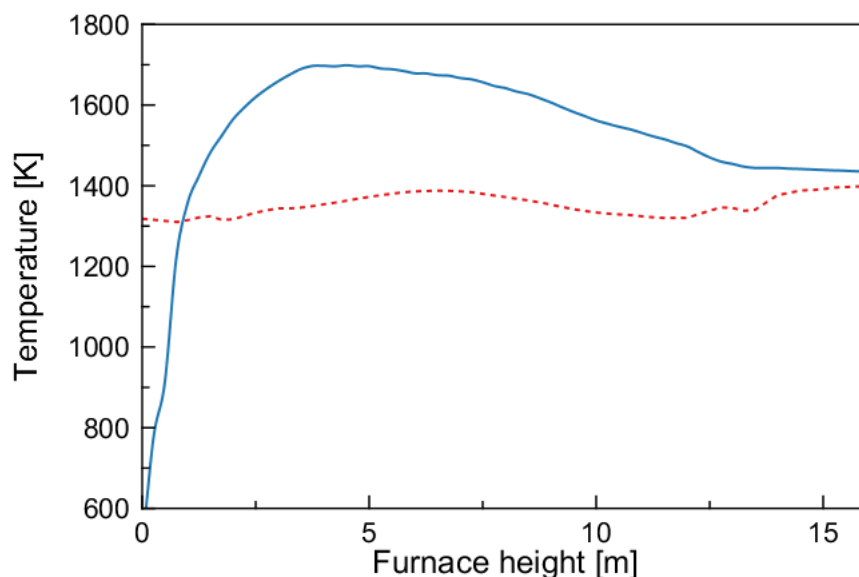


Figure 5-12: Mixing-cup weighted flue gas (full) and area-averaged refractory wall temperature (dashed) along the furnace height.

The influence of the gas absorption can also be clearly seen on the plot of incident radiation to the reactor per band, shown in Figure 5-13. Approximately 66.5% of the total radiation reaching the reactors is emitted in the uneven bands, being the spectral windows of the non-gray flue gas. As the flue gas is transparent in these bands, the majority of the radiation to the reactors originates directly from the refractory walls, with a minor contribution of radiation from reactor to reactor. When looking at the fraction of incident radiation in the even non-transparent bands and comparing them to the odd transparent bands, the seemingly intuitive but incorrect explanation for the lower fractions in the even bands would be that the gas absorbs part of the radiation. Rather, these bands are simply narrower and the theoretical cumulative amount of radiation emitted in these bands is by definition lower. In order to see the real impact of the flue gas on the fraction of incident radiation per bank, a comparison was made with a theoretical Planck black-body spectrum at the average refractory wall temperature of 1353 K, integrated over each of the bands and indicated in Figure 5-13 with the shaded bars. From this graph it can be seen that the relative contribution of radiation in the even gas absorption bands increases from the theoretical value of 25.3% to 33.5% by accounting for the flue gas absorption/emission. As the contributions in the spectral windows are unaffected, it can be concluded that direct flue gas

radiation yields a 12.3% increase in incident radiation towards the reactor walls. Another interesting observation is that seemingly a wrong value was used for the black-body temperature to calculate the theoretical distribution via Planck's law. This is especially visible when looking at the difference between the simulated and theoretically calculated fraction of incident radiation in the transparent bands 1 and 3. The relative difference between the power in bands 1 and 3 is expected to be the same for the simulation and the theoretical calculations using Planck's law if 1350 K was indeed the true "effective" radiation temperature. Using this criterion, an effective radiation temperature of 1259 K is obtained, which is, surprisingly, lower than both the refractory and flue gas temperature at any height in the furnace. However, this value is close to the average tube wall temperature, indicating that possibly a large fraction of the incident radiation on the reactor walls originates from neighboring tubes, causing the simulated incident radiation spectrum on the tubes to differ from the spectrum expected based on the radiation emitted by the refractory walls.

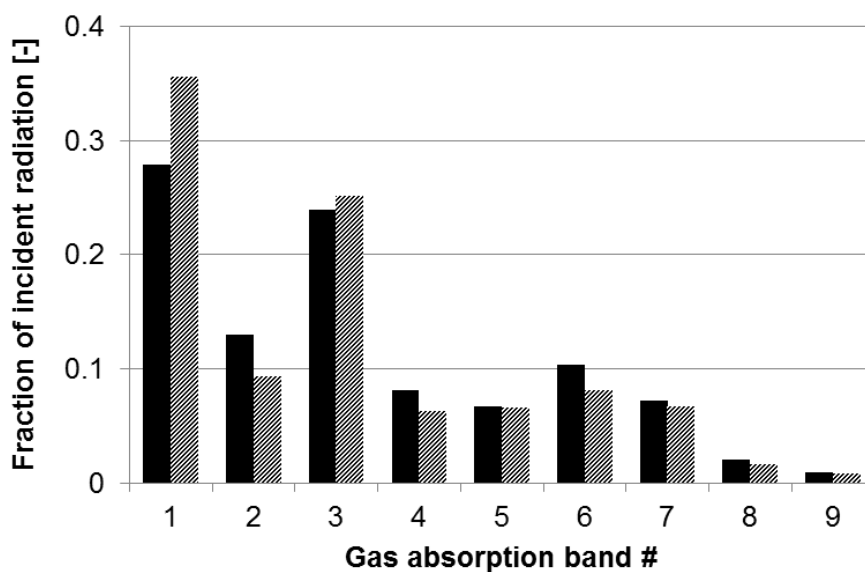


Figure 5-13: Wavelength distribution of incident radiation towards the reactors, integrated over the specified gas absorption bands, cf. Table 5-2. Black – present simulation, Shaded – theoretical Planck distribution at 1350 K.

The total incident radiative and convective heat flux averaged over all tubes is shown in Figure 5-14(a). Peak radiation at a reactor coordinate of 7.4 m and furnace height of 6.3 m corresponds closely to the position of peak refractory wall temperatures. The groove in the center of the furnace bottom is seen to be quite effective at protecting the manifold from excessive heat flux, as the incident radiative heat flux is roughly halved due to the shielding from direct radiation. While radiation is the primary heat transfer mechanism, the grid refinement around the reactor coils also allows an accurate description of flue gas convection. In the current simulation, convection amounts to between 13.7% and 16.6% of the net heat input to the process gas. Its peak flux is seen to be approximately 1 m higher up in the furnace than the radiative peak. This correlates with the downward flow of hot flue gasses which was shown to commence at a height of 9 m in Figure 5-11.

Differences between the different coils are shown in Figure 5-14(b). A clear effect of the staggered configuration of the two reactors can be seen: the side closer to the refractory walls expectedly receives higher fluxes. A view from the opposing side would show the inverse picture, leading to minor differences in total heat received, both within the strand of tubes and between the two reactors. Inlet legs 6-10 of the reactor with the shorter manifold receive 1% lower incident radiation, but this is compensated in the corresponding outlet legs, leading to a total deviation in transferred thermal power to the two reactors of only 0.3%. The largest differences within a set of coils can be seen for the outer legs, as leg 1 and 10 both receive 3% higher radiative flux than the average inlet, which is due to these clearly being the least shielded from radiation by surrounding tubes. As the flue gas flow is rather uniform over the different tubes independent of their position, the contribution of convection is similar for all the tubes. Only the outlet legs 11 and 12 are receiving less convective heat due to their higher tube metal temperatures and hence reduced temperature difference with the surrounding flue gas.

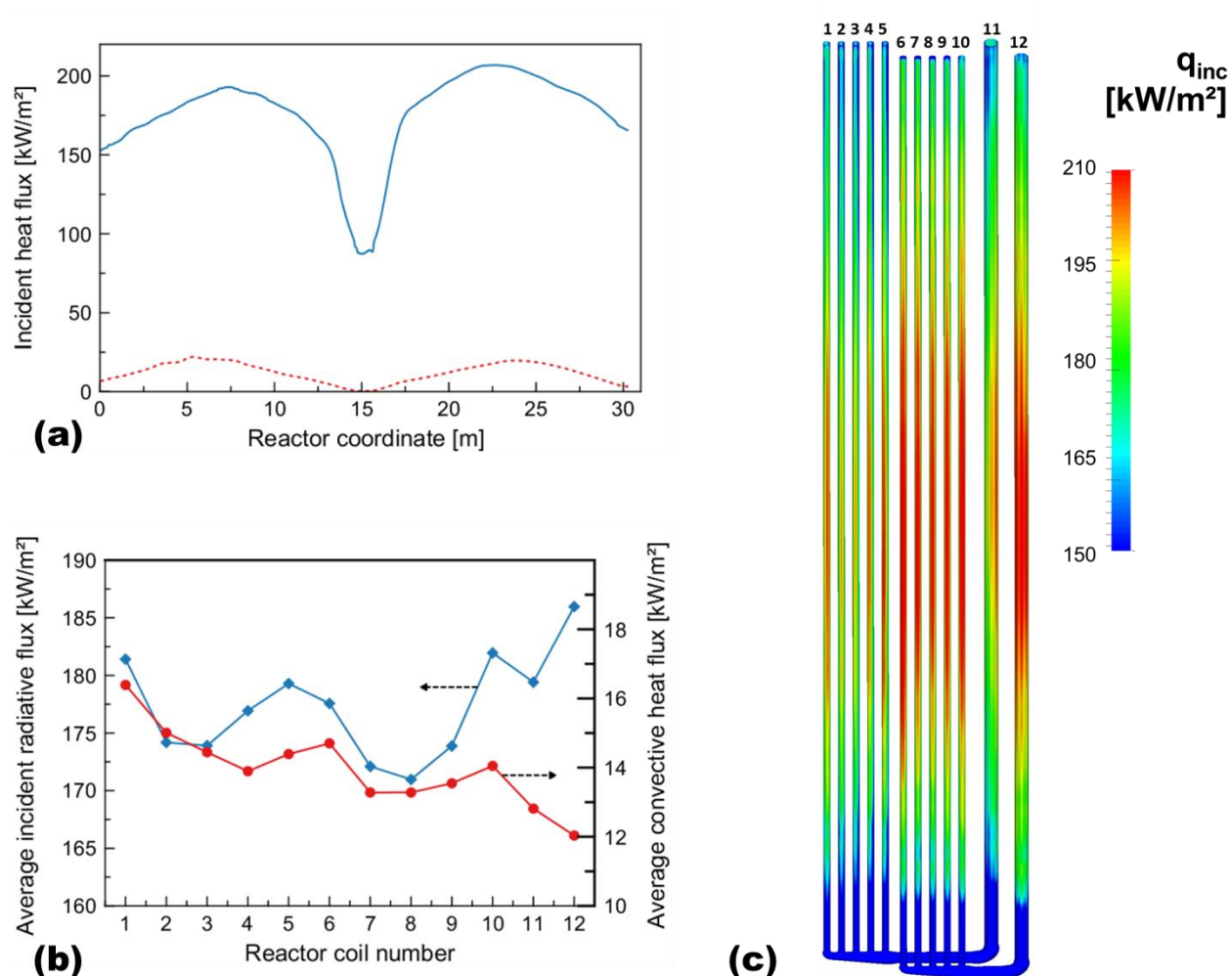


Figure 5-14: (a) Distribution of incident radiative (full) and convective (dashed) heat flux, along the reactor length, averaged over all legs. (b) Averaged heat flux towards each of the reactor legs, with 1-5&11 comprising the first reactor and 6-10&12 the second. (c) Contour plot of incident radiative flux on the outer reactor walls.

As the furnaces are the main energy consumers in an ethene production plant, their thermal efficiency becomes an important parameter. Including the heat recovery in the transfer line exchanger and convection sections, new plants can be designed to have a 93-95% energy efficiency⁵⁰. The thermal efficiency of the radiant section itself can be calculated as the ratio of the heat transferred to the reactors to the total heat released by combustion, where typical values range from 38-42% for side wall firing and 42-47% for floor firing. In the present simulation, a thermal efficiency of 37.7% was obtained, which is too low compared to what is commonly

observed in industry. Correspondingly, the simulated bridge wall temperature was overpredicted at 1453 K, compared to the industrially measured value of 1359 K, a difference of 94 K. Assuming all of this excess flue gas energy would be transferred to the reactors, a thermal efficiency of 43.4% would be obtained, which is in line with the design specifications of the furnace.

A number of possible causes for the low simulated thermal efficiency can be identified. First, the implemented two-step combustion mechanism combined with EDM turbulence-chemistry coupling is a relatively simplistic approach, even for a pure methane fuel. Ideally, a more detailed combustion reaction network is included and combined with a more accurate method to account for turbulence-chemistry interaction, for example through using the Eddy-Dissipation Concept⁴⁰, a PDF method⁶⁷ or laminar flamelet model⁶⁸. This would allow to account for the small amounts of hydrogen and ethene in the fuel, which can significantly impact the flame shape, heat release profile and emissivity^{69, 70}. With a better prediction of the flame ignition and spreading, the temperature profile of the refractory walls may differ, possibly resulting in higher radiative fluxes to the reactors.

Second, the formation of soot and the accompanying effect of soot radiation on the total emitted power requires further examination. While methane is not prone to soot formation during combustion at lab-scale conditions, it can soot quite heavily during combustion in industrial-scale burners where larger regions of high temperature and fuel-rich conditions coexist⁷¹. Although the formed soot is quickly oxidized as it exits this high-temperature fuel-rich region and hence does not require consideration as a pollutant leaving the furnace stack, the local soot formation still has an important impact on the heat release profile of the flame. As the industrial fuel also contains soot precursors such as ethene and C4-C6 components, the effect of soot in an industrial furnace can be considerable.

Third, although the simulated burner design contains as much detail as possible in terms of primary and secondary fuel inlets and burner tip drillings, some unknowns remained, such as the presence of additional flame stabilizing structures and the distribution of fuel over the different burner tips. Some assumptions still had to be made and one of the potential implications could be

that the layer of colder air in contact with the refractory walls below the flame attachment point at a height of 6.7 m is in fact a simulation artifact that does not correspond to reality. The impact of such a small deviation might seem minor but it significantly affects the simulated refractory wall temperatures and consequently the simulated radiation emitted at the lower part of the furnace.

5.4.3 Reactor simulation results

Simulations were performed for two different reactor configurations differing in the geometry of the second pass of the reactor: in the base case, this was a bare cylindrical coil while in the second case the bare tube was replaced by a helically ribbed coil (MERT). In order to assess the true impact of the reactor design, the simulation conditions should match the industrial conditions as closely as possible. This was far from straightforward due to the aforementioned discrepancy between the simulated and the industrially observed furnace thermal efficiency. Therefore, not the full coupling procedure between furnace and reactor described in section 5.3.4 was employed, as the resulting heat fluxes to the reactors would be considerably too low to reach the industrial design severity, i.e. a propene-to-ethene mass ratio (P/E) of 0.705. Instead, the incident radiation profiles given by the furnace simulation were scaled up to obtain the targeted cracking severity. The required scaling factor was 1.19 and 1.166 for respectively the bare reactor and the ribbed reactor. As previously shown by Colannino⁷², a linear relationship exists between the total heat release and the incident radiative heat flux, where the shape of the incident radiative heat flux profile is preserved under changing total heat release. The use of a uniform scaling factor for the entire field is hence considered to be acceptable, certainly in the context of comparing the two types of reactor.

Figure 5-15 shows the resulting process gas pressure and temperature along the reactor length. The influence of the modified coil geometry in the outlet leg is clearly visible from the pressure drop in the second pass, being 2.91 times higher than for the bare reactor coil. The pressure drop over the manifold section is seen to be significant, as it accounts for over 25% of the total pressure drop for the bare reactor.

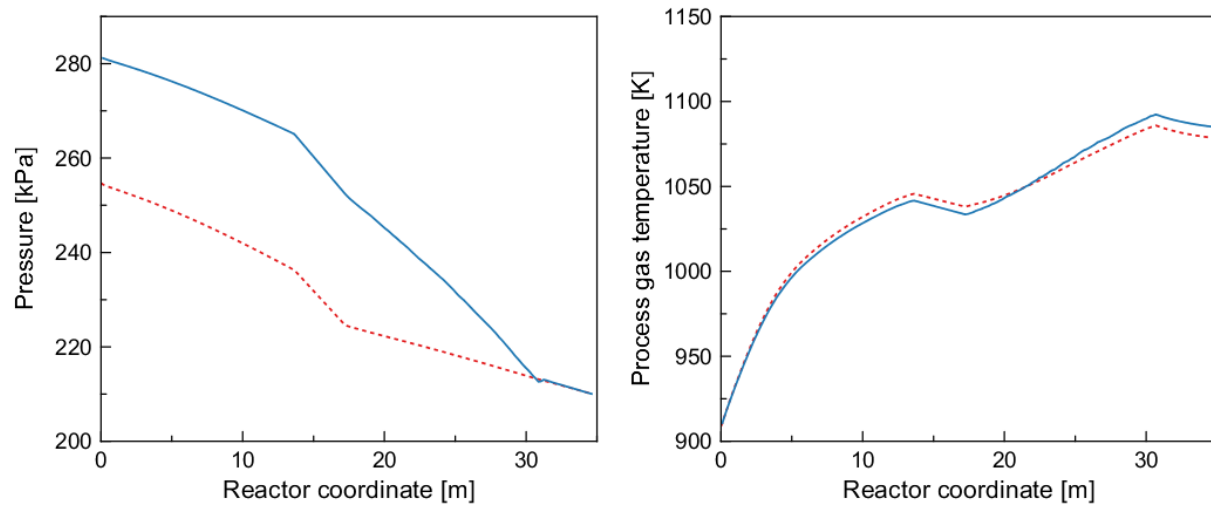


Figure 5-15: Mixing-cup averaged process gas pressure (left) and temperature (right) along the reactor axial coordinate for the bare reactor (red dashed line) and the ribbed reactor (blue full line).

A small but noticeable difference in the process gas temperature can be seen between the two designs. While the shape of the incident radiative heat flux profile imposed in both reactor simulations is identical, the modified geometry in the outlet leg of the ribbed reactor clearly causes a larger total heat flux to the process gas in the ribbed reactor compared to the bare reactor. This can easily be understood from the main rationale behind the use of surface enhancements, namely reducing the TMT. These are plotted in Figure 5-16, along with the net heat flux to the process gas. The ribbed tube clearly succeeds at increasing the convective heat transfer towards the process gas, as the maximum TMT is 44 K lower compared to the bare reactor. According to the Stefan-Boltzmann law, this reduces the radiation emitted by the tube itself. A greater fraction of the incident radiative flux towards the outlet leg will hence be absorbed by the process gas, leading to a net heat flux that is 11.9% higher than that for the bare reactor outlet. In order to operate at the same cracking severity, the furnace firing rate needs to be reduced. This explains the difference of 2% in the flux scaling factor and the lower temperature in the inlet part of the reactor with the helically ribbed outlet.

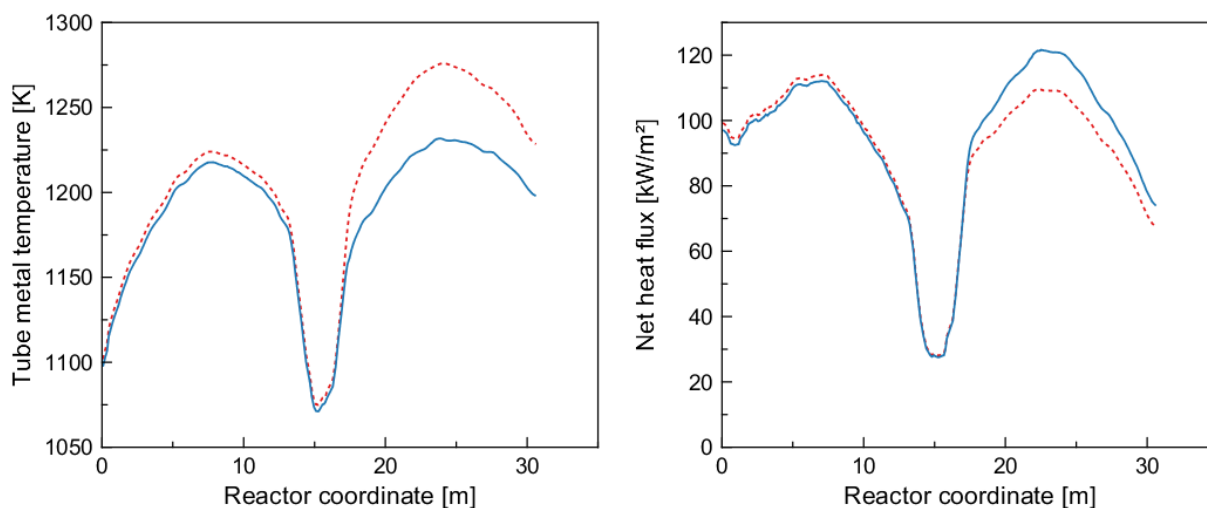


Figure 5-16: Azimuthally averaged external tube metal temperature (left) and net heat flux through the reactor wall (right) along the reactor axial coordinate for the bare reactor (red dashed line) and the ribbed reactor (blue full line).

A corresponding shift can be seen for the olefin mass fraction profiles in Figure 5-17, as the bare reactor initially has a higher olefin yield. However, this is compensated in the outlet leg since the ribbed reactor operates at higher process gas temperatures in the second pass. Both designs are seen to operate past the peak of propene yield and close to the point of maximum total olefin yield (P+E).

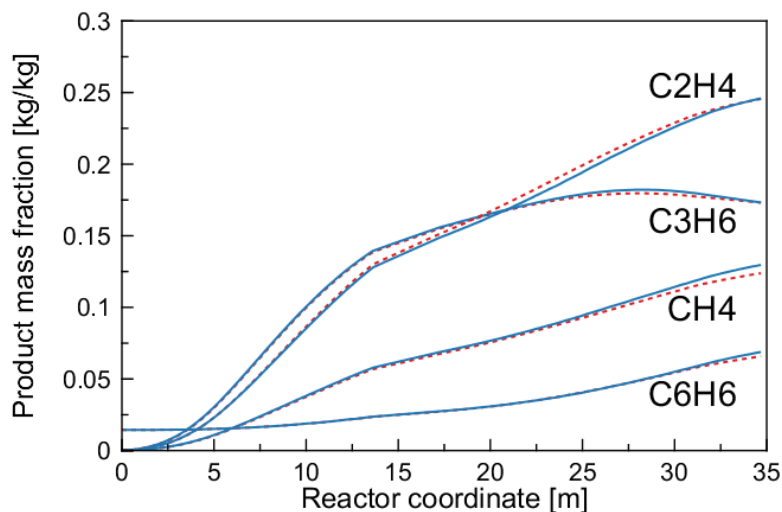


Figure 5-17: Mixing-cup averaged ethene, propene, methane and benzene yields along the reactor axial coordinate for the bare reactor (red dashed line) and the ribbed reactor (blue full line).

Product yields of the most important components are listed in Table 5-5 and compared to the composition analysis of the industrial cracked gas. The differences between the two designs are remarkably small, especially with respect to olefin yields. The higher coil outlet temperature for the ribbed reactor results mostly in an increased feedstock conversion and corresponding production of methane and aromatics such as benzene, toluene and naphthalene. Good agreement with the industrial data is obtained. The most striking difference is the relatively high fractions of unconverted iso-paraffins in the industrial effluent, while the model predicts almost total conversion of these components because of their increased susceptibility to hydrogen abstractions compared to n-paraffins. The root cause might be the lumping procedure that was employed to reproduce the chemical reactivity of isomer mixtures. Additional uncertainty arises from the feedstock composition as in the simulation an “average” naphtha composition was used that does not correspond exactly to the industrial naphtha of that specific time.

using adaptive detailed chemistry methods

Table 5-5: Start-of-run reactor conditions and product yields for the bare and the ribbed reactor and comparison with industrially measured data.

	Industrial Bare	Bare	Ribbed	$\Delta Y_{\text{Ribbed-Bare}}$ [rel. %]	
				1D	3D
Coil outlet temperature [K]	1075.9	1078.6	1085.1		
Pressure drop [kPa]	~50	44.71	71.26		
TMT _{max} [K]	~1273	1276	1232		
<i>Yields [wt %]</i>					
H ₂	0.82	0.82	0.81	~	-1
CH ₄	14.55	12.38	12.97	+3	+5
C ₂ H ₂	0.21	0.28	0.30	~	+8
C ₂ H ₄	23.25	24.56	24.60	~	~
C ₂ H ₆	4.86	3.99	4.08	+3	+2
m-Acetylene		0.22	0.23	~	+3
Propadiene	0.17	0.51	0.53	~	+3
C ₃ H ₆	17.15	17.31	17.32	~	~
C ₃ H ₈	0.58	0.59	0.59	-6	-1
1,3-Butadiene	4.10	4.33	4.30	+1	-1
1-Butene	1.63	1.96	1.83	-6	-6
2-Butene	1.21	0.68	0.67	-3	-1
i-Butene	3.18	3.39	3.37	-2	~
i-Butane	0.17	0.18	0.18	-7	-2
n-Butane	0.62	0.77	0.73	-10	-6

cyc-Pentadiene	2.23	2.16	2.16	-1	~
1,3-Pentadiene	0.53	0.63	0.63	-3	~
cyc-Pentene	0.22	0.28	0.27	-3	-4
Isoprene	0.85	0.60	0.61	-1	+2
1- & 2-Pentenenes		0.55	0.48	-9	-14
m-Butenes		0.51	0.49	-6	-4
m-Cyclopentadiene		1.28	1.26	-3	-2
m-Cyclohexadiene		1.02	1.02	-3	~
i-Pentane	0.94	1.13	1.00	-9	-11
n-Pentane		1.75	1.57	-10	-11
i-C ₆ H ₁₄	1.80	0.45	0.34	-11	-24
i-C ₇ H ₁₆	1.02	0.22	0.15	-14	-32
i-C ₈ H ₁₈	0.65	0.04	0.02	-17	-39
Benzene	7.57	6.59	6.89	~	+5
Toluene	2.84	2.65	2.79	+2	+5
Xylenes	0.84	0.79	0.81	+1	+3
e-Benzene	0.23	0.19	0.19	+2	-2
Cumene		0.93	0.93	-7	-1
Naphthalene		1.14	1.20	+10	+5
Styrene	0.78	0.70	0.69	+7	-1

Since the differences in yields between the two designs are relatively small, and smaller than anticipated, the benefits of performing extensive 3D simulations may appear to not outweigh the high computational cost for these simulations. However, it is important to note that the

conclusions drawn based on the simulations in this work, could not have been obtained by any other means. To justify this claim, the heat flux and pressure profiles obtained from the 3D simulations for both cases were imposed as operating conditions in corresponding 1D simulations. The influence of higher hydrocarbon partial pressure and hence more secondary bimolecular reactions, is expected to cause reduced olefin yield in the design with the greater pressure drop, being the ribbed reactor. This effect can be seen in the deltas between the two geometries when accounting only for the pressure effect in 1D as given in Table 5-5: olefin yields drop by 0.3 rel.%.

When accounting for radial gradients in full 3D simulations, the opposite is observed: the total olefin yield increases slightly. The effects for the presently studied naphtha cracker are less decisive than those previously observed when cracking propane^{36, 37}. The most probable explanation is the longer residence time of the process gas in the naphtha cracking reactor, amounting to approximately 0.32 s compared to 0.13 s in the aforementioned Millisecond propane cracker. Because of the longer residence time, the higher average pressure in the first 20 m of the reactor impact the final yield distribution to a lesser extent, as the process gas has sufficient time to return closer towards “equilibrium” composition when passing through the adiabatic section, where pressures are identical. The effects induced by the radial gradients are also less severe since the process gas temperature and furnace firing rate are generally lower in naphtha cracking, resulting in smaller radial temperature and concentration gradients³⁵.

Though yield gains are not to be expected from enhanced reactor designs, the main motivation for their use remains the potential for extended run lengths. On top of the simulated 44 K reduction in TMT, the reduced resistance to convective heat transfer also lowers the temperature at the process gas interface where coke is formed. As during a run, coke is predominantly formed through the heterogeneous non-catalytic mechanism⁷³, temperature significantly influences the rate of coke deposition. In this manner the improved heat transfer results in reduced coking rates and hence longer run lengths. This was demonstrated in the present work by applying the semi-empirical coking model of Reyniers⁷⁴, developed specifically for heavy feedstocks by accounting for 12 important coke precursors: acetylene, propadiene, ethylene, propylene, 1-butene, iso-

butene, 1,3-butadiene, 1,3-cyclopentadiene, benzene, toluene, xylene and styrene. Figure 5-18 shows the resulting coking rate at start-of-run conditions along the length of the reactor for both designs.

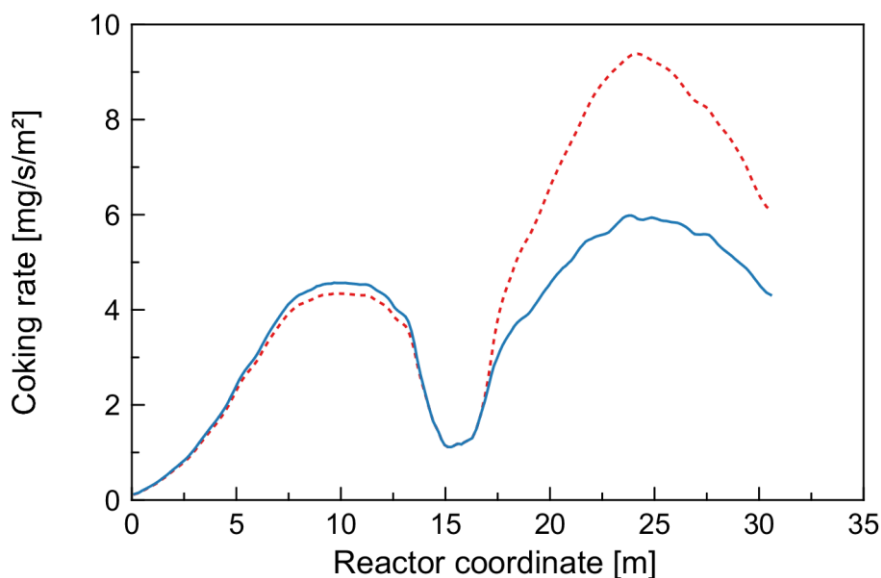


Figure 5-18: Azimuthally averaged coking rate on the reactor internal surface along the reactor axial coordinate for the bare reactor (red dashed line) and the ribbed reactor (blue full line).

The improved heat transfer and the resulting lower temperatures in the outlet leg of the ribbed reactor is seen to reduce the maximum coking rate by as much as 36%. Assuming this improvement is preserved during the complete run, the run length could be extended by an impressive 56%, disregarding the run length extension that could be obtained if the reactor run length is limited by the tube metal temperature. Interestingly, the 6 K lower gas-wall interface temperature in the inlet leg of the enhanced 3D reactor does not result in decreased coking rates. This is explained by the higher pressures in this section of the reactor, causing higher precursor concentrations, offsetting the beneficial effect of a lower temperature. It is important to note that the applied coking model is first order in the species concentrations and hence scales linearly with pressure. This is still a point of controversy, as coking models with up to a third order pressure dependence have been developed^{74, 75}, which would imply that the ribbed design leads to considerably increased coke formation in the inlet legs. Though the inlet legs are less likely to

reach TMT limitations, the smaller diameter of these tubes does make them more vulnerable to clogging of the cross section by coke, requiring immediate decoking. It is hence not entirely unlikely that the reactor as a whole may become pressure limited rather than TMT limited, which would result in only a minor increase in run length. Particularly when also considering the aforementioned intra-coil redistribution of the net heat flux to the process gas, it is seen that applying surface enhancements to only part of a reactor can have unexpected and undesired consequences. Computational fluid dynamics can therefore serve as a valuable tool to assess the effects already in the design phase, before the final investment is made.

5.5 Conclusions

A new chemistry library was implemented in OpenFOAM allowing dynamic chemistry reduction and in-situ adaptive tabulation to be combined with on-the-fly application of the pseudo-steady state approximation. Validation on a two-dimensional test case for propane steam cracking illustrated speedups factors of over 200, as the three methods exhibit significant synergies.

This allowed the proposed library to be applied to the simulation of a full industrial naphtha cracker, where both the fire-side and reactor side were described in 3D using OpenFOAM. In the furnace the discrete ordinates method combined with a EWBM for the flue gas radiative properties allowed a detailed evaluation of the heat fluxes towards the reactors. Radiative heat transfer accounts for 83-86% of the total heat flux towards the reactor, with the refractory walls being the primary source of radiation towards the reactor coils. While the flue gas plays an important role in convective heat transfer to the walls and reactors, it also has a considerable *direct* radiative contribution, amounting to about 12% of the total radiative heat flux to the reactors.

Two-way coupling between the fire-side and the reactor side was achieved through spatial interpolation between the different cases. Rather than simply exchanging tube wall temperature and total heat flux profiles, a coupling procedure including the process gas temperature and incident radiative flux profiles resulted in significantly faster convergence.

On the reactor side, a free radical naphtha cracking network consisting of 152 species, 856 reversible elementary reactions and 1138 lumped reactions was applied. Thanks to this previously unattainable level of detail in the kinetics, a quantitative comparison could be made between a standard reactor geometry and one with a helically ribbed outlet leg. In contrast to previous studies on 3D reactor geometries using lighter feedstocks, no loss of olefin selectivity was observed for the enhanced geometry. Despite the 2.9 times higher pressure drop over the ribbed reactor, olefin yields were in fact 0.2 rel.% higher than for the bare reactor. The minor influence of enhancing both pressure and radial mixing can be explained by the longer residence time and lower peak temperatures of naphtha crackers compared to crackers that operate with lighter feedstocks such as propane. The improved convective heat transfer induced by the helical ribs did succeed in reducing the maximum tube metal temperature in the outlet leg by 44 K, along with a 36 % reduction in the rate of coke formation at start-of-run conditions. These kind of reactor enhancements can hence be expected to significantly extend run lengths and coil lifetime expectancies, with computational fluid dynamics serving as a valuable and indispensable tool for making such evaluations.

References

1. Vinu, R. and L.J. Broadbelt, *Unraveling Reaction Pathways and Specifying Reaction Kinetics for Complex Systems*, in *Annual Review of Chemical and Biomolecular Engineering, Vol 3*, J.M. Prausnitz, Editor 2012. p. 29-54.
2. Ranzi, E., T. Faravelli, P. Gaffuri, and A. Sogaro, *Low-temperature combustion: Automatic generation of primary oxidation reactions and lumping procedures*. Combustion and Flame, 1995. **102**(1-2): p. 179-192.
3. Côme, G.M., V. Warth, P.A. Glaude, R. Fournet, F. Battin-Leclerc, and G. Scacchi, *Computer-aided design of gas-phase oxidation mechanisms—Application to the modeling of n-heptane and iso-octane oxidation*. Symposium (International) on Combustion, 1996. **26**(1): p. 755-762.
4. Broadbelt, L.J., S.M. Stark, and M.T. Klein, *Computer-generated pyrolysis modeling - On the fly generation of species, reactions and rates*. Industrial & Engineering Chemistry Research, 1994. **33**(4): p. 790-799.
5. Vandewiele, N.M., K.M. Van Geem, M.F. Reyniers, and G.B. Marin, *Genesys: Kinetic model construction using chemo-informatics*. Chemical Engineering Journal, 2012. **207**: p. 526-538.
6. Blurock, E.S., *Detailed mechanism generation. 1. Generalized reactive properties as reaction class substructures*. Journal of Chemical Information and Computer Sciences, 2004. **44**(4): p. 1336-1347.
7. Blurock, E.S., *Detailed mechanism generation. 2. Aldehydes, ketones, and olefins*. Journal of Chemical Information and Computer Sciences, 2004. **44**(4): p. 1348-1357.
8. Rangarajan, S., A. Bhan, and P. Daoutidis, *Language-oriented rule-based reaction network generation and analysis: Description of RING*. Computers & Chemical Engineering, 2012. **45**: p. 114-123.
9. Rangarajan, S., A. Bhan, and P. Daoutidis, *Language-oriented rule-based reaction network generation and analysis: Applications of RING*. Computers & Chemical Engineering, 2012. **46**: p. 141-152.
10. Van de Vijver, R., N.M. Vandewiele, P.L. Bhoorasingh, B.L. Slakman, F. Seyedzadeh Khanshan, H.-H. Carstensen, M.-F. Reyniers, G.B. Marin, R.H. West, and K.M. Van Geem, *Automatic Mechanism and Kinetic Model Generation for Gas- and Solution-Phase Processes: A Perspective on Best Practices, Recent Advances, and Future Challenges*. International Journal of Chemical Kinetics, 2015. **47**(4): p. 199-231.
11. William H. Green, J.W.A., Beat A. Buesser, Robert W. Ashcraft, Gregory J. Beran, Caleb A. Class, Connie Gao, C. Franklin Goldsmith, Michael R. Harper, Amrit Jalan, Murat Keceli, Gregory R. Magoon, David M. Matheu, Shamel S. Merchant, Jeffrey D. Mo, Sarah Petway, Sumathy Raman, Sandeep Sharma, Jing Song, Yury Suleymanov, Kevin M. Van Geem, John

- Wen, Richard H. West, Andrew Wong, Hsi-Wu Wong, Paul E. Yelvington, Nathan Yee, Joanna Yu, *RMG - Reaction Mechanism Generator v4.0.1*, 2013.
12. Herbinet, O., W.J. Pitz, and C.K. Westbrook, *Detailed chemical kinetic oxidation mechanism for a biodiesel surrogate*. Combustion and Flame, 2008. **154**(3): p. 507-528.
 13. Glaude, P.A., O. Herbinet, S. Bax, J. Biet, V. Warth, and F. Battin-Leclerc, *Modeling of the oxidation of methyl esters-Validation for methyl hexanoate, methyl heptanoate, and methyl decanoate in a jet-stirred reactor*. Combustion and Flame, 2010. **157**(11): p. 2035-2050.
 14. Van Geem, K.M., M.F. Reyniers, and G.B. Marin, *Challenges of modeling steam cracking of heavy feedstocks*. Oil & Gas Science and Technology-Revue De L Institut Francais Du Petrole, 2008. **63**(1): p. 79-94.
 15. van Goethem, M.W.M., F.I. Kleinendorst, C. van Leeuwen, and N. van Velzen, *Equation-based SPYRO® model and solver for the simulation of the steam cracking process*. Computers & Chemical Engineering, 2001. **25**(4-6): p. 905-911.
 16. Lu, T.F. and C.K. Law, *Toward accommodating realistic fuel chemistry in large-scale computations*. Progress in Energy and Combustion Science, 2009. **35**(2): p. 192-215.
 17. Lu, T. and C.K. Law, *A directed relation graph method for mechanism reduction*. Proceedings of the Combustion Institute, 2005. **30**(1): p. 1333-1341.
 18. Vajda, S., P. Valko, and T. Turányi, *Principal component analysis of kinetic models*. International Journal of Chemical Kinetics, 1985. **17**(1): p. 55-81.
 19. Elliott, L., D.B. Ingham, A.G. Kyne, N.S. Mera, M. Pourkashanian, and C.W. Wilson, *Reaction Mechanism Reduction and Optimization Using Genetic Algorithms*. Industrial & Engineering Chemistry Research, 2005. **44**(4): p. 658-667.
 20. Bhattacharjee, B., D.A. Schwer, P.I. Barton, and W.H. Green, *Optimally-reduced kinetic models: reaction elimination in large-scale kinetic mechanisms*. Combustion and Flame, 2003. **135**(3): p. 191-208.
 21. Oluwole, O.O., P.I. Barton, and W.H. Green, *Obtaining accurate solutions using reduced chemical kinetic models: a new model reduction method for models rigorously validated over ranges*. Combustion Theory and Modelling, 2007. **11**(1): p. 127-146.
 22. Ranzi, E., M. Dente, A. Goldaniga, G. Bozzano, and T. Faravelli, *Lumping procedures in detailed kinetic modeling of gasification, pyrolysis, partial oxidation and combustion of hydrocarbon mixtures*. Progress in Energy and Combustion Science, 2001. **27**(1): p. 99-139.
 23. Lu, T. and C.K. Law, *Diffusion coefficient reduction through species bundling*. Combustion and Flame, 2007. **148**(3): p. 117-126.
 24. Maas, U. and S.B. Pope, *Simplifying chemical kinetics: Intrinsic low-dimensional manifolds in composition space*. Combustion and Flame, 1992. **88**(3): p. 239-264.

25. Lam, S.H. and D.A. Goussis, *The CSP method for simplifying kinetics*. International Journal of Chemical Kinetics, 1994. **26**(4): p. 461-486.
26. Pope, S.B., *Computationally efficient implementation of combustion chemistry using in situ adaptive tabulation*. Combustion Theory and Modelling, 1997. **1**(1): p. 41-63.
27. Tonse, S.R., N.W. Moriarty, N.J. Brown, and M. Frenklach, *PRISM: Piecewise reusable implementation of solution mapping. an economical strategy for chemical kinetics*. Israel Journal of Chemistry, 1999. **39**(1): p. 97-106.
28. Liang, L., J.G. Stevens, and J.T. Farrell, *A dynamic adaptive chemistry scheme for reactive flow computations*. Proceedings of the Combustion Institute, 2009. **32**(1): p. 527-534.
29. Tosatto, L., B.A.V. Bennett, and M.D. Smooke, *A transport-flux-based directed relation graph method for the spatially inhomogeneous instantaneous reduction of chemical kinetic mechanisms*. Combustion and Flame, 2011. **158**(5): p. 820-835.
30. He, K., I.P. Androulakis, and M.G. Ierapetritou, *On-the-fly reduction of kinetic mechanisms using element flux analysis*. Chemical Engineering Science, 2010. **65**(3): p. 1173-1184.
31. Sun, W., Z. Chen, X. Gou, and Y. Ju, *A path flux analysis method for the reduction of detailed chemical kinetic mechanisms*. Combustion and Flame, 2010. **157**(7): p. 1298-1307.
32. Tang, Q. and S.B. Pope, *Implementation of combustion chemistry by in situ adaptive tabulation of rate-controlled constrained equilibrium manifolds*. Proceedings of the Combustion Institute, 2002. **29**(1): p. 1411-1417.
33. Contino, F., H. Jeanmart, T. Lucchini, and G. D'Errico, *Coupling of in situ adaptive tabulation and dynamic adaptive chemistry: An effective method for solving combustion in engine simulations*. Proceedings of the Combustion Institute, 2011. **33**(2): p. 3057-3064.
34. Ren, Z., S.B. Pope, A. Vladimirov, and J.M. Guckenheimer, *Application of the ICE-PIC method for the dimension reduction of chemical kinetics coupled with transport*. Proceedings of the Combustion Institute, 2007. **31**(1): p. 473-481.
35. Van Geem, K.M., G.J. Heynderickx, and G.B. Marin, *Effect of radial temperature profiles on yields in steam cracking*. AIChE Journal, 2004. **50**(1): p. 173-183.
36. Van Cauwenberge, D.J., L.A. Vandewalle, P.A. Reyniers, K.M. Van Geem, G.B. Marin, and J. Floré, *Periodic reactive flow simulation: Proof of concept for steam cracking coils*. AIChE Journal, 2017. **63**(5): p. 1715-1726.
37. Schietekat, C.M., D.J. Van Cauwenberge, K.M. Van Geem, and G.B. Marin, *Computational fluid dynamics-based design of finned steam cracking reactors*. AIChE Journal, 2013. **60**(2): p. 794-808.
38. Westbrook, C.K. and F.L. Dryer, *Simplified reaction mechanisms for the oxidation of hydrocarbon fuels in flames*. Combustion science and technology, 1981. **27**(1-2): p. 31-43.

39. Spalding, D.B., *Mixing and chemical reaction in steady confined turbulent flames*. Symposium (International) on Combustion, 1971. **13**(1): p. 649-657.
40. Magnussen, B.F. and B.H. Hjertager, *On mathematical modeling of turbulent combustion with special emphasis on soot formation and combustion*. Symposium (International) on Combustion, 1977. **16**(1): p. 719-729.
41. Yeoh, G.H. and K.K. Yuen, *Computational Fluid Dynamics in Fire Engineering - Theory, Modelling and Practice*. 2009, Burlington: Butterworth-Heinemann.
42. Stefanidis, G.D., B. Merci, G.J. Heynderickx, and G.B. Marin, *Gray/nongray gas radiation modeling in steam cracker CFD calculations*. AIChE Journal, 2007. **53**(7): p. 1658-1669.
43. Chandrasekhar, S., *Radiative transfer*. 1950, London: Oxford University Press.
44. Carlson, B.G. and K.D. Lathrop, *Transport theory: the method of discrete ordinates*. 1965: Los Alamos Scientific Laboratory of the University of California.
45. Edwards, D. and W. Menard, *Comparison of models for correlation of total band absorption*. Applied Optics, 1964. **3**(5): p. 621-625.
46. Stefanidis, G., B. Merci, G. Heynderickx, and G. Marin, *Gray/nongray gas radiation modeling in steam cracker CFD calculations*. AIChE journal, 2007. **53**(7): p. 1658-1669.
47. Zhang, Y., F. Qian, C.M. Schietekat, K.M. Van Geem, and G.B. Marin, *Impact of flue gas radiative properties and burner geometry in furnace simulations*. AIChE Journal, 2015. **61**(3): p. 936-954.
48. Soufiani, A. and J. Taine, *High temperature gas radiative property parameters of statistical narrow-band model for H₂O, CO₂ and CO, and correlated-K model for H₂O and CO₂*. International journal of heat and mass transfer, 1997. **40**(4): p. 987-991.
49. Leckner, B., *Spectral and total emissivity of water vapor and carbon dioxide*. Combustion and Flame, 1972. **19**(1): p. 33-48.
50. Zimmermann, H. and R. Walzl, *Ethylene*, in *Ullmann's Encyclopedia of Industrial Chemistry*, 2000, Wiley-VCH Verlag GmbH & Co. KGaA. p. 469-493.
51. Jayatilke, C.L.V., *The influence of Prandtl number and surface roughness on the resistance of the laminar sub-layer to momentum and heat transfer*. 1966: University of London.
52. Pope, S.B., *An explanation of the turbulent round-jet/plane-jet anomaly*. AIAA Journal, 1978. **16**(3): p. 279-281.
53. Jasak, H., H.G. Weller, and A.D. Gosman, *High resolution NVD differencing scheme for arbitrarily unstructured meshes*. International Journal for Numerical Methods in Fluids, 1999. **31**(2): p. 431-449.
54. Bird, R.B., W.E. Stewart, and E.N. Lightfoot, *Transport Phenomena*. 2006, New York: Wiley.

55. Torigoe, T., K. Hamada, M. Furuta, M. Sakashita, K. Otsubo, and M. Tomita, *Mixing Element Radiant Tube (MERT) Improves Cracking Furnace Performance*, in *11th Ethylene Producers' Conference*, 1999: Houston, TX.
56. Froment, G.F., *Kinetics and reactor design in the thermal cracking for olefins production*. Chemical Engineering Science, 1992. **47**(9): p. 2163-2177.
57. Pyl, S.P., K.M. Van Geem, M.-F. Reyniers, and G.B. Marin, *Molecular reconstruction of complex hydrocarbon mixtures: An application of principal component analysis*. AIChE Journal, 2010. **56**(12): p. 3174-3188.
58. Van Geem, K.M., M.F. Reyniers, and G.B. Marin, *Challenges of Modeling Steam Cracking of Heavy Feedstocks*. Oil Gas Sci. Technol., 2008. **63**(1): p. 79-94.
59. Sabbe, M.K., M. Saeys, M.-F. Reyniers, G.B. Marin, V. Van Speybroeck, and M. Waroquier, *Group Additive Values for the Gas Phase Standard Enthalpy of Formation of Hydrocarbons and Hydrocarbon Radicals*. The Journal of Physical Chemistry A, 2005. **109**(33): p. 7466-7480.
60. Benson, S.W. and J.H. Buss, *Additivity Rules for the Estimation of Molecular Properties. Thermodynamic Properties*. The Journal of Chemical Physics, 1958. **29**(3): p. 546-572.
61. Sabbe, M.K., M.-F. Reyniers, V. Van Speybroeck, M. Waroquier, and G.B. Marin, *Carbon-Centered Radical Addition and β -Scission Reactions: Modeling of Activation Energies and Pre-exponential Factors*. ChemPhysChem, 2008. **9**(1): p. 124-140.
62. Dijkmans, T., S.P. Pyl, M.-F. Reyniers, R. Abhari, K.M. Van Geem, and G.B. Marin, *Production of bio-ethene and propene: alternatives for bulk chemicals and polymers*. Green Chemistry, 2013. **15**(11): p. 3064-3076.
63. Contino, F., *Combustion in homogeneous charge compression ignition engines : experimental analysis using ethyl esters and development of a method to include detailed chemistry in numerical simulations*, 2011, UC Louvain.
64. Reyniers, P.A., C.M. Schietekat, D.J. Van Cauwenberge, L.A. Vandewalle, K.M. Van Geem, and G.B. Marin, *Necessity and Feasibility of 3D Simulations of Steam Cracking Reactors*. Industrial & Engineering Chemistry Research, 2015. **54**(49): p. 12270-12282.
65. Plehiers, P.M., G.C. Reyniers, and G.F. Froment, *Simulation of the run length of an ethane cracking furnace*. Industrial & Engineering Chemistry Research, 1990. **29**(4): p. 636-641.
66. Zhang, Y., P.A. Reyniers, W. Du, F. Qian, K.M. Van Geem, and G.B. Marin, *Incident Radiative Heat Flux Based Method for the Coupled Run Length Simulation of Steam Cracking Furnaces*. Industrial & Engineering Chemistry Research, 2017. **56**(14): p. 4156-4172.
67. Pope, S.B., *PDF methods for turbulent reactive flows*. Progress in Energy and Combustion Science, 1985. **11**(2): p. 119-192.
68. Peters, N., *Turbulent Combustion*. Cambridge Monographs on Mechanics. 2000, Cambridge: Cambridge University Press.

- 69. Yu, G., C.K. Law, and C.K. Wu, *Laminar flame speeds of hydrocarbon + air mixtures with hydrogen addition*. Combustion and Flame, 1986. **63**(3): p. 339-347.
- 70. Weber, R., *The Spirit of Ijmuiden*. 1998, Ijmuiden, NL: International Flame Research Foundation.
- 71. Brookes, S.J. and J.B. Moss, *Measurements of soot production and thermal radiation from confined turbulent jet diffusion flames of methane*. Combustion and Flame, 1999. **116**(1–2): p. 49-61.
- 72. Colannino, J., *Mathematical models for characterizing and predicting heat flux profiles from ethylene cracking units*, in *AIChE Annual Meeting Conference Proceedings*, 2007, American Institute of Chemical Engineers (AIChE): Houston, TX.
- 73. Wauters, S. and G.B. Marin, *Kinetic Modeling of Coke Formation during Steam Cracking*. Industrial and Engineering Chemistry Research, 2002. **41**(10): p. 2379-2391.
- 74. Reyniers, G.C., G.F. Froment, F.-D. Kopinke, and G. Zimmermann, *Coke Formation in the Thermal Cracking of Hydrocarbons. 4. Modeling of Coke Formation in Naphtha Cracking*. Industrial & Engineering Chemistry Research, 1994. **33**(11): p. 2584-2590.
- 75. Kumar, P. and D. Kunzru, *Kinetics of coke deposition in naphtha pyrolysis*. The Canadian Journal of Chemical Engineering, 1985. **63**(4): p. 598-604.

6

Dynamic simulation of fouling in steam cracking reactors using CFD

*“Science is what we understand well enough to explain
to a computer; art is everything else.”*

Donald Ervin Knuth (1938 –)

This chapter has been published as :

Vandewalle, L.A., Van Cauwenberge, D.J., Dedeyne, J.N., Van Geem, K.M., Marin, G.B.
Dynamic simulation of fouling in steam cracking reactors using CFD. Chem. Eng. J. 2017.

Abstract

Recently computational fluid dynamics (CFD) has been successfully applied for the evaluation of the start-of-run performance of three-dimensional (3D) coil geometries in steam cracking reactors. However, determining the full economic potential of a coil involves tracking its performance throughout the run and not only at start-of-run. Therefore in this work a novel method has been developed that allows to assess the most debated characteristic of these 3D coil geometries, i.e. the potential extension of the run length in combination with the evolution of the product yields during the time on stream. An algorithm based on dynamic mesh generation is presented for simulating coke formation in 3D steam cracking reactor geometries, tracking the apparent geometry deformation caused by the growing coke layer. As a proof-of-concept, a Millisecond propane cracker is simulated over the first days of its run length, and this for three different coil designs: a bare tube, a finned tube and a continuously ribbed reactor design. Our simulations show that the ribbed reactors overall outperform the others although in these enhanced tubular geometries the growth of the coke layer is far from uniform. Because of this, the reactor geometry will change over time, which will in turn influence the fluid dynamics, product yields and successive coke formation substantially.

6.1 Introduction

Steam cracking of hydrocarbons is the predominant industrial process for the production of many commercially important base chemicals such as light olefins (ethene, propene, butadiene) and aromatics (benzene, toluene, xylenes). These base chemicals are the key building blocks for large-volume polymers and other high-value chemicals. Steam cracking is one of the most energy-intensive processes in the chemical industry, representing approximately 8% of the sector's primary energy consumption¹. A major factor for the process energy efficiency is the formation of coke on the inner wall of the tubular cracking reactors. This growing carbonaceous layer has two negative effects. First of all, the reactor pressure drop increases as the cross-sectional flow area decreases, resulting in a loss of selectivity to ethylene, the process' main

Dynamic simulation of fouling in steam cracking reactors using CFD

product². Secondly, the highly insulating coke layer blocks the heat transfer from the furnace to the process gas. To maintain the same cracking severity, the heat input is increased to counteract the increased heat transfer resistance, leading to higher tube metal temperatures (TMT) and still higher coking rates. Eventually, either due to an excessive pressure drop over the reactor or due to metallurgical constraints of the reactor tube alloy, production needs to be halted to decoke the reactor. These periodic production interruptions have a clear negative effect on the process economics. Furthermore, the reactor lifetime deteriorates with successive coking-decoking cycles because of tube corrosion, carburization and erosion³⁻⁶.

In response to this economic and environmental drawback, several technologies to reduce coke formation have been investigated⁷⁻¹⁰. One such technology is the use of three-dimensional (3D) reactor geometries to enhance radial mixing and facilitate heat transfer to the process gas. As coke deposition is a chemical process, the reduced tube metal temperatures have been shown to result in lower coking rates and longer furnace run lengths¹¹. Previously, computational fluid dynamics (CFD) has been applied to evaluate the start-of-run performance of these 3D reactor geometries and to assess their effect on pressure drop, coking rates and product yields^{11, 12}. However, as the most attractive characteristic of the enhanced reactor designs is the extension of the furnace run length, not only start-of-run performance should be evaluated to determine the potential of a 3D coil but also its performance throughout the run, i.e., as function of the time-on-stream. In the case of 3D tubular geometries or reactors with a strongly non-uniform heat flux profile (e.g. due to shadow effects), the growth of the coke layer will generally not be uniform. Because of this, the apparent reactor geometry will change in time, which will in turn influence the fluid dynamics, product yields and successive coke formation. In order to obtain an accurate prediction of a reactor's run length, all these phenomena need to be accounted for and hence the coke layer growth needs to be incorporated in the CFD simulations. The methodology presented in this work allows to track the apparent deformation of the flow domain caused by the growing coke layer, in this way making it possible to perform run length simulations of (industrial-scale) steam cracking reactors. The method is based on dynamic mesh generation, and can be applied for a variety of frequently encountered reactor designs. As a proof-of-concept, the method is used

to simulate a Millisecond propane cracker over the first days of its run, and this for a bare tube, a longitudinally finned tube and a continuously ribbed tube design.

6.2 CFD model

6.2.1 Governing equations

The steady-state governing equations for a compressible, reactive, single-phase fluid flow are the following:

$$\text{Continuity} \quad \frac{\partial \rho u_i}{\partial x_i} = 0 \quad (6.1)$$

$$\text{Momentum} \quad \frac{\partial \rho u_i u_j}{\partial x_i} = -\frac{\partial p}{\partial x_j} + \frac{\partial \tau_{ij}}{\partial x_i} \quad (6.2)$$

$$\text{Gas-phase energy} \quad \frac{\partial \rho u_i h}{\partial x_i} = \frac{\partial q_i}{\partial x_i} + S_h \quad (6.3)$$

$$\text{Species transport} \quad \frac{\partial \rho Y_k u_i}{\partial x_i} = -\frac{\partial J_{k,i}}{\partial x_i} + R_k \quad (\forall k = 1, n_k-1) \quad (6.4)$$

To be able to explicitly account for the conjugate heat transfer from the metal reactor outer wall to the process gas, the Laplace equations for thermal conduction in the coke layer and metal tube wall surrounding the process gas are solved simultaneously with the governing equations for the fluid flow.

$$\text{Solid-phase energy} \quad \nabla \cdot (\lambda_s \nabla T) = 0 \quad (6.5)$$

In the above equations, τ_{ij} is the viscous shear stress tensor, which is evaluated using the Boussinesq eddy viscosity concept. The sensible enthalpy flux q_i and the diffusion flux $J_{k,i}$ are both modeled using an eddy diffusivity approach:

$$\tau_{ij} = (\mu + \mu_t) \left(\frac{\partial u_i}{\partial x_j} + \frac{\partial u_j}{\partial x_i} \right) - \frac{2}{3} \rho k \delta_{ij} \quad (6.6)$$

$$q_i = c_p \left(\frac{\mu}{Pr} + \frac{\mu_t}{Pr_t} \right) \frac{\partial T}{\partial x_i} \quad (6.7)$$

$$J_{k,i} = \left(\frac{\mu}{Sc} + \frac{\mu_t}{Sc_t} \right) \frac{\partial Y_k}{\partial x_i} \quad (6.8)$$

The turbulent Prandtl number Pr_t and turbulent Schmidt number Sc_t are defined as the ratio of the momentum eddy diffusivity to the heat and mass eddy diffusivity respectively. A value of 0.85 was chosen for these numbers, in accordance to the typical recommendations for gaseous flows¹³⁻¹⁵.

The turbulent eddy viscosity μ_t appearing in Eqs. (6.6)-(6.8) is calculated using the shear stress transport (SST) $k-\omega$ turbulence model developed by Menter¹⁶. This two-equation turbulence model blends the robust and accurate formulation of the $k-\omega$ model in the near-wall region with the freestream independence of the $k-\epsilon$ model in the far field. These features make the SST $k-\omega$ model more accurate and reliable for a wider class of flows than the standard $k-\omega$ model. As shown by Van Cauwenberge et al.¹⁷, the SST $k-\omega$ turbulence model performs well in predicting the global flow characteristics in bare and finned steam cracking reactor geometries. As mainly the global flow characteristics are important for the estimation of coke formation and growth, it can be assumed that the conclusions and main results presented in this paper are independent of the adopted turbulence model.

6.2.2 Chemistry model

Steam cracking of hydrocarbons mainly proceeds through a free-radical mechanism, which is inherently characterized by a large number of species and reactions¹⁸⁻²⁰. The incorporation of such detailed kinetic networks is computationally prohibitively expensive. Therefore, the full single-event microkinetic CRACKSIM model²¹⁻²⁵, developed in-house, was reduced to its relevant core for propane cracking. The final network consists of 151 reactions between 29 species, of which 13 radical species. This network can be found in CHEMKIN format in the Supporting Information. The pseudo-steady state assumption was applied to the radical reaction intermediates, transforming the ODEs for these short-lived species into algebraic equations. In

Dynamic simulation of fouling in steam cracking reactors using CFD

this way the fastest transients are removed from the system of differential equations, resulting in an overall reduction of the kinetic model stiffness²⁶. Following the procedure adopted by Reyniers et al.¹², the concentration of each radical β_j is calculated numerically on the fly, i.e. during the flow simulations by expressing the rate for consumption $R_{\beta_j}^c$ to be equal to the rate of production $R_{\beta_j}^p$:

$$-R_{\beta_j}^c(\mathbf{c}_M, \mathbf{c}_\beta) = R_{\beta_j}^p(\mathbf{c}_M, \mathbf{c}_\beta) \quad (6.9)$$

More details about the procedure and validation of this approach is given by Reyniers et al.¹².

The Reaction Mechanism Generator (RMG) Transport estimator²⁷ was used for the estimation of the Lennard-Jones (L-J) model parameters. These were then used in the kinetic theory method for calculation of the species' individual thermal conductivities and viscosities. Using the same L-J parameters, the Chapman Enskog formula was used to quantify the diffusion coefficients. Properties of the multicomponent mixture were calculated by ideal gas mixing laws. To simplify the diffusion terms a unity Lewis number ($Le = Sc/Pr$) was assumed, which is justified given the dominance of turbulent over laminar diffusion in steam cracking.

In the current paper, turbulence chemistry interactions were not taken into account, as their effect on the temperature profile and ethene/propene concentrations in the case of steam cracking was found to be negligible²⁸.

6.2.3 Numerical model

The governing equations were solved using the open source CFD package OpenFOAM®²⁹. The Semi-Implicit Method for Pressure-Linked Equations (SIMPLE) was used to couple the momentum and continuity equation, with one additional non-orthogonal correction step where necessary.

A second order central differencing spatial discretization scheme was used. The cell face values of the Gaussian surface integral were obtained through linear interpolation. The linear solvers

Dynamic simulation of fouling in steam cracking reactors using CFD

adopted for the different transport equations, as well as some information about the solution procedure and convergence criteria, can be found in the Supporting Information.

6.2.4 Computational grid and boundary conditions

The simulation procedure is validated for a bare reactor tube, which serves as the base case. Then a comparison is made between two enhanced tubular reactor geometries, namely a longitudinally finned reactor and a reactor with a continuous rib with a sinusoidal cross section orthogonal to the flow (see Figure 6-1).

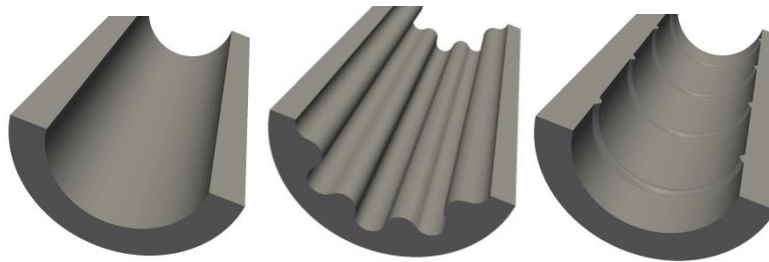


Figure 6-1. Illustration of the reactor geometries simulated in this work. From left to right: bare tube, longitudinally finned tube, continuously ribbed tube^{11, 30-32}.

The 3D computational grids were generated by extruding a specified number of layers from a cylindrical surface to the surface of the 3D tube geometry, as explained further in §6.2.5. Because the bare and continuously ribbed reactor tubes both exhibit axisymmetry, these cases were discretized on 2D wedge grids. The computational domain for the finned tube was limited to 1/8th of the tube's cross section (corresponding to one fin), while rotationally periodic boundary conditions were applied at the azimuthal domain boundaries. Near-wall grid resolution satisfied the $y^+ < 1$ condition, hereby ensuring that the first cell lies within the viscous sublayer. As shown by Schietekat et al.¹¹ grid independence in 3D steam cracking coils is observed for grid sizes in wall units $\{R\Delta\theta^+, \Delta y^+, \Delta x^+\} = \{50, 0.8-50, 333\}$. In the present study, grid sizes in wall units were $\{R\Delta\theta^+, \Delta y^+, \Delta x^+\} = \{42.5-75, 1.0, 115-290\}$. Therefore, it can be assumed that the conclusions and main results are independent of the adopted mesh.

The inner reactor surface was treated as a no-slip, no-species flux solid wall. At the inlet boundary, the process gas temperature, mass flow rate, turbulence parameters, and composition

Dynamic simulation of fouling in steam cracking reactors using CFD

of the process gas were imposed. At the reactor outlet, a constant pressure boundary condition was set. A heat flux profile was imposed at the outer surface of the reactor, i.e., the metal tube wall. Thermal coupling between the solid regions and the process gas was established through use of Robin boundary conditions at the metal-coke and coke-gas interfaces. Flux through all surfaces is preserved by setting the interface temperature as:

$$T_{int} = \frac{\frac{\lambda_s}{\Delta_s}}{\frac{\lambda_f}{\Delta_f} + \frac{\lambda_s}{\Delta_s}} T_s + \frac{\frac{\lambda_f}{\Delta_f}}{\frac{\lambda_f}{\Delta_f} + \frac{\lambda_s}{\Delta_s}} T_f \quad (6.10)$$

with Δ being the grid spacing between the first cell center and the interface. The temperature dependent thermal conductivity λ in the metal phase is taken from a reference Incoloy 800HT reactor coil material³³, while that in the fluid phase is the effective thermal conductivity, calculated using the formula proposed by Jayatilke³⁴. Thermal conductivity of the cokes was estimated based on the work of Plehiers³⁵.

6.2.5 Modeling coke formation

The overall methodology for the run length simulations presented in this work is shown in Figure 6-2. In this method, the reactor mesh is updated on a regular basis as coke deposits on the reactor wall until an end-of-run constraint is met, indicating that decoking is required. In industry, two constraints are typically used to end a furnace run and commence decoking: pressure drop and tube metal skin temperature (TMT). The algorithm hence finishes when either of these exceeds a critical value at the end of a simulation run.

Dynamic simulation of fouling in steam cracking reactors using CFD

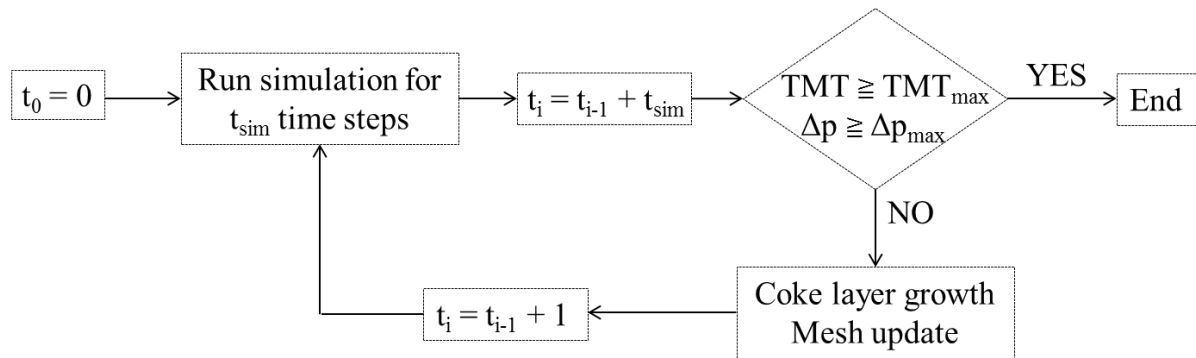


Figure 6-2. Run length simulation methodology.

To perform the mesh update step, the open source CFD package OpenFOAM®²⁹ has been extended with a new post-processing utility for dynamically simulating the growing coke layer. The ultimate goal of the utility is to generate a new mesh, consisting of three different regions for the gas, coke and tube metal, whereby the thickness of the coke layer is updated using the coking rate calculated from the simulation. A schematic representation of the different steps in the mesh generation process is given in Figure 6-3. The mesh generation starts from an initial core cylindrical mesh, which remains unchanged for the entire run length simulation. Cell layers are added to this initial mesh by extruding them in the radial direction starting from the core cylindrical wall. In this way, the gas region is extruded first, followed by extrusion of the coke layer and extrusion of the tube metal wall region. In step 1b in Figure 6-3, the extrusion distance is calculated by a geometry-specific extrusion model that is included in a newly developed OpenFOAM® library. This newly developed library of extrusion models contains the analytical surface definitions of several commonly applied enhanced tube geometries and is the key for success of the algorithm. An example surface definition is shown in Figure 6-4 for a longitudinally finned tube.

Dynamic simulation of fouling in steam cracking reactors using CFD

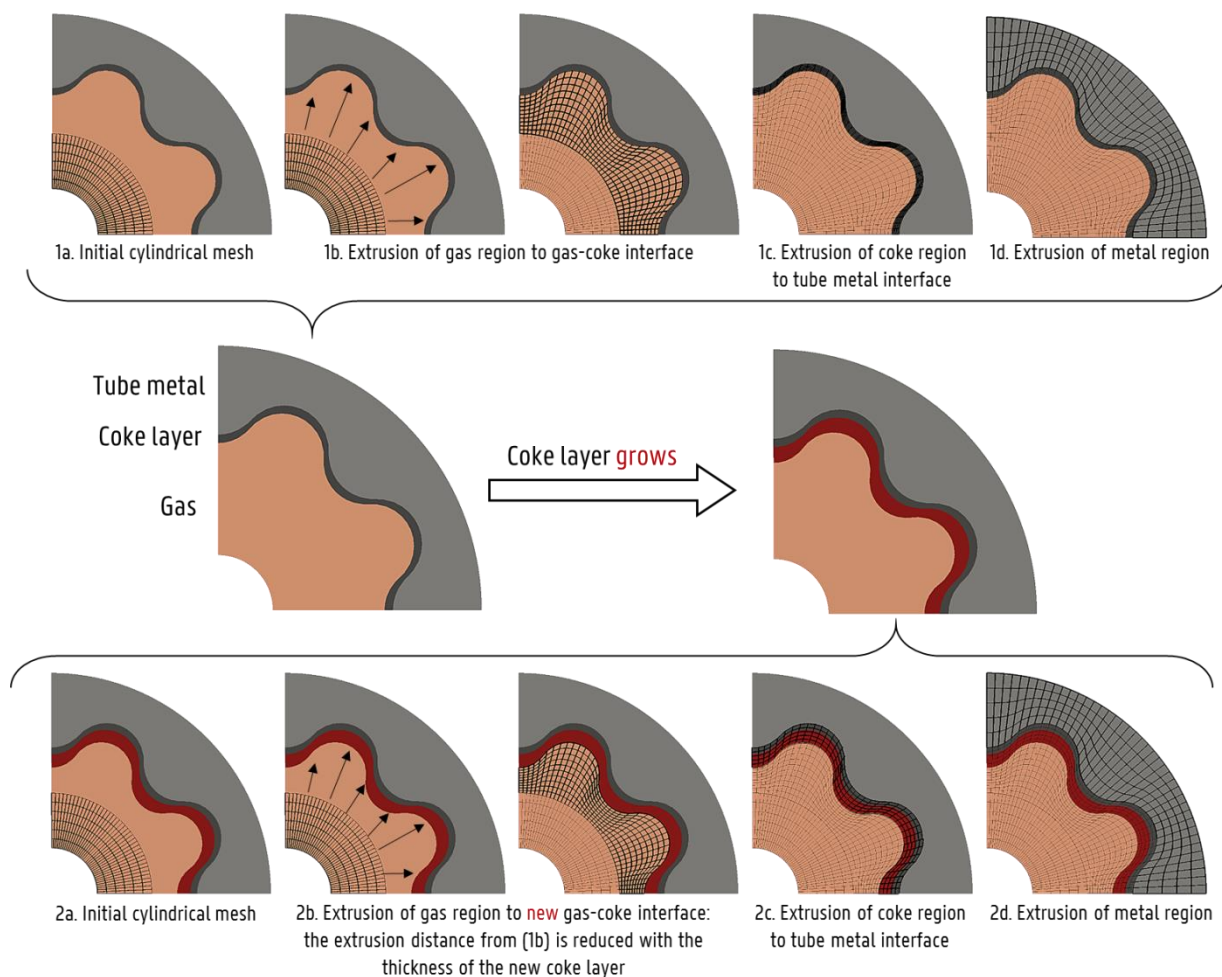


Figure 6-3. Illustration of extrusion algorithm for longitudinally finned tubes.

When the coke layer grows the extrusion distance calculated by the geometry-specific model is reduced with the thickness of the coke layer. This is also illustrated in Figure 6-3. The thickness of the coke layer is obtained by multiplying the coking rate with a duration over which coke formation is assumed to be constant. Hereby, the coking rate is calculated with the semi-empirical model developed by Plehiers³⁵, which uses the temperature and mass fractions of ethylene and propylene at the gas-coke interface resulting from the CFD simulation. The coke layer thickness is updated each time the utility is called, and the procedure can be repeated multiple times for different stages in the coking process.

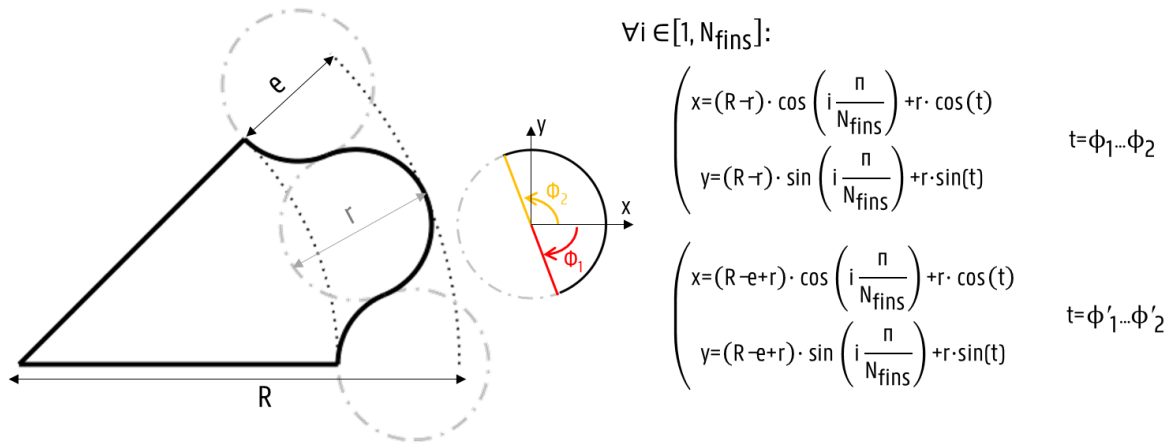


Figure 6-4. Geometric parameters and corresponding parametric equations for a longitudinally finned tube. This surface definition is included in a geometry-specific extrusion model.

6.3 Run length simulation of an industrial propane cracker

Reactive simulations of an industrial Millisecond reactor were performed to evaluate the effect of the growing coke layer on the fluid dynamics, product yields and successive coke formation. The simulated reactor has been previously described by Schietekat et al.¹¹ and is known to achieve very high selectivity towards ethene due to the short residence times in order of milliseconds. Disadvantages of this design are the very high operating temperatures and very short run lengths, sometimes as short as a week.

6.3.1 Process conditions and reactor configuration

The feedstock to the reactor consists of 100 % pure propane. The hydrocarbon and steam flow rate are respectively 0.03292 and 0.01075 kg/s, corresponding to a steam dilution of 0.326. The temperature at the inlet of the reactor was set to 903.7 K, whereas the reactor outlet pressure, that is, upstream of the transfer line exchanger, remains fixed at 170 kPa for the entire run. Because a coupled reactor-furnace simulation is deemed too computationally expensive, a heat flux profile was imposed on the outer wall of the reactor. For the bare tube simulations, this heat flux profile is identical to that used by Reyniers et al.¹² and was taken from a furnace simulation where the

Dynamic simulation of fouling in steam cracking reactors using CFD

boundary condition applied to the reactor tubes was the industrially measured outer wall temperature profile. For the simulations with the 3D tube geometries, the original heat flux profile was scaled in such a way as to obtain the same propane conversion in each simulation case. Also after each mesh update, the heat input is scaled with an appropriate factor to make sure that the propane conversion remains constant throughout the run. Remark that in reality, the adjustment ratio may not change by one constant factor from the beginning to the end of the coil but will be position-dependent. This is also investigated in the recent paper by Zhang et. al.³⁶. However, to take this into account a fully-coupled CFD simulation of both the furnace and the reactor side would be required, which is deemed too computationally expensive for the purpose of the present work. Furthermore, in this study, the inlet temperature to the reactor is kept at a constant value throughout the run. In reality the adjusted firing rate throughout the duration of the run will also impact preheating in the convection section of the furnace, causing variations in the cross-over temperature. Accounting for this phenomenon would however require a full furnace-reactor coupling, which was deemed outside of the scope of the present work.

The details of the three reactor configurations simulated in this work are summarized in Table 6-1. First, a bare tube was simulated as a reference case. Second, an industrially applied finned reactor was considered, identical to the one simulated by Schietekat et al.¹¹. Finally, a continuously ribbed geometry was simulated, with the same inner diameter as the bare tube reactor. It was chosen to keep the minimum metal thickness fixed to a value of 6.75×10^{-3} m. In practice, this is done for structural stability. An adiabatic entrance zone was added upstream of all reactors to ensure fully developed profiles for velocity and turbulence parameters at the reactor inlet.

Table 6-1. Reactor configurations^{11, 30-32}.

Reactor ID	Bare	Finned	c-Ribbed
Reactor length [m]	10.556	10.556	10.556
Adiabatic inlet section [m]	0.444	0.444	0.46

Dynamic simulation of fouling in steam cracking reactors using CFD

Maximum inner diameter [10^{-3} m]	30.2	34.8	30.2
Initial coke layer thickness [10^{-3} m]	0.1	0.1	0.1
Number of fins / ribs [-]	-	8	1
Pitch [10^{-3} m]	-	-	24.0
Outer diameter [10^{-3} m]	43.7	48.3	43.7
Metal thickness [10^{-3} m]	6.75	6.75	6.75
Fin / rib height [10^{-3} m]	-	4.8	1.0
Fin / rib width [10^{-3} m]	-	-	3.0
Cross-sectional surface area [10^{-6} m ²]	716	716	706

6.3.2 Results and discussion

6.3.2.1 Start-of-run performance

Figure 6-5 shows the pressure as function of the axial position for the different reactor geometries. The pressure drop is found to vary drastically with the continuously ribbed reactor design showing the highest pressure drop. Figure 6-6 shows the azimuthally area-averaged tube metal skin temperature as function of axial position. The maximum TMT occurs at around 3.5 m corresponding to the position of maximum heat flux to the reactor. For the bare reactor the maximum TMT is 1299 K, which is already close to the maximum allowable TMT of approximately 1370 K. The maximum TMT is 27 and 60 K lower than the bare tube for the longitudinally finned and the continuously ribbed reactor designs, respectively. Due to the lower wall temperatures, the 3D reactor designs also yield lower coking rates. Figure 6-7 shows the azimuthally area-averaged coking rate as function of axial position for the different reactor configurations. All profiles show two maxima: the first around 6 m and the second at the reactor outlet. As reported by Schietekat et al.¹¹, this can be explained by considering three major factors:

Dynamic simulation of fouling in steam cracking reactors using CFD

inner wall temperature, concentration of ethene and concentration of propene. Comparing the continuously ribbed tube to the bare tube, coking rates are lowered by approximately 55 % and 45 % at the first and second maximum, respectively.

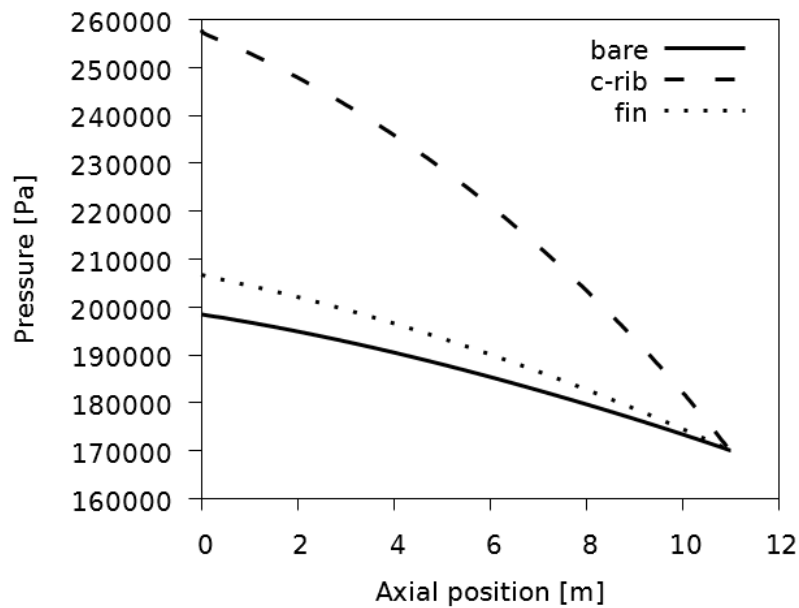


Figure 6-5. Axial pressure profile (for operating conditions as described in §6.3.1).

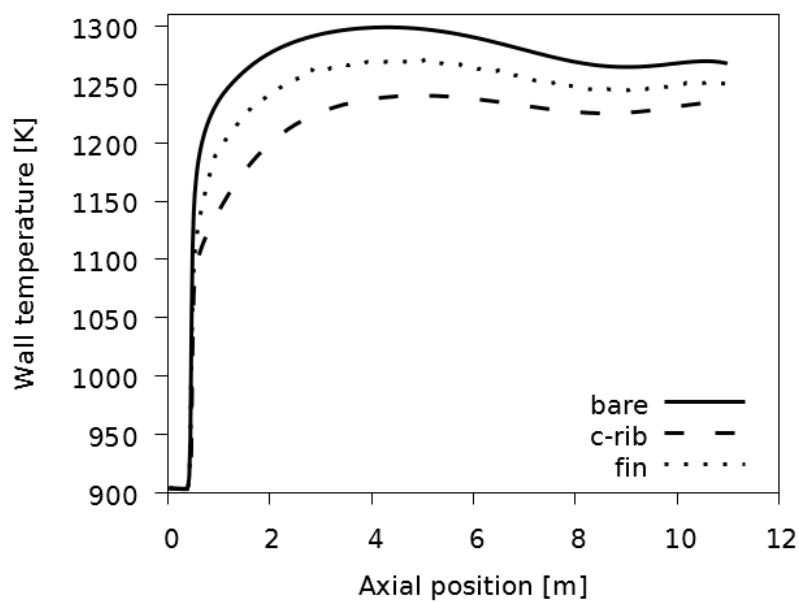


Figure 6-6. Azimuthally area-averaged tube metal skin temperature as function of axial position (for operating conditions as described in §6.3.1).

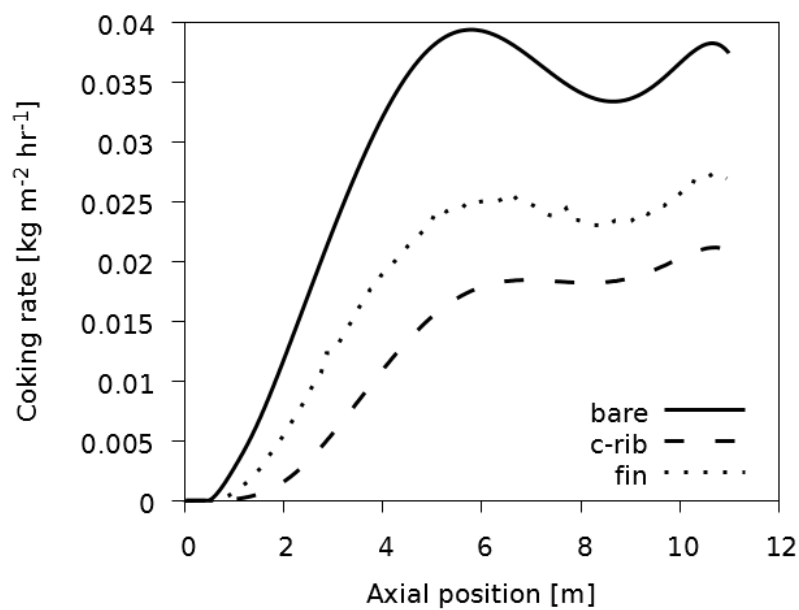


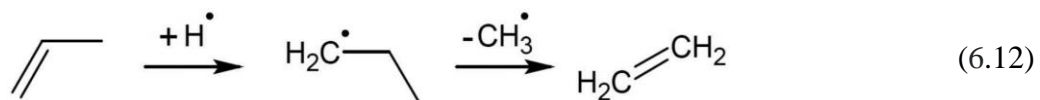
Figure 6-7. Azimuthally area-averaged coking rate as function of axial position (for operating conditions as described in §6.3.1).

Dynamic simulation of fouling in steam cracking reactors using CFD

Table 6-2 summarizes the most important process conditions, product yields, and selectivities. The listed values are mixing cup averages, defined as:

$$\overline{\varphi}_{mixcup} = \frac{\int_{\partial V} \rho u_z \varphi dA}{\int_{\partial V} \rho u_z dA} \quad (6.11)$$

Comparing the different reactor geometries some small differences in COT can be seen. These differences can be assigned to different pressure and temperature profiles in the reactors, resulting in different reaction rates and heat production rates. The coil inlet pressure increases drastically with a factor of 1.29 for the longitudinally finned reactor and 3.10 for the continuously ribbed reactor geometry. Looking at the selectivity differences, the high temperature zones in the fin valleys of the finned tubes are found to cause a slight increase in ethene selectivity, even at the same propane conversion. As bimolecular reactions are favored at higher pressure, the overall selectivity towards light olefins produced by monomolecular beta scissions should be reduced at higher pressures. However, this effect is only observable for the finned reactor geometry. In the ribbed reactor geometry the very high selectivity towards propene causes the overall selectivity towards valuable light olefins to be clearly higher than in the bare tube, even though the pressure drop is 3 times larger. The high propene selectivity in the ribbed reactor design can be attributed to reduced radial temperature gradients in these reactor geometries. As reported by Schietekat et al.¹¹, a rate of production analysis reveals that an important fraction of propene is consumed through an addition reaction of the hydrogen radical, resulting in a 1-propyl radical that decomposes further to ethene and a methyl radical:



Hydrogen radicals exhibit a very strong temperature sensitivity and their concentration may vary an order of magnitude between the core of the flow and the near-wall values. The reduced radial temperature gradients in the ribbed reactor geometry cause near-wall concentrations of hydrogen

Dynamic simulation of fouling in steam cracking reactors using CFD

radicals to be lower, explaining the increased propene yields. These observations compare well with the recent work of Van Cauwenberge et al.³² which also shows reduced total olefin yield for finned reactor designs, while the negative effect of high pressure drop in ribbed tubes is largely offset by the reduced radial temperature gradients.

As a matter of illustration, the ethene and propene mass fraction as function of axial position are shown in Figure 6-8 and Figure 6-9.

Table 6-2. Start-of-run reactor conditions, product yields and selectivities for the different reactor configurations (for operating conditions as described in §6.3.1).

	Bare	Fin	c-Rib
Coil outlet temperature [K]	1168.0	1165.0	1168.2
Pressure drop [kPa]	28.45	36.72	88.14
Pressure drop ratio [-]	1.00	1.29	3.10
Propane conversion [%]	80.15	80.14	80.16
P/E ratio [wt % / wt%]	0.522	0.513	0.555
<i>Yields [wt %]</i>			
H ₂	1.50	1.48	1.46
CH ₄	19.06	19.24	19.17
C ₂ H ₂	1.64	1.66	1.44
C ₂ H ₄	33.73	33.77	33.26
C ₂ H ₆	1.59	1.59	1.53
C ₃ H ₄	0.64	0.63	0.63
C ₃ H ₆	17.60	17.31	18.47
C ₃ H ₈	19.85	19.86	19.84

Dynamic simulation of fouling in steam cracking reactors using CFD

1,3-C ₄ H ₆	1.62	1.66	1.54
1-C ₄ H ₈	1.15	1.12	1.17
2-C ₄ H ₈	0.10	0.10	0.11
n-C ₄ H ₁₀	0.01	0.01	0.01
Valuable light olefins ^a	52.95	52.74	53.27
<i>Product selectivities [%]</i>			
H ₂	1.87	1.85	1.82
CH ₄	23.79	24.01	23.92
C ₂ H ₂	2.04	2.07	1.79
C ₂ H ₄	42.09	42.14	41.50
C ₂ H ₆	1.99	1.99	1.91
C ₃ H ₄	0.80	0.78	0.78
C ₃ H ₆	21.95	21.60	23.04
1,3-C ₄ H ₆	2.03	2.07	1.92
1-C ₄ H ₈	1.44	1.40	1.46
2-C ₄ H ₈	0.13	0.13	0.14
n-C ₄ H ₁₀	0.01	0.01	0.01
Valuable light olefins ^a	66.07	65.81	66.45

^aValuable light olefins is the sum of ethene, propene, and 1,3-butadiene.

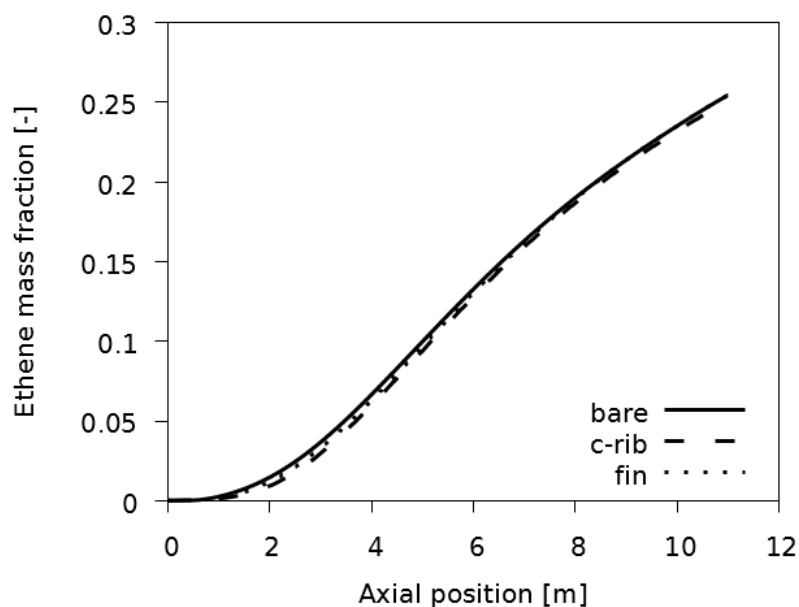


Figure 6-8. Ethene mass fraction mixing-cup averaged over a cross-section as function of axial position (for operating conditions as described in §6.3.1).

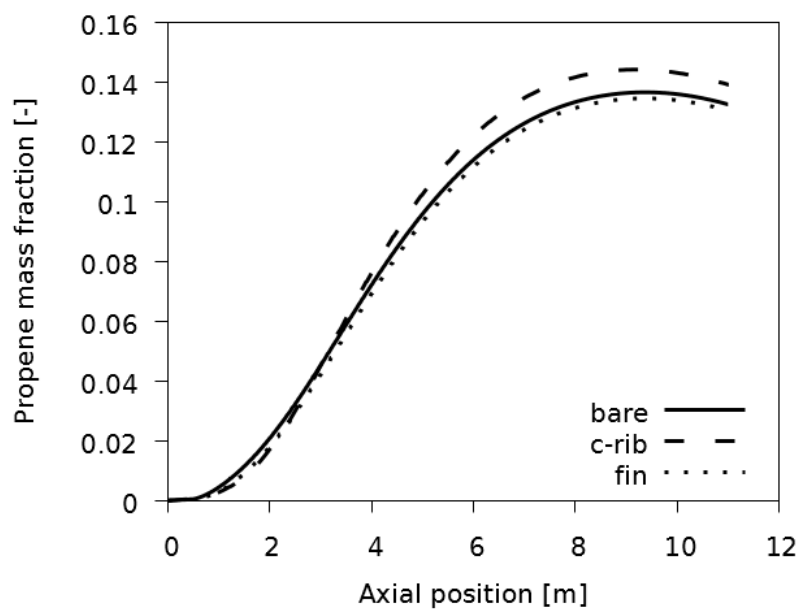


Figure 6-9. Propene mass fraction mixing-cup averaged over a cross-section as function of axial position (for operating conditions as described in §6.3.1).

6.3.2.2 Coke layer growth

Figure 6-10 shows the start-of-run coking rate as a function of the relative fin arc length. This relative fin arc length is defined as the running arc length from one fin top to the next divided by the total arc length of one fin. The shape of the coking rate profile along the fin arc is a direct result of the non-uniform temperature at the reactor inner wall. A similar effect is expected behind the ribs in the ribbed reactor geometry. The large non-uniformity of the coking rate will lead to local buildup of cokes over time affecting the subsequent reactor performance.

Figure 6-11 and Figure 6-12 show the velocity fields at start-of-run and after some time of coke formation, for the finned reactor and the continuously ribbed reactor geometry respectively. Comparing the velocity profiles at start-of-run with the profiles after some period of coke formation, the velocity increases due to the reduction of cross-sectional surface area as the coke layer grows. It is also confirmed in the figures that the coke formation is very non-uniform. After 10 days of coke formation in the continuously ribbed tube geometry, the rib has almost disappeared due to the non-uniform formation of cokes around it.

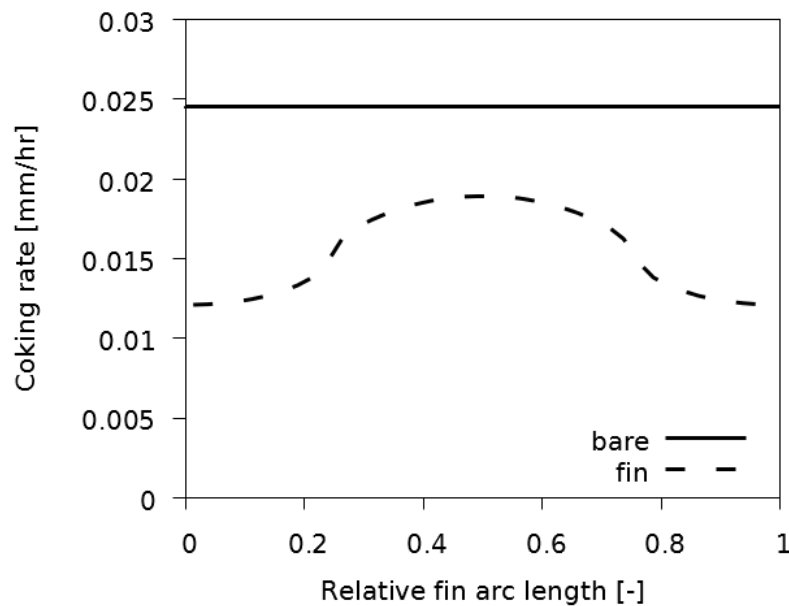


Figure 6-10. Coking rate as function of the relative fin arc length (0: top, 0.5: valley, 1:top) (for operating conditions as described in §6.3.1).

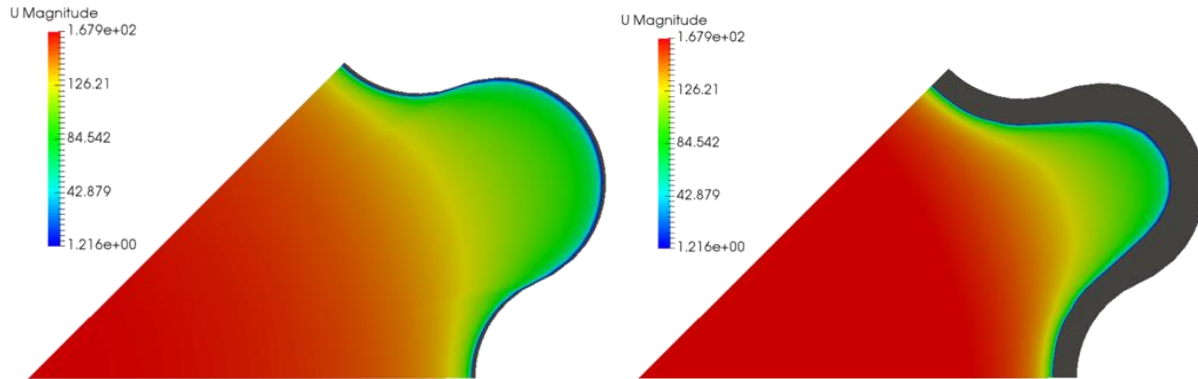


Figure 6-11. Fields of velocity magnitude [m/s] in the finned reactor geometry: (left) at start-of-run, and (right) after 48 hrs of coke layer growth (for operating conditions as described in §6.3.1).

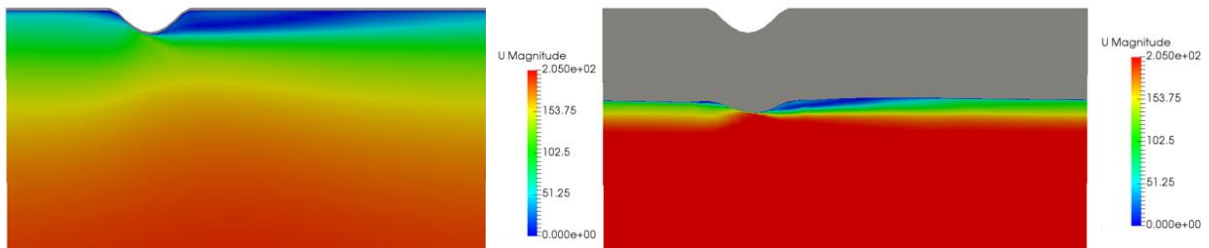


Figure 6-12. Fields of velocity magnitude [m/s] in the continuously ribbed reactor geometry: (left) at start-of-run, and (right) after 10 days of coke layer growth (for operating conditions as described in §6.3.1).

Figure 6-13 shows the temperature field in the ribbed tube geometry, at start-of-run and after 12 days of cracking, for both the process gas and cokes. As a consequence of the high thermal resistance, a large temperature gradient over the coke layer is observed. This results in significantly increased tube metal skin temperatures.

Dynamic simulation of fouling in steam cracking reactors using CFD

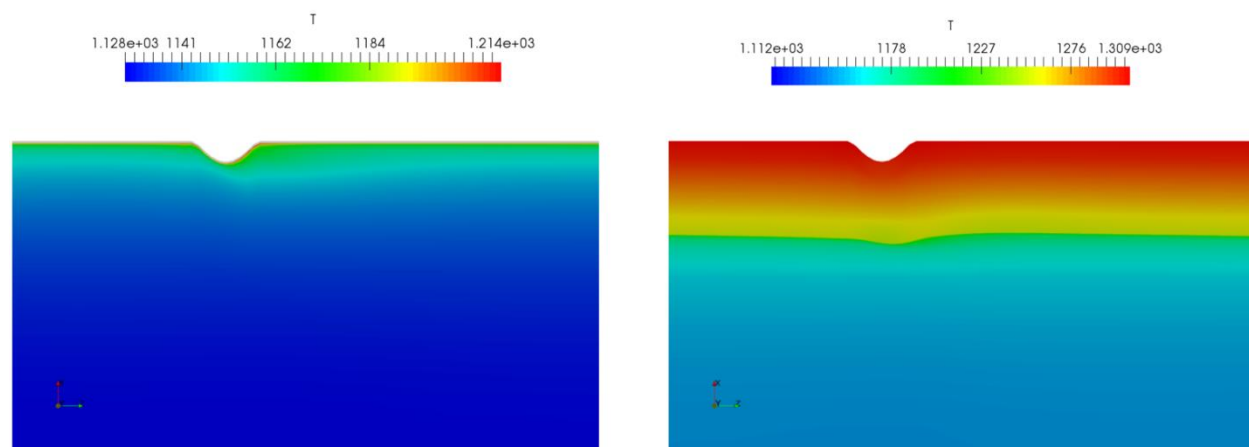


Figure 6-13. Fields of temperature [K] in the continuously ribbed reactor geometry: (left) at start-of-run, and (right) after 12 days of coke layer growth (for operating conditions as described in §6.3.1).

Figure 6-10 shows that the coke layer growth is much smaller in the finned tube compared to the bare tube geometry. Because of the enhanced internal surface area in the finned tube however, the total volume of coke is of the same order of magnitude for both reactor geometries. Hence, the total amount of coke can be larger, even though the thickness is smaller.

Because of the high thermal resistance of the coke layer, more coke means more extra heating required to achieve the same propane conversion at the outlet of the reactor. The heat flux correction factor, shown in Figure 6-14, is hence a good measure for the total amount of coke formed in the reactor. The heat flux correction factor for the bare and finned reactor geometries is almost equal throughout the run, confirming that a comparable amount of coke is formed in these geometries. It is also seen that the heat flux correction factor throughout the run is substantially lower for the ribbed tube geometry than for the bare and finned tube geometries, indicating that the total amount of coke formed throughout the run is significantly larger for the latter geometries.

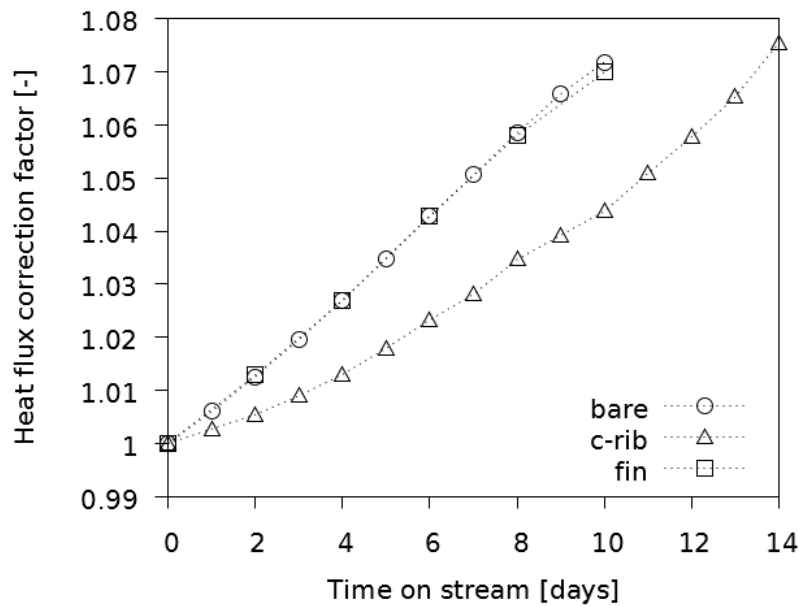


Figure 6-14. Heat flux correction factor as a function of the time on stream (for operating conditions as described in §6.3.1).

6.3.2.3 End-of-run

As already mentioned above, two constraints are typically used to end a furnace run and start decoking: pressure drop and tube metal skin temperature (TMT). Figure 6-15 and Figure 6-16 show the reactor pressure drop and maximum tube metal skin temperature as a function of time on stream.

The pressure drop in the bare and finned reactor geometries is found to increase at approximately the same rate, with the pressure drop in the finned reactor geometry always remaining higher than that in the bare tube. This is a result of the comparable amount of coke formed in these reactor geometries, yielding a comparable reduction of the cross-sectional flow area and hence a similar increase in pressure drop. An entirely different evolution of the pressure drop is seen for the ribbed reactor geometry. At start-of-run, the pressure drop in the ribbed geometry is more than 3 times higher than that in the bare and finned reactor geometries. This is mainly due to the high artificial tube roughness introduced by the ribs. As the coke layer grows, two effects become

Dynamic simulation of fouling in steam cracking reactors using CFD

important. First of all, the pressure drop will increase because of the reduction in cross-sectional flow area, similar to what is seen in the bare and finned tube geometries. On the other hand, the artificial tube roughness will decrease because of the non-uniform coke layer growth around the ribs (see Figure 6-12 and Figure 6-13), causing a reduction of the pressure drop. It is the interplay between these two effects that gives rise to the profile shown in Figure 6-15. During the first days of the run, the two phenomena seem to balance each other as the pressure drop remains almost constant. Later, when the ribs have almost disappeared because of the non-uniform formation of coke around them, the reduction of cross-sectional flow area becomes the dominant factor and the pressure drop starts to increase rapidly.

Significant increase of pressure drop will lead to loss of critical flow at the venturi pipes. It is difficult to define a hard end-of run criterion for pressure drop which is valid for all steam-cracking furnaces, because maximum allowable pressure drop depends on the venturi pipe geometry. The maximum allowable TMT on the other hand follows from the metallurgical constraints of the reactor alloy and is typically around 1370 K. Looking at the results in Figure 6-16, a run length of approximately 6 days, 8 days and 12 days is found for the bare, finned and continuously ribbed reactor designs, respectively. An extension of the run length of a factor of 1.5 to 2 between the finned and ribbed reactor geometries is in agreement with what is typically found in industry, confirming the validity of the simulated results. A table similar to Table 6-2, but for end-of-run conditions, can be found in the Supporting Information.

Dynamic simulation of fouling in steam cracking reactors using CFD

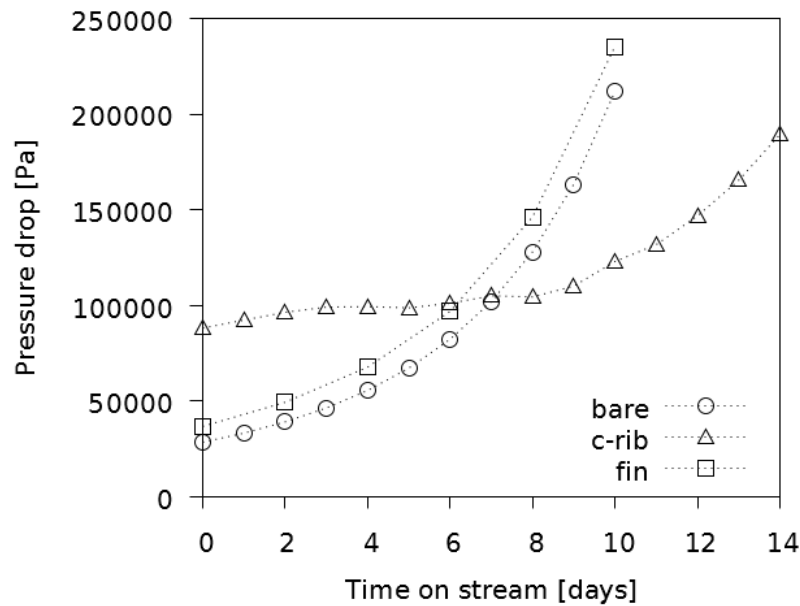


Figure 6-15. Reactor pressure drop as a function of the time on stream (for operating conditions as described in §6.3.1).

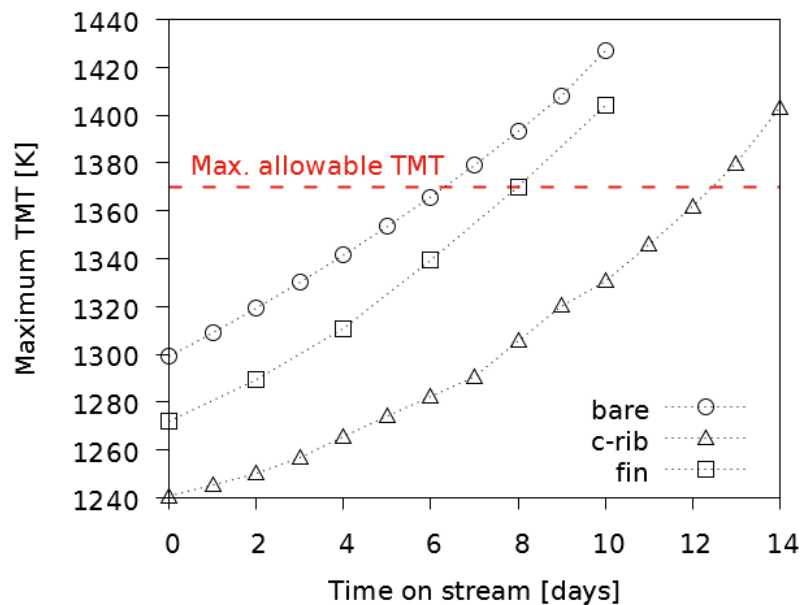


Figure 6-16. Maximum tube metal skin temperature as a function of the time on stream (for operating conditions as described in §6.3.1).

6.3.2.4 *Product selectivities throughout the run*

Figure 6-17 shows the ethene selectivity as a function of the time on stream. The decreasing ethene selectivity in the bare and finned reactor geometries follows directly from the increasing pressure drop and hence the favoring of bimolecular reactions that consume ethene. Although the reactor pressure drop increases similarly in the two reactor geometries (see Figure 6-15), the ethene selectivity shows a different behavior. The high temperature zones in the fin valleys of the finned tubes initially cause a slightly higher selectivity of ethene compared to the bare tube. Because of the non-uniform coke layer growth, these high temperature zones tend to become smaller, which results in a drop of ethene selectivity below that obtained in the bare tube. With the high temperature zones in the fin valleys slowly disappearing, the overall radial temperature gradients become smaller, causing the propene selectivity to increase as explained in §6.3.2.1 for the ribbed geometry. This is confirmed by Figure 6-18 where the propene-to-ethene ratio at the reactor outlet is shown as a function of time on stream.

The evolution of the ethene selectivity and propene-to-ethene ratio as a function of time on stream for the ribbed reactor geometry follows similarly from an interplay between pressure drop and radial temperature effects.

Dynamic simulation of fouling in steam cracking reactors using CFD

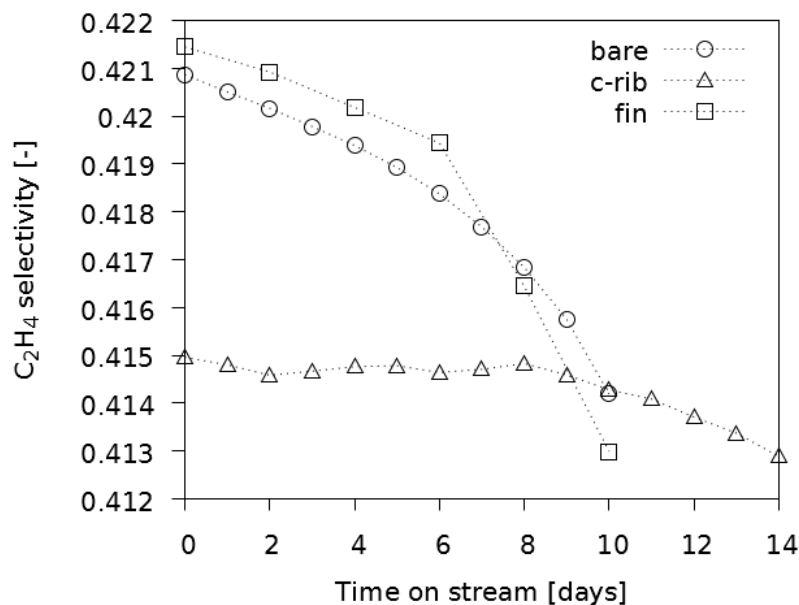


Figure 6-17. Ethene selectivity at the reactor outlet as a function of the time on stream (for operating conditions as described in §6.3.1).

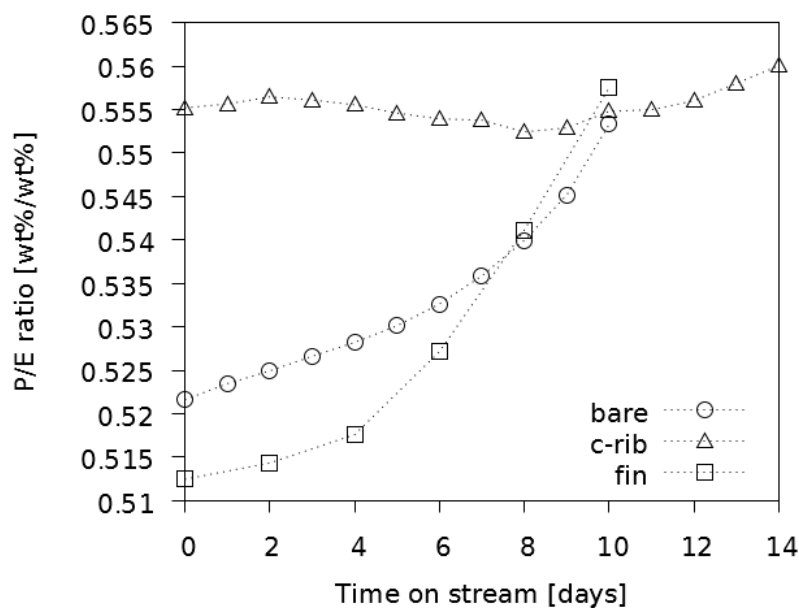


Figure 6-18. Propene-to-ethene ratio at the reactor outlet as a function of the time on stream (for operating conditions as described in §6.3.1).

6.4 Conclusions

In this work a methodology was presented for simulating the run length of an industrial steam cracking reactor while tracking the apparent geometry deformation caused by a growing coke layer. As a proof-of-concept, the method was used to simulate a Millisecond propane cracker over the first days of its run, and this for three different reactor geometries: a bare tube, a finned tube and a continuously ribbed reactor design. The influence of the growing coke layer on reactor pressure drop, tube metal skin temperatures and product selectivities was studied. The ribbed reactor geometry was found to result in the longest run length and best product yields. Comparing finned and ribbed reactor geometries, an extension of the run length with a factor of 1.5 was found for the ribbed designs in a scenario where tube metal temperature is the limiting factor, which is in agreement with industrial observations.

The presented method can serve as a screening tool for evaluating the performance of different 3D reactor geometries throughout their run, and not only at start-of-run. As the most attractive characteristic of these 3D reactor designs is the extension of the furnace run length, this tracking of the reactor performance as a function of the time on stream is a prerequisite to assess the real potential of an enhanced reactor design.

References

1. Ren, T., M. Patel, and K. Blok, *Olefins from conventional and heavy feedstocks: Energy use in steam cracking and alternative processes*. Energy, 2006. **31**(4): p. 425-451.
2. Van Geem, K.M., *Two severity indices for scale-up of steam cracking coils*. Industrial & Engineering Chemistry Research, 2005. **44**: p. 3402-3411.
3. Zimmermann, G., W. Zychlinski, H.M. Woerde, and P. van den Oosterkamp, *Absolute Rates of Coke Formation: A Relative Measure for the Assessment of the Chemical Behavior of High-Temperature Steels of Different Sources*. Industrial & Engineering Chemistry Research, 1998. **37**: p. 4302-4305.
4. Zychlinski, W., K.A. Wynns, and B. Ganser, *Characterization of material samples for coking behavior of HP40 material both coated and uncoated using naphtha and ethane feedstock*. Materials and Corrosion, 2002. **53**: p. 30-36.
5. Nishiyama, Y. and N. Otsuka, *Degradation of Surface Oxide Scale on Fe-Ni-Cr-Si Alloys upon Cyclic Coking and Decoking Procedures in a Simulated Ethylene Pyrolysis Gas Environment*. Corrosion, 2005. **61**(1): p. 84-93.
6. Muñoz Gandarillas, A.E., K.M. Van Geem, M.-F. Reyniers, and G.B. Marin, *Influence of the Reactor Material Composition on Coke Formation during Ethane Steam Cracking*. Industrial & Engineering Chemistry Research, 2014. **53**(15): p. 6358-6371.
7. Wang, J., M.F. Reyniers, and G.B. Marin, *Influence of Dimethyl Disulfide on Coke Formation during Steam Cracking of Hydrocarbons*. Industrial & Engineering Chemistry Research, 2007. **46**: p. 4134-4148.
8. Wang, J., M.F. Reyniers, K.M. Van Geem, and G.B. Marin, *Influence of Silicon and Silicon/Sulfur-Containing Additives on Coke Formation during Steam Cracking of Hydrocarbons*. Industrial & Engineering Chemistry Research, 2008. **47**: p. 1468-1482.
9. Reyniers, M.-F.S.G. and G.F. Froment, *Influence of Metal Surface and Sulfur Addition on Coke Deposition in the Thermal Cracking of Hydrocarbons*. Industrial & Engineering Chemistry Research, 1995. **34**(3): p. 773-785.
10. Schietekat, C.M., S.A. Sarris, P.A. Reyniers, L.B. Kool, W. Peng, P. Lucas, K.M. Van Geem, and G.B. Marin, *Catalytic Coating for Reduced Coke Formation in Steam Cracking Reactors*. Industrial & Engineering Chemistry Research, 2015. **54**(39): p. 9525-9535.
11. Schietekat, C.M., M.W.M. van Goethem, K.M. Van Geem, and G.B. Marin, *Swirl flow tube reactor technology: An experimental and computational fluid dynamics study*. Chemical Engineering Journal, 2014. **238**(0): p. 56-65.

Dynamic simulation of fouling in steam cracking reactors using CFD

12. Reyniers, P.A., C.M. Schietekat, D.J. Van Cauwenberge, L.A. Vandewalle, K.M. Van Geem, and G.B. Marin, *Necessity and Feasibility of 3D Simulations of Steam Cracking Reactors*. Industrial & Engineering Chemistry Research, 2015. **54**(49): p. 12270-12282.
13. Moin, P., K. Squires, W. Cabot, and S. Lee, *A dynamic subgrid-scale model for compressible turbulence and scalar transport*. Physics of Fluids A, 1991. **3**(11): p. 2746-2757.
14. William Kays, M.C., Bernhard Weigand, *Convective Heat and Mass Transfer*. 4th ed. 2004: Mcgraw-Hill (Tx).
15. Pope, S.B., *Turbulent Flows*. 2000: Cambridge University Press.
16. Menter, F.R., *Two-equation eddy-viscosity turbulence models for engineering applications*. AIAA Journal, 1994. **32**(8): p. 1598-1605.
17. Van Cauwenberge, D.J., C.M. Schietekat, J. Floré, K.M. Van Geem, and G.B. Marin, *CFD-based design of 3D pyrolysis reactors: RANS vs. LES*. Chemical Engineering Journal, 2015. **282**: p. 66-76.
18. Ranzi, E., A. Frassoldati, S. Granata, and T. Faravelli, *Wide-Range Kinetic Modeling Study of the Pyrolysis, Partial Oxidation, and Combustion of Heavy n-Alkanes*. Industrial & Engineering Chemistry Research, 2005. **44**(14): p. 5170-5183.
19. Dijkmans, T., S.P. Pyl, M.-F. Reyniers, R. Abhari, K.M. Van Geem, and G.B. Marin, *Production of bio-ethene and propene: alternatives for bulk chemicals and polymers*. Green Chemistry, 2013. **15**(11): p. 3064-3076.
20. Pyl, S.P., K.M. Van Geem, M.-F. Reyniers, and G.B. Marin, *Molecular reconstruction of complex hydrocarbon mixtures: An application of principal component analysis*. AIChE Journal, 2010. **56**(12): p. 3174-3188.
21. Clymans, P.J. and G.F. Froment, *Computer-generation of reaction paths and rate equations in the thermal cracking of normal and branched paraffins*. Computers & Chemical Engineering, 1984. **8**(2): p. 137-142.
22. Hillewaert, L.P., J.L. Dierickx, and G.F. Froment, *Computer generation of reaction schemes and rate equations for thermal cracking*. AIChE Journal, 1988. **34**(1): p. 17-24.
23. Van Geem, K.M., M.F. Reyniers, and G.B. Marin, *Challenges of Modeling Steam Cracking of Heavy Feedstocks*. Oil & Gas Science and Technology - Revue de l'IFP, 2008. **63**(1): p. 79-94.
24. Willems, P.A. and G.F. Froment, *Kinetic modeling of the thermal cracking of hydrocarbons. 1. Calculation of frequency factors*. Industrial & Engineering Chemistry Research, 1988. **27**(11): p. 1959-1966.
25. Willems, P.A. and G.F. Froment, *Kinetic modeling of the thermal cracking of hydrocarbons. 2. Calculation of activation energies*. Industrial & Engineering Chemistry Research, 1988. **27**(11): p. 1966-1971.

Dynamic simulation of fouling in steam cracking reactors using CFD

26. Turanyi, T., A.S. Tomlin, and M.J. Pilling, *On the error of the quasi-steady-state approximation*. The Journal of Physical Chemistry, 1993. **97**(1): p. 163-172.
27. William H. Green, J.W.A., Beat A. Buesser, Robert W. Ashcraft, Gregory J. Beran, Caleb A. Class, Connie Gao, C. Franklin Goldsmith, Michael R. Harper, Amrit Jalan, Murat Keceli, Gregory R. Magoon, David M. Matheu, Shamel S. Merchant, Jeffrey D. Mo, Sarah Petway, Sumathy Raman, Sandeep Sharma, Jing Song, Yury Suleymanov, Kevin M. Van Geem, John Wen, Richard H. West, Andrew Wong, Hsi-Wu Wong, Paul E. Yelvington, Nathan Yee, Joanna Yu, *RMG - Reaction Mechanism Generator v4.0.1*, 2013.
28. Reyniers, P.A., D.J. Van Cauwenberge, G.B. Marin, and K.M. Van Geem. *Towards large eddy simulations with detailed kinetics*. in *The 10th International Conference on Chemical Kinetics* 2017. Chicago.
29. *OpenFOAM - The Open Source CFD Toolbox - User's Guide*, 2013, OpenCFD Ltd: United Kingdom.
30. Albano, J.V., K.M. Sundaram, and M.J. Maddock, *Application of Extended Surfaces in Pyrolysis Coils*. Energy Progress, 1988. **8**(3): p. 160-168.
31. Gyorffy, M., M. Hineno, K. Hashimoto, S.-H. Park, and M.-S. You. *Mert performance and technology update*. in *AIChE Spring Meeting: Ethylene Producers Conference, Tampa Bay, USA*. 2009.
32. Van Cauwenberge, D.J., L.A. Vandewalle, P.A. Reyniers, K.M. Van Geem, G.B. Marin, and J. Floré, *Periodic reactive flow simulation: Proof of concept for steam cracking coils*. AIChE Journal, 2017. **63**(5): p. 1715-1726.
33. metals, S. *INCOLOY® alloy 800H & 800HT®*. [cited 2016; <http://www.specialmetals.com/assets/documents/alloys/incoloy/incoloy-alloys-800h-800ht.pdf>]. Available from: <http://www.specialmetals.com/assets/documents/alloys/incoloy/incoloy-alloys-800h-800ht.pdf>.
34. Jayatilleke, C.L.V., *The influence of Prandtl number and surface roughness on the resistance of the laminar sub-layer to momentum and heat transfer*. 1966: University of London.
35. Plehiers, P.M., G.C. Reyniers, and G.F. Froment, *Simulation of the run length of an ethane cracking furnace*. Industrial & Engineering Chemistry Research, 1990. **29**(4): p. 636-641.
36. Zhang, Y., P.A. Reyniers, W. Du, F. Qian, K.M. Van Geem, and G.B. Marin, *Incident Radiative Heat Flux Based Method for the Coupled Run Length Simulation of Steam Cracking Furnaces*. Industrial & Engineering Chemistry Research, 2017. **56**(14): p. 4156-4172.

7

Conclusions and perspectives

*“Two there are, who are never satisfied;
The lover of the world and the lover of Knowledge.”*

Jalal ad-Din Rumi (1207 – 1273)

7.1 Conclusions

The subject of this work was the development of tools for the simulation and design of steam cracking reactors. More specifically, the focus was on the application of computational fluid dynamics (CFD) for the design of steam cracker installations and the potential for three dimensional reactor technologies to enhance heat transfer in these reactors.

Simulation of industrial processes typically requires a multiscale approach in which different levels of theory are combined. In the steam cracking process a broad range of physical and chemical phenomena need to be accounted for, from chemical kinetics and thermodynamics, to transport and material properties, turbulence and radiation. Combination of these different aspects obviously raises questions of accuracy and efficiency, as it becomes computationally infeasible to apply all of these phenomena to their ultimate level of detail. Development of a multiphysics simulation tool hence involves making concessions in certain areas, in order to improve the global simulation accuracy by including a greater level of theory elsewhere. Integrating all these phenomena then requires a flexible computational framework, with good parallelization for large-

scale computation, limited black-box behavior and the possibility for error quantification at each individual level. Rather than using a commercial package, these arguments led to the use of the open-source CFD framework OpenFOAM for all the results presented in this work.

Given the numerous steam cracking studies performed at the Laboratory for Chemical Technology on the matter, the present work focused less on the underlying chemistry, but rather on its implementation in a computationally efficient way. This was less of an issue in the past due to steam cracking reactors operating at moderately high Reynolds numbers and in long tubular reactors, leading to the plug flow assumption being commonly applied. Simulation of enhanced reactor designs however not only necessitates the three-dimensional Navier-Stokes equations to be solved, but also warrants an investigation into the impact of different turbulence modeling approaches.

This was performed in the first chapters of the present work, as implementation of a periodic approach in OpenFOAM allowed fully developed flow statistics to be obtained for a wide variety of geometrical configurations and turbulence models. The results were validated by comparison with direct numerical and experimental datasets found in literature. Next, a comparison was made between a Reynolds-averaged Navier-Stokes (RANS) turbulence model and the use of eddy-resolving techniques in the form of wall-resolved large eddy simulation (LES). These simulations illustrated the potential of both longitudinally finned tubes and the Swirl Flow Tube[®] design for application in steam cracking reactors. With heat transfer improvements of respectively 29 % and 37 %, tube metal temperatures in industrial operation of a typical ethane cracker were predicted to be approximately 40 K lower, while coke formation was reduced by 34 – 40 %. These benefits are expected to come at the cost of a 0.5 – 0.7 rel% loss of ethene selectivity, based solely on the higher pressure drop in these devices. While agreement for the global flow properties was reasonable, the RANS model clearly failed in capturing the different secondary flows arising in both geometries. This has considerable consequences on the predictions of local shear stresses and temperatures inside the tube material.

A more fundamental investigation was performed for tubes with a helical rib attached to the internal surface, as these are the most commercially successful reactor enhancement in the field

of steam cracking. Despite their widespread use in various heat exchangers, literature correlations on the global performance of these devices were seen to be very inconsistent. Relying on the expertise of the von Karman Institute for Fluid Dynamics in obtaining a high-fidelity dataset of local velocities and wall temperatures, led to an invaluable validation case for the performed LES on this design. Excellent agreement between both datasets was seen, as both predict a heat transfer improvement of over a factor two, at the cost of a roughly six-fold increase in pressure losses. Given the failure of the applied $k\omega$ -SST model in reproducing these results, an alternative was proposed by extending an existing near-wall Reynolds stress transport model (RSTM) with an algebraic heat flux model calibrated to the LES predictions. This model was seen to yield improved results over a broader range of Reynolds numbers at a cost comparable to the two-equation RANS model.

Next, the focus was shifted to the efficient integration of the fluid dynamics elements of the previous chapters with the chemistry routines developed over the years at the Laboratory for Chemical Technology. Through an innovative transformation of the space and time domains, the concept of streamwise periodicity was extended to non-equilibrium reacting flows. By only requiring a small volume of fluid to simulate a full scale reactor, the computational cost of these simulations was decreased by one to two orders of magnitude. Despite the approximate nature of the method no significant loss of accuracy was observed, as all major product yields were predicted to be within 1 rel.% error compared to the full reactor simulation, without relying on any tunable parameters. This was done for three different designs of an industrial Millisecond-type propane cracker, illustrating the potential of the method as a quick reactor screening tool or as a means of including a higher level of theory in existing simulations.

Other than a reduction of the computational domain, the use of on-the-fly chemistry reduction routines with the aim of reducing the number of reaction rate evaluations was also investigated. This led to a new chemistry library in OpenFOAM, combining in-situ adaptive rate tabulation with dynamic chemistry reduction, while applying the pseudo-steady state approximation to reduce the stiffness of the resulting set of equations. Validation on a 2D axisymmetric simulation of a propane steam cracker demonstrated speedup factors of 50 – 200, as the three on-the-fly methods clearly exhibited strong synergy. The developed library was used to evaluate a helically

ribbed reactor geometry for an industrial SRT-VI naphtha cracker using a reaction network consisting of 152 species and 1994 elementary reactions. Realistic heat flux profiles for these simulations were obtained by performing a 3D-3D coupling with the radiant section of the furnace, in which radiation was accounted for in detail by using a discrete ordinates method with an exponential wide band model for the flue gas radiative properties. Comparison of the helically ribbed reactor with a bare reactor showed a 36 % reduction in the rate of coke formation at start-of-run conditions for the former, at the cost of a 2.9 times higher pressure drop. Despite this obviously detrimental effect, no product losses were observed, as the total olefin yield was 0.2 rel.% higher than for the bare reactor due to the compensating effect of improved radial mixing.

Finally, the performance of enhanced reactor designs over a full run was investigated by explicitly including the growing coke layer in the simulations. The method generates a new grid at fixed intervals in the run, based on the local rate of coke formation. In this manner, the evolution of tube metal temperatures, pressure losses and product yields can be tracked throughout the run length. Comparison of a bare, finned and ribbed reactor design for a Millisecond propane cracker illustrated the value of this approach, as the different designs were seen to exhibit very different fouling behavior. While the ribbed reactor has a high base pressure drop, the reduced wall temperatures and the high coke formation in the wake of the element, lead to only a minor increase in pressure drop throughout the roughly 12 days on stream. The bare and finned tubes reach their end-of-run condition already after respectively 6 and 8 days, at which point their pressure drop exceeds that of the ribbed design. With longer run lengths forming the key motivation behind use of 3D reactor technology, the developed method clearly has value in assessing the true potential of such devices in industrial operation.

7.2 Perspectives

The conclusions drawn in the present work on the simulation and design of alternative reactor geometries has raised several possible areas of improvement.

7.2.1 Hybrid RANS/LES modeling

It is clear that the accuracy and more fundamental modeling approach of large eddy simulations make it a very promising means of investigating both simple and complex flow configurations. In light of advances in computational power and the availability of LES models in most CFD software, it has become an accessible tool for academics. In the chemical processing industry however, the stringent grid requirements for wall-bounded flows are likely to pose a challenge for the foreseeable future. Various attempts have hence been made to bypass this near-wall layer and model its effects in a global sense. Such wall-models can be categorized into three main approaches, listed according to increasing level of complexity: wall-stress models, zonal approaches and hybrid RANS/LES methods.

The first constitute a relatively simple class of methods that rely on similarity to an equilibrium boundary layer. Instead of applying a no-slip condition on a strongly refined grid, the first grid cell is located in the logarithmic layer ($y^+ > 40$) and is assigned a wall-stress based on its position and an assumed equilibrium wall-law. Though successful in equilibrium flows, wall-stress models understandably loses accuracy in flows involving flow separation and reattachment, as is the case for many practical applications. Among the zonal approaches, the two-layer model by Balaras and Benocci¹ is the most well-known. This method solves simplified two-dimensional turbulent boundary-layer equations on an embedded grid between the first grid point and the wall. The resulting cell-averaged wall-stress can then be used as an instantaneous boundary condition in the first grid cell. Hybrid methods solving the RANS equations in the near-wall inner layer, while employing LES away from the wall, offer even greater flexibility. Various adaptations and improvements to Spalart's detached eddy simulation (DES) approach² have seen successful industrial application in automotive and aeronautics engineering. A comprehensive review on these hybrid RANS/LES methods can be found in the work of Fröhlich³ and Piomelli⁴. It would be interesting to investigate the use of these techniques in the context of pipe flow in order to attain the Reynolds numbers prevalent in industrial steam cracking.

7.2.2 Multi-objective optimization

Once sufficient confidence is achieved in a simulation approach, it should always be the aim of the CFD engineer to strive for design optimization. The present work on enhanced heat transfer in tubular reactors is a clear example of a two-objective optimization problem where the aim is to maximize heat transfer at minimal additional pressure drop. Combining the two objectives into a single objective function allows further simplification, as for example maximization of Nu/f_f and $Nu/f_f^{1/3}$ is common in the field of heat exchangers. The parameters to be optimized can then range from simply having a variable element height, to full geometrical pattern of such elements, or even the shape of these elements itself. With most current grid generation software offering the possibility of batch scripting, the possibilities for automated optimization are limitless. Depending on the scale of the optimization, the number of design parameters and the level of theory involved in the design evaluation phase, optimization can then be performed using either gradient-based or evolutionary algorithms.

7.2.3 Adaptive chemistry methods

The present work only briefly touched on the potential gains of applying on-the-fly chemistry reduction methods for the simulation of steam cracking reactors. While use of the pseudo-steady state approximation (PSSA) is now relatively accepted in the community, other reduction methods have not received this level of attention. Important to note is that the majority of literature on gas-phase chemistry reduction is still focused on the modeling of combustion rather than steam cracking, which are governed by vastly different phenomena and hence do not automatically make equally good use of a certain network reduction method. For example, though the present work successfully applied dynamic mechanism reduction techniques, steam cracking does not exhibit clear ignition/extinction regions. There are hence no clear subsets of the full network that can locally be (de)activated, making such methods only marginally effective.

On the other hand, methods that aim to simply limit the number of rate evaluations can quite easily be adapted between both fields. Adaptive tabulation techniques or cell clustering methods for example offer the potential of significant time savings at virtually no loss of accuracy. Steam

cracking is also a likely candidate to benefit from further dimensionality reduction, beyond just the application of PSSA to the free radicals. It is in fact industrial practice to relate the full product spectrum to just a limited number of severity indices, with the most common being the propene-to-ethene ratio, the ethene-to-ethane ratio and the methane yield. This indicates to some extent the existence of low-dimensional attractors in the thermochemical phase space, which could be identified using techniques such as the intrinsic low-dimensional manifold (ILDM) approach or deep learning algorithms.

7.2.4 Coke formation kinetics

Compared to the complexity of the pyrolysis kinetics used in the present work, relatively simple models were applied for determining the local rate of coke formation, with both the Plehiers et al.⁵ and Reyniers et al.⁶ models being developed over two decades ago. Especially the relation between coke formation and pressure remains unclear throughout these studies, as both linear and cubic dependencies having been reported. While more fundamental approaches using group additivity and ab initio calculations have been pursued⁷, these have not led to easily implemented models for industrial simulation. One of the factors that has complicated development is the difficulty in validating these models with experimental data. Throughout the different experimental setups that were used in these studies, the description of these setups for model validation has traditionally relied on perfectly-stirred or 1D plug flow assumptions. More recent CFD studies on these setups have however demonstrated this assumed uniformity to not be guaranteed⁸, especially for the radical coke precursors. There is hence a definite potential for an improved fundamental modeling of coke formation through a combination of automated network generation with advanced experimental and numerical techniques.

7.2.5 Industrial plant operation

In the present work, computationally costly simulations were performed in order to track the geometrical deformation of the reactor coils under coke formation and its effect on temperatures and product yields. While relevant for determining the performance of 3D reactor technology, perhaps even more important from an operational perspective is the decoking phase. As this involves exothermically burning off the coke layer with an air and/or steam mixture, the potential

for impacting the coil service life makes this is a critical procedure. A lack of understanding in the mechanisms of decoking⁹ have led to often very conservative decoking schemes being followed, which extend the duration of the decoking operation and hence the time off-stream. It would therefore be interesting to see whether the proposed dynamic grid adaptation methods lead to improved insights into this process.

Another interesting perspective for the methods developed in this work is their application in an industrial setting for continuous optimization. Traditionally, industrial steam crackers employ furnace simulation at three different stages of operation: model predictive control simulations running every minute, economic optimization of the entire plant on an hourly basis and finally in a day-to-day evaluation of potential profits from different naphtha sources on the market. Despite these different requirements in calculation frequency, these simulations currently all apply the same level of theory on the reactor level. Significant benefits could hence be expected from the use of more advanced modeling strategies for optimization, whether in the form of true 3D simulations or enhanced “1.5D” approaches that to some degree account for the inhomogeneity inside the reactor.

7.2.6 Combustion modeling

Another aspect that warrants further attention is the modeling of the floor-fired furnace to provide heat flux boundary conditions to the reactor simulation. This was seen quite clearly in the 3D-3D coupled naphtha cracking furnace simulations. Despite the effort in using a non-grey model for the flue gas radiative properties and application of a discrete ordinates method with 32 directions, an underprediction of the industrial thermal efficiency by about 7 % was observed. A number of potential areas of improvement could be identified.

First, improved predictions of the flame shape and heat release profile can be expected from using more fundamental combustion kinetics than merely a two-step reaction. This goes beyond the limitations of the currently applied eddy dissipation/break-up model (EDM), and thus requires turbulence-chemistry to be accounted for by using either the eddy dissipation concept, PDF methods or a laminar diffusion flamelet model. Steady and unsteady laminar flamelet models in particular have shown to be both accurate and efficient for turbulent diffusion flames.

Second, the formation of soot and in particular the effect of soot radiation on the total emitted power requires further examination. While methane is not prone to soot formation in lab-scale flames, it can soot quite heavily during combustion in industrial-scale burners where larger regions of high temperature and fuel-rich conditions coexist. As the industrial fuel also contains soot precursors such as ethene and C4-C6 components, soot radiation could have an important contribution to the flame heat release rate. Third, the non-linearity between radiative emission and temperature can cause the total heat release to be strongly impacted by the turbulent fluctuations in the flue gas. Though much uncertainty remains in how to properly account for this turbulence-radiation interaction, experimental studies have demonstrated between 45-90 % increases in radiative emissions compared to those that would be obtained from the mean values of temperature and absorption coefficients¹⁰.

Improved furnace modeling capabilities may also allow the investigation of some promising routes for further furnace optimization. High emissivity coatings is one example that has been used to effectively transfer heat by radiation in applications ranging from traditional boiler furnaces to heat shields on space vehicles. According to Kirchhoff's law, at equilibrium the emissivity of a body is equal to its absorption. This implies that for any two bodies that exchange radiation, an increase of either emissivity value will reduce the temperature difference between these bodies. In the case of steam cracking, coating either the refractory walls or the reactor tubes to increase its emissivity would hence lead to more heat being transmitted towards the process gas inside the cooler reactor tubes. Based on these considerations, suppliers have reported the potential for 5-10 % fuel savings. This improved efficiency of course also results in a reduction of the flue gas temperature, and a reduced potential for heat recovery in the convective part of the furnace. Retrofitting existing furnaces with these coatings must hence be done with care, as they may affect steam generation capacities or even carry the risk of having feedstock that is not fully evaporated entering the radiant section.

Another interesting development in light of stricter environmental regulation, is oxy-fuel combustion. By burning the fuel using pure oxygen instead of air, NO_x formation is eliminated and a highly concentrated CO₂ stream is produced that may warrant the use of carbon capture and

storage (CCS) methods. Such combustion units could also be made significantly smaller, illustrating the potential for improved modeling strategies in developing these solutions.

References

1. Balaras, E., C. Benocci, and U. Piomelli, *Two-layer approximate boundary conditions for large-eddy simulations*. AIAA Journal, 1996. **34**(6): p. 1111-1119.
2. Spalart, P., W. Jou, M. Strelets, and S. Allmaras. *Comments of feasibility of LES for wings, and on a hybrid {RANS/LES} approach*. in *International Conference on {DNS/LES}*, Aug. 4-8, Ruston, Louisiana. 1997.
3. Fröhlich, J. and D. von Terzi, *Hybrid LES/RANS methods for the simulation of turbulent flows*. Progress in Aerospace Sciences, 2008. **44**(5): p. 349-377.
4. Piomelli, U., *Wall-layer models for large-eddy simulations*. Progress in Aerospace Sciences, 2008. **44**(6): p. 437-446.
5. Plehiers, P.M., G.C. Reyniers, and G.F. Froment, *Simulation of the run length of an ethane cracking furnace*. Industrial & Engineering Chemistry Research, 1990. **29**(4): p. 636-641.
6. Reyniers, G.C., G.F. Froment, F.-D. Kopinke, and G. Zimmermann, *Coke Formation in the Thermal Cracking of Hydrocarbons. 4. Modeling of Coke Formation in Naphtha Cracking*. Industrial & Engineering Chemistry Research, 1994. **33**(11): p. 2584-2590.
7. Wauters, S. and G.B. Marin, *Kinetic Modeling of Coke Formation during Steam Cracking*. Industrial & Engineering Chemistry Research, 2002. **41**(10): p. 2379-2391.
8. Reyniers, P.A., S.A. Sarris, G.B. Marin, and K.M. Van Geem, *Computational Fluid Dynamic Design of Jet Stirred Reactors for Measuring Intrinsic Kinetics of Gas-Phase and Gas-Solid Reactions*. International Journal of Chemical Kinetics, 2016. **48**(9): p. 556-569.
9. Schools, E.M. and G.F. Froment, *Simulation of decoking of thermal cracking coils by steam/air-mixtures*. AIChE Journal, 1997. **43**(1): p. 118-126.
10. Mehta, R.S., M.F. Modest, and D.C. Haworth, *Radiation characteristics and turbulence–radiation interactions in sooting turbulent jet flames*. Combustion Theory and Modelling, 2010. **14**(1): p. 105-124.

Appendix A

EP2017058850 – REACTOR FOR A CRACKING FURNACE

*“I’ll be more enthusiastic about encouraging thinking outside the box
when there’s evidence of any thinking going on inside it.”*

Terry Pratchett (1948 – 2015)

This appendix has been published as :

Van Cauwenberge, D.J., Van Geem, K.M., Floré, J., Marin, G.B., Laib, H. REACTOR FOR A
CRACKING FURNACE. EP2017058850, 2017.

Abstract

The invention relates to a reactor for cracking hydrocarbons wherein the reactor has an inner wall; characterized in that the inner wall comprises a plurality of concave dimples embedded in a surface of said inner wall.

A.1 Field of the invention

Provided herein is a reactor for cracking hydrocarbons, a furnace comprising the reactor for cracking hydrocarbons, and a method for producing light olefins from a hydrocarbon feedstock.

A.2 Background to the invention

In the petrochemical industry, smaller olefins are often produced from a precursor feedstock by a thermal cracking process. This cracking process involves heating up a precursor feedstock comprising larger hydrocarbons. As a result of the increased thermal energy, carbon bonds present in the precursors feedstock will be broken, thereby turning the long-chains of hydrocarbon molecules into shorter, smaller ones. The necessary temperatures to initiate the cracking process may reach up to a thousand degrees, depending on the supplied hydrocarbon and the desired cracked end-product. Usually, other cracking process conditions such as residence time, dilution, flow, pressure, etc., may be tuned to achieve the highest possible yield.

Commonly, the steam cracking process takes place inside a reactor suspended in a large, gas-fired furnace which heats up the reactor from the outside. Often tens to hundreds of these reactors are stacked together in one furnace to increase production capacities up to several thousand kilotons per year (kta). These reactors, sometimes called cracking tubes, are fabricated in many different shapes and sizes in an effort to increase the capacity, improve the selectivity, yield, and/or thermal efficiency of the process.

During steam cracking the precursor feedstock supplied in gas-state flows to the reactor at a high velocity where it is diluted with steam and heated without the presence of oxygen. However, as a

result of this process a deposition of coke, i.e., a solid residue composed of carbon, may build up on the inner wall of the reactor. This deposition of coke has several adverse effects on the productivity of these reactors:

- (1) Coke has a low thermal conductivity, so deposition of coke may lower the thermal efficiency of the system which will in turn require the fuel flow rate to be increased to maintain the same level of production, thus further increasing the coke deposition rate. Moreover, different coke deposition rates across a series of reactors suspended in a common furnace will prevent proper temperature control needed to maintain desired production selectivity. The low thermal conductivity of the cokes layer also results in higher tube metal temperatures, which may reach the design limits of the alloy that is used.
- (2) Sustained deposition of coke may decrease the cross-sectional area of a reactor available for the feedstock gas resulting in a higher process gas velocity and a higher pressure drop over the reactor. To compensate for this pressure drop, the overall pressure inside the reactor will have to be increased, which inadvertently leads to reduced process selectivity towards light olefins because of an increased rate of secondary reactions between those olefins.
- (3) Presence of coke decreases the carbon yield of the cracking process since all the carbon atoms that would otherwise be collected as light olefins are instead incorporated into the coke and are hence lost.

To limit the adverse effects of coke deposition over time a regular shutdown is required to decoke the reactors. The decoking process typically involves taking a whole furnace offline for 1 or more days to oxidize coke depositions and remove them from the inner wall of all the reactors. Consequently, a decoking process drastically decreases the productivity of a furnace by interrupting the run-length and increases the production costs, by stacking material and energy costs needed to perform the decoking process and thereafter restart the cracking process. Furthermore, given the exothermic nature of decoking, thermal damage may occur to the reactors during decoking.

Internal fins such as described in GB969796 may achieve improved heat transfer by increasing the internal surface area. As the exposed reactor surface area increases, however, so does the laminar flow layer in contact with the reactor wall. In this layer, high residence times are coupled with high temperatures, giving rise to significant losses of valuable product yields. Additionally, more of the reactor wall is exposed for formation of coke deposits. Hence, while the thermal performance of the tubes may be improved, the effect on coke formation and run lengths can even be negative.

US5950718 aims to resolve these issues by adding convex elements to the reactor wall in order to break up the laminar layer and promote turbulent mixing. While such devices may improve heat transfer coefficient, they typically suffer from excessive drag, as potential energy in the form of pressure is transformed into turbulent kinetic energy. Additionally, such obstructions in the flow induce recirculating flow patterns with locally high residence times which are prone to coke formation. The separate welding of each of the elements also adds an additional maintenance risk, as elements can break off because of the high local thermal and shear stresses they are exposed to.

Accordingly, there is a need for new technologies that allow for an increase of the run-lengths of steam cracking reactors and furnaces. There is also a need for technologies that aim to improve the olefin selectivity during the thermochemical process. There is also a need for technologies that aim to improve heat transfer. There is also a need for technologies that aim to decrease thermal stress. There is also a need for technologies that aim to operate at a higher severity by increasing the maximal process gas temperature. There is also a need for technologies that aim to operate at a higher throughput by increasing the maximum load. There is also a need for technologies that aim to limit the occurrence and/or magnitude of a pressure drop.

A.3 Detailed description of invention

Before the present system and method of the invention are described, it is to be understood that this invention is not limited to particular systems and methods or combinations described, since such systems and methods and combinations may, of course, vary. It is also to be understood that

the terminology used herein is not intended to be limiting, since the scope of the present invention will be limited only by the appended claims.

As used herein, the singular forms "a", "an", and "the" include both singular and plural referents unless the context clearly dictates otherwise. The terms "comprising", "comprises" and "comprised of" as used herein are synonymous with "including", "includes" or "containing", "contains", and are inclusive or open-ended and do not exclude additional, non-recited members, elements or method steps. It will be appreciated that the terms "comprising", "comprises" and "comprised of" as used herein comprise the terms "consisting of", "consists" and "consists of".

The recitation of numerical ranges by endpoints includes all numbers and fractions subsumed within the respective ranges, as well as the recited endpoints. The term "about" or "approximately" as used herein when referring to a measurable value such as a parameter, an amount, a temporal duration, and the like, is meant to encompass variations of +/-10% or less, preferably +/-5% or less, more preferably +/-1% or less, and still more preferably +/-0.1% or less of and from the specified value, insofar such variations are appropriate to perform in the disclosed invention. It is to be understood that the value to which the modifier "about" or "approximately" refers is itself also specifically, and preferably, disclosed.

Whereas the terms "one or more" or "at least one", such as one or more or at least one member(s) of a group of members, is clear *per se*, by means of further exemplification, the term encompasses *inter alia* a reference to any one of said members, or to any two or more of said members, such as, *e.g.*, any ≥ 3 , ≥ 4 , ≥ 5 , ≥ 6 or ≥ 7 etc. of said members, and up to all said members.

All references cited in the present specification are hereby incorporated by reference in their entirety. In particular, the teachings of all references herein specifically referred to are incorporated by reference.

Unless otherwise defined, all terms used in disclosing the invention, including technical and scientific terms, have the meaning as commonly understood by one of ordinary skill in the art to

which this invention belongs. By means of further guidance, term definitions are included to better appreciate the teaching of the present invention.

In the following passages, different aspects of the invention are defined in more detail. Each aspect so defined may be combined with any other aspect or aspects unless clearly indicated to the contrary. In particular, any feature or embodiment indicated as being preferred or advantageous may be combined with any other feature or embodiment indicated as being preferred or advantageous.

Reference throughout this specification to “one embodiment” or “an embodiment” means that a particular feature, structure or characteristic described in connection with the embodiment is included in at least one embodiment of the present invention. Thus, appearances of the phrases “in one embodiment” or “in an embodiment” in various places throughout this specification are not necessarily all referring to the same embodiment, but may. Furthermore, the particular features, structures or characteristics may be combined in any suitable manner, as would be apparent to a person skilled in the art from this disclosure, in one or more embodiments. Furthermore, while some embodiments described herein include some but not other features included in other embodiments, combinations of features of different embodiments are meant to be within the scope of the invention, and form different embodiments, as would be understood by those in the art. For example, in the appended claims, any of the claimed embodiments can be used in any combination.

In the present description of the invention, reference is made to the accompanying drawings that form a part hereof, and in which are shown by way of illustration only of specific embodiments in which the invention may be practiced. Parenthesized or emboldened reference numerals affixed to respective elements merely exemplify the elements by way of example, with which it is not intended to limit the respective elements. It is to be understood that other embodiments may be utilised and structural or logical changes may be made without departing from the scope of the present invention. The following detailed description, therefore, is not to be taken in a limiting sense, and the scope of the present invention is defined by the appended claims.

The term “steam cracking process” refers to a chemical reaction wherein one or more carbon bonds contained within a precursor feedstock are broken by thermal energy to split the large molecules of a precursor feedstock into shorter, preferably unsaturated molecules of a product. The term “pyrolysis” refers to a thermochemical decomposition of organic material at elevated temperatures in the absence of oxygen (or any halogen); it is a form of thermolysis and comprises any terms which may be considered related or synonymous by those skilled in the art. More details on steam cracking may be found in Zimmermann, H.; Walzl, R., Ethylene. In Ullmann's Encyclopedia of Industrial Chemistry, Wiley-VCH Verlag GmbH & Co. KGaA: 2000; pp 469-493, which is hereby incorporated in its entirety by reference.

The term “precursor feedstock” refers to a group of organic compounds which are supplied to the reactor where they undergo a thermochemical decomposition to be transformed into a product; preferably the precursor feedstock comprises hydrocarbons that are split into (light) olefins by a steam cracking process. Examples of suitable precursor feedstock may be selected from the group comprising: ethane, propane, butane, LPG, (renewable) naphtha, light gas oil, vacuum gas oil, gas condensates up to, (hydrotreated) crude oil, and so on, and/or co-cracking of combinations thereof. Any feedstock exhibiting coking (depositions) would particularly benefit from the present invention.

The term “product” refers to a group of organic compounds that are obtained from the reactor after a thermochemical reaction has transformed the precursor feedstock. Preferably the product comprises (light) olefins obtained from hydrocarbons broken by a steam cracking process. Examples of desired product may be selected from the group comprising: ethylene, propylene, benzene, butadiene, and so on, and/or combinations thereof.

The term “reactor” as used herein refers to a device or structure according to the present invention for containing a chemical reaction; preferably said chemical reaction involves steam cracking for olefin production. The term “inner wall” as used herein refers to the surface area comprised within the reactor structure; preferably in contact with the space wherein a chemical reaction takes place. The term “outer wall” as used herein refers to the surface area comprised outside the reactor structure; preferably with the space wherefrom thermal energy is supplied to

the reactor. Examples of varying shapes of reactor tubes may be found in van Goethem, M. W. M.; Jelsma, E., Numerical and experimental study of enhanced heat transfer and pressure drop for high temperature applications. *Chem. Eng. Res. Des.* 2014, 92 (4), 663-671, which is hereby incorporated in its entirety by reference.

The term “furnace” as used herein, also known as “oven”, refers to a device or structure comprising one or more reactors according to the present invention for containing a chemical reaction; preferably said chemical reaction involves steam cracking for olefin production. The furnace is adapted to be suitable for (very) high-temperature heating. The general structure of a furnace is known in the art and may further comprise one or more structures configured for heating and heat distribution; for example, heating place or fireplace, a chimney, connector pipes, and so on. More details on furnace designs suitable for steam cracking may be found in Zimmermann, H.; Walzl, R., Ethylene. In *Ullmann's Encyclopedia of Industrial Chemistry*, Wiley-VCH Verlag GmbH & Co. KGaA: 2000; pp 482-491, which is hereby incorporated in its entirety by reference.

The term “dimple” as used herein refers to a concave depression in the surface of an inner wall of a reactor; preferably wherein the dimple is a concave depression; preferably wherein the dimple is hollow with regards to the inner area of a reactor. The term “concave” as used herein refers to a surface area that curves inwards like the interior of a sphere or spheroid; it comprises the terms recessed, indented, inward, and so on. The term “pattern” as used herein refers to an ordered arrangement of dimples in a regular and repeated format distinguishable by a model or a design.

The Reynolds number (Re) is defined as the ratio of momentum (or inertial) forces to viscous forces, and thus consequently quantifies the relative importance of these two types of forces for given flow conditions. The momentum forces can be related to the flow velocity and a length scale. In the case of a cylindrical tube, this leads to the following definition: $Re = uD/\nu$, with ν the kinematic viscosity.

According to a first aspect, the invention encompasses a reactor for cracking hydrocarbons wherein the reactor has an inner wall; characterized in that the inner wall comprises a plurality of concave dimples embedded in a surface of said inner wall. Preferably, all dimples are concave.

Preferably, the reactor is a pyrolysis, thermal cracking, or steam cracking reactor. In some embodiments, the reactor is a thermochemical reactor. In some embodiments, the reactor is a reactor for thermolysis, more preferably a reactor for pyrolysis. In the most preferred embodiments the reactor is a steam cracking reactor.

Preferably, the reactor wall is essentially free of catalyst, preferably free of catalyst position within the reactor. For example, in a reforming reactor, the reactor will typically comprise catalyst positioned within the reactor. A pyrolysis, thermal cracking, or steam cracking reactor is usually free from having catalyst inside the reactor. However, the wall itself may comprise elements that have catalytic activity.

Preferably, the reactor is configured to withstand temperatures of 700 - 1200°C. A pyrolysis, thermal cracking, or steam cracking reactor is usually configured to withstand such temperatures. For example the reactor may be built from CrNi + steel, Cr + steel, or Al alloys.

Preferably, the reactor comprises a decoking system. Suitable decoking systems may be found in US20130239999A1 in paragraphs [0008] and [0009]. These paragraphs are hereby incorporated by reference. Suitable decoking systems may also be found in WO2016032730A, paragraph [0006]. This paragraph is hereby incorporated by reference.

In some embodiments, the decoking system comprises an air inlet and/or outlet. In some embodiments, the decoking system comprises a steam inlet and/or outlet. In some embodiments, the decoking systems comprises an air inlet and a steam inlet, preferably also an air outlet and a steam outlet. The outlet may release air and/or steam into the atmosphere.

The reactor comprises a reactor wall that partly seals of the “inside area” from the “outside area”; preferably, a reactor wall has at least an entry point and an exit point which allow a flow of molecules to pass through the reactor. The entry point through which the precursor feedstock is supplied to the reactor is hereby referred to as the “entry”, and the exit point through which the product is extracted and/or collected is hereby referred to as the “exit”. A reactor may consist of a plurality of entry points for each exit point. The reactor walls connected to these entry points are

then joined by one or multiple manifold structures at one or more locations downstream of the entry points.

In some embodiments, the reactor has an inner wall which is connected in space with the inside area of the reactor; preferably the inside area is the space where a thermochemical reaction takes place; more preferably is the space where steam cracking is performed. In some embodiments, the reactor has an outer wall which is connected in space with the outside area of the reactor; preferably the outside area is the space wherefrom energy is supplied to the reactor; more preferably the energy is supplied in the form of heat; most preferably the energy is supplied in the form of heat by a furnace.

Preferably, the inner wall comprises a plurality of concave dimples. In some embodiments, the reactor inner wall comprises a plurality of hollow dimples; preferably the dimples are recessed inward into the inner wall; most preferably the dimples are concave. In some embodiments, the reactor inner wall is characterized in that the inner wall comprises a plurality of concave dimples embedded in the surface of said inner wall; preferably the dimples form a part of the inner wall surface.

In some embodiments, the reactor is characterized in that the inner wall comprises a plurality of concave dimples embedded in a surface of said inner wall

By providing dimples inside the inner wall of a reactor several advantages are gained, such as an enhanced heat transfer and a reduced deposition rate. By enhancing the heat transfer in a reactor it may be possible to operate at a higher severity, i.e., temperature, which may allow a higher ethylene and total olefin selectivity, while maintaining the same throughput and run length; and/or operate at an increased load, which may allow more throughput for the same run length and severity. Additionally, by reducing the coke deposition rate it may be possible to increase the run lengths for a reactor thereby increasing the productivity of a reactor, increase the cost and energy efficiency of steam cracking, and obtain a higher yield rate by lowering the loss of carbon into deposited coke. Additionally, by enhancing the heat transfer in a reactor it may be possible to operate at reduced reactor wall temperatures thereby decreasing carburisation and increasing the life time of the reactor material.

In some embodiments, a secondary flow pattern is generated by the dimples. This flow pattern is characterized by entrainment of the process gas into the dimple by means of a suction force, due to the generation of a low pressure zone inside the cavity. Additionally, a rotating flow is generated inside the cavity, after which the hot process gas is ejected again towards the core of the tube. In some preferred embodiments, this ejected fluid leaves the dimple in a direction tangentially to the main flow, enhancing both radial and tangential mixing of the process gas (Figure A-7). In this manner, the existence of zones with high local residence times and temperatures may be avoided, as fluid is continuously ejected. This improved distribution of residence times can be expected to result in improved product yields, as demonstrated in A.4.4.

In a more preferred embodiment of the present invention, the described pattern exhibits an oscillatory motion. This implies that while the mean flow follows the axial direction, the fluid near the reactor wall has a tangential component that shifts direction at steady intervals in a self-sustained manner. The shifting of the flow direction can have important implications for the fouling in these reactors. As the direction of the shear on the surface will continuously change, it is expected that any coke formed on the walls will break off more easily because of the dimples. In this manner, the dimpled embodiment is expected to exhibit a “self-cleaning” effect. This was demonstrated in A.4.5, from which it can be seen that the surface parameters play an important role in obtaining this preferred flow pattern.

In some embodiments, the reactor is a thermochemical reactor. In some embodiments, the reactor is a reactor for thermolysis, more preferably a reactor for pyrolysis. In the most preferred embodiments the reactor is a steam cracking reactor.

In some embodiments, each dimple is characterized by a dimple depth e and a dimple diameter d . Preferably, each dimple of the plurality of concave dimples is characterized by a dimple depth e and a dimple diameter d . The subset of dimples from a plurality of dimples that share an equal dimple depth e are hereby referred to as dimples with “common dimple depth”. The subset of dimples from a plurality of dimples that share an equal dimple diameter d are hereby referred to as dimples with “common dimple diameter”.

The dimple depth e is measured as the distance between the cylindrical inner wall surface and a deepest point inside said dimple furthest away from the cylindrical surface; preferably the deepest point coincides with the centre of a dimple, but it need not be, should any secondary structure be situated within the dimple. In some embodiments, the dimple depth e is at least 0.01 cm and at most 1.0 cm, preferably at least 0.05 cm and at most 0.8 cm, most preferably at least 0.1 cm and at most 0.5 cm.

The dimple diameter d is measured as the maximal distance between two antipodal points of the dimple, i.e., diametrically opposite points, lying on the edge of a dimple running as a straight line segment while passing through the center of the dimple. In some embodiments, the dimple diameter d is at least 0.1 cm and at most 5.0 cm, preferably is at least 0.2 cm and at most 3.0 cm; most preferably is at least 0.5 cm and at most 2.0 cm.

In some embodiments, at least a portion of the plurality of dimples has a common dimple depth and a common dimple diameter; in some embodiments every dimple in a plurality of dimples has a common dimple depth and a common dimple diameter. In some embodiments, at least a portion of the plurality of dimples has a common dimple depth but may have a different dimple diameter; in some embodiments every dimple in a plurality of dimples has a common dimple depth but at least a portion of the plurality of said dimples has a different dimple diameter. In some embodiments, at least a portion of the plurality of dimples has a common dimple diameter but may have a different dimple depth; in some embodiments every dimple in a plurality of dimples has a common dimple diameter but at least a portion of the plurality of said dimples has a different dimple depth. In some embodiments, at least a portion of the plurality of dimples has a different dimple depth and a different dimple diameter; in some embodiments every dimple in a plurality of dimples has a different dimple depth and a different dimple diameter.

In some embodiments, two or more portions of dimples forming a plurality of dimples have a common dimple depth and a common dimple diameter. Preferably, the two or more portions of dimples forming a plurality of dimples with a common dimple depth and a common dimple diameter are configured such that they are comprised in different areas of a reactor inner wall that would benefit from different dimple parameters. By implementing portions of dimples with

different diameters and/or depths the proportions of the dimples may be adjusted to certain areas of the reactor; for instance certain hot-spots around reactor bends or curves where there is a higher rate of steam cracking, coke deposition, higher flow of molecules and/or pressure drops, may benefit more from deeper and/or wider dimples than areas close to the reactor exit where there is a lower rate. For example, shallow dimples, i.e., a dimple depth of 0.1 cm, may be situated in areas where the reactor forms a bend, while deeper dimples, i.e., a dimple depth of 0.3 cm, may be situated in areas where the reactor runs straight. For example, shallow dimples may be situated in the inlet tubes of the reactor (lower process temperatures, reduce pressure drop), while deeper dimples may be situated in hotspots or in the outlet tubes. This customization of dimple parameters may have advantages for run-lengths, selectivity, heat transfer, pressure drop, throughput and life cycle of the reactor.

In some embodiments, some dimples of the plurality of concave dimples are further characterized by a depth-to-diameter ratio (*DDR*), defined as

$$DDR = \text{dimple depth } e / \text{dimple diameter } d; \text{ (or } DDR = e/d).$$

In a further embodiment, each dimple forming a plurality of dimples is characterized by a *DDR*.

Preferably, the *DDR* is at least 0.01 and at most 0.5, preferably at least 0.05 and at most 0.3; more preferably at least 0.1 and at most 0.2; more preferably at least 0.15 and at most 0.25, for example about 0.20. In some embodiments, the *DDR* is at least 0.01 and at most 0.5, preferably at least 0.05 and at most 0.4; more preferably at least 0.1 and at most 0.3. Every portion of dimples from a plurality of dimples that share a common dimple depth and a common dimple diameter are hereby referred to as dimples with “common dimple *DDR*”.

The magnitude of *DDR* for a dimple is related to a degree of concaveness of a dimples inner surface. The level of concaveness may have an influence of the interaction of a dimple with the molecules present in the inner segment of a reactor. The altering of the level of concaveness may have advantages for run-lengths, heat transfer, throughput of a reactor.

In some embodiments, the shape of one or more dimples is characterized by a geometrical feature; in a further embodiment the shape of each dimple of the plurality of dimples is characterized by a geometrical feature. Preferably, the geometrical features are further characterized by a non-linear edge, such as a smooth, rounded or curved edge, preferably as in at least a section of a sphere, spheroid, ovoid, or a teardrop shape or combination thereof. In some embodiments, at least a portion of dimples forming a plurality of dimples is characterized by a similar geometrical feature. In some embodiments, each dimple forming a plurality of dimples is characterized by a similar geometrical feature.

In some embodiments, the shape of the teardrop projected on an axial section can be characterized by the parametric equation $x(t) = a \cdot \cos(t)$, $y(t) = b \cdot \sin(t) \sin^m(t/2)$ with m at least 0.5 and at most 5. Other preferred shapes include the piriform curve $x(t) = a \cdot (1 + \sin(t))$, $y(t) = b \cdot \cos(t) \cdot (1 + \sin(t))$; or the dumbbell curve $x(t) = a \cdot t$, $y(t) = a \cdot t^2 \cdot (1 - t^2)^{-1/2}$.

In some preferred embodiments, two or more portions of dimples forming a plurality of dimples are characterized by a similar geometrical feature. Preferably, the two or more portions of dimples forming a plurality of dimples characterized by a similar geometrical feature are configured such that they are comprised in different areas of a reactor inner wall that would benefit from different dimple geometry. By implementing portions of dimples with different geometrical features the geometry of the dimples may be adjusted to certain areas of the reactor, for instance certain hot-spots around reactor bends or curves where there is a higher rate of steam cracking, coke deposition, higher flow of molecules and/or pressure drops, may require more spherical dimples than areas close to the reactor exit where there is a lower rate. For example, spherical dimples may be situated in areas where the reactor forms a bend, while teardrop or oval dimples may be situated in areas where the reactor runs straight. This customization of geometrical features may have advantages for run-lengths, heat transfer, throughput and life cycle of the reactor.

In some embodiments, one or more dimples, preferably one or more concave dimples, comprise two or more secondary curvature areas of a different curvature radius than one or more other concave dimples situated around or on the one or more concave dimples. In an exemplary

embodiment additional protruding semicircles may surround the dimple, preferably these semicircles are aligned parallel to the dimple edges with their rounded edge convex to the gas flow. In another exemplary embodiment, an additional flat or convex area may be situated within the dimple, preferably not protruding outside of the surface area of the dimple.

The addition of two or more curvature areas around or inside the dimple may result in additional advantages for run-lengths, heat transfer, throughput of the reactor on top of the advantages reported for the implementation of a plurality of dimples without secondary curvature areas, for a similar pressure loss.

In some embodiments, at least a portion of a plurality of dimples is arranged in a pattern. In some embodiments, all of the dimples of a plurality of dimples are arranged in a pattern.

In some embodiments, at least a portion of a plurality of dimples are arranged in two or more patterns. The application of multiple patterns may be limited to certain areas within the reactor, such as using a different patterns for the entry, the central area, or the exit of a reactor; or alternatively, on opposite sides within a reactor, for example during a bend or a twist of the reactor a pattern may be used on the long bend and another pattern may be used on the opposite short bend. In some embodiments, two or more patterns may be intermixed thereby forming new patterns designs. In some embodiments, patterns may also be used to guide the gas flow within the reactor tube, such as with linear patterns alongside a reactor wall.

Examples of suitable patterns include: a linear pattern, staggered, crossed, and so on. Certain patterns may have improved or decreased effects on heat transfer, pressure drops or deposition rates. The arrangement of dimples into patterns along the inner wall may result in additional advantages for run-lengths, selectivity, heat transfer, throughput of the reactor.

The portions of the reactor inner wall not covered by any dimple are from hereupon referred to as “smooth”. In some embodiments, at least a portion of the inner wall is smooth. For certain regions within the reactor the addition of dimples may have little to no beneficial effects, such regions may show a low concentration of deposition precursors or deposition rate. The addition of dimples on these regions would only make a reactor more expensive, therefore the

implementation of smooth regions may have advantages for the production and production costs. Additionally, certain regions of the reactor may suffer from a decreased structural integrity due to a thinning of the inner wall, therefore these regions may strategically be left smooth to decrease the chances of any reactor damage and increase the lifetime of said reactor.

In some embodiments, certain regions may be configured to be smooth to better implement certain advantages of dimples and dimple patterns. For example, certain flow directions may be redirected by using dimples in a pattern to divert flow from a certain reactor wall region and have it follow the direction of smooth regions. In some embodiments, certain area such as angles, bends or twists may require smooth areas to improve flow of process gas.

The term “area coverage” are used herein is the percentage of total area of the inner wall covered by dimples, defined as $AC (\%) = \text{total area of the inner wall covered by dimples} / \text{total area of the inner wall} * 100$. In some preferred embodiments, the AC is at least 1% and at most 99%, more preferably at least 20% and at most 90%. The AC may not necessarily be a critical design parameter but may be a result of the distances between subsequent dimples, related to the dimple diameter and pattern, and/or aforementioned designs of dimples and smooth areas depending on the reactor region, i.e., entry, exit, bends, twists, angles, etc.

In some embodiments, the reactor has a tubular shape with a certain reactor length, inner diameter, outer diameter and wall thickness. In a preferred embodiment for maximal product selectivity the tubular reactor has a linear shape. However, other embodiments exists as well such a tubular reactors with multiple passes connected by bends, twists, etc. for reasons of thermal efficiency and reactor life cycle.

The reactor may be characterized by a reactor length, preferably wherein the length is at least 10m and at most 400m, for example at most 100m. The reactor may be further characterized by an inner diameter, corresponding with the diameter from two antipodal points along the inner wall of the reactor. The inner diameter is preferably at least 2 cm to at most 49 cm; more preferably at least 2.5 cm and at most 29 cm; most preferably at least 3 cm and at most 15 cm. The reactor may be further characterized by an outer diameter, corresponding with the diameter from two antipodal points along the outer wall of the reactor. The outer diameter is preferably at

least 3 cm and at most 50 cm; more preferably at least 4 cm and at most 30 cm; most preferably at least 5 cm and at most 17 cm. The reactor may be further characterized by a wall thickness, corresponding to half the difference between the outer diameter and the inner diameter, wherein the wall thickness is preferably at least 0.3 cm and at most 2.0 cm; more preferably at least 0.4 cm and at most 1.5 cm; most preferably at least 0.5 cm and at most 1 cm. The length, inner and outer diameter, and by extension the wall thickness, may be adjusted for reasons of process optimization, run-length, selectivity and thermal efficiency.

In some embodiments, the inner wall is substantially thicker than the dimple depth e ; otherwise structural and material integrity might be compromised resulting from the intense thermal energy present during a thermal cracking process.

A thicker reactor wall may result in lower thermal efficiency, and additionally, may be more expensive and difficult to produce, transport and install. Therefore an optimal design will seek to optimize the wall thickness to the maximal or average dimple depth.

The inventors have found that maintaining the minimal wall thickness constant with regards to the original design wall thickness, i.e. $t-e \approx t_0$, shows the best trade-off between structural integrity to thermal efficiency.

In some embodiments, a reactor inner wall may comprise a metal, a metal alloy, a ceramic, and/or a combination thereof. In a preferred embodiment, a reactor inner wall may comprise Ni-Cr-Fe-Al alloys, or ceramics.

In some embodiments, the inner wall may comprise additional post-fabrication treatments in the form of oxide layers or coatings in order to reduce the deposition of solid material on the inner wall and increase both the run length and the reactor life cycle. Barrier coating layers may contribute to the passivation of catalytic sites, reducing the catalytic deposition process. Catalytic coating layers may also contribute by gasifying already deposited layers. Alternatively, suitable coatings may also be procured from chemical companies such as BASF Qtech or GE (General Electric).

In some embodiments, the reactor inner wall comprises the same material as the reactor, the reactor wall, and/or the reactor outer wall.

In some embodiments, a dimple and/or the plurality of dimples may comprise a metal, a metal alloy, a ceramic, and/or a combination thereof. In some preferred embodiments, the plurality of dimples comprise the same material as the reactor; more preferably Ni-Cr-Fe-Al alloys, or ceramics.

In some preferred embodiments, the dimples are arranged in rows, preferably in a hexagonal pattern. The hexagonal pattern may be defined by the distance between two dimples t_1 within one row or by the distance between staggered rows of dimples t_2 (shown in Figure A-1). In a particular embodiment parameter t_1 refers to the azimuthal distance between neighbouring dimples and can be calculated from the number of dimples per cross section n and the tube diameter D as $\pi D/n$; t_2 refers the distance between subsequent dimple rows in the direction of the flow, positioned at a staggering angle γ from each other.

In some embodiments, the depth of the dimples e (shown in Figure A-2) is at least 0.5 mm, preferably at least 1.0 mm, preferably at least 1.5 mm, preferably at least 2.0 mm, for example at least 2.5 mm. In some embodiments, the diameter of the dimples d (shown in Figure A-1-8) is at least 5.0 mm, preferably at least 7.5 mm, preferably at least 10.0 mm, preferably at least 12.5 mm, for example at least 15.0 mm. In some embodiments, the distance t_1 is at least 5.0 mm, preferably at least 10.0 mm, preferably at least 15.0 mm, preferably at least 20.0 mm, preferably at least 25.0 mm, for example at least 30.0 mm, for example at least 35.0 mm. In some embodiments, the number of dimples per cross section is at least 3, preferably at least 5, for example at least 8. In some embodiments, the distance t_2 is at least 5.0 mm and at most 30 mm, preferably at least 10.0 mm and at most 20 mm, for example about 15.0 mm. Such embodiments have an improved heat transfer characteristic.

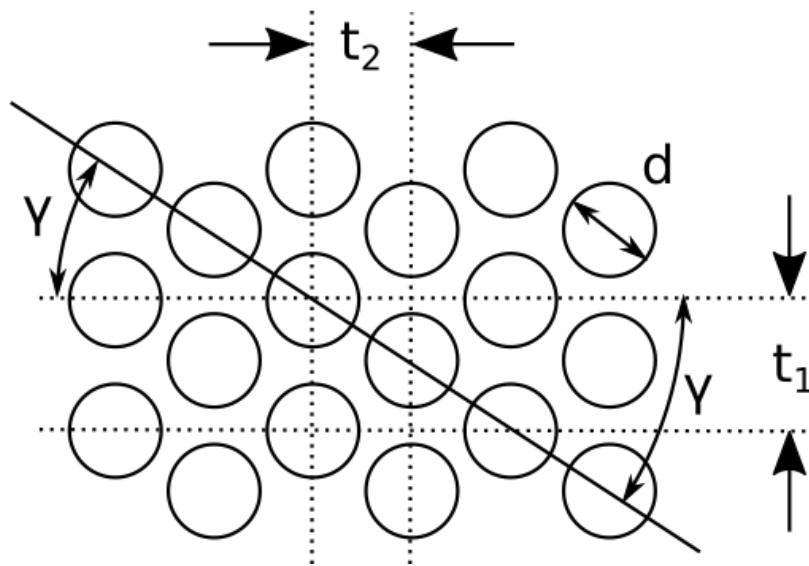


Figure A-1: Development of the inner surface of a tube of the invention for illustrating an embodiment of a dimple arrangement formed on a reactor inner surface. In this figure parameter d refers to the dimple diameter (measured in the direction of the flow). t_2 is the distance between subsequent dimple rows in the direction of the flow, positioned at a staggering angle γ from each other. Parameter t_1 refers to the azimuthal distance between neighbouring dimples and can be calculated from the number of dimples per cross section n and the tube diameter D as $\pi D/n$.

In some embodiments, the depth of the dimples e (shown in Figure A-2) is at most 2.5 mm, preferably at most 2.0 mm, preferably at most 1.5 mm, preferably at most 1.0 mm, for example at most 0.5 mm. In some embodiments, the diameter of the dimples d (shown in Figure A-1/2/3) is at most 15.0 mm, preferably at most 12.5 mm, preferably at most 10.0 mm, preferably at most 7.5 mm, for example at most 5.0 mm. In some embodiments, the number of dimples per cross section is at most 64, preferably at most 16, for example at most 8. In some embodiments, the distance t_1 is at most 35.0 mm, preferably at most 30.0 mm, preferably at most 25.0 mm, preferably at most 20.0 mm, preferably at most 15.0 mm, for example at most 10.0 mm, for example at most 5.0 mm. In some embodiments, the distance t_2 is at most 15.0 mm, preferably at most 10.0 mm, for example at most 5.0 mm. Such embodiments maintain a decent friction factor.

In some embodiments, the depth of the dimples e (shown in Figure A-2) is at least 1.0 mm, preferably at least 1.5 mm, preferably at least 2.0 mm, for example at least 2.5 mm. In some embodiments, the diameter of the dimples d (shown in Figure A-1/2/3) is at least 5.0 mm,

preferably at least 7.5 mm, preferably at least 10.0 mm, preferably at least 12.5 mm, for example at least 15.0 mm. In some embodiments, the number of dimples per cross section is at least 3, preferably at least 5, for example at least 8. In some embodiments, the distance t_2 is at least 5.0 mm and at most 30 mm, preferably at least 10.0 mm and at most 20 mm, for example about 15.0 mm. In some embodiments, the distance t_1 is at least 5.0 mm, preferably at least 10.0 mm, preferably at least 15.0 mm, preferably at least 20.0 mm, preferably at least 25.0 mm, for example at least 30.0 mm, for example at least 35.0 mm. In some embodiments, the dimples have an AC of at least 10% and at most 90%. In some embodiments, the dimples have an AC of at least 15% and at most 40%. In some embodiments, the dimples have an AC of at least 50% and at most 90%. Such embodiments have an improved thermal enhancement factor.

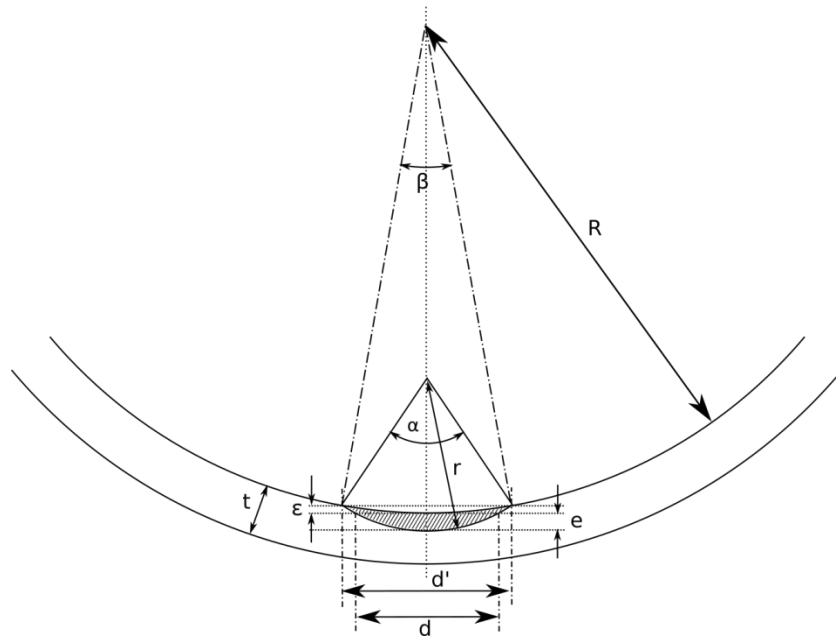


Figure A-2: View in cross-section of a dimple on a curved cylindrical surface for illustrating the different parameters of an individual dimple; described further in A.4.1. In this drawing a tube with radius R and wall thickness t is shown on which a dimple with spherical shape and radius r is imprinted. The angles α and β correspond to the subtended angle of the dimple arc from respectively the dimple centre and the tube centre. Due to the curved surface of the cylindrical tube, the dimple diameter d in the streamwise direction is different from the apparent diameter d' in the azimuthal direction. Additionally, the apparent depth $\epsilon+e$ may be larger than the true dimple depth e because of the curvature of the tube.

According to a second aspect, the invention relates to a furnace, comprising a reactor according to the first aspect, and preferred embodiments thereof. In some embodiments, one or more reactors comprising a plurality of dimples as described within the present invention on their respective inner wall are suspended in a common furnace.

By incorporating tens to hundreds of said reactors together in one furnace the production capacities may be increased up to several ten thousands kilotons per year (kta) while keeping the thermal costs, i.e., costs to heat up the reactors, sufficiently low to maintain a proper thermal efficiency. Large furnaces may be able to produce 500-700 tons of high value chemicals per day. The increased run lengths may result in an additional 10 to 30 production days per year by avoiding between 5 to 10 decoking cycles, corresponding with an additional production of 5 to 20 kta.

According to a third aspect, the invention relates to a method for producing a reactor according to the first aspect of the invention, and preferred embodiments thereof. In some embodiments, the plurality of dimples may be formed on the inner wall of a reactor by methods of moulding, spuncasting, excavation and/or deposition.

The production method of moulding may have benefits for production times as the reactor may be produced together with the dimples. In a first step a reactor may first be produced by casting the preferred material into a reactor mould comprising the inverted dimples, then in a next step the reactor may be folded to form a tubular shape characteristic of a tubular reactor used for thermal cracking.

The production method of spuncasting may have added benefits for production times as it allows the inner reactor to be formed separately in a rotating canister and be pressed against the outer wall of the canister by the centrifugal forces. This method is particularly effective in obtaining reactor with a low level of impurities, and hence better structural integrity.

The production method of excavation may have benefits for ease of production by allowing the reactor wall to be formed first, followed by an excavation of dimples using automated machinery. This method may be more suited for creating concave dimples.

The production method of deposition may allow the reactor wall to be formed separately from a layer comprising a plurality of concave dimples. The reactor wall and the separate layer could then be combined to form one structure, perhaps by means of thermal bonding. As a result the separate layer could form the inner wall of the reactor after bonding. This method may have benefits for ease and speed of production by allowing both structures to be produced simultaneously. In a preferred embodiment both the reactor and the separate layer comprise the same material as to prevent different rates of thermal expansion to jeopardize the structural integrity of the reactor tube during thermal cracking.

The choice between above described methods may be related to the choice of reactor materials (e.g. Ni-Cr-Fe-Al alloys, or ceramics). For example, the method of spuncasting is in particular well suited for producing metallic reactors but not for ceramic reactors. However, certain methods may require a combination of materials during the production process. For example, ceramic mold casting is a method which involves a group of metal casting processes that use a ceramics as the mold material.

The choice between above described methods may also be related to the desired reactor dimensions and structural properties. For example, the methods of spuncasting or moulding may be suited for producing reactors with a length of at least 10 m to at most 400 m; however, the method of excavation may be less suited for producing very long (>300m) reactors due to increased production times.

According to a fourth aspect, the invention relates to a method for producing light olefins in a reactor according to the first aspect of the invention, and preferred embodiments thereof, or in a furnace according to the second aspect of the invention, and preferred embodiments thereof. Preferably, the method comprises the step of cracking the hydrocarbon feedstock into light olefins at a temperature of at least 700°C and at most 900°C. By using higher temperatures selectivity towards lighter olefins can be obtained. Performing the method in the presence of steam at low pressures (approximately between 2 to 4 bar) further aids in reducing unwanted side reactions and improving product selectivity. Additional additives in the form of phosphorous, sulphur- or silicon-containing compounds can reduce this even further. More details on steam

cracking conditions may be found in Zimmermann, H.; Walzl, R., Ethylene. In Ullmann's Encyclopedia of Industrial Chemistry, Wiley-VCH Verlag GmbH & Co. KGaA: 2000; pp 469-482, which is hereby incorporated in its entirety by reference.

In some embodiments, the method comprises a decoking step. Suitable decoking steps may be found in US20130239999A1 in paragraphs [0008] and [0009]. These paragraphs are hereby incorporated by reference. Suitable decoking steps may also be found in WO2016032730A, paragraph [0006]. This paragraph is hereby incorporated by reference.

In some embodiments, the decoking step comprises the introduction of air into the reactor. In some embodiments, the decoking step comprises the introduction of steam into the reactor.

In some embodiments, the decoking step comprises the introduction of air and steam into the reactor.

In some embodiments, the method is for producing propylene.

Embodiments of the invention may allow the use of higher operating temperatures in order to increase reactor throughput or product selectivity. Increases in operating pressure are expected to remain minimal with careful selection of the design parameters with even the potential for a decrease in pressure at later stages in the run due to the decreased deposition rates.

A.4 Examples

A.4.1 Properties and dimensions of dimples

To better illustrate the examples, a reference is made to Figure A-2 and Figure A-3, which demonstrate the properties and dimensions of a dimple design. In particular, Figure A-2 depicts a cross-section of a dimple on a curved cylindrical surface; Figure A-3 illustrates the design of a dimple through application of three concentric curvature regions S1, S2 and S3 with respective curvature $1/r_1$, $-1/r_2$ and $-1/r_3$.

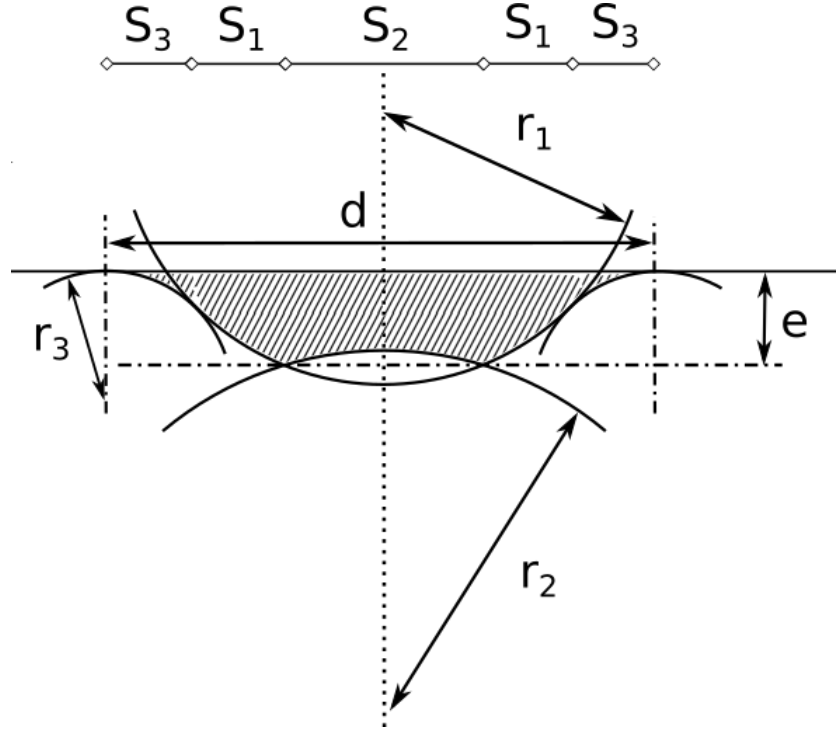


Figure A-3: Design of a dimple with potentially reduced pressure losses through application of three concentric curvature regions S1, S2 and S3 with respective curvature $1/r_1$, $-1/r_2$ and $-1/r_3$. In this case the dimple depth e and diameter d can be calculated as being the extreme values of the final dimple shape.

The radius (r) of the circle forming the spherical dimple is calculated according to the theory of a circular segment

$$r = \frac{e^2 + d^2/4}{2e}$$

The intersections in the tangential direction can be calculated by solving the system of equations consisting of respectively the spherical surface and the cylindrical tube:

$$(x - x_c)^2 + (y - y_c)^2 + (z - z_c)^2 = r^2$$

$$x^2 + y^2 = R^2, \forall z$$

The following substitutions can be made in the cross-sectional plane without affecting generality of the solution:

$$x_c = R + e - r, y_c = 0, x = R \cos \frac{\beta}{2}, y = R \sin \frac{\beta}{2},$$

from which the angle β and width (d) of the dimple readily follow:

$$\Rightarrow \beta = 2 \cos^{-1} \left(1 - \frac{er - e^2/2}{R^2 + eR - rR} \right)$$

$$d' = 2R \sin \frac{\beta}{2}$$

The percentage of the surface covered by dimples can be approximated by assuming the intersection to be an ellipse with major axis the circular arc on the cylindrical surface βR and minor axis the dimple diameter (d), multiplied by the number of dimples and divided by the unmodified cylindrical surface.

$$\text{Area Coverage (AC) [\%]} \cong \frac{100 * \text{Number of dimples} * \left(\frac{d\beta R}{4} \right)}{2LR}$$

A.4.2 Exemplary embodiments of dimples

For an exemplary embodiment according to the present invention of a dimple design a reference is made to Figure A-4, which depicts a development (top view) and a radial section (bottom view) of the inner surface of a reactor inner wall of four dimple shapes, including spherical (a), teardrop (b), spheroid (c) and inclined (d) spheroid dimple designs.

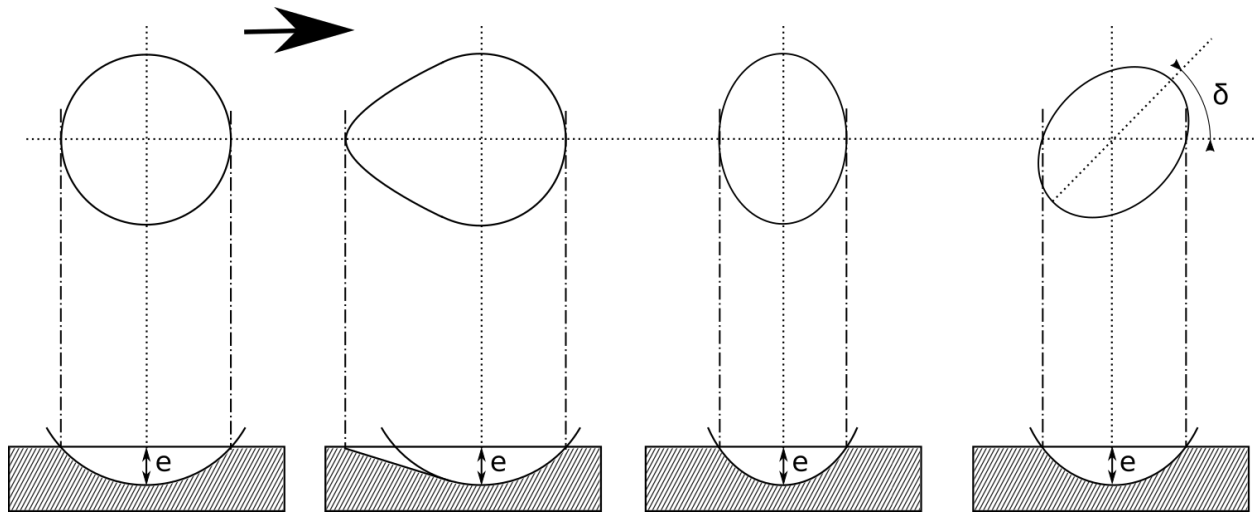


Figure A-4: Development (top) and radial section (bottom) of the inner surface of a tube of the invention for illustrating different dimple shapes, including spherical (a), teardrop (b), spheroid (c) and inclined (d) spheroid dimple designs. For the inclined spheroid dimple the angle δ is defined as the angle between the flow direction and the major axis of the spheroid.

Table A-1 presents an overview of the main physical properties of tested dimple designs. The ‘Prior Art’ tube in Table A-1 comprises a spiral ribbed tube, in which the rib is of semi-circular convex shape with a maximal height of 0.04 relative to the tube diameter and in which the rib is further attached to the tube inner surface at an angle of 65° to the axial flow direction, similar to the ‘heat exchange tube’ technology of Kubota (as described in US5950718, also labeled as ‘Prior Art 1’), which seeks to periodically break the laminar flow by the presence of inwardly oriented helical fins.

Table A-1: Parametric configuration of the tested dimple designs.

Test Tubes									
No.	I.D. [mm]	Shape	e [mm]	d [mm]	# [-]	γ [°]	t1 [mm]	t2 [mm]	AC [%]
CP1	50	Sphere	0.2	4	32	30	4.9	4	80.3
CP2	50	Sphere	0.4	4	32	30	4.9	4	75.4
CP3	50	Sphere	0.75	7.5	16	11.25	9.8	7.5	75.1
CP4	50	Sphere	1.5	15	8	22.5	19.6	15	90.4
CP5	50	Sphere	2.25	15	8	22.5	19.6	15	80.0
CP6	50	Sphere	3.0	15	8	22.5	19.6	15	71.7
N1 / P1	50	Sphere	1.5	15	8	0	19.6	15	90.2
N2	50	Sphere	1.5	15	6	0	26.2	15	82.5
N3 / X1 / W5	50	Sphere	1.5	15	4	0	39.3	15	56.9
P2	50	Sphere	1.5	15	8	0	19.6	16	85.3
P3	50	Sphere	1.5	15	8	0	19.6	20	67.6
P4	50	Sphere	1.5	15	8	0	19.6	30	45.1
P5	50	Sphere	1.5	15	8	0	19.6	60	22.5
X2	50	Sphere	1.5	15	4	30	39.3	15	56.9
X3	50	Sphere	1.5	15	4	45	39.3	15	56.9
X4	50	Sphere	2.5	15	6	0	26.2	30	29.6
X5	50	Sphere	2.5	15	6	45	26.2	30	29.6
W1	50	Sphere	1.5	5	4	0	39.3	5	10.3
W2	50	Sphere	1.5	8	4	0	39.3	8	17.6
W3	50	Sphere	1.5	10	4	0	39.3	10	23.4

W4	50	Sphere	1.5	12	4	0	39.3	12	31.8
R1	30.2	Sphere	0.9	6	8	45	11.9	4.1	65.8
R2	30.2	Sphere	1.9	7.5	8	0	11.9	12.5	39.4
R3	30.2	Sphere	3.9	8.5	4	0	23.7	12.5	31.9
Ref	50	-	-	-	-	-	-	-	0.0
Prior Art 1	50	Spiral convex rib	2	11.2	-	64.5	-	75	15.0
Prior Art 2	30.2	Longitudinal rounded fin	3.6	-	8	0	-	-	100
Prior Art 3	30.2	Perpendicular convex rib	1	3	-	90	-	24	12.5

A.4.3 Results of tested dimple designs.

The various dimple designs presented in A.4.2, cfr. Table A-1, were tested at a Reynolds number (Re) of 11,000 for heat transfer and friction characteristics and the results are set out in Table A-2, below. To better illustrate the results, Figure A-5 depicts a graph showing pressure loss and heat transfer augmentation compared to a reference tube (i.e., a bare tube without dimples) and prior art. Additionally, Figure A-6 illustrates the Re dependency for the relative heat transfer augmentation and pressure losses for two embodiments of the current invention, compared to prior art, as described in A.4.2.

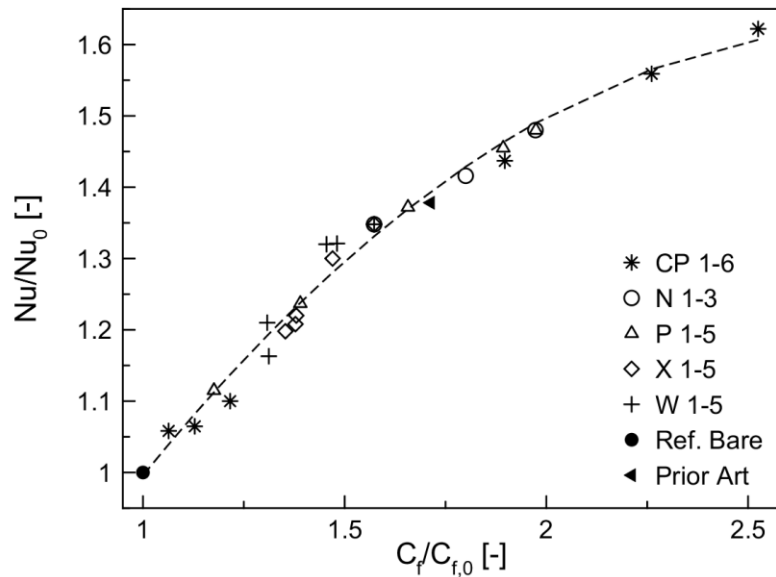


Figure A-5: Graph of relative pressure loss and heat transfer compared to a reference bare tube for the dimple parameter combinations and prior art of Table A-1.

The reduced sensitivity to Re may yield optimal performance over a wider range of flow conditions than the prior art, especially in the higher segment of Reynolds numbers.

Nu/Nu_0 is a heat transfer enhancement characteristic, $C_f/C_{f,0}$ is a friction enhancement factor, and $(Nu/Nu_0)/(C_f/C_{f,0})^{1/3}$ is a thermal enhancement factor of the augmented surface at equal pumping power.

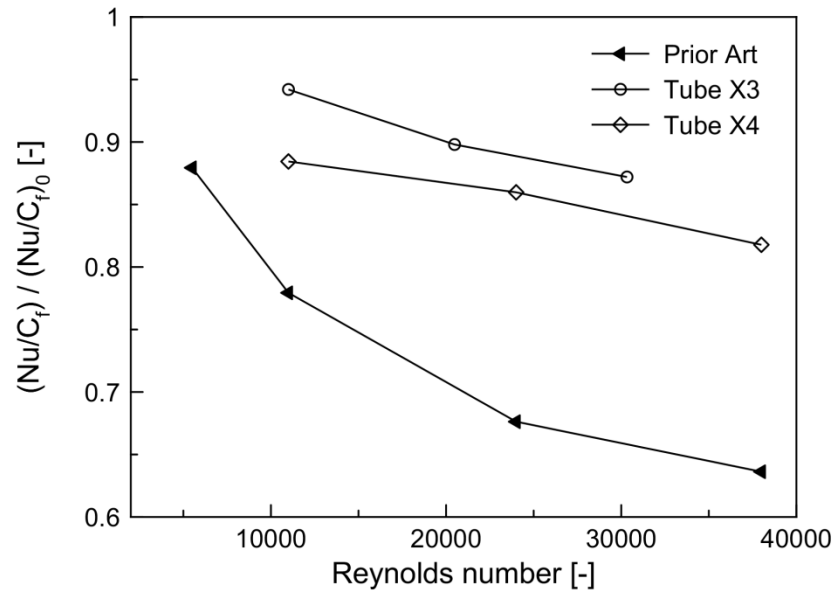


Figure A-6: Graph of the Reynolds number dependency for the relative heat transfer augmentation and pressure losses for two embodiments of the current invention, compared to a prior art tube.

Table A-2: Heat transfer improvement of the tested dimple designs.

Test Tubes	Re = 11,000		
No.	Nu/Nu ₀	C _f /C _{f,0}	(Nu/Nu ₀)/(C _f /C _{f,0}) ^{1/3}
CP1	1.06	1.06	1.04
CP2	1.06	1.13	1.02
CP3	1.10	1.22	1.03
CP4	1.44	1.90	1.16
CP5	1.56	2.26	1.19
CP6	1.62	2.53	1.19
N1 / P1	1.35	1.57	1.16
N2	1.42	1.80	1.16
N3 / X1 / W5	1.48	1.97	1.18
P2	1.46	1.89	1.18
P3	1.37	1.66	1.16
P4	1.24	1.39	1.11
P5	1.12	1.18	1.06
X2	1.21	1.38	1.09
X3	1.20	1.35	1.08
X4	1.30	1.47	1.14
X5	1.22	1.38	1.10
W1	1.16	1.31	1.06
W2	1.21	1.31	1.11
W3	1.32	1.46	1.16
W4	1.32	1.48	1.16

Ref	1.00	1.00	1.00
Prior Art 1	1.38	1.71	1.15

A.4.4 Impact on olefin yields in a steam cracker

Reactive CFD simulations were performed for a set of different dimple configurations, along with configurations according to the existing prior art. The geometries R1, R2, R3 were compared with a traditional bare tubular reactor, as well as a longitudinally finned reactor (as described in GB Patent 969796, also labelled as ‘Prior Art 2’) and a reactor with a convex rib applied perpendicular to the flow direction (similar to the design in US Patent 5950718, also labelled as ‘Prior Art 3’). The parameters of these designs are listed in Table A-1.

Simulations were performed using the open-source CFD package OpenFOAM, using a well-validated $k\omega$ -SST turbulence model and a free-radical reaction network suited for propane cracking. The simulated industrial geometry is of the single-pass Millisecond type, with a reactor diameter of 30.2mm and length of 10.56m.

Table A-3 lists the obtained results, indicating the advantages over using the prior art. It is clear that the positive effect on tube metal temperatures and coking rates can be achieved at a much lower penalty in pressure losses than for the ribbed design. While the finned design provides good heat transfer, the increased exposed surface area causes the fouling rate to be almost equal to the reference geometry. Additionally, yields are lost because of the large zone of high temperatures in between the fins, where unwanted side reactions occur.

Table A-3: Performance of the tested dimple designs in a propane Millisecond reactor.

	Ref	R1	R2	R3	Prior art 2	Prior art 3
ΔP [%]	-	+87	+59	+261	+29	+297
$\Delta T_{\text{wall, max}}$ [K]	-	-45	-35	-41	-27	-53
$\Delta r_{\text{cokes, max}}$ [%]	-	-39	-30	-31	-6	-50
Conversion [%]	75	75	75	75	75	75
$C_2H_4 + C_3H_6$ yield [%]	50.53	50.70	50.60	50.65	50.37	50.73

A.4.5 Self-cleaning effect of the dimpled designs

During large eddy simulations (LES) of flow over a single dimple, it was observed that a flow pattern emerges that causes the fluid to exit the dimples at an angle of 45° to the mean flow, enhancing the tangential mixing in the tube (Figure A-7). More importantly, this phenomenon is unstable but self-sustained, causing it to automatically switch flow direction with a certain frequency. The oscillatory behaviour occurs on a time scale that is in between the time scale of flow through the reactor (ms) and that of coke formation (hours). Because of this, it is expected that small particles of cokes can be spalled off continuously, in this manner achieving a sort of “self-cleaning” effect of the surface. This behaviour will be desirable in the process of coke removal, as more spalling will allow a faster return to operation and reduced downtime. Increased spalling during operation can also be desirable, provided that the downstream equipment can handle the fragments of spalled coke. If this is the case, substantially increased time can pass between reactor decokings and productivity will be improved.

Simulations were performed using a large eddy simulation framework where identical time-dependent inlet conditions were applied to three simulations with varying dimple depth-to-diameter ratios (DDR). Flow over a single dimple with fixed diameter was considered, in a

channel of height $h/d = 0.33$. The time-dependent velocities were monitored at both the left and right trailing edges of the concave dimple, at a relative angle of 45° with the mean flow, as illustrated in Figure A-7, along with a graphical representation of the flow, time-averaged over a period shorter than the time scale of the oscillations. Figure A-8 shows the instantaneous velocities for the highest DDR ratio, clearly illustrating the shifting direction of the fluid ejected from the dimple. Table A-4 lists the quantitative results for the four tested designs, obtained at an equal Reynolds number of 20,000. With increasing DDR, a positive impact on both the frequency and the amplitude of the oscillatory flows can be seen. For the most shallow dimple configurations, the flow still exits the dimple tangentially but remains symmetrical at all times and no large-scale oscillations were seen.

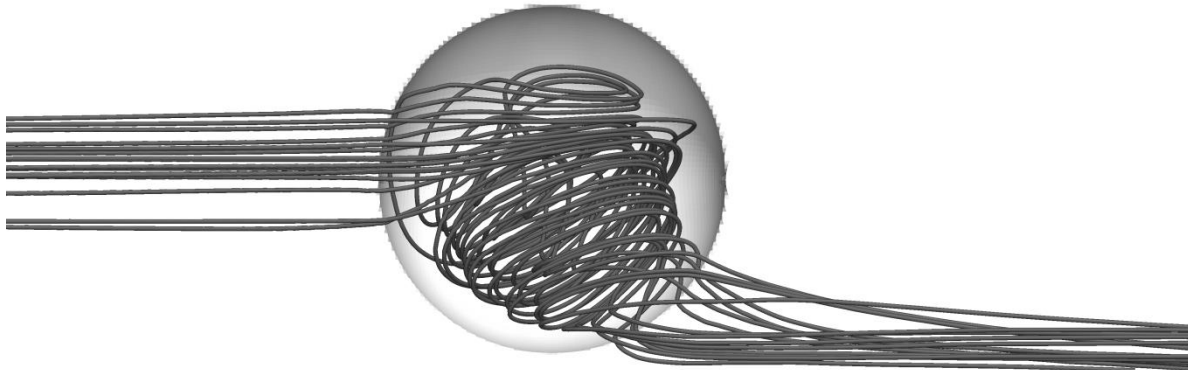


Figure A-7: Plot of the streamlines on a dimpled surface with dimple depth-to-diameter ratio of 0.45, obtained using the time-averaged large eddy simulation data between $t = 1.8s$ and $t = 2.0s$.

Table A-4: Properties of the self-sustained oscillatory flows responsible for a potential self-cleaning effect of the tested dimple designs.

	Frequency [1/s]	Amplitude-to-mean-velocity ratio [-]
DDR = 0.26	1.9	0.34
DDR = 0.45	4.5	0.53

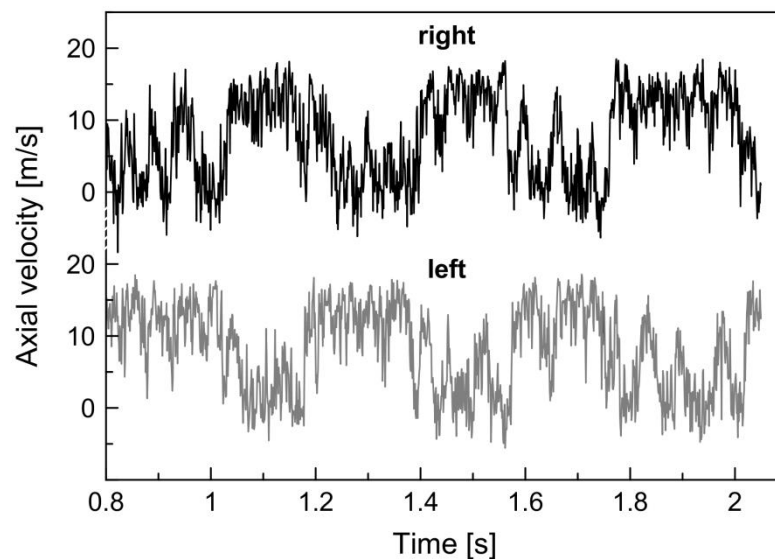


Figure A-8: Graph of instantaneous streamwise velocity at locations “left” and “right”, as indicated on Figure A-7.

A.5 Summary of the invention

The invention as described herein provides an answer to one or more of the above-mentioned needs. Preferred embodiments of the invention as described herein provide an answer one or more of the above-mentioned needs.

According to a first aspect, the invention relates to a reactor for cracking hydrocarbons wherein the reactor has an inner wall; characterized in that the inner wall comprises a plurality of concave

dimples embedded in a surface of said inner wall. Preferably, the reactor is a pyrolysis, thermal cracking, or steam cracking reactor.

In some preferred embodiments, each concave dimple of the plurality of concave dimples is characterized by a dimple depth e , wherein e is at least 0.01 cm and at most 1.0 cm, preferably at least 0.1 cm and at most 0.5 cm.

In some preferred embodiments, each concave dimple of the plurality of concave dimples is characterized by a dimple diameter d , wherein d is at least 0.1 cm and at most 5.0 cm, preferably at least 0.5 cm and at most 2.0 cm.

In some preferred embodiments, each concave dimple of the plurality of concave dimples is further characterized by a depth-to-diameter ratio (DDR), defined as

$$DDR = e/d;$$

wherein the DDR is at least 0.01 and at most 0.5, preferably at least 0.05 and at most 0.4; more preferably at least 0.1 and at most 0.3.

In some preferred embodiments, the shape of each dimple of the plurality of concave dimples is characterized by a geometrical feature, preferably by a smooth or curved edge, for example, at least a section of a sphere, a spheroid, an ovoid or a teardrop shape.

In some preferred embodiments, at least one dimple of the plurality of dimples further comprises two or more secondary curvature areas of a different curvature radius than the main concavity, wherein the secondary curvature areas are situated on the edge of, or within the main concavity. Figure A-3 exemplifies such secondary curvature areas.

In some preferred embodiments, at least a portion of the plurality of concave dimples is arranged in one or more patterns, preferably wherein the pattern is linear, staggered, and/or crossed.

In some preferred embodiments, at least a portion of the inner wall is smooth, *i.e.*, not covered by any concave dimples, further characterized by an area coverage (AC) defined as

$AC (\%) = \text{total area of the inner wall covered by dimples} / \text{total area of the inner wall} * 100$;

wherein the AC is at least 1% and at most 99%, preferably at least 20% and at most 90%.

In some preferred embodiments, the reactor has a tubular shape and is characterized by:

- a total reactor length of at least 10 m to at most 400 m;
- an inner diameter of at least 2 cm to at most 20 cm, preferably at least 3 cm and at most 15 cm;
- an outer diameter, larger than the inner diameter, of at least 3.0 cm and at most 22.0 cm, preferably at least 5.0 cm and at most 17.0 cm; and
- a wall thickness, defined as half the difference between the outer diameter and the inner diameter, of at least 0.3 cm and at most 2.0 cm, preferably at least 0.5 cm and at most 1 cm.

In some preferred embodiments, the wall thickness is greater than twice the dimple depth e ($2*e$), preferably wherein the wall thickness is greater than $3*e$. Typically the wall thickness is always greater than the dimple depth e .

In some preferred embodiments, the inner wall comprises a metal, a metal alloy, a ceramic, and/or a combination thereof.

In some preferred embodiments, each dimple of the plurality of concave dimples comprises the same material as the reactor.

According to a second aspect, the invention relates to a furnace, comprising a reactor according to the first aspect of the invention, and preferred embodiments thereof.

According to a third aspect, the invention relates to a method for producing a reactor according to the first aspect of the invention, and preferred embodiments thereof, the method comprising one of the following steps: moulding; casting; excavation; and/or deposition.

According to a fourth aspect, the invention relates to a method for producing light olefins in a reactor according to the first aspect of the invention, and preferred embodiments thereof, or in a

furnace according to the second aspect of the invention, and preferred embodiments thereof, the method comprising the step of cracking a hydrocarbon feedstock into light olefins at a temperature of at least 700°C and at most 900°C.

A.6 Claims

1. A pyrolysis, thermal cracking, or steam cracking reactor for cracking hydrocarbons wherein the reactor has an inner wall; characterized in that the inner wall comprises a plurality of concave dimples embedded in a surface of said inner wall.
2. The reactor according to claim 1, wherein the reactor is a steam cracking reactor.
3. The reactor according to claim 1 or 2, wherein each concave dimple of the plurality of concave dimples is characterized by a dimple depth e , wherein e is at least 0.01 cm and at most 1.0 cm, preferably at least 0.1 cm and at most 0.5 cm.
4. The reactor according to any one of claims 1 to 3, wherein each concave dimple of the plurality of concave dimples is characterized by a dimple diameter d , wherein d is at least 0.1 cm and at most 5.0 cm, preferably at least 0.5 cm and at most 2.0 cm.
5. The reactor according to claim 3 and 4, wherein each concave dimple of the plurality of concave dimples is further characterized by a depth-to-diameter ratio (DDR), defined as

$$DDR = e/d;$$

wherein the DDR is at least 0.01 and at most 0.5, preferably at least 0.05 and at most 0.4; more preferably at least 0.1 and at most 0.3.

6. The reactor according to any one of the preceding claims, wherein the shape of each dimple of the plurality of concave dimples is characterized by a geometrical feature, preferably by a smooth or curved edge, for example, at least a section of a sphere, a spheroid, an ovoid, or a teardrop shape.

7. The reactor according to claim 6, wherein at least one dimple of the plurality of dimples further comprises two or more secondary curvature areas of a different curvature radius than the dimple situated around, on top, or within the dimple.

8. The reactor according to any of the preceding claims, wherein at least a portion of the plurality of concave dimples is arranged in one or more patterns, preferably wherein the pattern is linear, staggered, and/or crossed.

9. The reactor according to any one of the preceding claims, wherein at least a portion of the inner wall is smooth, *i.e.*, not covered by any concave dimples, further characterized by an area coverage (AC) defined as $AC (\%) = \text{total area of the inner wall covered by dimples} / \text{total area of the inner wall} * 100$; wherein the AC is at least 1% and at most 99%, preferably at least 20% and at most 90%.

10. The reactor according to any one of the preceding claims, wherein the reactor has a tubular shape and is characterized by:

- a total reactor length of at least 10 m to at most 400 m;
- an inner diameter of at least 2 cm to at most 20 cm, preferably at least 3 cm and at most 15 cm;
- an outer diameter, larger than the inner diameter, of at least 3.0 cm and at most 22.0 cm, preferably at least 5.0 cm and at most 17.0 cm; and
- a wall thickness, defined as half the difference between the outer diameter and the inner diameter, of at least 0.3 cm and at most 2.0 cm, preferably at least 0.5 cm and at most 1 cm.

11. The reactor according to claim 10, wherein the wall thickness is greater than twice the dimple depth e , preferably wherein the wall thickness is greater than $3 * e$.

12. The reactor according to any of the preceding claims, wherein the inner wall comprises a metal, a metal alloy, a ceramic, and/or a combination thereof.

13. The reactor according to claim 12, wherein each dimple of the plurality of concave dimples comprises the same material as the reactor.

14. A furnace, comprising one or more reactors according to any one of the preceding claims.

15. A method for producing light olefins in a reactor according to any one of claims 1 to 13, or in a furnace according claim 14, the method comprising the step of cracking a hydrocarbon feedstock into light olefins at a temperature of at least 700°C and at most 900°C.

Appendix B

LES grid dependency study

To study the grid dependency, simulations were performed at four different levels of refinement, as listed in Table B-1.

Table B-1: Control volume dimensions

$N_r \times N_\theta \times N_z$	Grid spacing			
	Δr^+_{\min}	Δr^+_{\max}	$(r\Delta\theta)^+_{\max}$	Δz^+
35 x 80 x 80	0.41	16	27	64
50 x 120 x 188	0.41	11	18	27
65 x 180 x 260	0.41	7	12	20
84 x 240 x 376	0.41	5	8	14

The mean streamwise velocity profile normalized by friction velocity is shown in Figure B-1(a). It is clear that the linear velocity distribution for $y^+ < 5$ is well resolved for all the grids. For the region where $y^+ > 30$, the fine grid results agree very well with the DNS results and confirm the well-known deviation from the law of the wall in pipe flow¹. Root-mean-square velocity fluctuations as shown on Figure B-1(b) also tend to agree well with the DNS results, albeit with an underprediction of the radial and tangential components for the coarser grids. This was expected as the contribution of the unresolved smallest scale motions increases along with the grid spacing.

Profiles of the Reynolds shear stress τ_{res} , viscous shear stress τ_{vis} and the modeled subfilter-scale stresses τ_{sfs} are shown in Figure B-2. Relatively good agreement with DNS results is obtained for all

but the coarsest grids. The contribution of the modeled stresses is clearly higher for the coarser grids, especially in the near-wall region.

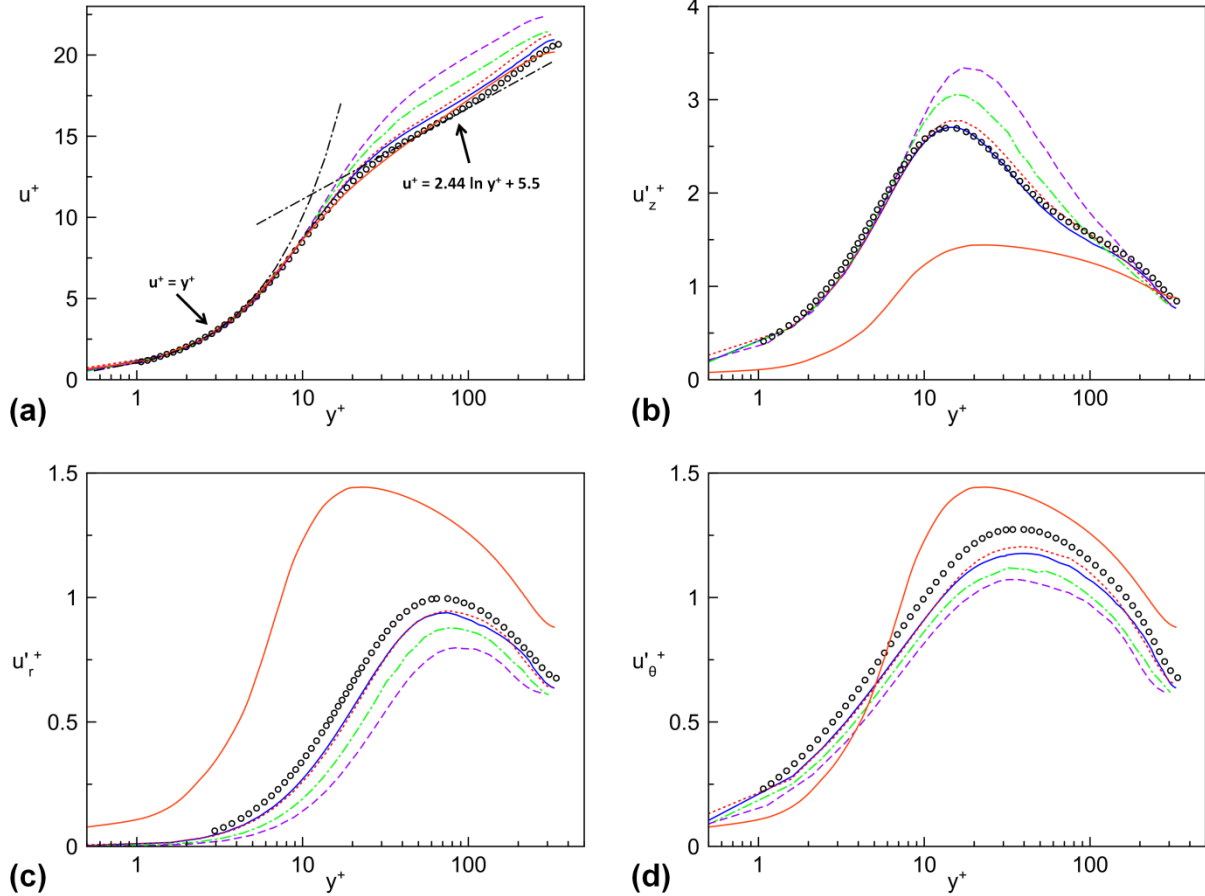


Figure B-1: (a) Mean streamwise velocity profile in wall coordinates. (b,c,d) Normalized root-mean-square velocity fluctuations. — - LES (84x240x376); - - - - LES (65x180x260); - · - · - LES (50x120x188); - - - - - LES (35x80x80); ○ - DNS El Khoury et al. ²; — - RANS (65x180x260)

The mean dimensionless temperatures and temperature fluctuations are plotted in wall units on Figure B-3(a) and (b). In the conductive sublayer the linear $\theta^+ = \text{Pr } y^+$ profile is discerned, followed by a logarithmic region, as previously observed for the velocity profile. Although no heat transfer DNS data in pipe flow was available at the present Reynolds number, the simulated overall trends correspond to those observed for the lower Reynolds number DNS data. The empirical correlation of Kader ³ is also showing good agreement with the present data. The near-wall behavior of temperature fluctuations is seen to depend on the type of boundary condition

that is applied. For the ideal iso-flux case, as performed by Piller⁴, a finite value is obtained near the wall. The fixed wall temperature conditions applied by Redjem-Saad et al.⁵ however dampens all fluctuations.

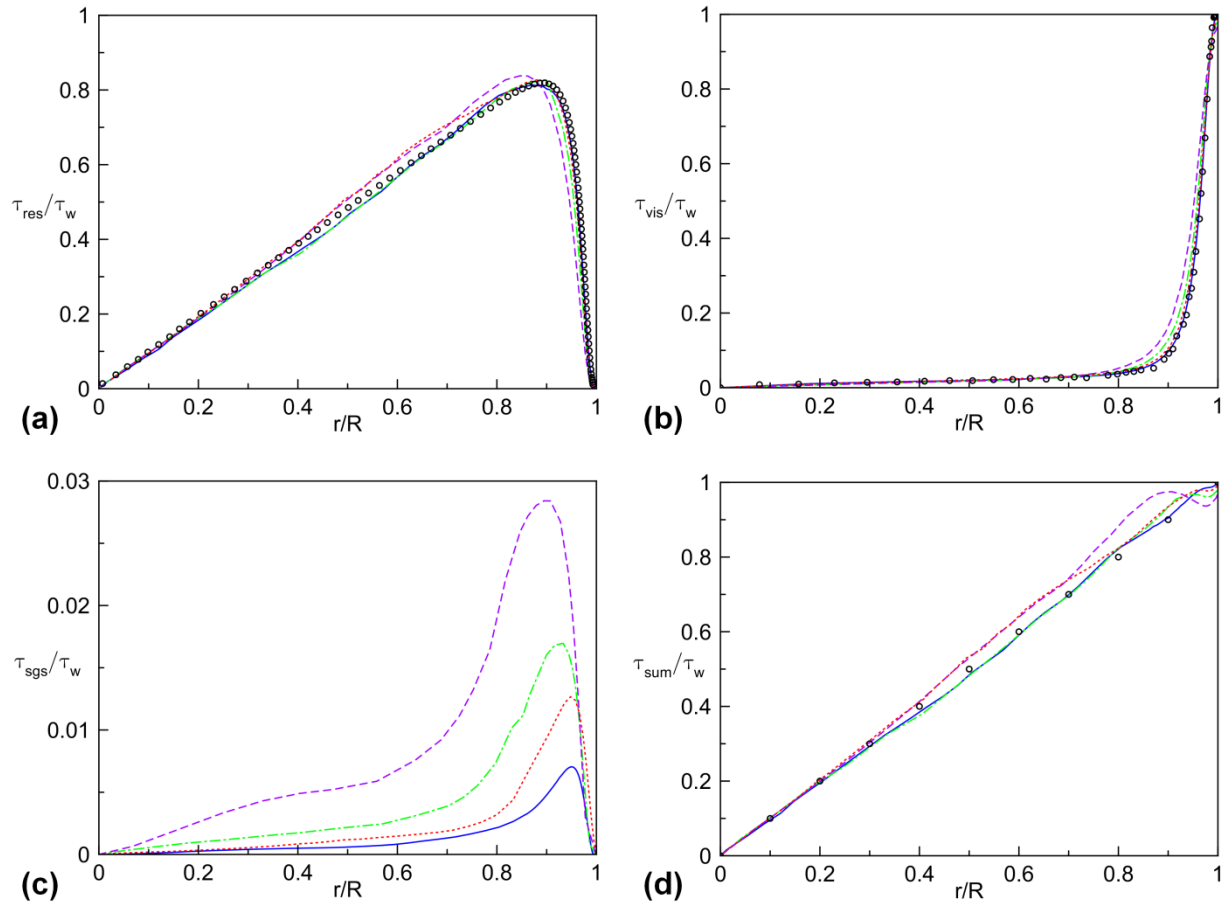


Figure B-2: (a) Resolved, (b) viscous, (c) modeled subfilter-scale and (d) total shear stress distributions scaled by wall shear stress. — - LES (84x240x376); ··· - LES (65x180x260); --- - LES (50x120x188); - · - LES (35x80x80); ○ - DNS El Khoury et al.²;

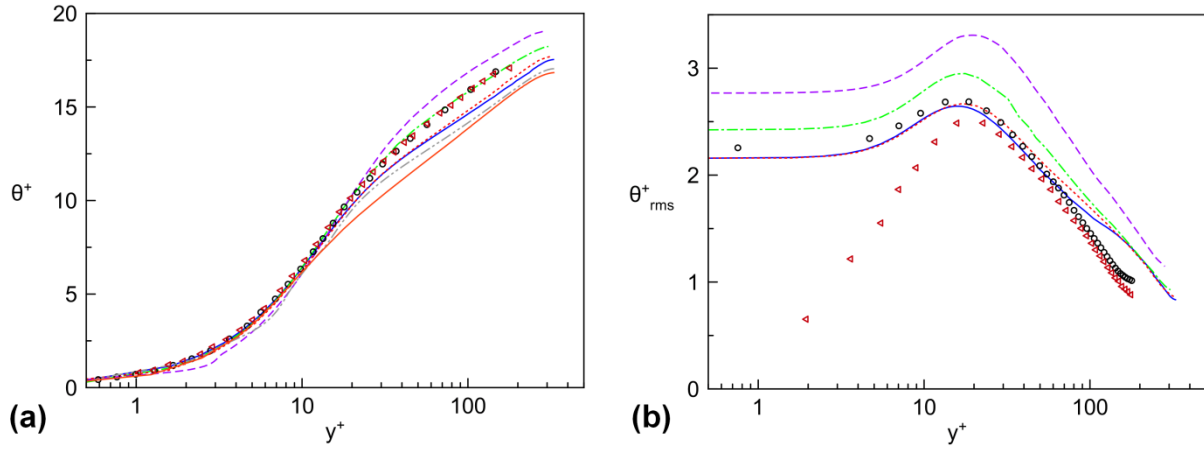


Figure B-3: Mean (a) and root-mean-square (b) temperature profile. — - LES (84x240x376); - - - - LES (65x180x260); - · - · - LES (50x120x188); - - - - LES (35x80x80); ○ - DNS Piller ⁴; ◁ - DNS Redjem-Saad et al. ⁵; - - - - Kader correlation ³; — - RANS (65x180x260)

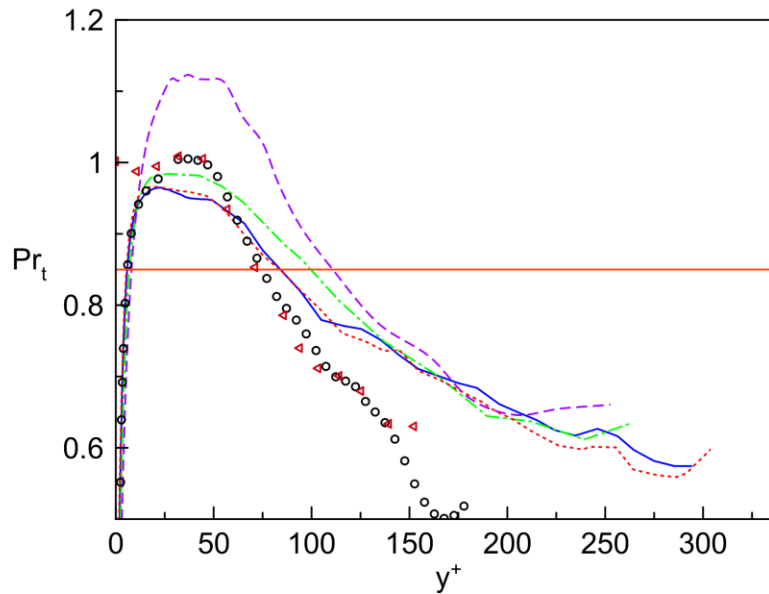


Figure B-4: Radial profiles of the turbulent Prandtl number. — - LES (84x240x376); - - - - LES (65x180x260); - · - · - LES (50x120x188); - - - - LES (35x80x80); ○ - DNS Piller ⁴; ◁ - DNS Redjem-Saad et al. ⁵; — - RANS

In addition to the profiles of velocity and temperature, the average friction coefficients and Nusselt numbers were compared to DNS results and various empirical correlations. The Fanning friction factor is obtained from the time-average of the dynamically adjusted momentum source term β :

$$f_f = \frac{\Delta p D}{2\rho u_b^2 \Delta z} = \frac{\beta}{4} \quad (\text{B.1})$$

The simulated global Nusselt number is calculated according to Eq. (B.2):

$$\text{Nu} = \frac{D_{eq} \left(\frac{\partial \tilde{\theta}}{\partial r} \right)_{y=0}}{(\tilde{\theta}_{wall} - \tilde{\theta}_{bulk})} \quad (\text{B.2})$$

A full overview of the applied correlations and simulation results is shown in Table B-2 and Table B-3. Results obtained on the finest two grids are seen to compare very well with the empirical correlations, demonstrating the capability of the applied finite volume formulation towards performing accurate large eddy simulations. An additional simulation was performed with the same grid resolution as the finest case but with an axial domain length that was only a quarter of the other cases. Results for friction factors and Nusselt numbers are seen to be very close to the full-length simulations. This indicates that if the primary interest is in determining global quantities, grid refinement in the radial and tangential direction will offer greater benefit than increasing the domain length for a similar computational cost.

Table B-2: Comparison of the Fanning friction factor for varying grid densities and empirical correlations

Source	Equation	$f_f \times 10^3$	% diff
Present LES (35 x 80 x 80)	-	6.076	-20.2
Present LES (50 x 120 x 188)	-	6.745	-11.4
Present LES (65 x 180 x 260)	-	7.209	-5.3
Present LES (84 x 240 x 376)	-	7.413	-2.6
Present LES - L/4 (84 x 240 x 94)	-	7.398	-2.8
Present RANS (65 x 180 x 260)	-	7.659	+0.6

DNS El Khoury et al. ²	-	7.614	-
Blasius ⁶	$0.079 Re^{-0.25}$	7.714	+1.3
Churchill ⁷	$2((8/Re)^{12} + (A + 37530/Re)^{-24})^{1/12}$ $A = -2.2113 \ln(7/Re)$	7.551	-0.8
Petukhov ⁸	$(3.64 \log_{10}(Re) - 3.28)^{-2}$	7.653	+0.5
Kays and Crawford ⁹	$0.046 Re^{-0.2}$	7.153	-6.1

Table B-3: Comparison of the Nusselt number for varying grid densities and empirical correlations

Source	Equation	Nu	% diff
Present LES (35 x 80 x 80)	-	26.32	-19.6
Present LES (50 x 120 x 188)	-	29.38	-10.3
Present LES (65 x 180 x 260)	-	32.04	-2.1
Present LES (84 x 240 x 376)	-	32.59	-0.5
Present LES - L/4 (84 x 240 x 94)	-	32.67	-0.2
Present RANS (65 x 180 x 260)	-	34.64	+5.8
Kader profile ³	-	32.74	-
McAdams ¹⁰	$0.021 Re^{0.8} Pr^{0.4}$	31.32	-4.3
Gnielinski ¹¹	$\frac{(C_f/2)(Re - 1000)Pr}{1 + 12.7(C_f/2)^{1/2}(Pr^{2/3} - 1)}$	32.36	-1.2
Kays and Crawford ⁹	$0.022 Re^{0.8} Pr^{0.5}$	31.71	-3.2

References

1. Lawn, C.J., *The determination of the rate of dissipation in turbulent pipe flow*. Journal of Fluid Mechanics, 1971. **48**(03): p. 477-505.
2. El Khoury, G.K., P. Schlatter, A. Noorani, P.F. Fischer, G. Brethouwer, and A.V. Johansson, *Direct Numerical Simulation of Turbulent Pipe Flow at Moderately High Reynolds Numbers*. Flow Turbul. Combust., 2013. **91**(3): p. 475-495.
3. Kader, B.A., *Temperature and concentration profiles in fully turbulent boundary layers*. International Journal of Heat and Mass Transfer, 1981. **24**(9): p. 1541-1544.
4. Piller, M., *Direct numerical simulation of turbulent forced convection in a pipe*. International Journal for Numerical Methods in Fluids, 2005. **49**(6): p. 583-602.
5. Redjem-Saad, L., M. Ould-Rouiss, and G. Lauriat, *Direct numerical simulation of turbulent heat transfer in pipe flows: Effect of Prandtl number*. International Journal of Heat and Fluid Flow, 2007. **28**(5): p. 847-861.
6. Blasius, H., *Das Aehnlichkeitsgesetz bei Reibungsvorgängen in Flüssigkeiten*, in *Mitteilungen über Forschungsarbeiten auf dem Gebiete des Ingenieurwesens*, 1913, Springer Berlin Heidelberg. p. 1-41.
7. Churchill, S.W., *Friction Factor Equations Spans all Fluid Flow Regimes*. Chemical Engineering, 1977. **84**: p. 91-102.
8. Petukhov, B.S., *Heat Transfer and Friction in Turbulent Pipe Flow with Variable Physical Properties*, in *Advances in Heat Transfer*, T.F.I. J. P. Hartnett, Editor 1970, Academic Press: New York.
9. Kays, W.M., M.E. Crawford, and B. Weigand, *Convective heat and mass transfer*. 2012: Tata McGraw-Hill Education.
10. McAdams, W.H., *Heat transmission*. Vol. 3. 1954, New York: McGraw-Hill.
11. Gnielinski, V., *New equations for heat and mass-transfer in turbulent pipe and channel flow*. International Chemical Engineering, 1976. **16**(2): p. 359-368.

Appendix C

JH-v2 model validation

C.1 Pipe flow

Along with channel flow, pipe flow is probably the most investigated turbulent flow. As such, it is imperative that any turbulence model be able to accurately describe the profiles in such a canonical flow configuration. For this purpose, the JH-v2 results were compared with the DNS data of Redjem-Saad et al. ¹ obtained at a bulk Reynolds number of 5,500.

Mean and root-mean-square velocities along the pipe radius are plotted in Figure C-1. The overall velocity profile appear well predicted, with a relative error of 1.3% on the friction velocity. It is seen that the Reynolds stress anisotropy is also well captured, though underpredictions of the axial and tangential components can be seen close to the wall. The wall-reflection terms in the model appears to function correctly however, as a very good near-wall profile can be seen for the wall-normal stresses. The obtained profiles are also in very close agreement with those obtained by Morsbach et al. ² for their implementation of the JH-v2 model. This indicates that the implementation in the OpenFOAM framework was successful and remaining error lies with the model formulation itself.

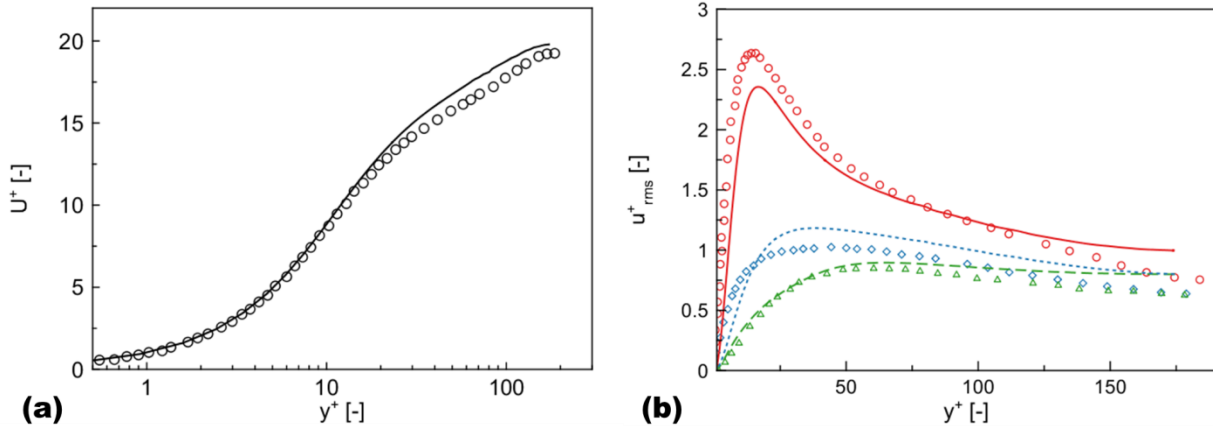


Figure C-1: Mean (a) streamwise velocity and (b) root-mean-square velocities in wall units along the pipe radius. —○— - u_{xx}^+ , —△— - u_{rr}^+ , —◇— - $u_{\theta\theta}^+$. Symbols: DNS Redjem-Saad et al. {Redjem-Saad, 2007 #2}; lines: JH-v2 model.

C.2 Square duct flow

Simulations of turbulent flow in a straight square duct were performed in order to validate the two-way coupling between the calculated Reynolds stresses and the flow. From literature, the existence of so-called secondary flows of Prandtl's second kind in geometries with sharp concave corners is well-known since their discovery by Nikuradse³. Due to the preferential orientation of coherent turbulent structures, a secondary flow is generated that drives fluid from the core of the duct towards the corners. It then follows the duct surface, until another one of these vortex structures is encountered and the fluid is driven back towards the core of the duct. In this manner the square duct induces a secondary motion consisting of eight vortex cells with alternating rotation signs. Though the secondary velocities amount to less than 2-3% of the bulk velocity, they significantly alter the primary flow and the distribution of shear stresses on the duct surface.

As these flows are directly caused by the Reynolds stresses anisotropy, they provide an excellent test case for the evaluation of newly implemented differential stress model. In the present work, comparison is made with the DNS data of Pinelli et al.⁴ obtained at a Reynolds number of 3,500, based on the duct half-height h .

Figure C-2 shows the streamwise and cross-stream mean and root-mean-square velocity components along the $z/h = -0.7$ edge. Relatively good agreement is seen for both the secondary flows and the Reynolds stress anisotropy that is responsible for them. As in the pipe flow simulations, the largest discrepancies can again be seen close to the duct surface, where the three normal stress components are underpredicted.

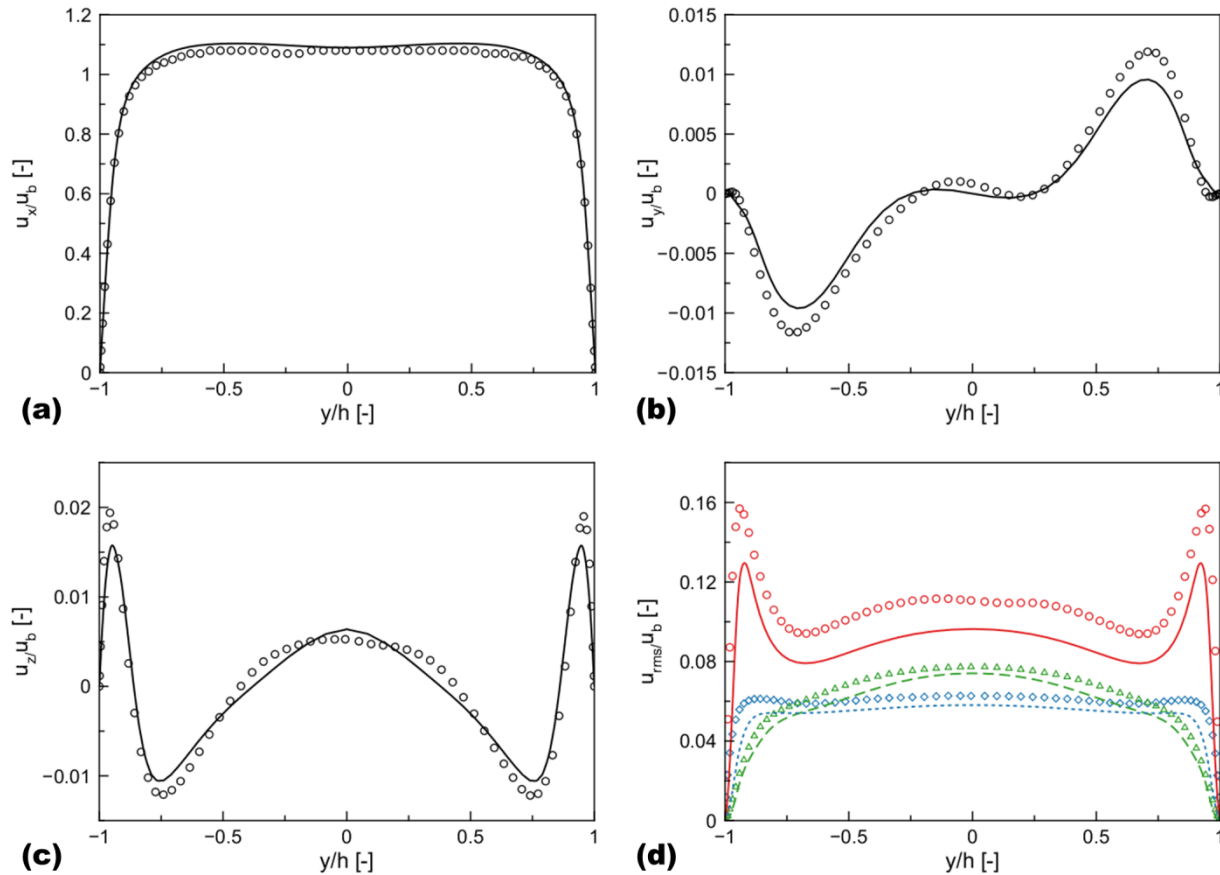


Figure C-2: Mean (a) streamwise, (b) wall-normal, (c) tangential velocities and (d) root-mean-square velocities along the $z/H = -0.7$ edge of a square duct; —○— - u_{xx} , —△— - u_{yy} , —◇— - u_{zz} . Symbols: DNS ⁴; lines: JH-v2 model.

The two counter-rotating vortex cells closely match the data of Pinelli et al. ⁴, as seen from the streamlines in the bottom-left quadrant of the square duct, shown in Figure C-3. The JH-v2 model is seen to shift the position of minimal secondary velocity towards the corner of the duct,

which is likely caused by the slight overprediction of the in-plane normal stresses relative to the streamwise stress component. Overall it can be concluded that the JH-v2 model succeeds reasonably well in the challenging task of reproducing the secondary flow features due to the Reynolds stress anisotropy.

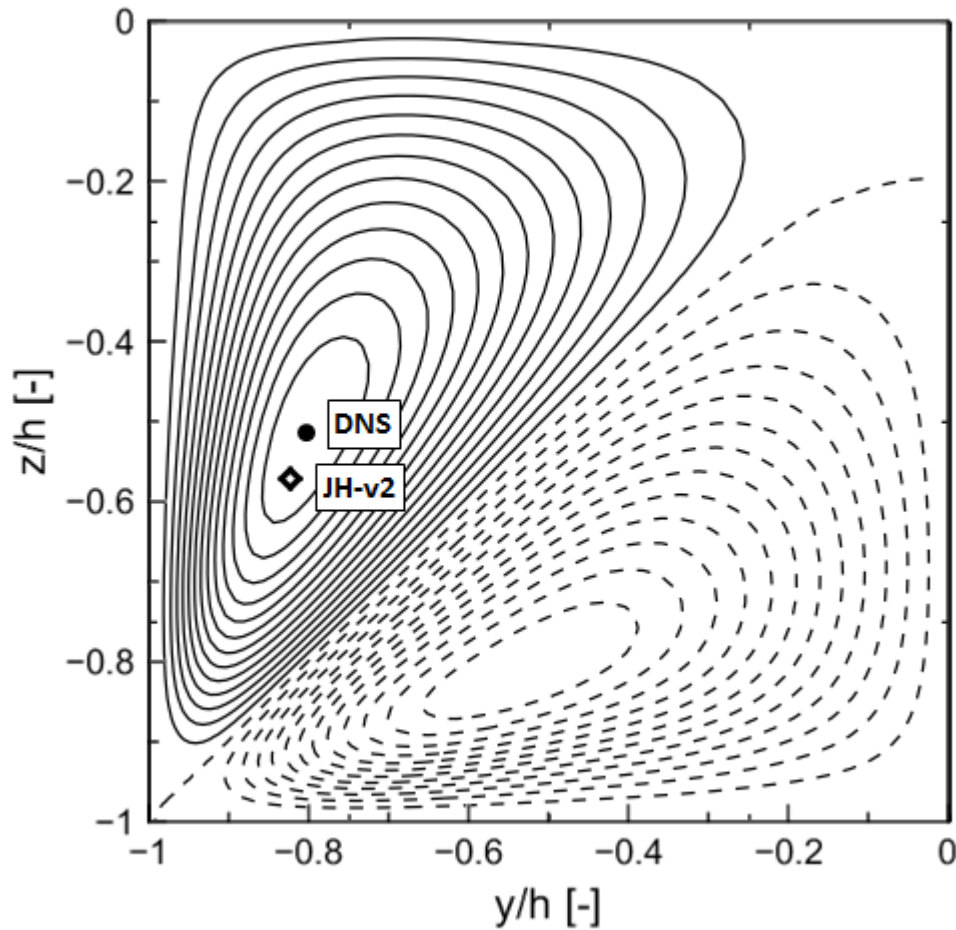


Figure C-3: Streamlines of secondary mean flow in the bottom-left corner of a square duct ⁴, along with the position of minimum secondary velocity for the DNS and JH-v2 model. Continuous and dashed lines correspond with respectively clockwise and counterclockwise rotation.

References

1. Redjem-Saad, L., M. Ould-Rouiss, and G. Lauriat, *Direct numerical simulation of turbulent heat transfer in pipe flows: Effect of Prandtl number*. International Journal of Heat and Fluid Flow, 2007. **28**(5): p. 847-861.
2. Morsbach, C., M. Franke, and F. di Mare, *Application of a Low Reynolds Differential Reynolds Stress Model to a Compressor Cascade Tip-Leakage Flow*, in *Differential Reynolds Stress Modeling for Separating Flows in Industrial Aerodynamics*, B. Eisfeld, Editor 2015, Springer International Publishing: Cham. p. 1-17.
3. Nikuradse, J., *Untersuchungen über die Geschwindigkeitsverteilung in turbulenten Strömungen*, 1926, Göttingen: VDI Forsch. 281.
4. Pinelli, A., M. Uhlmann, A. Sekimoto, and G. Kawahara, *Reynolds number dependence of mean flow structure in square duct turbulence*. Journal of Fluid Mechanics, 2010. **644**: p. 107-122.

